



HAL
open science

Performance and ageing quantification of electrochemical energy storage elements for aeronautical usage

Yuanci Zhang

► **To cite this version:**

Yuanci Zhang. Performance and ageing quantification of electrochemical energy storage elements for aeronautical usage. Electronics. Université de Bordeaux, 2019. English. NNT : 2019BORD0029 . tel-02275816

HAL Id: tel-02275816

<https://theses.hal.science/tel-02275816>

Submitted on 2 Sep 2019

HAL is a multi-disciplinary open access archive for the deposit and dissemination of scientific research documents, whether they are published or not. The documents may come from teaching and research institutions in France or abroad, or from public or private research centers.

L'archive ouverte pluridisciplinaire **HAL**, est destinée au dépôt et à la diffusion de documents scientifiques de niveau recherche, publiés ou non, émanant des établissements d'enseignement et de recherche français ou étrangers, des laboratoires publics ou privés.

THÈSE PRÉSENTÉE
POUR OBTENIR LE GRADE DE
DOCTEUR DE
L'UNIVERSITÉ DE BORDEAUX

ÉCOLE DOCTORALE SCIENCES PHYSIQUES ET DE L'INGÉNIEUR
SPÉCIALITÉ ÉLECTRONIQUE

par

Yuanci ZHANG

**Performance and ageing quantification of
electrochemical energy storage elements for aeronautical usage**

Sous la direction de : Jean-Michel VINASSA

Co-direction : Olivier BRIAT

Soutenue le 15/03/2019

Membres du jury :

Corinne ALONSO, Professeur à l'Université de Toulouse III Paul Sabatier, LAAS	Présidente
Christophe FORGEZ, Professeur à l'Université de Technologie de Compiègne, LEC	Rapporteur
Pascal VENET, Professeur à l'Université de Lyon 1, Ampère	Rapporteur
Delphine RIU, Professeur à Grenoble INP, G2Elab	Examinatrice
Loïc BOULON, Professeur à l'Université du Québec à Trois-Rivières, IRH	Examineur
Fabio COCETTI, Chef de pôle à l'IRT Saint-Exupéry	Examineur
Olivier BRIAT, Maître de Conférence HDR à l'Université de Bordeaux, IMS	Co-directeur de thèse
Jean-Michel VINASSA, Professeur à Bordeaux INP, IMS	Directeur de thèse

Remerciements

Ce manuscrit résume trois ans d'aventures inoubliables passées au Laboratoire de l'Intégration du Matériau au Système (IMS) au sein de l'équipe Puissance du groupe Fiabilité. Je ne pourrais pas commencer la présentation de ce mémoire sans remercier toutes les personnes ayant contribué de près ou de loin à mes travaux de thèse.

Je remercie en premier lieu Monsieur Yann Deval, directeur de l'IMS, ainsi que Mme Geneviève Duchamp responsable du groupe Fiabilité. Je remercie également l'IRT Saint Exupéry d'avoir financé ma thèse et de m'avoir fourni les moyens pour réaliser mes travaux de recherche dans les meilleures conditions. Je remercie Madame Régine Sutra-Orus, directrice du département Aéronef Plus Electrique à l'IRT, Monsieur Fabio Coccetti, responsable du pôle fiabilité et modélisation à l'IRT et Monsieur Guillaume Gager, chef de projet CELIA, pour leur soutien et leurs qualités humaines. Je remercie également les membres industriels de Safran Tech, Zodiac Aerospace et Airbus pour nos échanges intéressants lors de chaque réunion.

Je remercie vivement le Professeur Corinne Alonso d'avoir présidé le jury, son côté humain m'a impressionnée. Je suis honorée que le Professeur Pascal Venet et le Professeur Christophe Forgez aient accepté de rapporter ma thèse. Je les remercie énormément pour l'intérêt qu'ils ont porté à mon travail et pour les remarques constructives et pertinentes quant aux perspectives de mes travaux. Je remercie également le Professeur Delphine Riu et le Professeur Loïc Boulon d'avoir pris un temps précieux pour examiner et évaluer mes travaux.

Un merci infini au Professeur Jean-Michel Vinassa (mon ShiFu) d'avoir dirigé ma thèse. La patience de Jean-Michel pour initier les électroniciens, comme c'est mon cas, à l'électrochimie m'a été vraiment précieuse. La rigueur de Jean-Michel m'a permis de poser et creuser les points douteux que j'ai pu rencontrer durant mes travaux. Ses apports scientifiques m'ont toujours permis d'avancer à un niveau plus haut. De plus, sa franchise facilite les échanges quotidiens. Je tiens à remercier chaleureusement mon co-directeur, le Maître de Conférence HDR Olivier Briat pour son suivi quotidien, ses aides sur les logiciels de simulation, ses conseils sur les essais de vieillissement et ses corrections d'articles qui m'ont permis d'apprendre et de juger les travaux de manière réfléchie et critique. Un grand merci à tous les deux pour leur encadrement attentif et pédagogique qui m'a permis de réaliser ma thèse dans des conditions très favorables !

Je ne remercierai jamais assez PhD Jean-Yves Delétage pour son aide, sa disponibilité, ses conseils sur l'utilisation des équipements et son efficacité à intervenir dans la plateforme afin de dépanner les enceintes, les machines virtuelles, les logiciels de simulation durant ces trois années de thèse. Je remercie également Monsieur Cyril Martin pour tous ses excellents check-up, sa disponibilité pour lancer les essais à l'heure et son temps consacré à tous les essais de vieillissement. Je n'aurais pas pu finaliser ma thèse à temps sans vous deux !

Mes remerciements s'adressent maintenant à tous mes collègues de la magnifique groupe fiabilité. Madame Isabelle Favre m'a soutenu tous les temps quand je n'étais pas en forme, le délicieux fois-gras qu'elle m'a offert pour Noël m'a beaucoup touché. Alexandrine,

« Étudier sans réfléchir est une occupation vaine, réfléchir sans étudier est dangereux »

“To learn without thinking is blindness, to think without learning is idleness” - Confucius

学而不思则罔，思而不学则殆 - 孔子

Table of contents

Table of contents.....	i
General introduction.....	5
Chapter 1 State of art for electrochemical energy storage systems and aeronautical applications	9
1.1 Introduction	10
1.2 Electrochemical energy storage systems	10
1.2.1. The working principle of LiBs	12
1.2.2. The variety of Li-ion technologies	12
1.2.3. Form of LiBs	15
1.2.4. The working principle of SCaps.....	16
1.2.5. The working principle of LiCs	17
1.3 Characteristic of LiBs, SCaps and LiCs with characterization methods	18
1.3.1. Open Circuit Voltage	19
1.3.2. Internal resistance or ESR	21
1.3.3. Impedance	22
1.3.4. Capacity or capacitance.....	22
1.3.5. State of charge	23
1.3.6. Energy or power density	23
1.4 Electrochemical energy storage systems for aeronautical applications.....	24
1.4.1. Electrochemical energy storage systems used in aircraft.....	24
1.4.2. Energy and power requirements in more electrical aircraft	25
1.4.3. Issues of electrochemical energy storage elements for aeronautical usage	26
1.4.3.1 Gap between technologies of electrochemical energy storage and electrical energy requirements in aircraft.....	26
1.4.3.2 Issues related to aeronautical conditions	28
1.4.4. Standards and certifications	29
1.5 Conclusion.....	29
Chapter 2 Comparative performance quantification of electrochemical energy storage elements by experiments and modelling.....	31

2.1 Introduction	32
2.2 Experiments	32
2.2.1. Tested technologies of LiBs, SCaps, LiCs and Li-S	32
2.2.2. The CaCySSEE platform	35
2.3 Reference test design	36
2.3.1. Reception tests.....	36
2.3.2. Initial tests	36
2.3.3. Performance tests	37
2.3.3.1 Incremental discharge.....	37
2.3.3.2 Available discharged capacity.....	38
2.3.3.3 Maximal power discharge	38
2.3.4. Ageing tests	39
2.3.5. Abuse tests.....	39
2.3.6. Available discharged capacity for LiBs, LiCs and SCaps	39
2.4 Cell to cell characterization	41
2.5 Non-isothermal Ragone plots of 18650 Li-ion cells from datasheet and galvanostatic discharge tests	41
2.5.1. Performance quantification with experimental approach.....	42
2.5.2. Comparison for constant current discharge.....	43
2.5.3. Performance quantification with Ragone plot model.....	45
2.5.3.1 Electrical model.....	46
2.5.3.2 Thermal model	50
2.5.4. Validation of Ragone Plot model	53
2.5.4.1 Ragone plot model for 25°C.....	54
2.5.5. Extending Ragone plot model for wide operating temperature range	56
2.5.6. Enhanced non-isothermal Ragone plot	58
2.6 Conclusion.....	59
Chapter 3 Ageing study of electrochemical energy storage elements	61
3.1 Introduction	62
3.2 Overview of ageing mechanisms in electrochemical energy storage elements.....	62
3.2.1. Ageing mechanisms in LiBs	63
3.2.1.1 SEI formation	63
3.2.1.2 Lithium plating.....	64

3.2.1.3	Dissolution of transition-based materials	65
3.2.1.4	Other ageing mechanisms	65
3.2.2	Ageing mechanisms in SCaps and LiCs	65
3.3	Impact of ageing mechanisms on performance and security.....	66
3.4	Ageing types definition	69
3.4.1	Calendar ageing tests.....	69
3.4.2	Power cycling ageing	69
3.5	Ageing test experiments	69
3.5.1	Characteristics of calendar ageing tests	70
3.5.2	Characteristics of power cycling ageing tests	70
3.5.3	Check-up protocols	71
3.6	Calendar ageing results and analyses	73
3.6.1	Raw tests results	73
3.6.2	Capacity loss analyses under calendar ageing in a wide temperature range ...	76
3.7	Power cycling ageing results and analyses.....	81
3.8	Abuse tests and results.....	87
3.8.1	Thermal stability test.....	87
3.8.2	Overcharge test.....	89
3.8.3	Altitude simulation test	91
3.9	Comparison of different electrochemical energy storage elements.....	92
3.10	Conclusion	94
Chapter 4 SOH estimation of electrochemical energy storage elements.....		97
4.1	Introduction	97
4.2	Overview of SOH estimation methods.....	98
4.2.1	Experimental methods.....	99
4.2.2	Model-based estimation methods.....	99
4.3	Principles of Incremental Capacity Analysis.....	100
4.4	Raw tests results for qualitative and quantitative ICA study.....	101
4.5	Enhanced IC by moving average filter	102
4.6	ICA study.....	103
4.6.1	Current influence on ICA.....	103
4.6.2	Qualitative influence of different ageing types on ICA	105

4.6.3. Decomposition of IC curves based on Gaussian Lorentzian mixed function	107
4.6.4. Peak features with respect to normalized capacity and normalized resistance	108
4.6.5. Method validation for cells with unknown SOH	110
4.7 Conclusion	112
Chapter 5 Experiments and modelling of accelerated ageing with a specific aeronautical profile.....	115
5.1 Introduction	115
5.2 Design of the accelerated ageing tests	115
5.2.1. Proposed aeronautical profile.....	116
5.2.2. Characteristics of accelerated ageing tests	118
5.3 Experiments and raw results.....	119
5.4 Ageing modelling and SOH estimation.....	121
5.4.1. Temperature effects on the degradation rate of capacity	121
5.4.2. SOH estimation	123
5.4.2.1 Qualitative and quantitative ICA.....	123
5.4.2.2 Validation of the proposed method	126
5.5 Conclusion.....	127
General conclusion	129
Table of figures	133
References	137
Annexe	151

General introduction

Despite the global aviation sector produces only around 2% of anthropogenic Carbon Dioxide (CO₂) emissions, the growth of the airline is significant thanks to the globalization [1]. If left to continue at the current pace, the CO₂ emission of aviation could reach 10% by the middle of the century [2]. Besides the CO₂ emissions, the non-CO₂ emissions such as nitrogen oxide (NO_x), sulphur oxides (SO_x), hydrocarbons (HC) and black carbon particles emitted by aviation can cause a variety of environmental effects. Therefore, the Air Transport Action Group (ATAG) decided to introduce a regulatory framework to reduce aviation's emission in 2016 [1] [3]. An ambitious targets to mitigate the net aviation CO₂ emissions of 50% by 2050 compared to 2005 levels.

It is becoming increasingly clear that progress on engine and aircraft architecture are necessary but not sufficient to achieve this objective [2]. Hence, the growing interest is in electrification, which has the advantage of reducing dependence on fossil fuels, reducing CO₂ emissions and noises, making flight safer. As illustrated in Figure 0-1, the electrical power generating capacity has a significant growth in the last 20 years, especially for Boeing 787. In spite of the more electrical aircraft (MEA) represents multiple advantages compared to the conventional aircraft, the introduction of MEA leads to some new challenges concerning the technology, the efficient electrical systems, effective systems intergradation. The air companies around the world are working on these topics.

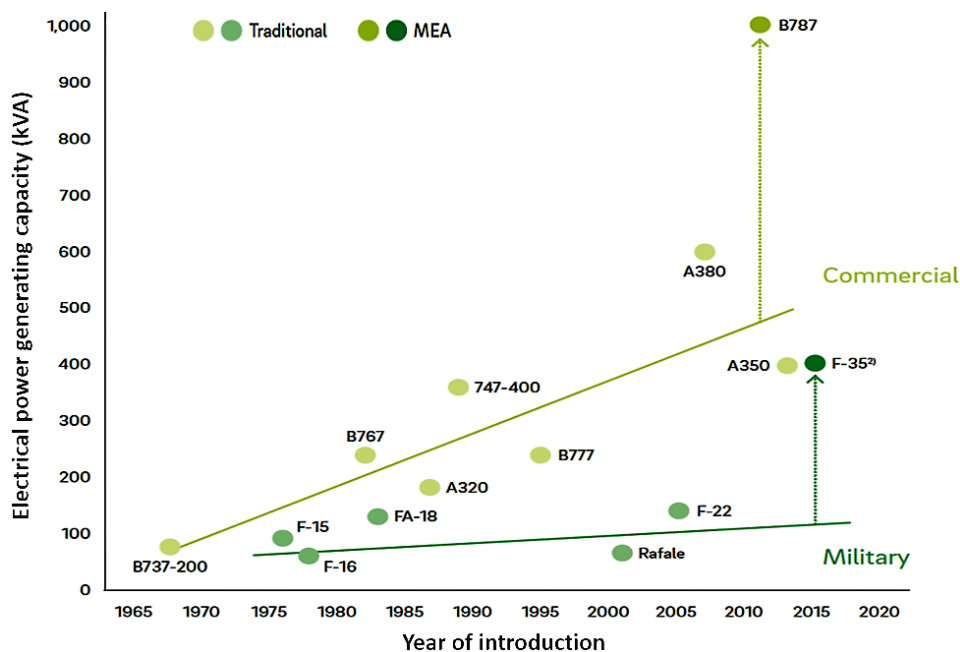


Figure 0-1 Electrical power generating capacity vs. introduction year [4]

Among these barriers, the electrochemical energy storage elements above all components, are becoming the most serious bottleneck for the development of more electrical aircraft due to their energy density, power density, limits over severe operating conditions, reliability, robustness and safety. According to [2], the electrical energy storage systems need

at minimum of 500Wh/kg for all-electric and hybrid aircraft. However, the energy density range of current commercial batteries is from 150-250Wh/kg, therefore, a technology gap is still crucial. Due to the accident of Li-ion battery failure in Boeing 787 (Figure 0-2) [5], the development of MEA must take into account these essential issues in order to integrate the electrochemical energy storage elements in the aircraft.

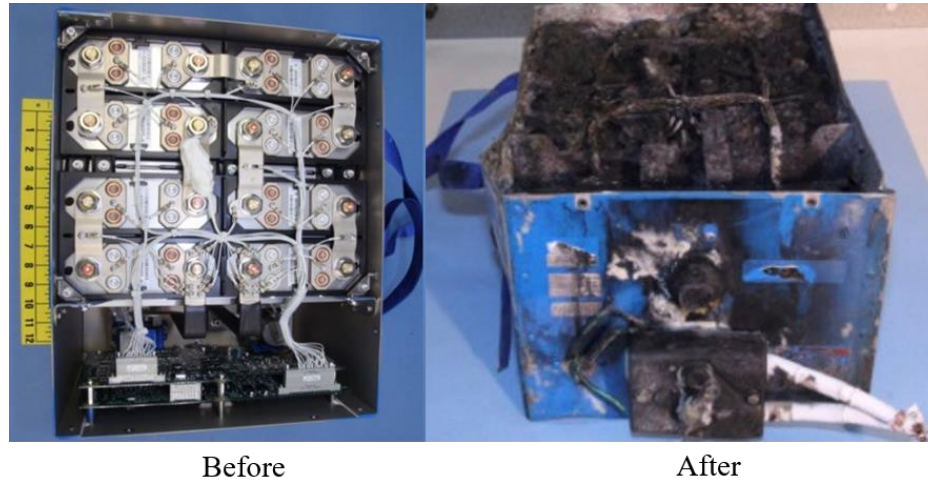


Figure 0-2 Li-ion battery of Boeing 787 Dreamliner airline before and after accident [5]

In this context, “CELIA” project has been conducted, which is supported by the Institute of Technology Saint-Exupéry and funded by the French National Research Agency. This project has several industrial partners: Zodiac Aerospace, Safran Tech, Airbus and academic laboratories: IMS-Bordeaux and LRCS-Amiens. The main objectives of this project are listed below.

For the short term:

- To promote the emergence of electrochemical energy storage technologies for aeronautical usage.
- To develop efficient methods to evaluate the commercial electrochemical energy storage elements for aeronautical applications.
- To deep understand the performance and ageing behaviours of different electrochemical energy storage types, including Li-ion cells, Supercapacitors (SCaps), Li-ion capacitors (LiCs) in aeronautical environment (extreme temperature, low pressure)
- To investigate models or tools to evaluate or estimate the reliability, the robustness and to identify the failure modes of electrochemical energy storage elements.

For the long term:

- To develop the new technologies to meet the energy and power needs for more electrical aircraft.
- To evaluate the practical energy density of Li-air technology, versus the theoretical energy density of 1300Wh/kg.

The thesis work presented in this manuscript and realized in IMS Laboratory, which is based on the framework of “CELIA” project and focused on the objectives for short term in particular. Nowadays, facing the diversity electrochemical energy storage elements provided by manufacturers, there is no specific reference tests to evaluate their performance, reliability and robustness during operation in the aeronautical environment. There is also a lack of knowledge about electrochemical energy storage elements behaviors under the abuse conditions in the case of dysfunction, such as thermal runaway, overcharge and under low pressure. Furthermore, no study was investigated on the coupling between ageing factors and an accelerated ageing laws relating to a specific profile for aeronautical usage.

In order to achieve these objectives, this manuscript is composed of five chapters. The chapter 1 is focused on an overview of diversity electrochemical energy storage elements and their applications for aeronautical usage. The working principle of Li-ion batteries, Supercapacitors and Li-ion capacitors are presented throughout their characteristic with multiple characterization methods. Then, the electrochemical energy storage elements used in aircraft are introduced. Finally, the essential challenges for aeronautical usage are listed.

The chapter 2 concerns the comparative performance quantification by experiments and modelling. Nine technologies of the latest generation of commercial elements are investigated in this thesis, including Li-ion cells (NMC/graphite + SiO, NCA/graphite, LFP/graphite, NMC/LTO), Lithium-Sulfur (Li-S), SCpas and LiCs. A reference tests taking into account the aeronautical environment and usage is proposed. In addition, an efficient electrical–thermal model is established in order to build a Ragone plot to quantify the energy density and power density for electrochemical energy storage elements.

The chapter 3 is devoted to the study of robustness and safety for investigated electrochemical energy storage elements. For this, calendar ageing and power cycling ageing as well as a synthesis of abuse tests results are investigated in the aeronautical environment. A summary of performance evaluation according to seven criteria (energy density, power density, available capacity at extreme temperatures, lifetime in calendar ageing type, self-discharge, number of cycles and safety) is proposed in order to select the most promising commercial electrochemical energy storage elements.

The results of the various periodic characterization throughout the calendar ageing and power cycling ageing tests in chapter 3 are used in the chapter 4 to investigate a SOH estimation for Li-ion cells. This method is based on qualitative and quantitative Incremental Capacity Analysis (ICA), which is able to identify the degradation modes during ageing tests, to estimate which ageing types Li-ion cells historically underwent and the internal resistance evolution.

The chapter 5 is dedicated to the evaluation of robustness for electrochemical energy storage elements in the accelerated ageing tests with a specific aeronautical profile. Only the most promising technologies of Li-ion are retained in this chapter. Thus, a specific aeronautical profile is proposed, which corresponds to a series of flight phases for an air travel in metropolitan France. The ageing models and SOH estimation methods proposed in the previous chapters are applied on these cells under this aeronautical profile.

Chapter 1

State of art for electrochemical energy storage systems and aeronautical applications

Table of contents

1.1 Introduction	10
1.2 Electrochemical energy storage systems	10
1.2.1. The working principle of LiBs	12
1.2.2. The variety of Li-ion technologies	12
1.2.3. Form of LiBs	15
1.2.4. The working principle of SCaps.....	16
1.2.5. The working principle of LiCs	17
1.3 Characteristic of LiBs, SCaps and LiCs with characterization methods.....	18
1.3.1. Open Circuit Voltage	19
1.3.2. Internal resistance or ESR	21
1.3.3. Impedance	22
1.3.4. Capacity or capacitance.....	22
1.3.5. State of charge	23
1.3.6. Energy or power density	23
1.4 Electrochemical energy storage systems for aeronautical applications.....	24
1.4.1. Electrochemical energy storage systems used in aircraft.....	24
1.4.2. Energy and power requirements in more electrical aircraft	25
1.4.3. Issues of electrochemical energy storage elements for aeronautical usage	26
1.4.3.1 Gap between technologies of electrochemical energy storage and electrical energy requirements in aircraft.....	26
1.4.3.2 Issues related to aeronautical conditions	28
1.4.4. Standards and certifications	29
1.5 Conclusion	29

1.1 Introduction

Over the last twenty years, global demand for energy is rising with overcrowding. Transport plays a significant role in human activities. Almost all transportation are powered by petroleum fuels. However, the combustion products of petroleum are the main pollutants emitted in the environment, which affects air quality and causes damage to human health. Therefore, numerous studies have been dedicated to finding other alternative fuels or enhancing the sustainability and reliability of energy storage systems in order to decrease fuel consumption, produce less CO₂ emissions and polluting gas [6]. Among the various choices of energy storage systems, the electrochemical energy storage systems above all offer several advantages. Lithium-ion batteries are integrated in the vehicle to meet the power and energy requirements with less CO₂ emissions. While, using the electrochemical storage systems becomes one of the hindrance to electrification of aircraft.

This first chapter is composed of two major sections. In the first section, the various electrochemical energy storage systems are presented and compared throughout their working principles and their characteristics. In particular for the Lithium-ion batteries (LiBs), the Supercapacitors (SCaps) and the Lithium-ion Capacitors (LiCs). The second section is devoted to present in details a state of art on the electrochemical energy storage systems for aeronautical usages. Furthermore, some issues about aeronautical environment and security of electrochemical energy storage systems are discussed. Finally, the standards and the certifications of LiBs and SCaps are listed, which are considered as a reference test to quantify and compare the performance of LiBs and SCaps in the future study.

1.2 Electrochemical energy storage systems

In order to reduce the dependence of fossil fuels, renewable energy is an alternative solution to complete other energies. In 2016, renewable sources (hydropower, biomass, wind, solar, geothermal) account for approximately 26% of global electricity [7]. However, most of the renewable energy sources are intermittent. The Electrical Storage Systems (ESSs) is one of the few ways to store and use electricity later [8]. The electrochemical storage system is one of the most used SSE in everyday life and industrial [9], such as the LiBs or SCaps used in the portable application (mobile phone, laptop, tablet, tools), or in the transport sector where the electrification of vehicles or airplanes, is gradually growing.

The electrochemical storage system converts chemical energy into electrical one and vice versa. Energy density and power density are the two commonly used indexes for quantifying the performance of electrochemical storage systems [10]. The energy density represents the energy that electrochemical storage systems can be stored/delivered per unit mass. While, the power density represents at which speed this energy can be stored/delivered.

In general, the Ragone plan allows to compare different ESSs. As illustrated in Figure 1-1 the different SSEs are positioned according to the characteristics between the energy density (Wh/kg) and the power density (W/kg). The fuel cell is located at the top left of this plan, it is therefore intended for energy applications. On the contrary, conventional capacitors are used for high power applications. The lines that cross this plan are the time constants, defined by the ratio of energy / power, which corresponds to the time required to fill/empty the storage system.

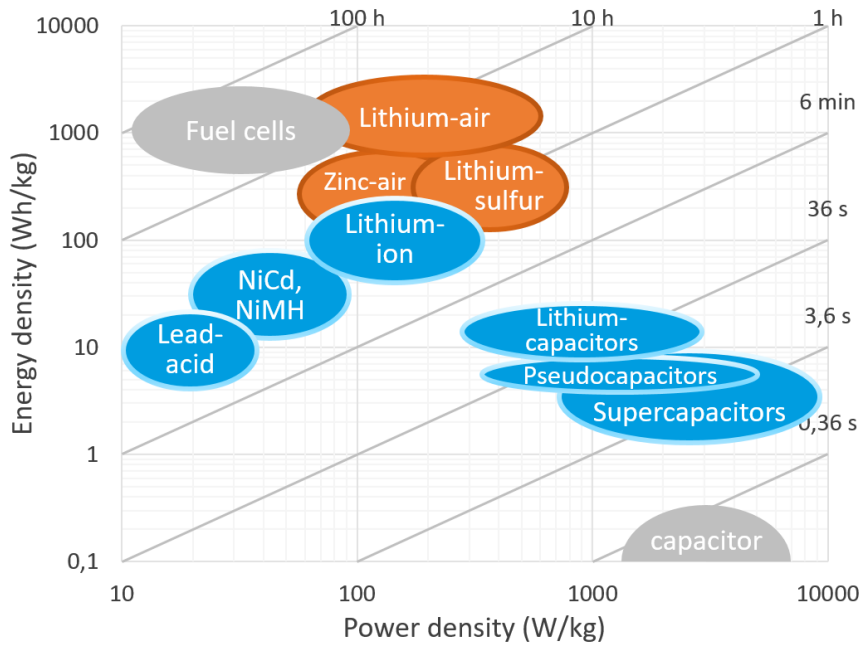


Figure 1-1 Ragone diagram of the main electrochemical energy storage elements

In this Ragone diagram, the electrochemical storage elements are positioned between the fuel cell and the conventional capacitor. In general, they can be classified into two major families: batteries and SCaps. The differences between them are related to the ways of storing electric charges.

For batteries, electrical energy is stored in the bulk electrode. As illustrated in the Figure 1-2, the intercalation/de-intercalation of Li^+ allows to have oxidation-reduction reactions of the electrode materials in the case of LiBs. This reaction type is accompanied with the charge transfer, which is also called faradic charge storage. The electrochemical reaction is controlled by the slow diffusion phenomenon [8]. Batteries are therefore considered as energetic elements.

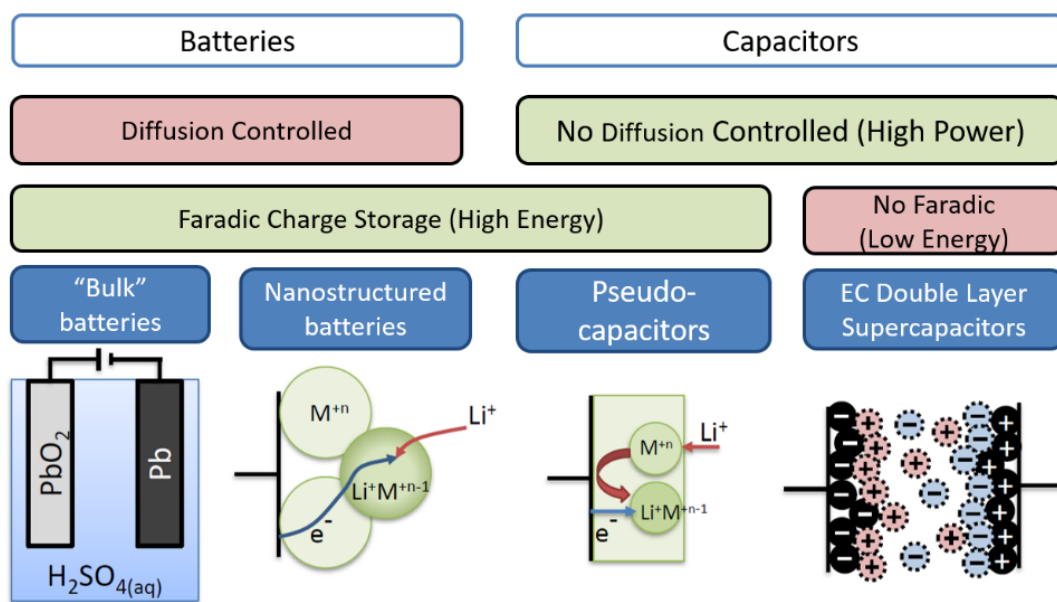


Figure 1-2 Classification for the main electrochemical energy storage elements (LiBs, SCaps) based on the way of storing electric charges [8]

On the contrary, in the case of SCaps, the electric charge is stored by ions adsorption in the electrolyte on the electrode surface. The reaction occurs fast without material transport, the SCaps are intended for power applications [11]. In addition, the LiCs mentioned in the Ragone plan combine energy and power.

The following paragraphs present individually the compositions and the working principles of the different technologies located in each family, in particular for LiBs, LiCs and SCaps.

1.2.1 The working principle of LiBs

Figure 1-3 represents the main working principle of a lithium-ion cell. A lithium-ion cell consists of two electrodes: positive and negative. Positive electrode are composed by Li metal oxide materials. While, graphite is the most common material used for negative electrode. The potential between two electrodes gives the cell voltage, which depends on the chemistry of the electrode materials and operating conditions. These two electrodes are connected to the external circuit by current collectors. In general, current collectors are made of aluminium for the positive electrode and copper for the negative one. These two electrodes are bathed in an electrolyte that is liquid, solid or gel. A porous separator is located between these two electrodes to avoid the short circuit.

The working principle of a lithium-ion cell is based on the intercalation/de-intercalation of Li^+ into the electrode materials. During the discharge, the Li^+ are removed from the graphite negative electrode (anode), they migrate into the electrolyte and then pass through the separator and insert into the positive electrode (cathode). At the same time, the charge transfer takes place on the electrode-electrolyte interface, the current is therefore created. During the charge, the displacement of Li^+ is opposite.

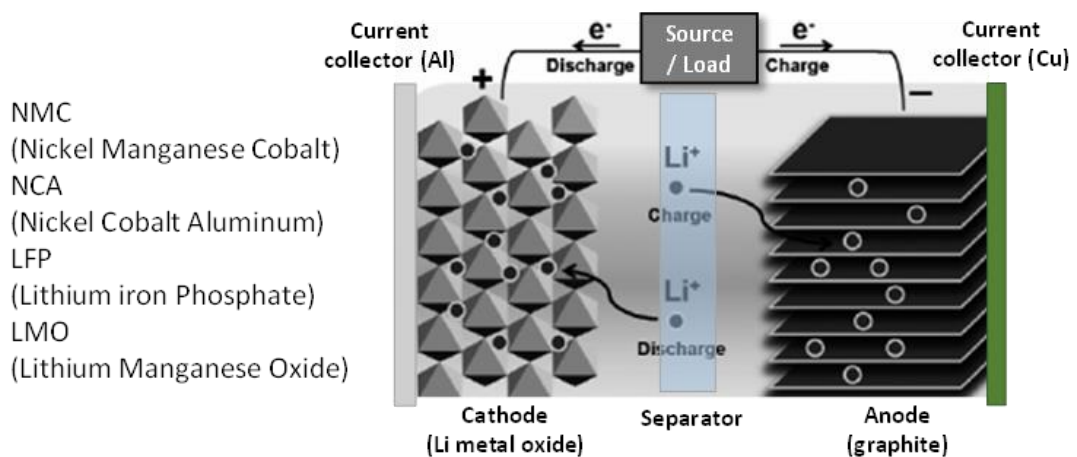


Figure 1-3 Working principle of Li-ion cell

1.2.2 The variety of Li-ion technologies

To meet the needs in terms of energy, power and price requirements for application, there are multiple lithium-ion technologies. They are distinguished by the materials used in the lithium-ion cell. However, their working principle is always based on the intercalation and the de-intercalation of Li^+ .

- **Negative electrode**

The main materials used in the negative electrode of LiBs are summarized in Table 1-1. The characteristics are referred by the review of Goriparti *et al.* [12].

Family	Abbreviation	Potential vs. Li ⁺ /Li (V)	Theoretical capacity (mAh/g)
Lithium-metal	Li	0	3862
Carbon materials (Graphite)	LiC ₆	0.02-0.3	372
X alloy (X: Si, Ge, SiO)	LiX	0.3-0.4	1000-3500
Titanate (Li ₄ Ti ₅ O ₁₂)	LTO	1.5	175

Table 1-1 Main materials of negative electrode used in LiBs [12] [13]

The first material used for the negative electrode is pure lithium thanks to its low weight, which allows to cells have a significant energy and power density. However, pure lithium-metal remains a very active element in contact with oxygen and water. In addition, the metal deposition of lithium can generate the internal short circuit during the cell operation, which introduces security issues.

Lithium metal is therefore replaced by carbon materials. Graphite is the most used material for the negative electrodes of LiBs compared to other materials because of its chemical and thermal stability and good reversibility during intercalation/de-intercalation reaction. In addition, this material is abundant and less expensive. Graphite has a layered, planar structure. Non-compact hexagonal layers are separated with a distance of 0.335nm. In each layer, 6 carbon atoms are strongly linked to each other by strong covalent bonds [12]. Bonding between layers is via weak Van der Waals bonds, which facilitates the intercalation and de-intercalation of lithium ions between each layer. Its potential is rather low and converges to that of lithium-metal. However, the theoretical capacity of graphite is a little weak.

The alloys that are often used in the negative electrodes have a high theoretical capacity compared to graphite. However, the main problem is that the silicon particle size increases during intercalation of Li⁺, this causes an expansion of the negative electrode [12]. As a result, the cycle life of LiBs is limited.

Titanate based materials are proposed by several studies. In fact, it has a good capability to deliver a high power. Furthermore, the operation of this technology can be ensured in a wide range of temperature [-40°C, 55°C], even at temperature below -20°C [13]. However, the high potential of LTO electrode gives a low specific energy for LiBs.

- **Positive electrode**

Currently, the materials used for the positive electrode are multiple. This type of material, called “host materials”, should be in a lithiated form. They are divided into three large families according to their crystalline structure. The main materials used in the positive electrode of LiBs are listed in Table 1-2.

LCO, NCA and NMC belong to the laminar oxide family. LiCoO₂ was the first material used for the positive electrode, it is still adapted to today's needs thanks to its high energy density [14]. Its cost and thermal instability because of cobalt presence remain the biggest disadvantages. To make LCO more stable, progress have been done thanks to the addition of materials such as nickel, manganese and aluminium. NCA and NMC are therefore widely used in commercial LiBs.

Family	Material	Abbreviation	Potential vs. Li ⁺ /Li (V)	Theoretical capacity (mAh/g)
Laminar oxide	LiCoO ₂	LCO	4	274
	LiNi _{0.8} Co _{0.15} Al _{0.05} O ₂	NCA	4	279
	LiNi _{1/3} Mn _{1/3} Co _{1/3} O ₂	NMC	4	280
Spinel oxide	LiMn ₂ O ₄	LMO	4	148
Olivine phosphate	LiFePO ₄	LFP	3.5	170
Sulfur	Li ₂ S ₈	Li-S	2	1672

Table 1-2 Main materials of positive electrode used in LiBs [13] [14]

LMO is considered as an element of spinel materials family for positive electrode. Its three-dimensional structure increases the availability of Li⁺ insertion. The diffusion of Li⁺ is therefore taking place faster. However, it remains unstable at high temperature, the manganese in positive electrode can be dissolved in the electrolyte [15].

Goodenough synthesized LiFePO₄ for the positive electrode material. Its structure called "Olivine". Iron is an abundant and non-toxic material. In addition, LiFePO₄ has a good thermal stability. However, its low potential leads to a low energy density.

Li-S is an interesting candidate for the positive electrode material due to its high specific capacity, which can be reached 8 to 10 times higher than other materials of positive electrode. Despite this strong point, there are two manufacturers commercialize this technology. There are still some hindrances to overcome, such as strong self-discharge and low lifetime [16].

- **Electrolyte**

The electrolyte assures the Li⁺ transfer between two electrodes. The electrolytes used in LiBs are often classified into two groups: the liquid electrolyte and the solid or gelled electrolyte [17]. The liquid electrolyte consists of soluble lithium salts, such as hexafluorophosphate of

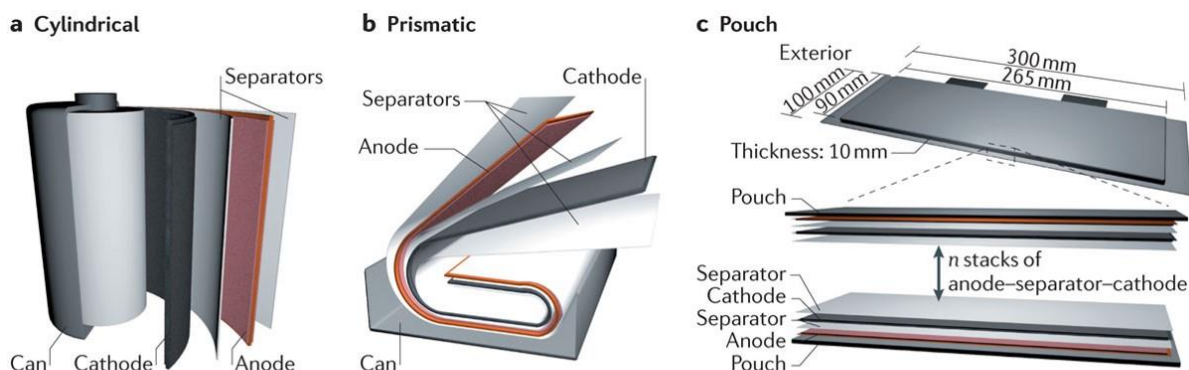
lithium (LiPF_6) in organic solvents as Ethylene Carbonate (EC), Propylene Carbonate (PC) or Methyl Ethyl Carbonate (MEC). For the solid or gelled electrolyte, the lithium salts are incorporated into the polymer matrix. Then, they are shaped into a film or gel. For all types of electrolytes, they must be a good ionic conductor. Furthermore, they must have good electrochemical and thermal stability over a wide range of voltage and temperature to prevent its decomposition [13].

- **Separator**

The role of the separator is to separate the two electrodes and to provide the ionic conductivity needed during LiBs working. The separator is made of a polymer membrane of a few tens of micrometres in thickness. Polyethylene (PE) and Polypropylene (PP) are often used as separator material with a porous structure [18]. PP ensures the mechanical strength thus making the LiBs more safe thanks to its low melting point. Separators with a sandwich structure (PP/PE/PP) are also found in LiBs [19]. This three-layer structure can operate as a switch when the battery is overloaded.

1.2.3 Form of LiBs

A lithium-ion battery consists of several cells in series to increase its terminal voltage or in parallel to improve its current range. To choose a specific technology of LiBs, apart from the materials used in the cell, assembly of cell is very important. The latter depends on the form of cell. Figure 1-4 illustrates the three different forms of the lithium-ion cells: cylindrical, prismatic and pouch forms.



Nature Reviews | [Materials](#)

Figure 1-4 Different forms of Li-ion cell (a) Cylindrical, (b) Prismatic, (c) Pouch [20]

The cylindrical cells follow a standard size model, such as 18650 or 26650. For the 18650 cell, it has 18mm in diameter and 65mm in height. The same definition for 26650. The cylindrical cell is based on the superposition of layers in anode-separator-cathode. This arrangement makes it possible to increase the surface of active materials in electrodes. Then, these layers are wound around a central pivot and spooled on several turns, finally the whole is installed in a steel compartment and impregnated in the electrolyte [21]. Moreover, a valve system can control the cell internal pressure to put the cell in a secure condition.

The prismatic cell uses the flat electrodes stacked in a rectangular container. This ensures a good mechanical strength and a high volumetric energy density [22].

The cell in pouch form is the most recent design. Multiple positive electrodes-separators-negative electrodes are stacked and enclosed in a plasticized aluminium film envelope, which makes the cells lighter and more flexible. However, this flexible envelope can produce the cell swelling because of the gas generated by the decomposition of the electrolyte [23].

1.2.4 The working principle of SCaps

The SCaps consist of two activated carbon electrodes that are separated by a porous membrane. The whole is impregnated into electrolyte as shown in Figure 1-5.

Both porous electrodes based on activated carbon have a high specific surface area (typically $2000\text{m}^2\text{g}^{-1}$) [8]. Mastering the porosity and the pore diameter are predominant in the carbon activation process, since they are directly related to the kinetic of electrolyte ions adsorption process at the surface of electrode.

The ideal electrolyte in the SCaps must have a wide voltage window, a high ionic concentration, a high electrochemical stability and a low resistivity [24]. Furthermore, the ion sizes in the electrolyte must be compatible with the pore sizes in the electrodes to promote the adsorption process. Among aqueous, organic electrolytes and ionic liquids, the organic electrolyte based on acetonitrile or Propylene Carbon (PC) is often used [22]. In fact, this type of electrolyte offers a voltage window up to 3.5V, which avoids the electrolysis of water.

The separator for the SCaps has the same characteristics as in the LiBs. It must have good ionic conductivity, high thermal and chemical stability. Polyethylene (PE) or PolyVinylidene Fluoride (PVDF) is commonly used as the electrolyte material in SCaps.

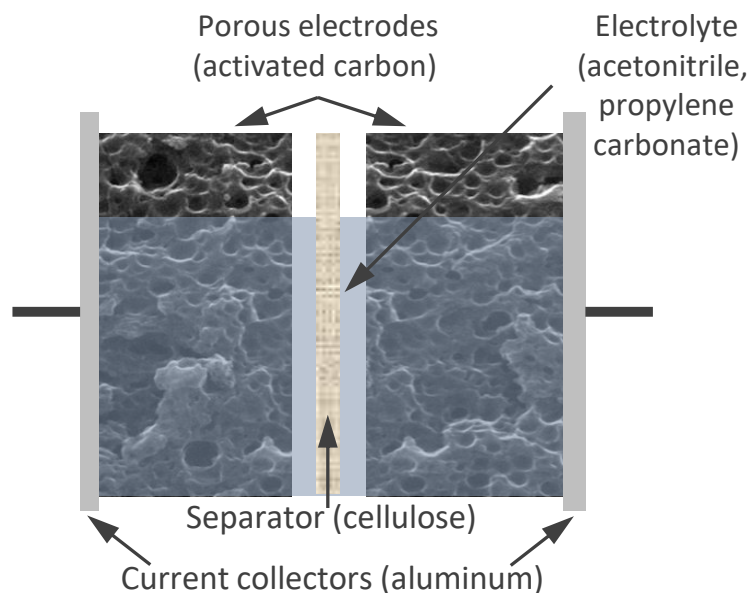


Figure 1-5 Composition of SCaps

The SCaps store the electric charge directly by the electrostatic. Once the electric field applies on the SCaps, the positive electrode attracts the negative ions (anion) in the electrolyte, while the negative electrode attracts the positive ions (cation). Consequently, two double layers

with the order of magnitude 10 to $20\mu\text{Fcm}^{-2}$ are formed at the electrode and electrolyte interface on each side [8]. This structure is considered as two capacitors in series. The specific capacitance can reach 100F/g thanks to the activated carbon [8].

1.2.5 The working principle of LiCs

To finish this horizontal tour of different electrochemical storage elements, we present here the LiCs. Lithium-ion capacitor is an asymmetric device of electrochemical energy storage system. Figure 1-6 illustrates the composition and working principle of LiCs. A LiC consists of a positive activated carbon electrode as in the SCaps, while the negative electrode is composed of carbon doped with Li^+ as for LiBs. Both of electrodes are immersed in an electrolyte with the lithium salt. The electrolyte of LiCs has often the same composition as in LiBs [25].

The asymmetrical structure provides a dual storage proprieties. Two energy storage ways are present in LiCs during the charging and discharging process. The anion adsorption/desorption takes place at the activated carbon positive electrode surface, the intercalation /de- intercalation of the Li^+ occurs at the negative electrode [26]. Another symmetrical structure of LiCs can be found out on the market , which compose the mixed materials of activated carbon and Li-doped carbon as mentioned in the asymmetrical structure. This technology can also provide the dual storage proprieties. In this study, the symmetrical structure had been selected in the project.

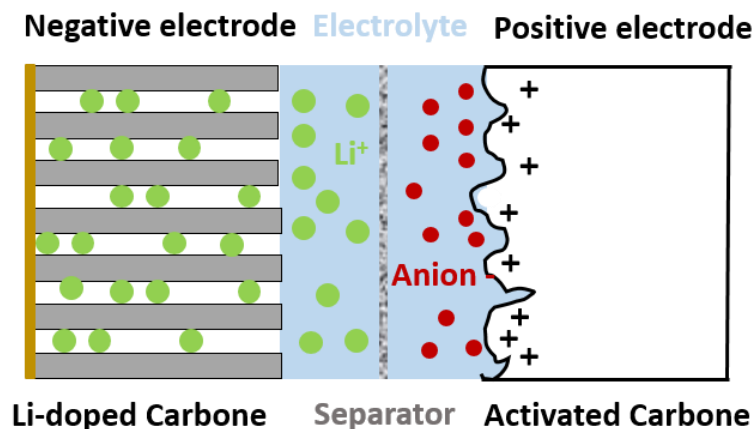


Figure 1-6 LiCs compositions with working principle

In theory, LiCs can provide a higher power density compared to LiBs, as well as a higher energy density compared to SCaps. In fact, the imbalance between two electrodes is one of the major difficulties for the LiCs development. Since the intercalation kinetics of Li^+ is slower than the adsorption reaction at the positive electrode surface, which limits the LiCs for energy and power application [27].

The commercial LiCs arrived after the LiBs and SCaps. Figure 1-7 illustrates some examples of commercial products provided by leading international manufacturers. They are cylindrical, prismatic or flexible pouch form. The capacity of LiCs can be expressed in Farad or ampere-hour according to the manufacturer. In general, the nominal voltage is lower than 3V .

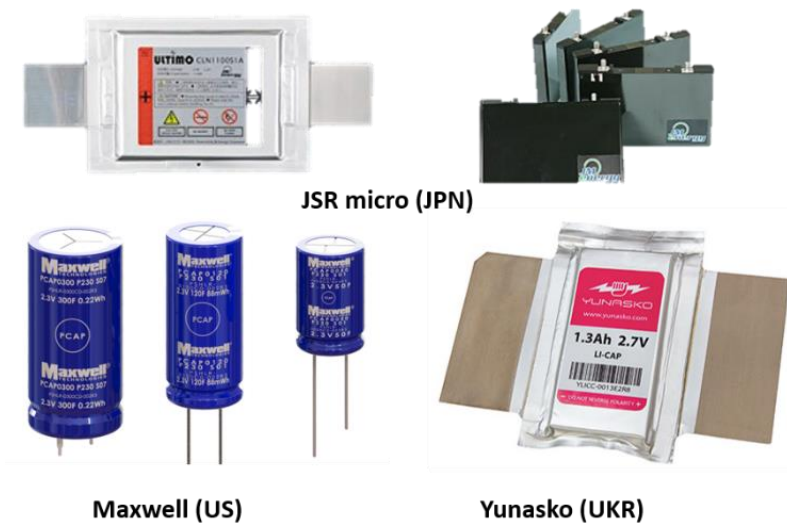


Figure 1-7 Examples of commercial LiCs from different manufacturers

1.3 Characteristic of LiBs, SCaps and LiCs with characterization methods

In this section, the characteristic of LiBs, SCaps and LiCs with characterization methods are introduced and compared. Despite that the working principle is different between the LiBs, SCaps and LiCs, most of parameters used to quantify their characteristics on a macroscopic scale are in common (Table 1-3).

Symbol (Unit)	Definition of characteristic parameters		
	LiBs	SCaps	LiCs
OCV (V)	Open Circuit Voltage		
$I_{dch/ch}$ (A)	Discharge/charge current		
U (V)	Voltage		
R_{int} (Ω) ESR (Ω)	Internal resistance		
Z (Ω)	Impedance		
Q (Ah) C (F)	Capacity	Capacitance	Capacity/Capacitance
SOC (%)	State Of Charge		
E (Wh/kg)	Energy density		
P (W/kg)	Power density		

Table 1-3 Main parameters of LiBs, SCaps and LiCs

These parameters can be measured by protocols in international standards. For instance, the tests concerning the performance, robustness and abuse of rechargeable LiBs are defined in

IEC 62660 standard [28] [29] for the application of electric or hybrid vehicles. Furthermore, the IEC 62576 standard [30] specifies the electrical characterizations for SCaps. In addition to international standards, electrochemical techniques such as Galvanostatic Intermittent Titration Technique (GITT) allows to characterize the OCV, internal resistance of LiBs in the time domain. While, Electrochemical Impedance Spectroscopy (EIS) is applied to characterize the impedance of LiBs, SCaps and LiCs in the frequency domain.

The definitions of these parameters and the associated characterisation methods will be detailed in the following paragraph. The characterisation methods are based on the individual electrochemical energy storage element, which corresponds to the case in our study. To date, there is no specific standard for LiCs. But their hybrid structure and working principle combining LiBs and SCaps indicate that the protocol of LiBs and SCaps can be applied on LiCs.

1.3.1 Open Circuit Voltage

OCV is the potential difference between positive and negative electrodes when the electrochemical energy storage elements are stored. This voltage depends on the active materials in the electrochemical energy storage elements, it varies with the SOC, the temperature and the State Of Health (SOH) of the electrochemical energy storage elements [31]. OCV can be measured by two techniques: GITT or by applying a low charge/discharge current.

GITT consists of a series of charge/discharge current pulse alternated by a break. As shown in Figure 1-8, this diagram illustrates the OCV measurement by GITT. The discharge/charge current pulse allows the LiBs to be placed at the different SOC. Then the cell is put to rest in order to reach its thermodynamic equilibrium, the OCV is the value at the end of the relaxation phase, which represents by a cycle for discharge and by a cross for charge. The relaxation time depends on the discharge/charge current, the SOC and the discharge/charge temperature. Sauer et al. [31] showed that high current, low SOC and low temperature required a long relaxation time.

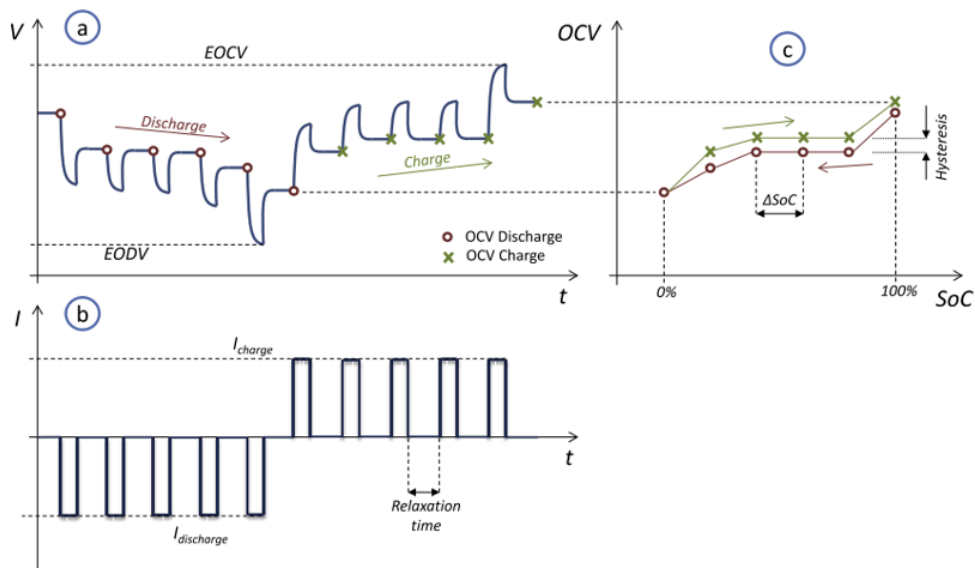


Figure 1-8 Schematic representation of OCV measurement by GITT for a Li-ion cell (a) voltage profile (b) current profile (c) OCV vs. SOC [32]

According to the literatures [33] [34] [35], the OCV obtained by a charge/discharge at low current (less than C/20) is considered as the pseudo-OCV. In theory, the state of charge can be determined from a simple reading of pseudo-OCV. However, the temperature slightly impacts the pseudo-OCV versus SOC curve [36]. Otherwise, an OCV value can significantly distort the SOC determination for LFP/graphite Li-ion cell (Figure 1-9), from 10% to 90% SOC, the pseudo-OCV value is always 3.25V [37].

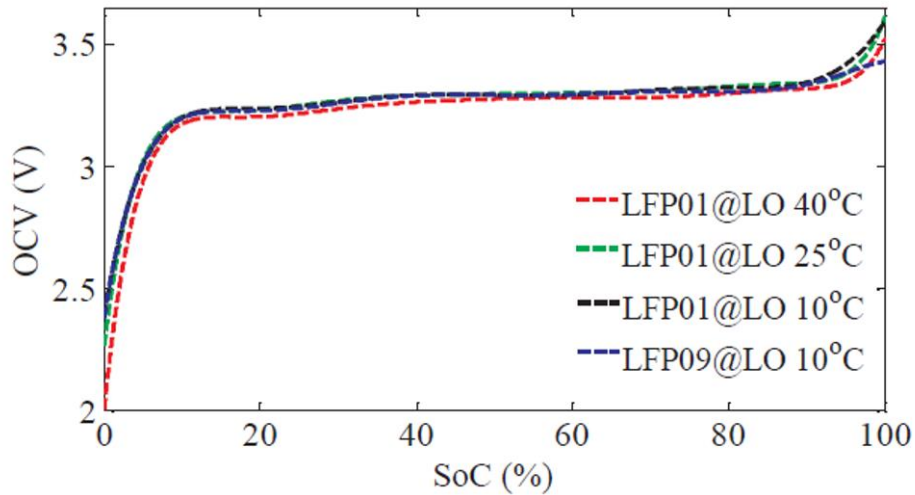


Figure 1-9 Pseudo OCV-SOC curves based on discharge at different temperatures for a LFP/graphite cell [35]

Compared to these two techniques, the GITT allows measuring both OCV and internal resistance through a relaxation phase. However, the duration of relaxation to obtain an OCV after a pulse discharge at -20 °C and 0 °C was approximately six times higher than that for an OCV measured at 25 °C and 55 °C for a Li-ion cell (Figure 1-10). Therefore, the test lasts on average more than 50h by applying the GITT technique at low temperature. In addition, the relaxation time depends on the SOC. While, the low current discharging lasts less time in this case.

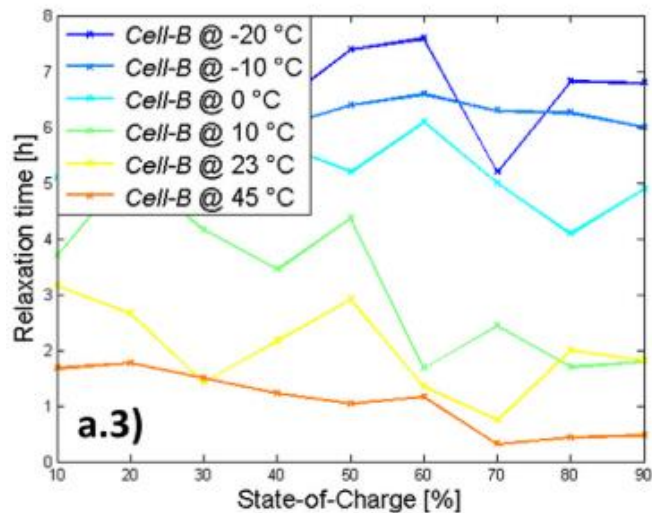


Figure 1-10 Relaxation time required at different temperatures and varied SOCs by technique of GITT for a NMC/LTO Li-ion cell [31]

For SCaps, a significant self-discharge behaviour is observed after a relaxation phase. Voltage losses in the range of 5-60% occur over two weeks [38]. It is therefore not common to use the OCV parameter in the case of SCaps. The high potential and temperature promote the self-discharge. Furthermore, the self-discharge introduces a leakage current, which is the sum of the currents of all processes because of the parasite reactions and the replacement of electric charge through the SCaps. The self-discharge rate is higher in the SCaps compared to the LiBs [39].

1.3.2 Internal resistance or ESR

When the current flows through the cell, a voltage drop appears that is considered due to the internal resistance. The internal resistance is tens milliohms for the LiBs and over hundred microhms for the SCaps at the fresh state. The electrochemical energy storage element is considered at the first End Of Life (EOL) when its internal resistance doubles.

According to the IEC 62660-1 standard [28], the internal resistance of LiBs is characterized by the voltage repose to a current excitation profile. This profile consists of several 10s discharge/charge current pulse alternated by 10min rest time. Furthermore, the current amplitude varies and increases successively. This profile is applied at 3 SOCs (20%, 50%, 80%) and at 4 temperatures (40°C, 25°C, 0°C, -20°C). The profile for internal resistance measurement in this study is illustrated in Figure 1-11 (a), 20s of discharge/charge pulse currents with 40s rest are selected. Thereby, the internal resistance is calculated by equation (1.1), where U_{xs} is the voltage at the end of 20 second, U_{0s} is the voltage before the pulse and $I_{dch/ch}$ is the discharge or charge pulse current.

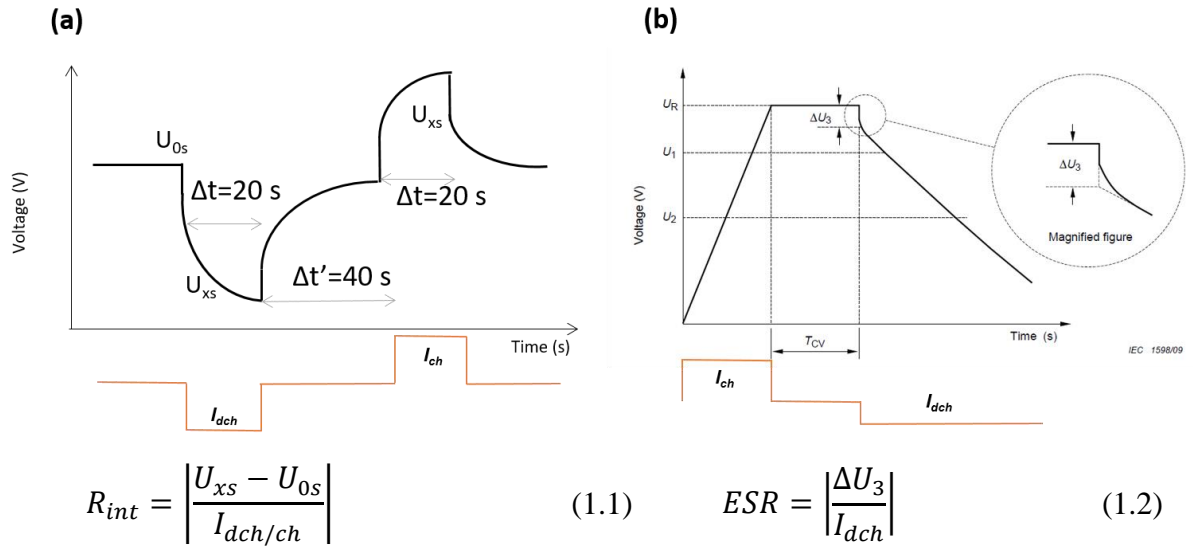


Figure 1-11 (a) Pulse current profile for R_{int} determination of LiBs (b) Voltage profile for ESR determination of SCaps in IEC 62576 standard [30]

For SCaps, the internal resistance is represented by the Equivalent Series Resistance (ESR). In the IEC 62576 standard [30], ESR is characterized by the profile Figure 1-11 (b), the values U_1 and U_2 correspond to $0.9U_R$ and $0.7U_R$, U_R is the rated voltage of SCaps. ESR is calculated from equation (1.2). ΔU_3 is the difference of potential defined according to the voltage before discharge. The defined voltage is obtained by the intersection of the tangent

curve through U_1 , U_2 and the point at the beginning of discharge. I_{dch} is the discharge current. Another method for ESR characterization is often found in literatures. This method is based on a measurement of 5s potential difference ΔU . The difference of potential is calculated before and after 5s when the charge/discharge current becomes zero.

1.3.3 Impedance

The internal resistance is the ration between a voltage drop and direct current (DC). However, if the applied voltage is oscillated by a sinusoidal wave, the current will be converted to alternative (AC). The proportionality between potential and current is a complex number, which is the impedance of electrochemical energy storage systems. Electrochemical Impedance Spectroscopy (EIS) is a technique that is used to characterize the impedance of different electrochemical energy storage systems. There are two modes of EIS. In potentiostatic mode, the excitation is performed by a low amplitude sinusoidal voltage ($\sim 10\text{mV}$). While, in galvanostatic mode, the excitation is based on a low current ($\sim 100\text{mA}$). EIS is a characterization technique based on the frequency domain, which signifies that the impedance measurement is performed at multiple frequencies. The wide frequency range covers from 10mHz to 10kHz allows to identify all the physical and chemical phenomena in electrochemical energy storage systems.

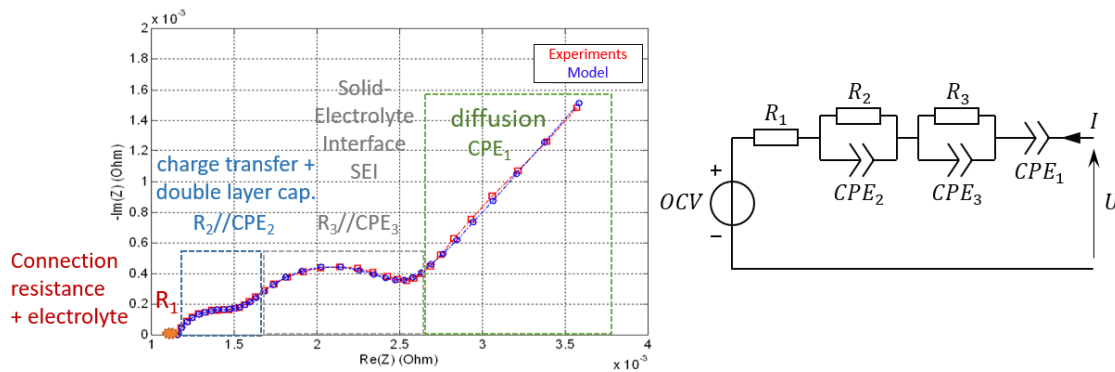


Figure 1-12 Impedance spectrum for NMC/graphite Li-ion cell at 30% SOC at 45°C in galvanostatic mode [10mHz-10kHz] with corresponding equivalent circuit model

A typical impedance spectrum for Li-ion cell is shown in Figure 1-12, where the physical-chemical phenomena of Li-ion cell can be characterized at the specific frequency. At high frequency range, R_1 is due to the connection resistance and electrolyte. At mi-frequency range, the charge transfer with SEI can be determined by the two half circles. At low frequency, the diffusion phenomenon is detected at low frequency range. In addition, this spectrum can be simulated by an equivalent circuit with various electrical components (Resistance (R), Constant Phase Element (CPE)) with a voltage source (OCV). The values of R and CPE under various conditions (T, SOC, ageing state) can be followed to evaluate the properties of different phenomena in Li-ion cells.

1.3.4 Capacity or capacitance

Capacity or capacitance is the amount of the electric charge delivered or stored by an electrochemical energy storage element. For LiBs, the available capacity (Q in Ah) is determined by the equation (1.3), it is calculated by the integral of the discharge current I_{dch}

over a given period dt between initial state e_i and final state e_f . In IEC 62660 [28], the initial state is the maximum voltage, the final state is the minimum voltage defined by the manufacturer for discharge. For SCaps, according to IEC 62576 [30], the capacitance (C in F) is determined by equation (1.4), where U_1 and U_2 are $0.9U_r$ and $0.7U_r$, respectively, as illustrated in Figure 1-11 (b), E is the variation of energy between these two potentials. As internal resistance, the capacitance is another criterion to evaluate the performance of electrochemical energy storage elements. When the capacity reaches 80% of its initial value, the elements are considered as the first EOL.

Several parameters can impact the capacity/capacitance value, such as the discharge current, the temperature of test and the previous charge method. In the case of LiBs, the discharge current is defined by the discharge rate, it is expressed in combination of a number and a letter C. Concerning the example of a cell of capacity 10Ah, when the regime of discharge is C/2, this means that the Li-ion cell can provide the continuous discharged current of 5A during 2 hours. Furthermore, when the discharge rate is 10C, the cell delivers 100A during 6 minutes.

According to the IEC 62660 standard [28], C/3 is considered as a standard current for the lithium-ion cell that is dedicated to energy-type applications, while 1C for the power-type applications.

$$Q = \int_{e_i}^{e_f} I_{dch} dt \quad (1.3)$$

$$C = \frac{2E}{U_2^2 - U_1^2} \quad (1.4)$$

1.3.5 State of charge

In LiBs, SOC is defined by the equation (1.5), it is the available capacity (Q_{disp}) relatively to a reference capacity (Q_{ref}), the reference capacity is often defined by users. For the SCaps, the SOC is calculated differently. It is expressed in the equation (1.6), where U_{oc} is the voltage of SCaps after the relaxation and U_{max} is the maximum voltage. SOC varies between 0% and 100%. This parameter is sensitive to the current, the temperature and the SOH of electrochemical energy storage elements.

$$SOC_{LiB} = \frac{Q_{disp}}{Q_{ref}} \times 100\% \quad (1.5)$$

$$SOC_{SCap} = \left(\frac{U_{oc}}{U_{max}}\right)^2 \times 100\% \quad (1.6)$$

1.3.6 Energy or power density

The energy or power density (E or P) is the ratio of energy/power relatively to the mass of LiBs, SCaps and LiCs. These two parameters allows to establish the Ragone diagram. According to the IEC 62660 [28] and the IEC 62576 [30] standards, the energy density is determined by the equation (1.7) for LiBs and by equation (1.8) for SCaps. The expression of

these equations is similar, but the energy of LiBs is stored between initial and final states, which correspond to the maximum voltage and the minimum voltage. Traditionally, the energy of SCap is stored between $0.5U_R$ et U_R , respectively, because the electric charge is nearly void below $0.5U_R$ for SCaps.

Equation (1.9) and equation (1.10) show the power density for LiBs and SCaps, respectively. The test, which makes it possible to determine the power density for the LiBs, is based on the current profile in IEC 62660 (Figure 1-11 (a)), where U_{10s} is the voltage of 10s by applying a current pulse and I_{dch_max} is the maximum current pulse. For SCaps, the power density is dependent on ESR . The energy/power densities are all sensitive to the temperature, the current, the SOC as well as the SOH.

$$E_{LiB} = \frac{1}{m} \int_{e_i}^{e_f} I_{dch} U(t) dt \quad (1.7) \quad E_{SCap} = \frac{1}{m} \int_{t_{U_r}}^{t_{0.5U_r}} I_{dch} U(t) dt \quad (1.8)$$

$$P_{LiB} = \frac{U_{10s} \times I_{dch_max}}{m} \quad (1.9) \quad P_{SCap} = \frac{0.25U_r^2}{m \times ESR} \quad (1.10)$$

1.4 Electrochemical energy storage systems for aeronautical applications

Developing the more electrical aircraft is ongoing to meet the regulation of environment. In France, the objective on reduction of polluting emission by aircraft must be reached more than 20% until 2025. The only primary source of energy for a civil aircraft today is kerosene. Based on this kerosene, three sub-sources of energy are generated according to hydraulic, pneumatic and electric system. The More Electrical Aircraft (MEA) aims to replace the hydraulic and/or pneumatic systems by electrical systems [40].

Electrochemical energy storage elements are one of the indispensable components in the electrical system for an aircraft [41]. They are used to start the engines and Auxiliary Power Unit (APU), to maintain the AC/DC network, to guarantee energy and power for avionics equipment in case of emergency situation, to feed navigation units, flight controls and to provide electricity for ground maintenance [42] [43]. Most of these functions are critical.

1.4.1 Electrochemical energy storage systems used in aircraft

Historically, Vented Lead-Acid batteries (VLA) was installed in aircraft until the 1950s. Then, Vented Nickel-Cadmium batteries (VNC) were replaced. After that, Sealed Nickel Cadmium (SNC) and Sealed Lead Acid (SLA) batteries are widely developed and installed in military and commercial aircraft, such as the C-130 military aircraft, the F-16 fighter and Boeing 777[42] [43]. In the 2000s, LiBs began to be applied in aircraft thanks to their high energy and power density compared to SNC and SLA.

Figure 1-13 illustrates some examples of batteries used in aircraft. They are all housed in an aluminium container. These batteries serve as a secondary energy source in aircraft. In general, several cells are put in series in a battery to provide a voltage around 28V, which corresponds to the voltage level of 28V DC bus in aircraft. The number of cells placed in series depends on the technology.

In Figure 1-13, the voltage of RG-145-2 lead acid battery manufactured by CONCORDE contains 12 cells in series. This battery has a capacity of 17Ah. The 2758 Ni-Cd battery from SAFT contains 20 cells in series, its capacity is 23Ah. It is installed in A318, A319, A320 and A321. The SAFT 450 VH1 lithium-ion battery has a capacity of 45Ah, it contains 7 cells in series, which is installed in A350 XWB.



Figure 1-13 Example of batteries used in aircrafts

Besides the batteries, SCaps can be also found in A380. They allow to open the aircraft safety doors in case of emergency. The operation of these heavy doors is controlled by a supercapacitor module, which is independent of the central power system in the aircraft [44].

1.4.2 Energy and power requirements in more electrical aircraft

As illustrated in Table 1-4, the on-board electric power requirements for aircraft have increased particularly in last decade years. This increase is directly linked with the power requirements of additional avionics systems and passenger comfort [45].

The more electrical aircraft A380 already flies in 2005 (Table 1-4). It has 4 main generators of 150kVA to ensure the electrical power requirements. The innovate architect based on 2 hydraulic and 2 electrical systems replace the traditional 3 hydraulic and 2 electrical systems [46]. Another example of the MEA is the Boeing 787 (Table 1-4), which has 4 generators of 250kW without the pneumatic systems [46]. The evolution of a conventional aircraft towards the MEA is possible thanks to the new architect of electrical distribution system and progress on the reliability and robustness of the components used in electrical system.

Aircraft	Concorde	A300	A300	A340	A380	B787
Year	1969	1972	1992	1991	2005	2009
Power (kVA)	240	250	300	460	600	1000

Table 1-4 Evolution of electrical power requirements in aircraft [46]

In the MEA, electrical energy is essentially stored in electrochemical energy storage system. The electrochemical energy storage elements are connected to the DC bus-bar to supply power to the DC bus [46]. The increased electric energy level requires an important capability

of electrochemical energy storage. Electrochemical energy storage systems could be a one type of the promising candidate for the electrification of non-propulsive functions and electric propulsion [47] [48]. The current electric propulsion aircraft is yet limited to small aircraft. Airbus group has launched an « E-Fan » project in 2011. E-fan is a prototype of the aircraft with 100% electric propulsion. It has two electric motors powered by lithium-ion polymer batteries of 250V with 1h autonomy.

1.4.3 Issues of electrochemical energy storage elements for aeronautical usage

Current technologies of electrochemical energy storage have multiple limitations for aeronautical usage. Two major issues are discussed in detail below. The first one concerns the gap of the energy and power densities for electrochemical energy storage elements versus the electrical energy requirements in aircraft. The second one concerns the reliability and robustness of these electrochemical energy storage elements under the aeronautical conditions [43].

1.4.3.1 Gap between technologies of electrochemical energy storage and electrical energy requirements in aircraft

Despite the significant improvements are made to the latest generation electrochemical energy storage technologies, their energy and power density are still lower than the on-board electrical requirements in aircraft. For instance, a long line aircraft cruise for two hours requires about 100kWh of electrical energy. To accomplish this mission, the aircraft must carry a mass of battery 60 times larger than its kerosene equivalent [49].

Increasing the energy density in the complete system is a crucial challenge for the electrification of aircraft. Aeronautical manufacturers estimate that the minimum energy density required for a more electrical airliner is 500Wh/kg [4]. The energy density for the different technologies of batteries is shown in Figure 1-14, among the current technologies, LiBs have a higher energy density that is in the range of 200Wh/kg.

To achieve the goal of 500Wh/kg, new technologies are being developed. Future LiBs and lithium-sulfur batteries based on new electrode materials allow to increase energy density. The concept of zinc-air and lithium-air is similar. This type of battery has a negative metal electrode (zinc or lithium) and a positive porous carbon electrode, both are immersed in the electrolyte. It can offer a high energy density, since the active material of oxygen does not need to be stored in the electrode, it is access in the air. Therefore, the energy density can be enhanced 5 times than LiBs theoretically.

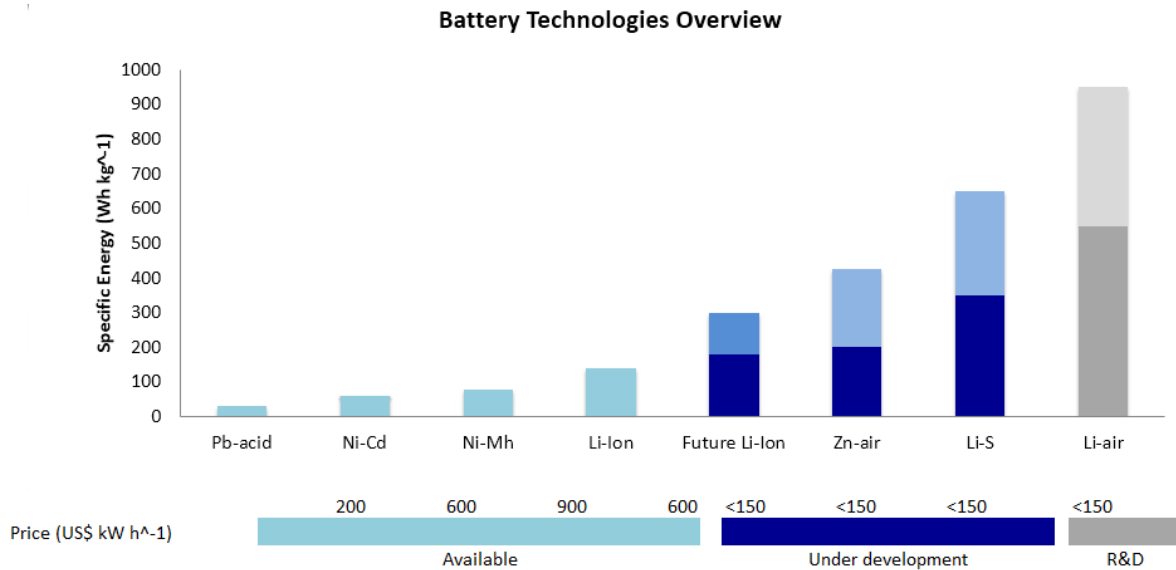


Figure 1-14 Battery technologies overview regarding energy densities (current, expected) and price [50]

Despite the eventual electrochemical energy storage technologies could not provide the energy requirements in aircraft. However, the multiple storage technologies such as the LiBs, the SCaps and the fuel cell are able to meet the different electrical energy needs in aircraft, especially for the non-propulsive functions. As illustrated in Figure 1-15 the diagram represents the variety electrical energy needs in the MEA. It can be observed that each application has a specific energy and power needs. Overall, the technology ensures the most of aeronautical applications if it can be operated between 1C to 20C. Therefore the electrochemical energy storage elements can be envisaged for aeronautical usage.

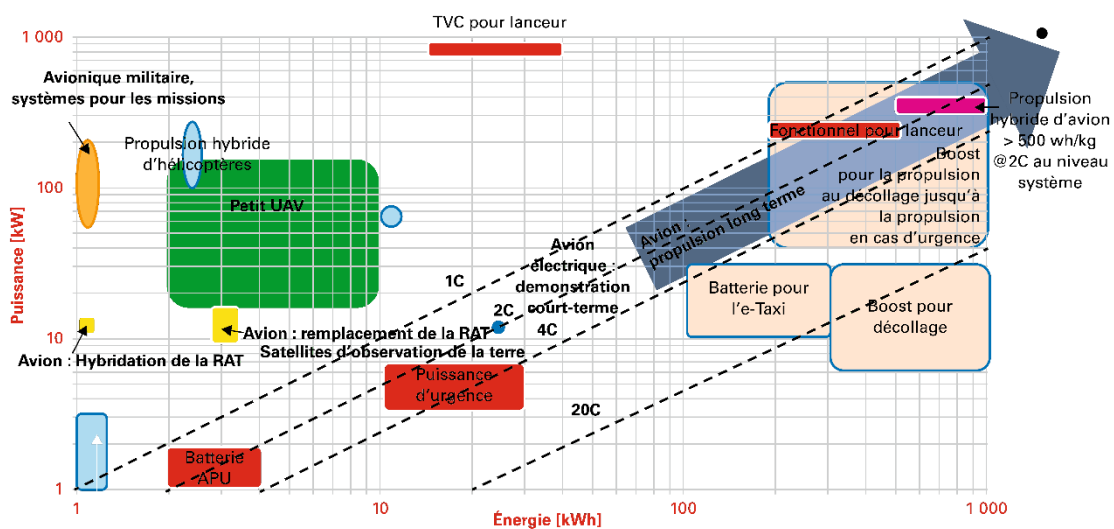


Figure 1-15 On-board multiple electrical energy requirements in aircraft [51]

Based on the previous discussion, thus mastering the selection and sizing of electrochemical energy storage elements for the electrification of aircraft is not directly by the different scenarios of electrification, it is also depends on the barriers and maturity of technology.

1.4.3.2 Issues related to aeronautical conditions

The LiBs and SCaps for aeronautical usage under specific conditions is critical, especially, the safety concerns the operation and the performance in extreme conditions.

- **The safety issues of electrochemical energy storage elements**

The safety during operation is the first criterion to be considered before integrating an electrochemical energy storage element in aircraft. In 2011, Boeing 787-8 Dreamliner was the first airliner using the LiBs. Two identical rechargeable Li-ion batteries are installed in Boeing 787. Each battery has a capacity of 75Ah, which contains eight cells, ranging from 2.5V to 4.2V [52]. Lithium Cobalt Dioxide (LiCoO₂) technology had been chosen as the positive electrode material for these cells. However, the LiBs were rejected after a few incidents between January and May of 2013 [53]. In January 2013, a Li-ion battery in Boeing 787 overheated and caught fire. According to the National Transportation Safety Board (NTSB), the thermal runaway of this battery was probably due to the internal short circuit. In the same year, Airbus therefore abandoned the use of LiBs in the A350. Afterwards, Boeing has made some improvements on the battery case to avoid the thermal runaway propagation. However, a flight was cancelled following the discovery of smoke from a lithium-ion battery during pre-boarding control [53].

The smoke, fire or even explosion caused by thermal runaway are the unacceptable issues in aircraft. Thermal runaway occurs when the cell is under abuse conditions [54]. For example, the mechanical abuse can trigger a short circuit in the cell, which introduces a large amount of heat. The cell is therefore overheated then its temperature exceeded certain threshold and thermal runaway is occurred.

The risks of thermal runaway is difficult to predict because it is an steeply phenomenon that could be occurred during the battery dysfunction [55]. In order to reduce these risks, in addition to the use of more stable and safe materials for electrochemical energy storage elements, enhance the mechanical proprieties of packaging is necessary. This allows to avoid the mechanical abuse. Using the electronic devices can prevent external short circuit, overcharging or over-discharging. For example, the Positive Thermal Coefficient (PTC) switches the current off when the cell is overheated. The Battery Management System (BMS) is used to monitor the battery SOH by warning users when there is a potential hazard [54].

- **Performance of electrochemical energy storage elements under extreme conditions**

The LiBs and SCaps are installed in the electronic equipment bay or in the cabin of the aircraft, these zones are under pressure [56]. But in the system failure situation, the LiBs and SCaps must be able to provide power to the avionic equipment at low temperature and low pressure. Regarding the temperature, as shown in Figure 1-16, the available capacity decreases with temperature for the different technologies of LiBs, which limits the energy; the resistance increases as the temperature drops, which limits the power.

Regarding the high amplitude, Jeevarajan [57] performed electrical tests under low pressure, it observed that the capacity of a pouch lithium cell loses 35% relatively to its initial

capacity after 6 hours at 0.6Bar. Therefore, mastering the characteristics of electrochemical energy storage elements extreme conditions are predominant for aeronautical usage.

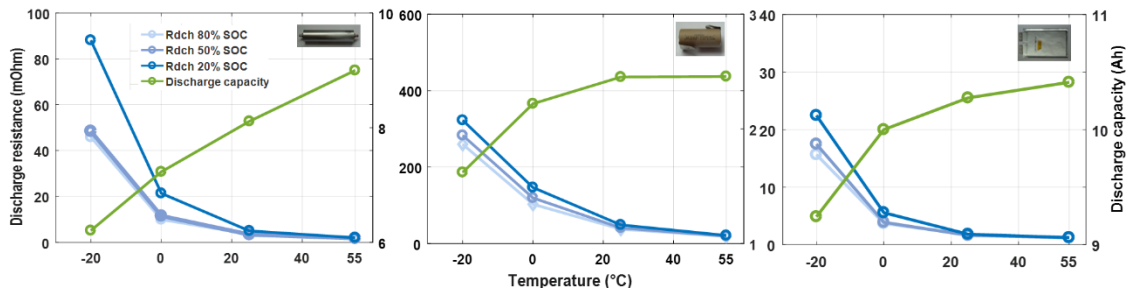


Figure 1-16 Discharged capacity and resistance of Li-ion cells at different temperatures (-20°C, 0°C, 25°C et 55°C) [58]

1.4.4 Standards and certifications

The challenges of embedding the electrochemical storage elements in MEA are not only at the level of technology and the aeronautical conditions, but also a complex issue on the definition of regulations, standards and certifications. In general, aeronautical standards are always developed by the experts in the aviation committee, such as the International Civil Aviation Organization (ICAO), the European Aviation Safety Agency (EASA) in Europe and the Federal Aviation Administration (FAA) in the USA, etc.

Specific standards concerning the usage of batteries for civil aircraft equipment are several, such as the RTCA standards DO-293, DO-311, DO-188 and DO-160 [59]. The standard of DO-293 addresses the nickel-cadmium, nickel-metal-hydride and lead-acid batteries on the choice of technologies, sizing, packaging, ventilation and the conditions for the storage and operation of these batteries. The DO-311 is applied to rechargeable LiBs installed permanently in the aircraft. It offers the characterization protocols of the performance of LiBs. In addition, the standard criteria are constructed to verify the reliability and to ensure the safety operation of LiBs. Respecting these standard requirements ensures the safety of battery systems under aeronautical conditions. The standard of DO-188 focuses on Emergency Locator Transmitter (ELT) battery regulations. Furthermore, the environmental conditions of tests, including the investigation and the maintenance after incidents of the battery systems are defined in the standard DO-160.

1.5 Conclusion

In this chapter, the chemical compositions, the working principles and the different forms of LiBs, SCaps and LiCs are presented in detail and compared between themselves. The materials used in these elements and the way of storing the electric charges determine their application roles (energy or power type) in a system.

Then, the main parameters of LiBs, SCaps and LiCs are introduced through electrochemical techniques and test protocols in international standards. Most of these

parameters are in common for LiBs, SCaps and LiCs. These interdependent parameters allow to quantify the performance of the electrochemical storage elements.

Finally, the development of electrochemical energy storage technologies used on board the aircraft is presented. The electrochemical storage element seems to be a promising candidate to integrate in the MEA. But above all, issues related to safety and performance under aeronautical conditions need to be addressed. The specific aeronautical standards related to the implantation of LiBs exist to ensure the least risks.

Chapter 2

Comparative performance quantification of electrochemical energy storage elements by experiments and modelling

Table of contents

2.1 Introduction	32
2.2 Experiments	32
2.2.1. Tested technologies of LiBs, SCaps, LiCs and Li-S	32
2.2.2. The CaCySSEE platform	35
2.3 Reference test design	36
2.3.1. Reception tests.....	36
2.3.2. Initial tests	36
2.3.3. Performance tests	37
2.3.3.1 Incremental discharge.....	37
2.3.3.2 Available discharged capacity	38
2.3.3.3 Maximal power discharge	38
2.3.4. Ageing tests	39
2.3.5. Abuse tests.....	39
2.3.6. Available discharged capacity for LiBs, LiCs and SCaps	39
2.4 Cell to cell characterization	41
2.5 Non-isothermal Ragone plots of 18650 Li-ion cells from datasheet and galvanostatic discharge tests	41
2.5.1. Performance quantification with experimental approach.....	42
2.5.2. Comparison for constant current discharge.....	43
2.5.3. Performance quantification with Ragone plot model.....	45
2.5.3.1 Electrical model.....	46

2.5.3.2 Thermal model	50
2.5.4. Validation of Ragone Plot model	53
2.5.4.1 Ragone plot model for 25°C.....	54
2.5.5. Extending Ragone plot model for wide operating temperature range	56
2.5.6. Enhanced non-isothermal Ragone plot	58
2.6 Conclusion.....	59

2.1 Introduction

In this chapter, we focus on the comparative study of performance quantification for all investigated ElectroChemical Energy Storage (ECES) elements. Two main sections are included in this chapter.

The first section is dedicated to introduce the characteristic of investigated LiBs, SCaps, LiCs and the experimental equipment. Then, a large experimental matrix is built by considering all the technical datasheet and aeronautical conditions. A series of specific protocols are considered as the reference tests to quantify the performance of different electrochemical energy storage elements, especially, in terms of energy density and power density. Furthermore, the experimental tests cover a wide temperature range from -20°C to 55°C and it was designed for the energy-type, the power-type and the high power-type of applications.

In the second section, the study focuses on establishing a Ragone plot for generic chemistry (NMC/graphite+SiO, NCA/graphite) of Li-ion cells. The proposed method is based on a simple and efficient coupled electrical-thermal model. This model is parametrized by the experimental data from the investigated reference tests. In addition, the proposed Ragone plot model can be extended to a wide operating temperature range [-20°C, 55°C] under multiple power levels and it has a good accuracy. A non-isothermal Ragone plot is established for the first time, which could be employed as a conception aid tool for the selection of Li-ion cells in system design process.

Finally, the energy density and the power density at the fresh state in a wide temperature range [-20°C, 55°C] can be quantified according to experiments and modelling.

2.2 Experiments

2.2.1 Tested technologies of LiBs, SCaps, LiCs and Li-S

In this study, nine technologies of commercial LiBs, SCaps, LiCs and Li-S are investigated. Among them, 6 LiBs technologies, 1 SCap technology, 1 LiC technology and 1 Li-S technology. They are considered as the promising candidates for aeronautical usage according to industrial partners. All the main characteristics such as manufacturer, form, chemistry (CHEM), capacity or capacitance (C), energy density (E), power density (P), minimal and maximal voltage (U_{min} - U_{max}), nominal voltage (U_n), internal resistance or ESR (R_{int}/ESR), recommended maximal current of charge and discharge (I_{ch}/I_{dch}) and temperature (T) range for charge and discharge are summarized in Table 2-1.

- **LiBs technologies**

For all the technologies of LiBs, not only the conventional LiBs have been selected such as the NCA/graphite, NMC/graphite, LFP/graphite chemistry cells, but also the latest generation of LiBs, such as NMC/graphite+SiO, NMC/LTO. Among them, NCA/graphite and NMC/graphite+SiO LiBs provide a high energy and power densities that can meet the energy and power needs for aeronautical applications. While, LFP/graphite is selected thanks to the safety. NMC/LTO cell is chosen thanks to the working capability in low temperatures. In Table 2-1, it can be observed that each technology has the specific characteristic and operating condition (T , I_{ch}/I_{dch}). For almost LiBs, the voltage range of LiBs is in 2.5V-4V besides NMC/LTO cells (1.5-3V). Furthermore, the temperature and current ranges of charge is smaller than temperature and current ranges of discharge.

- **SCaps technology**

One technology of SCaps has been selected. This SCaps has 500F with a cylindrical form. Compared to the LiBs, the voltage range is between 0-3V. The capacitance of SCaps depends on its voltage. It is always measured between $0.5U_n-U_n$. The ESR (0.18m Ω) is ten times less than the internal resistance of LiBs (~1m Ω). The operating temperature range is identical for discharge and charge operating conditions.

- **LiCs technology**

One LiC technology with pouch form has been chosen. As shown in Table 2-1, it can be seen that the electrode terminals are not on the same side of cell. The capacity given by manufacturer is expressed in ampere hours, which is similar as the LiBs. But, the voltage range and operating temperature are similar as the SCaps.

- **Lithium sulfur technology**

A Li-S technology has also been selected. It has 10Ah capacity in pouch form. The voltage range value of Li-S is lower than the classical LiBs. The operating of cell can be assured until 80°C, but its working capability is limited at -5°C. In addition, a lot of precautions must be required according to manufacturer for the experimental tests. Only abuse tests were performed on Li-S cells.

Item	Prop.	Manufacturer	Form (mm)	CHEM	C (Ah/F)	E (Wh/kg)	P (W/kg)	U_{min} - U_{max} (V)	U_n (V)	R_{int}/ESR (m Ω)	I_{cst}/I_{dch} (A)	T_{cst}/T_{dch} range (°C)
	LIBs	LG Chem	18650	NMC/graphite+ SiO	3 (C/S)	240	1742	2.5-4.2	3.6	14-16	10/20	0-50 -20-75
		Samsung	18650	NCA/graphite	2.5 (C/S)	209	1815	2.5-4.2	3.6	14-16	10/20	0-60 -20-75
		EAS	34x1440	NCA/graphite	7.5 (C/S)	84	2340	2.7-4.2	3.6	<6.5	15/150	0-45 -30-60
		K2 Energy	26650	LFP/graphite	2.6 (C/S)	103	1242	2-3.65	3.2	<9	10/42	0-50 -20-60
		Valence	26650	LFMgP/graphite	2.5 (C/S)	101	2531	2-3.65	3.2	<6.5	15/25	0-55 -20-55
		EIG	Pouch 222x130x7.8	NCA/LTO	10 (1C)	54	3100	1.5-3	2.4	<1	10/200	-40-55
	SCaps	Skeleton	40x63	AC	500F	5.6	45 000	0-3	2.85	0.18	600 (1s)	-40-65
	LiCs	Yunasko	Pouch 120x75x11	AC/Li doped carbon	1.3 (1C)	37	40000	0-2.7	No	<1	200	-40-60
	Li-S	Oxis	Pouch 174x112x7.3	S/Li	10 (C/S)	152	912	1.5-2.45	2.05	<13	10/30	23-80 -5-80

Table 2-1 Datasheet for all the investigated electrochemical energy storage elements

2.2.2 The CaCySSEE platform

In this study, all experimental tests (exc. abuse tests) were performed in Characterization and Cycling of Embedded Energy Storage Systems (CaCySSEE) platform of IMS laboratory. Some main equipment can be seen in Figure 2-1, it contains several test channels for power cycling ageing tests, EIS or different combined test modes. This equipment provides the electrical characterization of the samples in a controlled thermal environment. The acquisition of voltages, currents and temperatures are insured continuously throughout the tests or occasionally during specific characterization phases are insured. In addition, the security of the platform is controlled by a network of gas and fire sensors associated with a supervision and an alarm central.

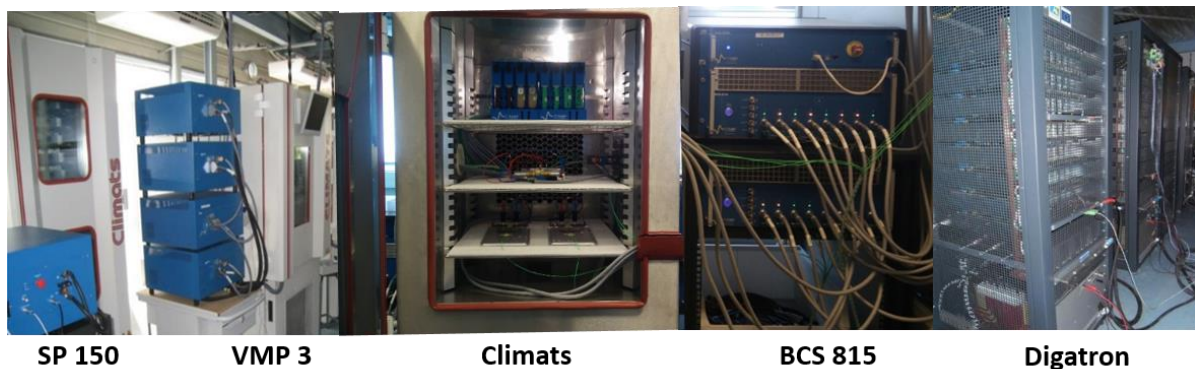


Figure 2-1 Overview of main equipment in CaCySSEE platform

Electrochemical stations including one SP 150, three VMP 3 and six BCS 815 are available on the platform. VMP-3 composes a potentiostat and a frequency analysis module (10 μ Hz-100kHz), it is connected on a current amplifier which can deliver up to 100A. All these devices allows to increase the EIS accuracy for impedance measurement at low frequency. The voltage range of SP150 that can be provided is low [-10V, 10V] compared to BCS 815 [0V, 9V], it is especially used to characterize the SCaps. BCS 815 offers 8 channels of 15A for electrical characterization. Furthermore, the parallelization of two or four channels can be implemented in order to increase the charge and discharge current, which offers a flexible configuration for experimental tests. All the electrochemical stations ensure the impedance measurement, the constant current charge-discharge, the constant power charge-discharge, the cyclic voltammetry, EIS, etc.

Digatron allows to characterize the high power electrochemical energy storage elements, such as the SCaps. Since it can supply a high level of current for power cycling ageing or current pulse. Several channel can provide the continuously current at ± 400 A or 1000A peak current for charge and discharge.

Climatic chambers and ovens are used to impose the temperature of tests. In addition, it can provide a confined environment and a safe protection in case of failure of a device under test.

2.3 Reference test design

In order to quantify and compare the performance of investigated electrochemical storage elements, a reference test must be defined firstly by considering the operating limits listed in Table 2-1. In addition, the conditions of this reference test must fulfil the operating exigencies for aeronautical usage. This reference test includes two parts: the first part is focused on the performance quantification in terms of energy density and power density in a wide temperature range [-20°C, 55°C] for LiBs, SCpas and LiCs at the fresh state; the second part is devoted to the study of ageing behaviors under different endured conditions to evaluate the lifespan of all investigated electrochemical energy storage elements. Furthermore, in this reference test, some abuse testing are defined to evaluate the safety of different electrochemical energy storage elements. In this chapter, the performance of LiBs, SCaps and LiCs are quantified and compared at the fresh state by experiments and modelling. While, the chapter 3 will be dedicated to the ageing and safety study.

From Table 2-1, it can be observed that the characteristic between the investigated electrochemical energy storage elements are quite different. Inspired by the IEC 62660 standard [28] for the application of electric or hybrid vehicles, two current levels are defined according to the vehicle type. C/3 for electric vehicle and 1C for hybrid vehicle. Thereby, a classification depending on the application type is carried out at first. Three types of application can be defined according to the technical datasheet of elements, especially on the charge/discharge current levels and energy and power densities. Three types of application are defined in total, LG (LiBs) and Oxis (Li-S) are in the energy-type, Yunasko (LiCs) and Skeleton (SCaps) are in the high power-type, the others are in the power-type. The colour nuance in Table 2-1 corresponds to different type respectively, such as the energy-type (light orange), power-type (orange) and High power-type (dark orange). This classification allows to divide all the electrochemical energy storage elements into three families. From this, the current level can be defined correctly to avoid overestimating or underestimating the performance of LiBs, SCaps and LiCs.

Four tests are included in the reference test, which are the reception tests, initial tests, performance tests and ageing tests. Each test has their specific roles.

2.3.1 Reception tests

The reception tests propose is to measure the main physical characteristics in order to check if they evolve during the reference test campaigns. This tests includes the visual inspection, cell marking, mass and dimension measurement, OCV and EIS measurement.

2.3.2 Initial tests

The goal of the initial tests is to determine the capacity of the cell. This capacity is considered as the reference to set the corresponding SOC in the performance and ageing test campaigns. A standard CC–CV charging method at specific C rate (Table 2-2) was applied until the maximal voltage and the tests were stopped when the cut-off current reaches at C/20. Then, the cell was discharged at different rates as indicated in Table 2-2 to measure its capacity. C/2 for energy type elements, 1C for power, 3C for LiCs and 50A ($0.1 \text{ AF}^{-1} \times 500\text{F}$) for SCaps. Furthermore, all LiBs were discharged between maximal and minimal voltages. While LiCs

were discharged between 2.7V and 1.35V and SCaps were discharged between 2.85V (U_n) and 1.425V ($0.5U_n$). The initial tests were performed in a climatic chamber at 25°C.

Cells type	Energy	Power	High power
C rate	C/2	1C	3C or 0.1AF ⁻¹

Table 2-2 Charge/discharge rate for reference capacity measurement

2.3.3 Performance tests

In the performance tests, OCV, internal resistance, available discharged capacity and maximal power measurements in a wide temperature range [-20°C, 55°C] are all investigated. The performance tests were performed on 2 cells at each temperature (-20, 0, 25, 55°C), which corresponds to the aeronautical temperature conditions. The main goal of performance tests is to evaluate the available discharged energy and power density in a wide temperature range from -20°C to 55°C. Thereby, all the cells were charged by the classical CC-CV charge method as in the initial tests at 25°C. Furthermore, the temperature at the surface of all elements are measured during the performance tests. The test program must include the limits given by technical datasheet for temperature, voltage and current to avoid safe issues.

2.3.3.1 Incremental discharge

Incremental discharge method is proposed for OCV and discharged internal resistance at the same time, this method is similar with the GITT, however, a charge and discharge pulses are applied after the SOC reset. The voltage profile of cell is illustrated in Figure 2-2 (a).

After a thermal stabilization of 3h at the targeted temperature (0°C, 25°C, 55°C) in a climatic chamber, the incremental discharge was performed at 1C by steps of 5% or 10% SOC until 0% SOC. At each SOC, the OCV measurement was done after a recovery time that ranges from 0.5 to 3h, depending on SOC step and temperature of test. Then, at this SOC, for resistance measurement purpose, a 20s discharge current pulse (1C) followed by a 20s charge current pulse (1C) are applied, the two pulses are separated by a recovery time of 40s, For tests ran at -20°C, the discharge and charge pulses are applied at the required temperature, but incremental discharge of SOC was done at 25°C.

The discharge resistance is determined according to equation (1.1), which is the ration between the voltage drop ($U_{10s}-U_{ocv}$) and the constant current (I). The profile of voltage drop is depicted in Figure 2-2 (b) under 1C discharge pulse at different temperatures for a cell from EAS. It can be observed that the voltage drop increases when the temperature of tests decreases under the same current level, which signifies the internal resistance at low temperature is more significant.

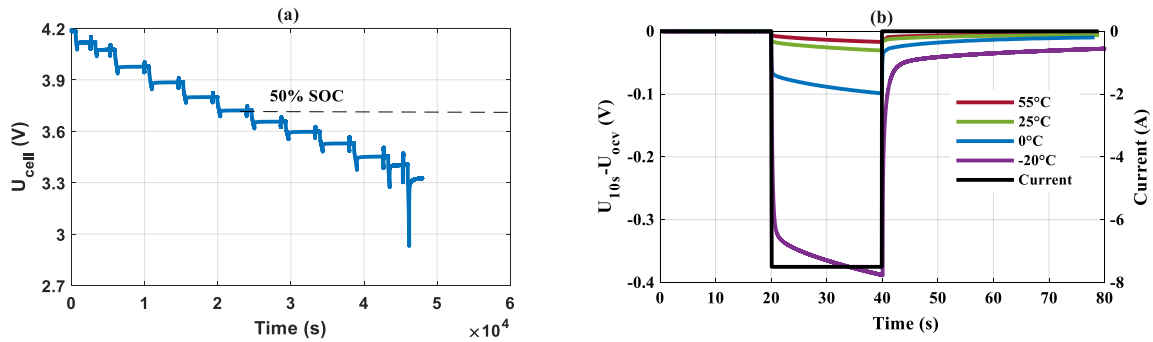


Figure 2-2(a) Voltage profile during incremental discharge at 1C and 25°C (b) Zoom on voltage drop ($U_{10s}-U_{ocv}$) at 50% SOC and -20, 0, 25, 55°C under 1C discharge current pulse for EAS cell

The method of incremental discharge was only carried on LiBs and LiCs, because the self-discharge is too significant to measure the OCV of SCaps. Besides the incremental discharge tests, the continuous charge and discharge at C/20 were performed at -20, 0, 25 and 55°C for pseudo-OCV measurement.

2.3.3.2 Available discharged capacity

The available discharged capacity measurement is performed at different discharge rates and at multiple temperatures (-20, 0, 25, 55°C). This test allows to evaluate the available discharged capacity in aeronautical temperature conditions. As indicated in the Table 2-3, three C rates had been chosen for each type of cells. Among the different current levels, it can be seen that there is always one C rate in common for all the electrochemical energy storage elements. This could be a common parameter during the performance comparison.

C rate	C/3	1C	3C or 0.1AF ⁻¹	5C or 0.2AF ⁻¹	10C or 0.4 AF ⁻¹
Energy	X	X	X		
Power		X	X	X	
High power			X	X	X

Table 2-3 Discharge rates according to element types for capacity measurement at -20°C, 0°C, 25°C and 55°C

2.3.3.3 Maximal power discharge

The goal of the maximal power test is to quantify the maximal power of investigated elements. The maximal power discharge tests are defined in the IEC62660-1 standard [28], where three current levels were applied on the elements. The cell was set at the required SOC by applying a constant discharge current with the current level defined in Table 2-2. After SOC reset, the cell was charged and discharged by applying 10s pulses, each of them separated by a recovery time of 10min. Discharge current pulse and charge current pulse are alternated, moreover the amplitude of the pulses increased. The last two current levels are listed in Table 2-3 according to the type with the maximal currents defined in technical datasheet. These three current levels compose all the C rates of maximal power discharge. The test was run at 2 different temperatures (+25°C and 0°C) and at 2 different SOC's (20% and 80%).

2.3.4 Ageing tests

Two generic types of ageing tests including calendar ageing and power cycling ageing are defined in the reference tests in order to compare the lifespan for investigated elements in aeronautical environment $[-20^{\circ}\text{C}, 55^{\circ}\text{C}]$. The experimental tests and results will be presented in chapter 3.

2.3.5 Abuse tests

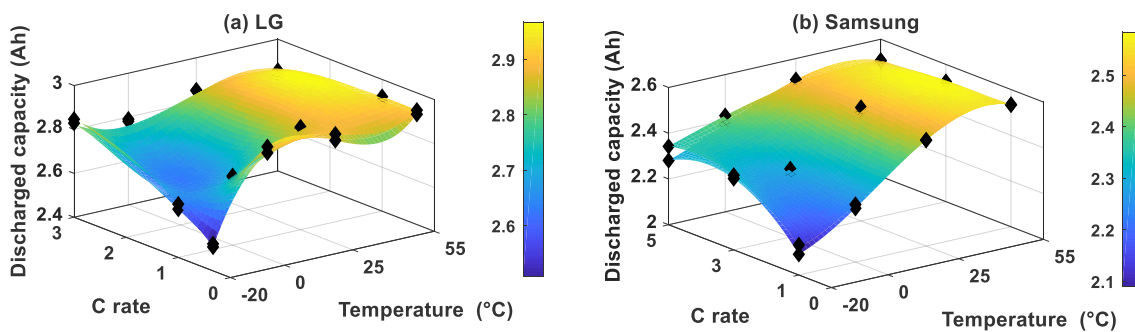
Three types of abuse testing are also in the reference tests to evaluate the safety of investigated electrochemical energy storage, which are the thermal stability, overcharge and altitude simulation. The experimental results will be discussed and analysed in chapter 3.

2.3.6 Available discharged capacity for LiBs, LiCs and SCaps

Figure 2-3 (a-h) illustrates the results of available discharged capacity tests for all investigated electrochemical energy storage elements. The black diamond represents the experimental discharged capacity versus the temperature and C rate (Table 2-3), two cells available discharge capacity are presented on each plot. The 3D mapping is constructed with the “*spline*” function in Matlab®.

It can be seen that for almost all technologies, the capacity measurement has a good consistency under all conditions (T, C rate). However, the discharged capacity at -20°C under 5C of one cell from K2 is quite different between two cells as illustrated in Figure 2-3 (d). In fact, the voltage of this cell reached the minimal voltage limit (2.3V) at the beginning of test, which was due to the huge internal resistance at -20°C . For Valence, a slight difference is observed at 25°C under 1C (Figure 2-3 (e)).

For all the technologies, it can be noticed that the available discharged capacity increases with the temperature for all C rates. In the case of SCaps (Figure 2-3 (h)), the temperature of discharge at 55°C under 5C and 10C exceeds the maximal temperature. Therefore, the discharged capacity in these conditions are not available.



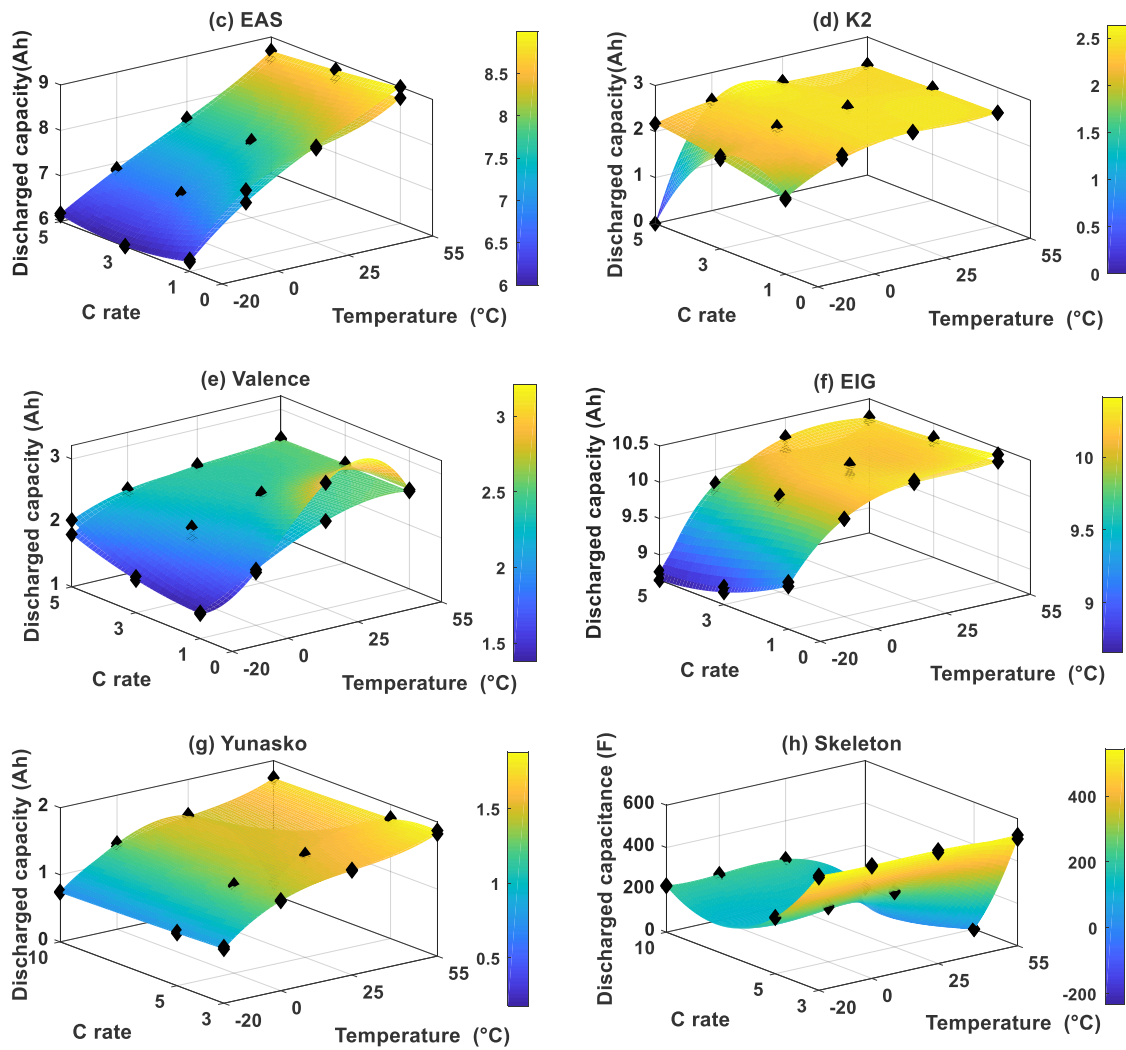


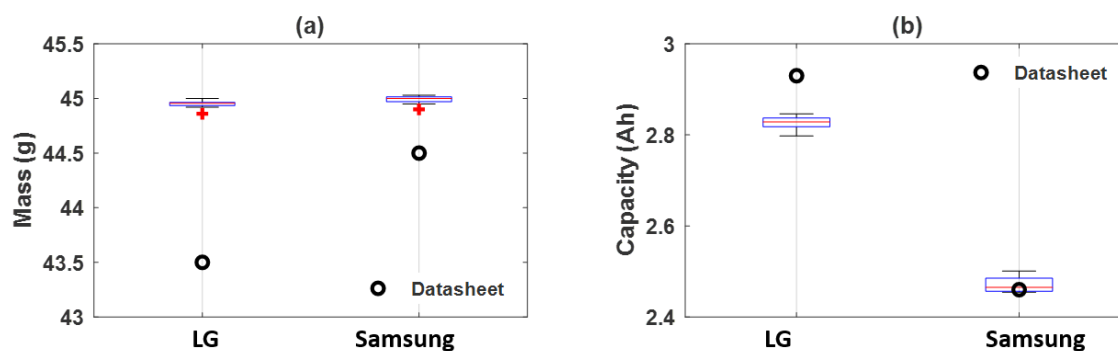
Figure 2-3 Available discharged capacity for all electrochemical energy storage elements at 55°C, 25°C, 0°C and -20°C under 3 C rates (C/3, 1C, 3C for energy type, 1C, 3C, 5C for power type, 3C, 5C and 10C for high power type)

Peukert’s law indicates that the capacity decreases when the C rate increases. However, it can be noted that besides the technologies EAS, EIG, Yunasko and Skeleton, the other technologies (LG, Samsung, K2 and Valence) do not follow the Peukert’s law. In fact, all these technologies are in cylindrical form, the heat generated during discharge could not cool down enough fast due to the smaller Surface-Area-To-Volume ration (SA/VOL) compared to the prismatic or the pouch cells. Therefore, the significant cell temperature increase leads to an improved capacity under high current levels.

These experimental results are used to determine the energy density and power density according to equations (1.7-1.10) respectively. In addition, a relative capacity can be defined (chapter 3), which is used to evaluate the capability of all the electrochemical energy storage elements working capability at extreme temperatures (-20°C and 55°C) or extreme C rates.

2.4 Cell to cell characterization

As the design of experiments for the reference tests is quite large. Only two cells were tested for the temperature conditions. Thereby, a study of cell-to-cell consistency is indispensable. The mass and initial capacity consistencies versus the datasheet from manufacturer are compared. One example for technologies LG and Samsung is shown in Figure 2-4. The maximal, minimal, median, upper and lower quartile of mass and capacity for 20 cells of these two technologies are presented in boxplot. Considering the mass, both technologies have a short boxplot, which means the overall cells have a high level of consistency, moreover, their standard deviation of mass is small. Considering the capacity as shown in boxplot on Figure 2-4 (b), both technologies have a good consistency between them. Although the difference exists between the experimental measurement and datasheets, 20 selected cells for both technologies have a slight cell-to-cell variation. The same boxplot based on statistical method is applied to the other technologies. Overall, a good consistency and authenticity are observed. This good consistency ensure a high degree of trust for analysing and applying the results under various tests conditions hereafter.



	LG	Samsung
Mass from datasheet (g)	43.5	44.5
Average mass (g)	44.95	44.99
Standard deviation (g)	0.041	0.043
Capacity datasheet (Ah)	2.93 (0.5C)	2.46 (1C)
Average capacity (Ah)	2.83	2.47
Standard deviation (Ah)	0.015	0.020

Figure 2-4 Boxplot of the cell-to-cell variation vs. datasheet and statistics results based on 20 cells measurements of (a) mass, (b) Discharged capacity at 25°C

2.5 Non-isothermal Ragone plots of 18650 Li-ion cells from datasheet and galvanostatic discharge tests

Two LiBs technologies are selected for the performance quantification by modelling. They are 18650 NMC/graphite+SiO cell from LG and NCA/graphite cell from Samsung. In this section, a non-isothermal Ragone plots are investigated for these two chemistries of LiBs.

2.5.1 Performance quantification with experimental approach

Before developing a generic methodology to obtain Ragone plots without dedicated experiments, regular experimental Ragone plots are established for further comparison purposes for both technologies at -20°C , 0°C , 25°C and 55°C under low (3W), medium (15W), and high (30W) constant discharge power levels. A standard CC–CV charging method at 1 C is employed for both technologies until the cut-off current reaches $C/20$. Next, multiple constant power discharges are investigated for a specific temperature after the thermal stabilisation in the climatic chamber, respectively. Figure 2-5 illustrates the experimental procedure of the constant power discharge under three power levels for Samsung cell at 25°C . In the constant power discharge, the high power leads to a high current. Therefore, the duration of the constant power discharge decreases under high power levels.

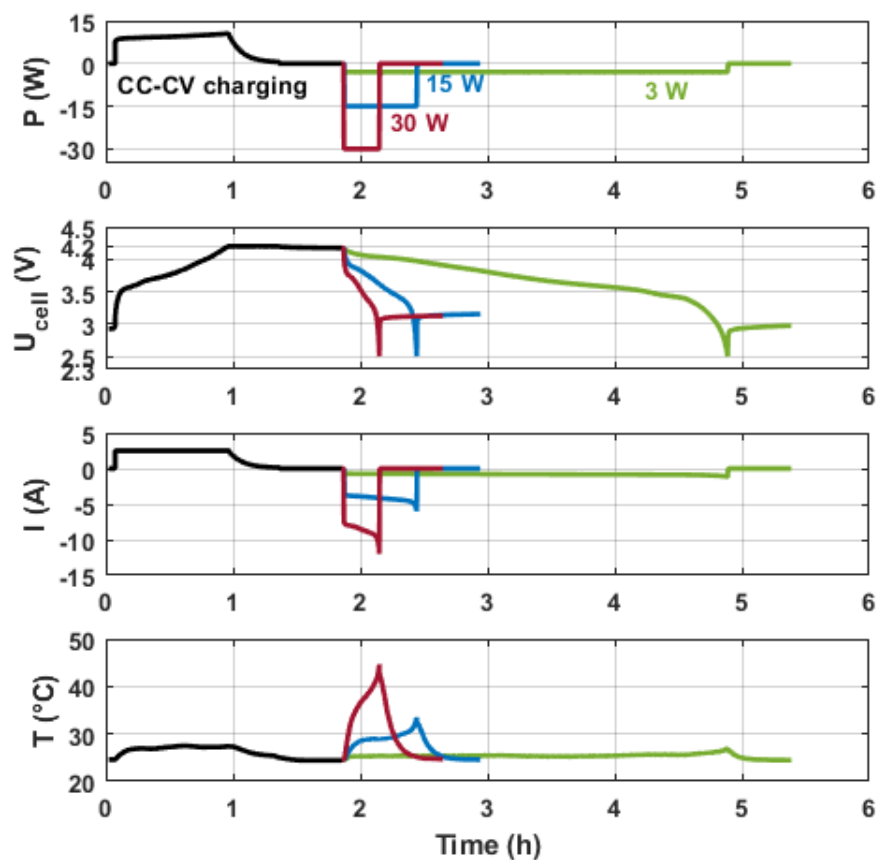


Figure 2-5 Experimental constant power discharge procedure for Samsung at 25°C ; power, cell voltage, current and temperature versus time, respectively

Regarding the Ragone plot, the power density is determined with equation (1.7) and equation (1.9). In a conventional Ragone plot, the performance quantification of the electrochemical ESSs is performed at the beginning of the life cycle; when the cells are in a fresh state.

Figure 2-6 illustrates the experimental Ragone plot for a constant power discharge. The discharged energy densities are plotted versus the power density based on equation (1.7) and equation (1.9). The dotted lines correspond to the time needed to perform a complete constant power discharge.

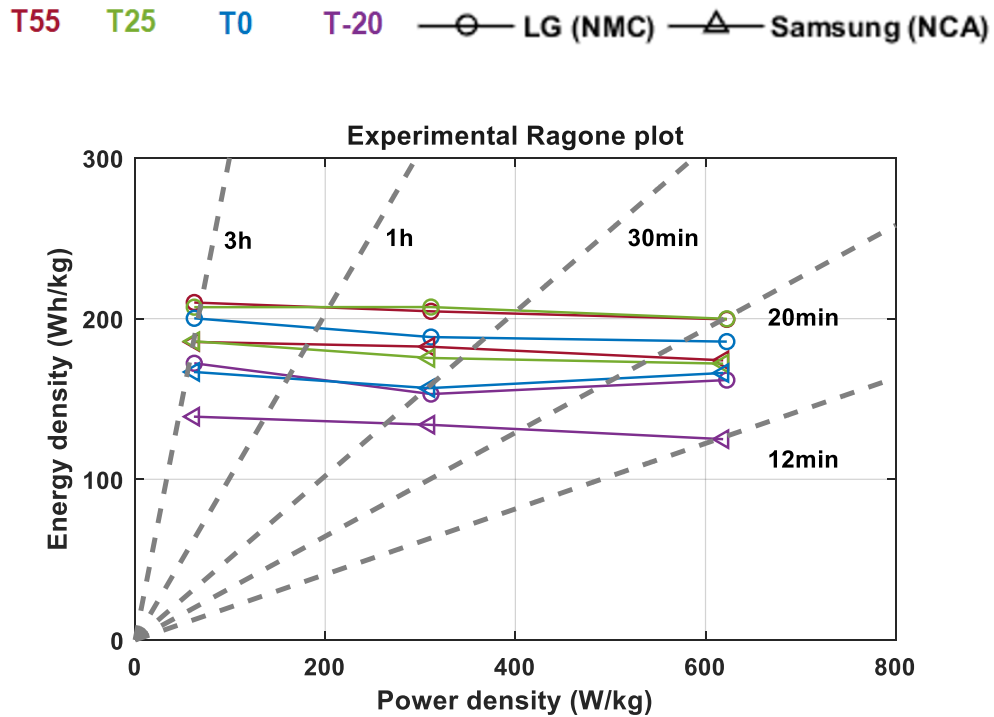


Figure 2-6 Experimental Ragone plot for LG (NMC) and Samsung (NCA) at -20°C , 0°C , 25°C and 55°C

Firstly, for both technologies, it can be observed that the available energy increases with increasing temperature under equal discharged power levels. The energy density increases by approximately 20% for the investigated large temperature range [-20°C , 55°C]. Hence, the available energy is limited by the cold environment. Secondly, at all operating temperatures, LG exhibits higher energy densities than Samsung. It seems that LG has a better performance. This point will be further discussed in the following section.

2.5.2 Comparison for constant current discharge

Instead of quantifying the energy and power densities of Li-ion cells under a constant power discharge, a constant current discharge is usually applied. Therefore, the previous continuous discharges at 1C, 3C, and 5C applied at -20°C , 0°C , 25°C , and 55°C are served here for the comparison.

Figure 2-7 presents the cell voltage and increased temperature at the cell surface versus the discharged capacity during the constant current discharge. The discharged capacity depends on the temperature and current in both technologies. It increases with the temperature at all current rates for both technologies. However, the constant current discharge for Samsung at 55°C and -20°C is incomplete owing to the limits of safe operating conditions. As illustrated in Figure 2-7 (a3), during a constant current discharge at 55°C , the temperature at the cell surface exceeds 75°C . This is the maximal operating temperature and the constant current discharge is therefore interrupted to avoid a thermal runaway [60]. The cell voltage reaches 2.5V at -20°C , which is the minimal voltage. This behaviour is owing to the high internal resistance at low temperatures.

For a continuous discharge current at 1C and 3C, the increased temperature at -20°C is approximately four times higher than that at 55°C . For 5C, this difference decreases, which indicates that the high current has an important contribution to the cell self-heating during the discharge [61].

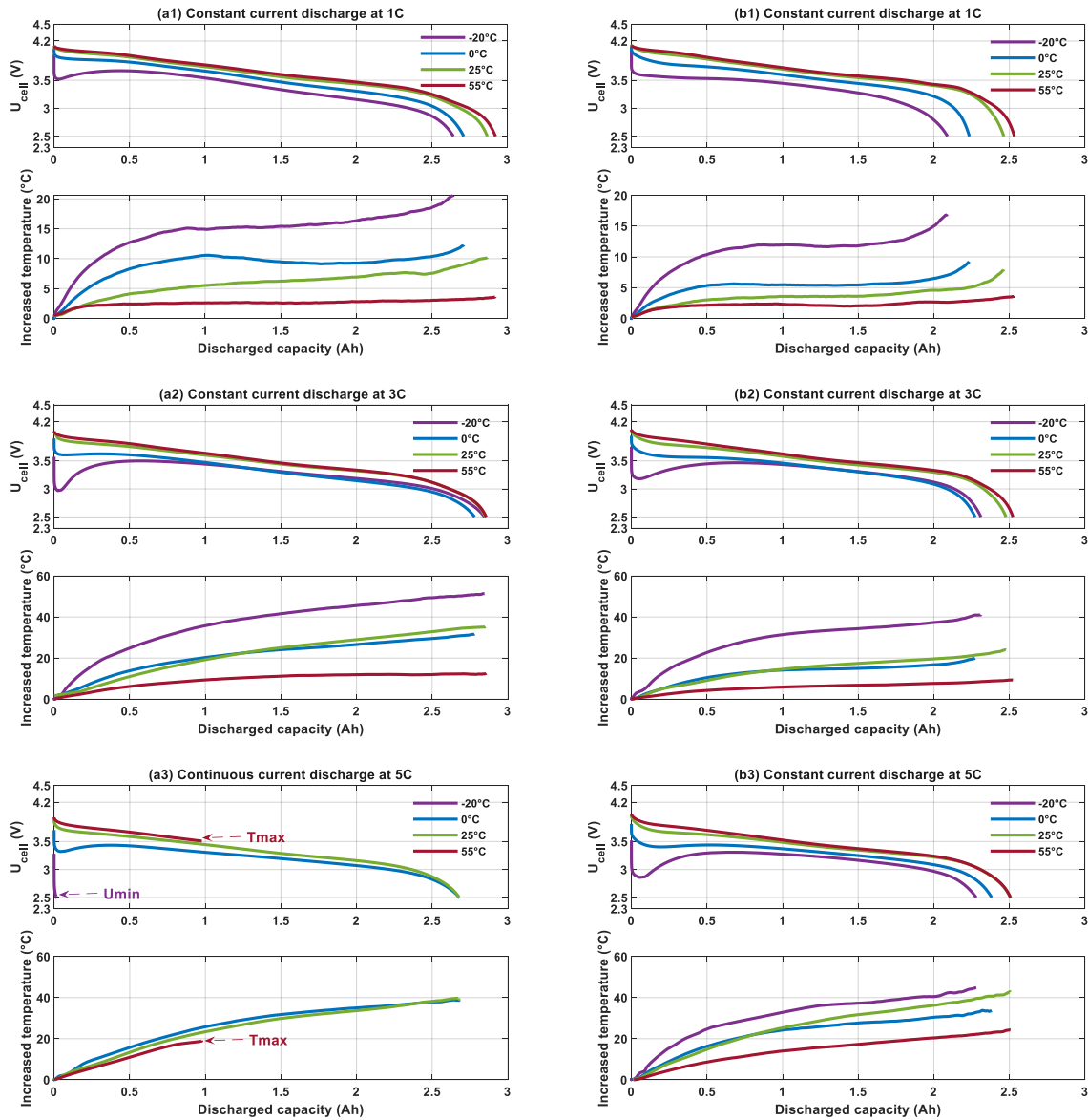


Figure 2-7 U_{cell} and increased temperature versus discharged capacity at -20°C , 0°C , 25°C , 55°C during constant current discharge under 1C, 3C and 5C for LG (left) and Samsung (right)

The energy density for a continuous discharge can be determined with equation (1.7). The power density is the product of cell voltage and cell current during a complete discharge. Because the discharge test procedure is changed, it is assumed that the values of energy and power densities might be different. However, only few papers mention this difference [62].

Figure 2-8 compares the energy and power densities determined via the two test procedures. Regarding LG, the energy and power densities are more than 15% higher under constant current discharge compared with the values for the constant power discharge. This difference is more significant for Samsung. The energy densities determined for a constant

current discharge are more than 25% higher at 55°C and -20°C with respect to the values for a constant power discharge. Our results are in a good agreement with those reported by Sarpal et al. [63].

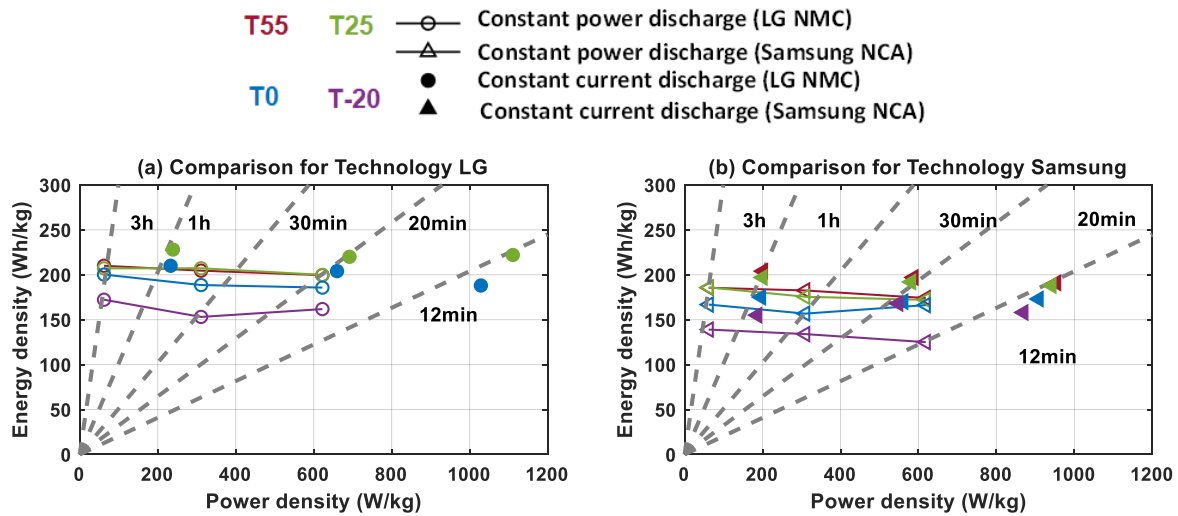


Figure 2-8 Energy density versus power density at -20°C, 0°C, 25°C and 55°C determined for constant current discharge (1C, 3C, 5C) and constant power discharge (3W, 15W, 20W) for LG (left) and Samsung (right)

The most common test procedures employ a constant current discharge to characterise Li-ion cell performances. However, the energy and power densities based on a constant current discharge are higher than the values determined for a constant power discharge. To select optimal Li-ion technology for a given application, the next part investigates the parameterisation of a model based on constant current tests in order to simulate constant power discharges and obtain Ragone plots. In addition, because the constant current discharge curves are often provided by the manufacturer, the accuracy of the process can be directly evaluated with the datasheets.

2.5.3 Performance quantification with Ragone plot model

The Ragone plot model must be able to predict the voltage, current, discharge duration, and discharged energy of the Li-ion cell for a constant power discharge. Moreover, because the proposed model must be validated for different operating temperatures, a thermal model must be included. In a conventional Ragone plot, the performance quantification of electrochemical energy storage systems is performed at the beginning of a life cycle. Hence, the batteries are in a fresh state and the ageing model is not considered. The overview of electrical-thermal model structure is illustrated in Figure 2-9 with input and output parameters. Then, the electrical and thermal model will be presented separately in the following sections.

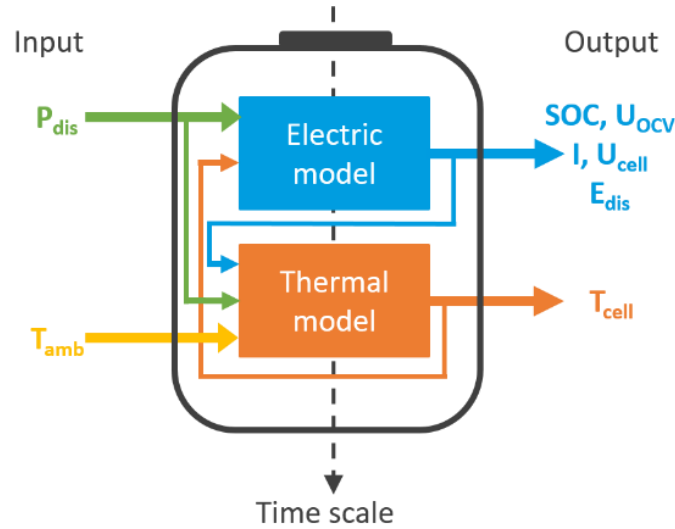


Figure 2-9 Overview of electrical-thermal model structure

2.5.3.1 Electrical model

Equivalent Circuit Models (ECMs) are selected to simulate the performance of various devices as LiBs [36] [64] and SCaps [65] [66] thanks to their easier implantation in BMS and a sufficient accuracy [67]. Different ECMs are proposed and compared by the previous literatures [64] [68]. Among them, two common ECMs types used for Li-ion cell are shown in Figure 2-10 with corresponding model mathematical equations and identified parameters number listed in Table 2-4.

For the R_{int} model, two parameters (U_{ocv} , R_{int}) are needed to be identified, where U_{ocv} is the voltage of Li-ion cell at the open circuit state, this parameter depends on SOC and temperature. The other is the total internal resistance R_{int} of Li-ion cell, it depends on SOC, temperature and current of cell. The SOC of the LiBs is defined as the equation (1.5), $I(t)$ is the charge current.

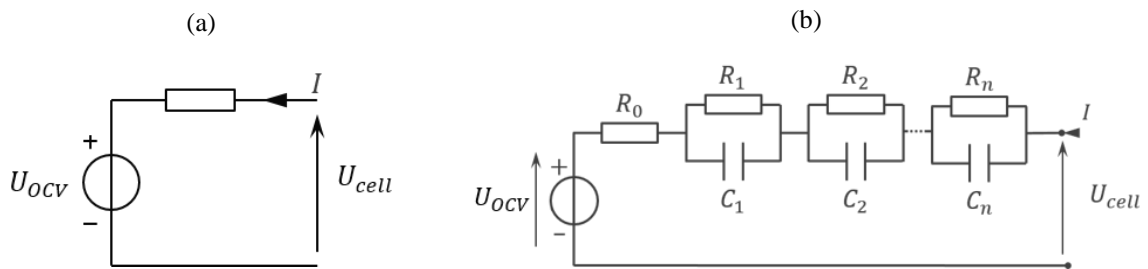


Figure 2-10 (a) R_{int} equivalent circuit model (b) n -RC equivalent circuit model

Based on the R_{int} model, Thevenin model can be obtained by adding one R//C in series. In this model, U_{ocv} is the same as in R_{int} model, but R_0 , R_1 and C_1 are the parameters which can be identified by a relaxation phase of cell with hybrid pulse power characterization (HPPC) test profile [64], this model is able to simulate the dynamic behavior of Li-ion cell. All identified parameters depend on SOC, temperature and current. Another model with 2 R//C circuits is called the Dural Polarization (DP) model, this model can distinguish the polarization resistance introduced by the concentration and the kinetic in Li-ion cell. R_1, C_1, R_2 and C_2 are all depended

on SOC, temperature and current, which can be also identified by the phase of relaxation for cell [69] or by the EIS [70].

In addition, more R//C can be added on the DP model to simulate the characteristic of Li-ion cell with the high accuracy. However, more parameters ($2n+2$) must be identified as in the case of n-RC model (Table 2-4), it requires more experimental tests and computational complexity during the identification process. In addition, the R//C used in ECMs mainly allows to predict the dynamic behavior of LiBs.

Type of ECMs	Model equations	No. of identified parameters
Rint model	$U_{cell} = U_{OCV} - I \times R_{int}$	2
Thevenin model (n=1)	$\begin{cases} U_{cell} = U_{OCV} - I \times R_0 - U_1 \\ \dot{U}_1 = \frac{I}{C_1} - \frac{U_1}{R_1 C_1} \end{cases}$	4
DP model (n=2)	$\begin{cases} U_{cell} = U_{OCV} - I \times R_0 - U_1 - U_2 \\ \dot{U}_1 = \frac{I}{C_1} - \frac{U_1}{R_1 C_1} \\ \dot{U}_2 = \frac{I}{C_2} - \frac{U_2}{R_2 C_2} \end{cases}$	6
n-RC model	$U_{cell} = U_{OCV} - I \times [R_0 + \sum_{i=1}^{i=n} R_i (1 - e^{-\frac{t}{R_i C_i}})]$	$2n+2$

Table 2-4 ECMs of LiBs with models equations and number of identified parameters

In our investigated study, the R_{int} model is selected for following reasons. At first, in order to predict the energy density and power density of various Li-ion technologies based on ECMs, the number of identified parameters is considerable for users. The less identified parameters users have, the less experimental tests and identification are required, but above all, the good accuracy must be insured. Barreras et al. [71] used R_{int} model based on the manufacturer's datasheet to simulate a continuous discharge under various currents, a good accuracy have been demonstrated. Secondly, in the conventional Ragone Plot, the available discharged energy is always calculated under a constant power discharge from maximal voltage to minimal voltage [72], which is considered as a quasi-static behavior of Li-ion cell [58], therefore the dynamic behavior is not taken into account in proposed Ragone Plot model.

- **Uocv identification**

In contrast to the identification of U_{OCV} by a pulse discharge characterization test [69] [73], the pseudo-OCV results from reference test design is used in Rint model. Figure 2-11 illustrates the pseudo-OCV at different temperatures and corresponding polynomial function for LG and Samsung. It can be observed that the temperature has an impact on U_{OCV} for extreme SOCs. However, for both technologies, besides the pseudo-OCV at -20°C , the other curves of $U_{OCV} = f(\text{SOC})$ are almost superposed, therefore one fitting curve can be obtained by applying

the average of all curves, then the pseudo-OCV versus SOC is fitted with a polynomial function (Table 2-5) by using the Matlab® *curve fitting tool*.

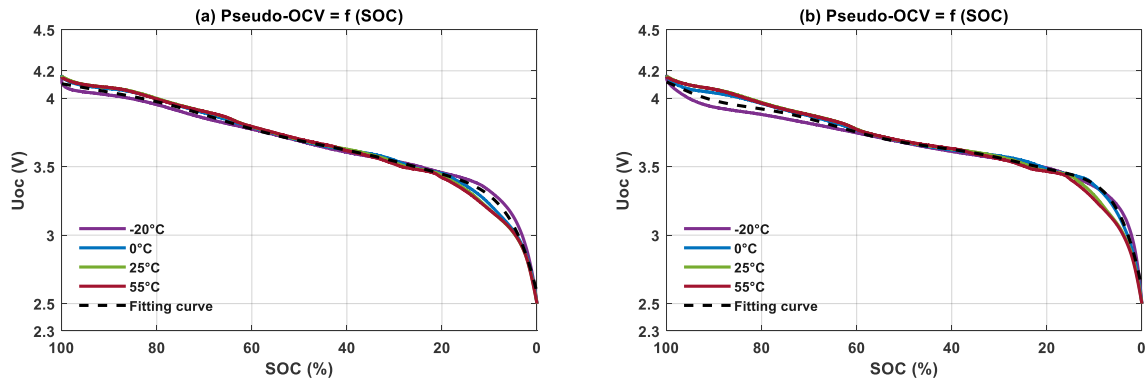


Figure 2-11 Pseudo-OCV at -20°C, 0°C, 25°C and 55°C for (a) LG (b) Samsung

Technology	Polynomial functions
LG	$a = \frac{50 - SOC}{28.87} \text{ with } SOC \in [0: 100]$ $U_{OCV} = -0.012a^8 - 0.026a^7 + 0.041a^6 + 0.087a^5 - 0.077a^4 - 0.102 \times a^3 - 0.068a^2 - 0.212a + 3.690$
Samsung	$a = \frac{50 - SOC}{28.87} \text{ with } SOC \in [0: 100]$ $U_{OCV} = -0.024a^8 - 0.037a^7 + 0.111a^6 + 0.124a^5 - 0.193a^4 - 0.13 \times a^3 + 0.136a^2 - 0.168a + 3.676$

Table 2-5 Polynomial function of $U_{ocv} = f(SOC)$ for LG and Samsung

• R_{int} identification

The internal resistance can be calculated according to equation (2.1), where U_{cell} is the cell voltage during the constant current discharge and depends on the SOC, which is the available ampere hour in relation to the total maximal discharged capacity for each operating condition, temperature (T), and current (I); U_{OCV} can be determined with the polynomial function in Table 2-5. The internal resistance is determined from two quasi-static regimes, which also correspond to the regime of a constant power discharge.

$$R_{int}(SOC, T, I) = \frac{U_{cell}(SOC, T, I) - U_{OCV}(SOC)}{I} \quad (2.1)$$

As the internal resistance depends on three variables, a multiple linear regression based on a stepwise method can be applied. Mathieu et al. [74] used this method to investigate the dependency between the degradation rate of the Li-ion batteries and ageing factors (temperature, current and SOC) to predict the capacity fade. A good accuracy was achieved. Multiple linear regression based on the stepwise method is designed to use a minimal set of

independent variables of a regression model while maximising the adjusted determination coefficient and minimising the mean squared deviation from the regression model. This method involves, in its first step, the construction of a model containing all potentially dependent variables. These are gradually eliminated to obtain a model with maximal determination coefficients and maintain significance of the parameters [75].

In our case, the dependent variable is the internal resistance. The independent variables are SOC, temperature, and current. Several studies [58] [76] have shown that the logarithmic internal resistance has a linear dependency of $1/T$ (T in Kelvin). Thus, a transformation of the internal resistance and temperature terms is conducted. The proposed multiple linear regression function is described in equation (2.2). It includes all first-order terms, second-order interactions, and quadratic terms for the three variables. The stepwise method is executed with the Matlab® function `stepwiselm` of the Statistics and Machine Learning Toolbox. Table 2-6 lists all coefficients obtained for each term in the multiple regression and the corresponding coefficients of determination for LG and Samsung.

Some coefficients like β_{13} and β_{11} are too small. Hence, the corresponding variable has a weak impact on the internal resistance. Further, there is no second-order interaction for the SOC current for LG. Samsung has a weak second-order interaction for the SOC current. In addition, both technologies have a weak quadratic coefficient in front of SOC^2 .

$$\begin{aligned} \ln(R_{int}) = \varepsilon + \beta_1 \times SOC + \beta_2 \times \frac{1}{T} + \beta_3 \times I + \beta_{12} \times SOC \times \frac{1}{T} + \beta_{13} \times \frac{1}{T} \times I \\ + \beta_{23} \times SOC \times I + \beta_{11} \times SOC^2 + \beta_{22} \times \frac{1}{T^2} \end{aligned} \quad (2.2)$$

LG (NMC/graphite+SiO)	Samsung (NCA/graphite)
$R^2 = 0.83$	$R^2 = 0.81$
$\varepsilon = 0.87$	$\varepsilon = 3.9$
$\beta_1 = 0.052, \beta_2 = -5730, \beta_3 = 0.25$	$\beta_1 = 0.022, \beta_2 = -7146, \beta_3 = 0.22$
$\beta_{12} = -12.5, \beta_{13} = 0, \beta_{23} = -78.2$	$\beta_{12} = -12.7, \beta_{13} = 4e^{-4}, \beta_{23} = -82.4$
$\beta_{11} = -1.3e^{-4}, \beta_{22} = 1.34e^6$	$\beta_{11} = 7.73e^{-5}, \beta_{22} = 1.59e^6$

Table 2-6 Coefficient of multiple linear regression $\ln(R_{int}) = f(SOC, \frac{1}{T}, I)$ for LG and Samsung

In Figure 2-12, the black circles represent the experimental internal resistance versus the temperature and SOC according to equation (2.1). The 3D mapping is constructed with the proposed multiple linear regression determined via equation (2.2) for LG and Samsung at 1 C, 3 C, and 5 C, respectively. For both technologies, the experimental data is located at the surface of the 3D map. It can be observed that the internal resistance increases with decreasing temperature and SOC. Further, the internal resistance decreases with increasing current. These

tendencies correspond to the internal resistance behaviour of Li-ion batteries [77]. Moreover, a good coefficient of determination (R^2) (Table 2-6) is found for both technologies.

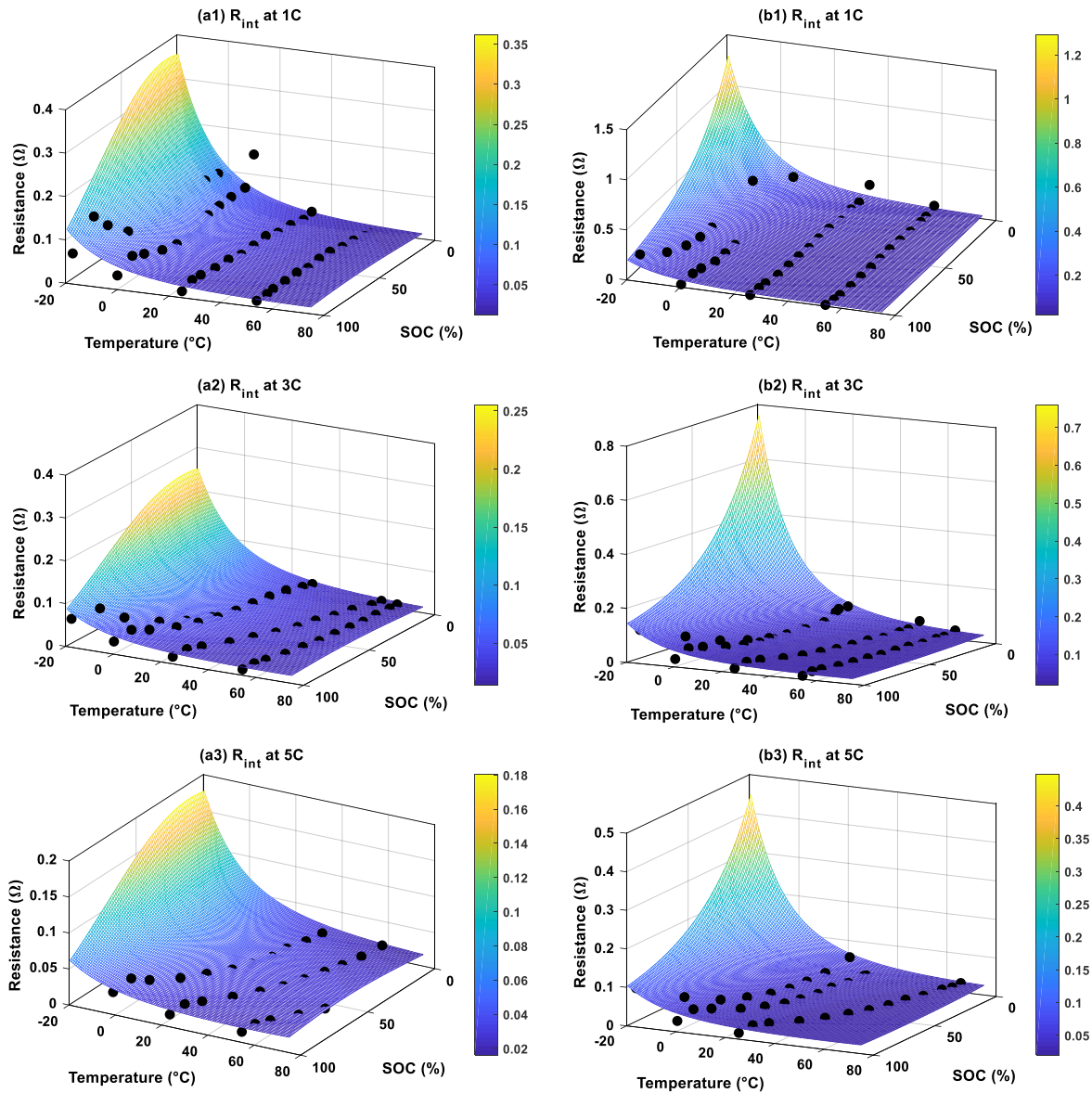


Figure 2-12 Experimental internal resistance and 3D mapping of $R_{int} = f(SOC, T)$ at 1C, 3C and 5C for LG (left) and Samsung (right) according to stepwise regression. The coloured axis represents the value of R_{int}

2.5.3.2 Thermal model

To simulate the temperature at the surface of Li-ion battery, Cicconi et al. [78] demonstrated that different heat sources appeared in Li-ion cell during charge or discharge, which included the Joule heat, reversible heat, the mixing process heat, the thermal conduction heat and the convection heat. In our study, the thermal model is simplified with some hypothesis [79]. Only the irreversible heat, reversible heat and convection heat appear in the thermal model [69], moreover, the cell specific heat is considered as a constant value that is independent of the temperature [80]. Therefore, the proposed thermal model is established by the thermal energy balance expressed in equation (2.3), where m (kg) is the masse of cell; C_p (J.kg⁻¹.K⁻¹) is the cell calorific capacity; T (K) is the cell temperature; t (s) is the time of

constant power discharge; Q_{irr} , Q_{rev} and Q_{conv} correspond the irreversible heat, reversible heat and convection heat respectively. Masse and the calorific capacity of both technologies are listed in Table 2-7.

$$mC_p \frac{dT}{dt} = Q_{irr} + Q_{rev} + Q_{conv} \quad (2.3)$$

$$Q_{irr} = I \times (U_{oc} - U_{cell}) = I^2 R_{int} \quad (2.4)$$

$$Q_{rev} = -I \times T \frac{dOCV}{dT} \quad (2.5)$$

$$Q_{conv} = h \times A \times (T_{air} - T) \quad (2.6)$$

Technology	C_p (J.kg ⁻¹ .K ⁻¹)	m (kg)
LG (NMC/graphite+SiO)	1070	0.0482
Samsung (NCA/graphite)	939	0.0485

Table 2-7 Caloric capacity and mass for LG and Samsung of tested cells

- **Irreversible heat**

The irreversible heat, also called Joule heat, is described in equation (2.4). This heat source is determined by the cell operating current and overpotential. The overpotential is the voltage drop owing to the internal resistance. This internal resistance is found in the electrical model that depends on SOC, temperature, and current. Therefore, the thermal model is associated with the electrical model.

- **Reversible heat**

As determined via equation (2.5), the reversible heat is a derivative term of OCV with respect to the temperature. This heat source represents the entropy variation in a charge or discharge process in the Li-ion cell. It is strongly influenced by the SOC and chemistry. Liu et al. [81] reported a significant contribution of reversible heat during the operation of a Li-ion cell at a low current and high temperature. The reversible heat represented 50% of the total heat for a cell discharged at 45°C with 1C. By contrast, Huang et al. [82] found out that the reversible heat was more significant for a high discharge rate of a Li-ion cell. Thus, the contribution of the reversible heat source are still not clarified. Nevertheless, the reversible heat cannot be ignored in a thermal model for constant power discharge at different operating temperatures.

The impact of the temperature on the entropic potential ($dOCV/dT$) is still unclarified. However, this parameter can always be determined for a positive temperature range. For example, Manikandan et al. [83] determined the entropic potential for 35 °C–55 °C. Eddahech et al. [84] measured the entropic potential for 15°C–55°C, and Marcicki et al. [85] obtained this value with experimental tests at 0°C–55°C. These studies found a linear relation between OCV and temperature at different SOCs.

Another problem is the duration of the waiting time for the OCV acquisition. If the waiting time is too long, the self-discharge of the Li-ion cell will occur particularly at high

temperatures and SOCs [86] [87]. If the waiting time is too short, the cell voltage relaxation can cause an error in the entropic potential measurement [87]. To minimise these impacts, Forgez et al. [87] proposed an OCV method based on a linear regression as a function of temperature and time. This method allows to extract the OCV change based only on the variation in the temperature.

Because much uncertainty still exists regarding the negative temperature range impact on the OCV variation, the entropic potential is determined for a temperature range of $-15\text{ }^{\circ}\text{C}$ – $25\text{ }^{\circ}\text{C}$ with OCV correction in our proposed model. The potentiometric method is used to determine the entropic potential. The experimental test process is the same as in [84]. However, the temperature steps are now: $25\text{ }^{\circ}\text{C}$, $15\text{ }^{\circ}\text{C}$, $5\text{ }^{\circ}\text{C}$, $-5\text{ }^{\circ}\text{C}$, and $-15\text{ }^{\circ}\text{C}$, successively. One example of Samsung at 60% SOC is presented in Figure 2-13. The temperature and OCV versus the time are presented, respectively. Regarding Figure 2-13 (b), a linear function is used to remove the self-discharge impact on the OCV variation. A clear linear dependency is observed between the average corrected OCV and temperature in Figure 2-13 (c). The slope of the linear regression represents the entropic potential.

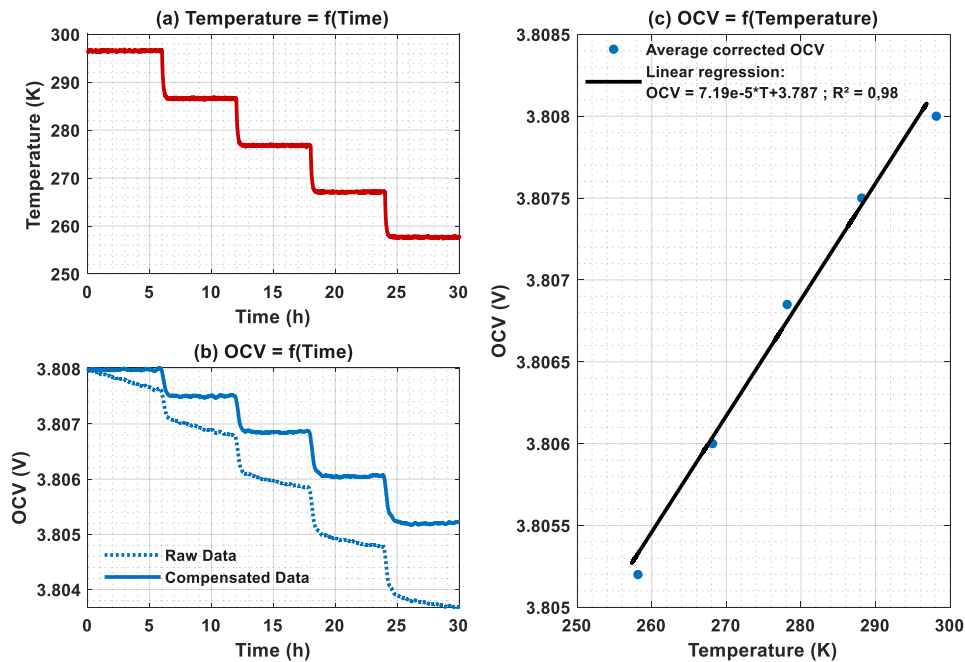


Figure 2-13 Potentiometric tests results for Samsung at 60% SOC (a) Temperature versus time, (b) OCV versus time, (c) OCV versus temperature

Based on the same method, the entropic potentials at different SOCs for both technologies (NMC/graphite+SiO and NCA/graphite) are presented in Figure 2-14. The entropic potential is negative at low SOCs and positive at high SOCs for both Li-ion technology chemistries. The sign of the entropic potential indicates the thermodynamic behavior: endothermic and exothermic reactions coexist during the complete discharge process [88].

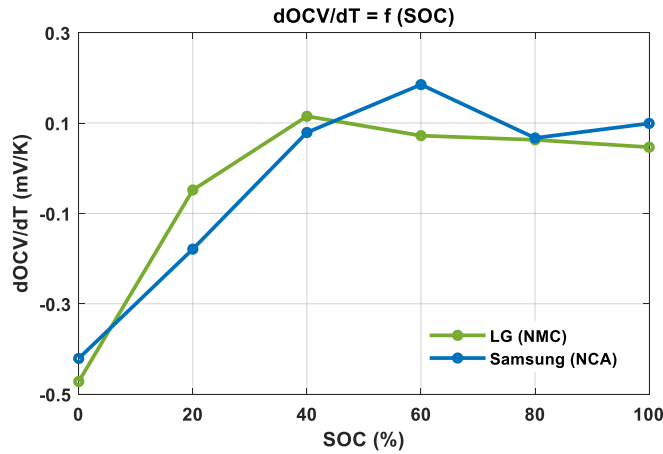


Figure 2-14 Entropic potential versus SOC for Technology LG (NMC/graphite+SiO) and technology Samsung (NCA/graphite)

• Convection heat

As the proposed thermal model must be able to predict the cell temperature for a large range of operating temperatures, the convection heat must be considered. Equation (2.6) describes the convection heat, where h ($\text{W}\cdot\text{m}^{-2}\cdot\text{K}^{-1}$) is the heat transfer coefficient, A (m^2) the exchange area, T_{air} (K) the environmental fluid temperature that is imposed by the thermal chamber and T (K) the temperature at the center of the surface of the 18650 cell. The convection heat depends on the object geometry. The exchange surface in this study is the total surface of the 18650 cell (Table 2-8).

The heat transfer coefficient of the 18650 cell in the thermal model depends on the temperature and current [61] [69]. According to Table 2-8 the heat transfer coefficient increases with current and low temperature has a high heat transfer coefficient. In our study, it is assumed that the heat transfer coefficient is determined based on the initial operating conditions. This parameter stays constant in the proposed thermal model.

Cell	Surface A (m^2)	Current C rate	Heat transfer coefficient h ($\text{W}\cdot\text{m}^{-2}\cdot\text{K}^{-1}$)			
			$T = 55^\circ\text{C}$	$T = 25^\circ\text{C}$	$T = 0^\circ\text{C}$	$T = -20^\circ\text{C}$
18650 cells	0.0042	C/3	10.5 [89]	11 [90]	12	15.47
		1C	11.5 [89]	13.48 [89]	20	28.4 [69]
		3C	14 [89]	28.4 [69]	28.4 [69]	30

Table 2-8 Surface and heat transfer coefficient in thermal model [61] [69] [89] [90]

2.5.4 Validation of Ragone Plot model

In this section, the proposed Ragone plot model is first validated at 25°C with a constant current discharge. In addition, we found out that the prediction of the energy and power densities is possible by directly using the discharge curves provided by the manufacturer. The

Ragone plot model can be extended to 55 °C, 0 °C, and -20 °C to construct a non-isothermal Ragone plot.

2.5.4.1 Ragone plot model for 25°C

Figure 2-16 illustrates the voltage and increased temperature of the cell under 3 W, 15 W, and 30 W for constant power discharges at 25°C. The experimental data of the cell voltage and cell temperature are in a good agreement with the simulated results based on the galvanostatic curves for both technologies. Because these discharge curves are provided by the manufacturer (Figure 2-15), it is possible to directly establish a model with the technical datasheet. For that, the cell voltage (U_{cell}) for multiple currents at different SOCs can be recorded. After data acquisition, the same modelling and simulation process is used. For the internal resistance (R_{int}) simulation blocks, the 2-D lookup table is replaced by the multiple linear regression function.

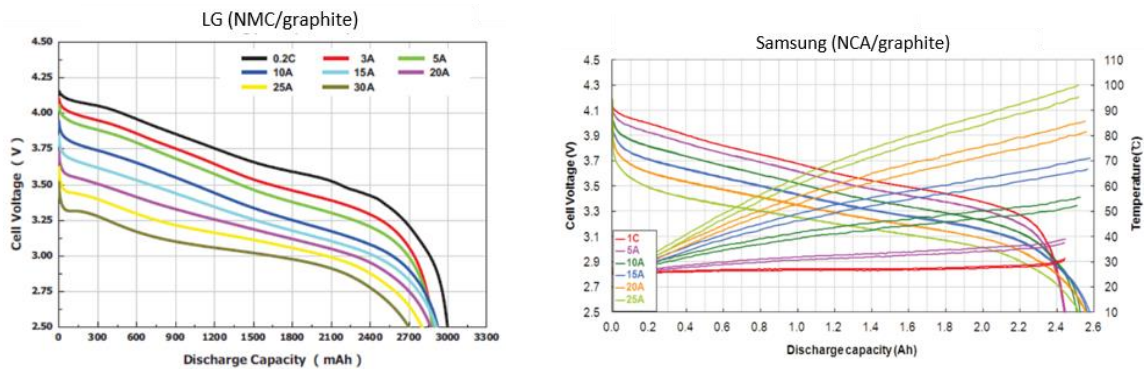
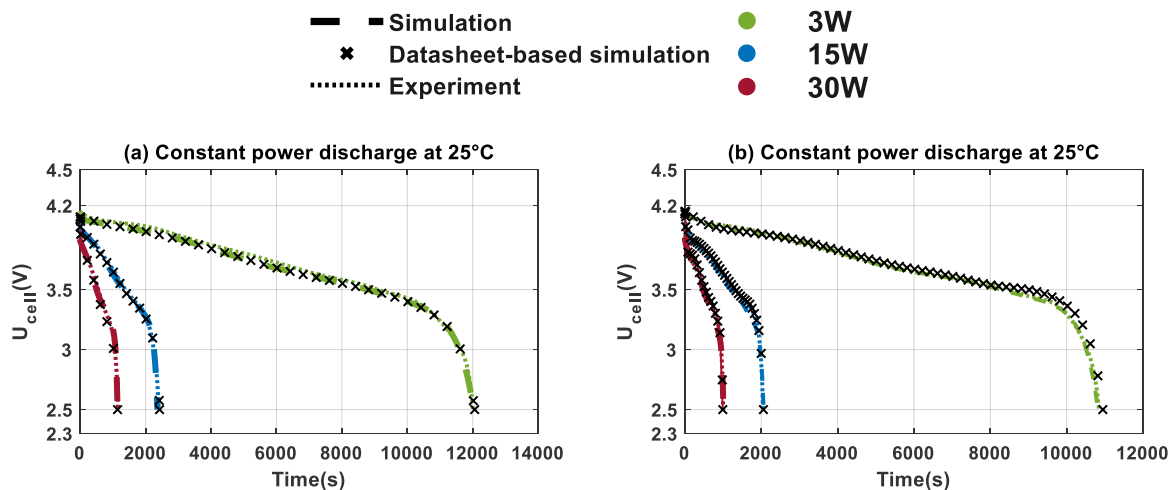


Figure 2-15 Constant current discharges curves at 25°C for multiple C rates of LG (left) [91] and Samsung (right) [92]



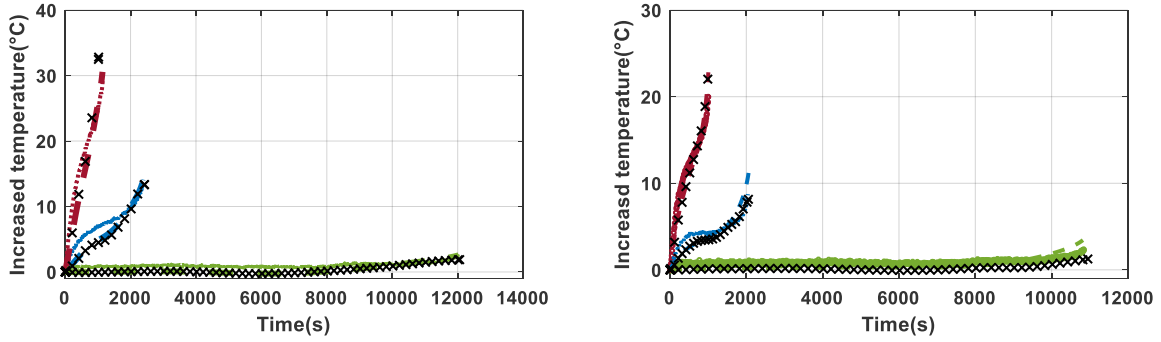


Figure 2-16 Simulation versus experimental data for cell voltage and increased temperature for LG (a) and Samsung (b) under constant power discharge (3W, 15W and 30W) at 25°C

Moreover, Figure 2-16 also presents the datasheet-based discharge curves for cell voltage and temperature during a constant power discharge at 25°C. The datasheet-based curves are all superimposed on the experimental curves. However, regarding LG, the simulated temperature for 30W exceeds the experimental temperature at the end of the discharge. This behaviour might be owing to the internal resistance. The internal resistance in the 2-D lookup table is independent of the temperature, which increases much under a high power discharge. Consequently, the cell voltage, cell temperature, and available energy and power can be predicted directly by using the technical datasheet for both Li-ion cell chemistries.

Figure 2-17 presents the Ragone plots of the experimental and simulated galvanostatic-based and datasheet-based results at 25 °C. The simulated and experimental results are in a good agreement. Thus, the proposed electrical–thermal model is able to predict the cell voltage, cell temperature, and available discharged energy with galvanostatic curves under a low, medium, and high constant power discharge at 25 °C for two 18650 Li-ion cell chemistries.

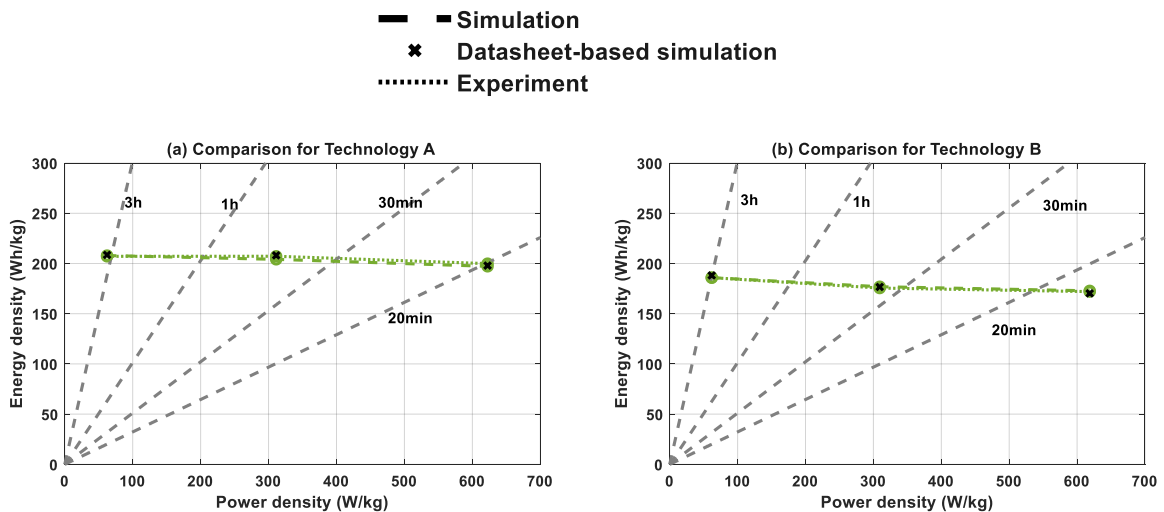


Figure 2-17 Comparison of simulated energy density versus power density: galvanostatic-based, datasheet-based and experimental results for LG (left) and Samsung (right)

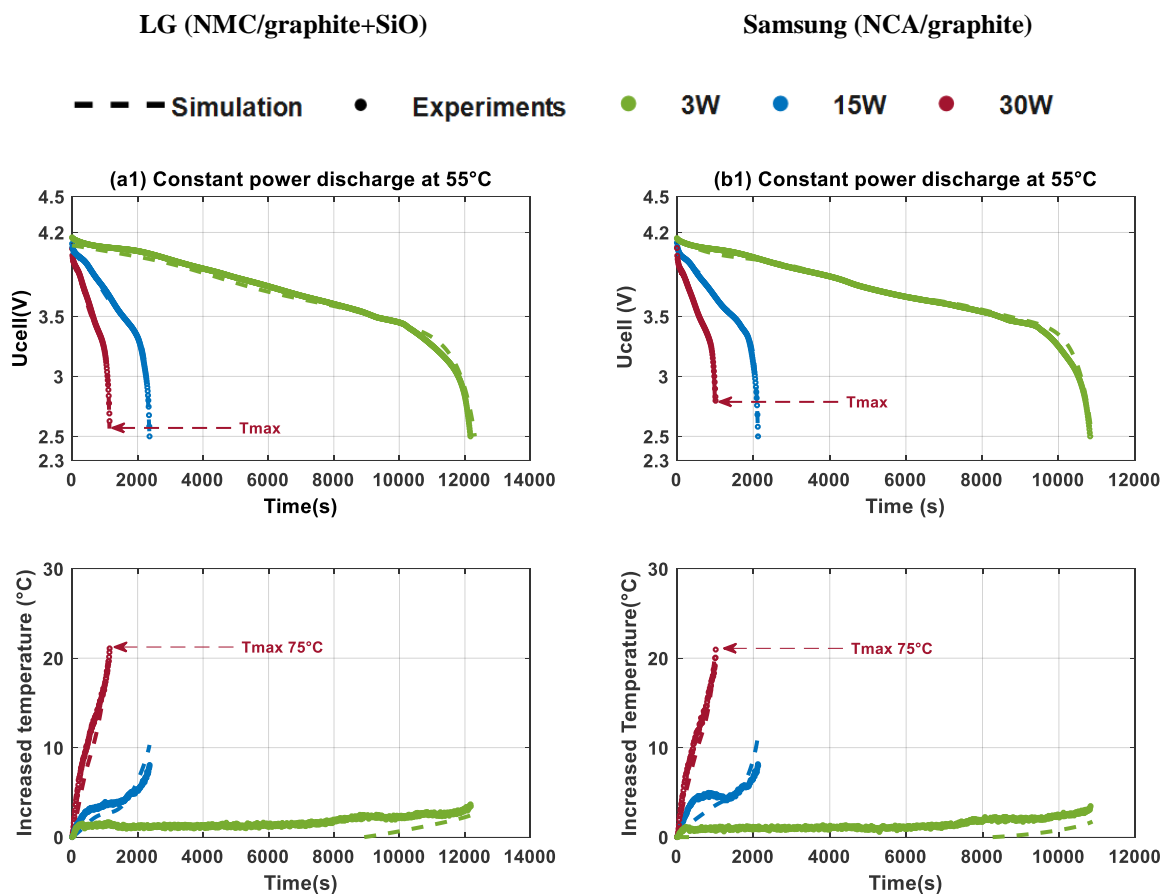
2.5.5 Extending Ragone plot model for wide operating temperature range

The Ragone plot model based on galvanostatic curves is extended onto a wide operating temperature range. Figure 2-18 compares examples of simulated curves to experimental curves for the cell voltage and temperature of LG and Samsung at 55 °C, 0°C and -20 °C.

At 55 °C (Figure 2-18 (a1, b1)), the cells of both technologies reach the maximal operating temperature (75 °C) at 30 W for a constant power discharge. A small discrepancy is observed between the simulated and experimental curves regarding the cell temperature at 3W. However, this slight temperature deviation (1°C) has the same magnitude as the thermocouple precision.

At 0°C (Figure 2-18 (a2, b2)), the experimental data of cell voltage and cell temperature are in good agreement with the simulated results for both technologies. At 0°C, the increased temperature of LG is less important than Samsung at all levels of power. However, this characteristic is the opposite at 25°C (Figure 2-16).

As illustrated in Figure 2-18 (a3, b3), the difference between simulation and experimental data is obvious at -20°C for Samsung. This difference is not only owing to the internal resistance (as for LG) but also owing to the heat transfer coefficient (h). Li et al. [61] showed that the performance of a Li-ion cell is more sensitive to h at -20°C with a high current. However, in our proposed thermal model, this parameter is constant during a constant power discharge. Therefore, the temperature gap is more significant at 15W and 30W.



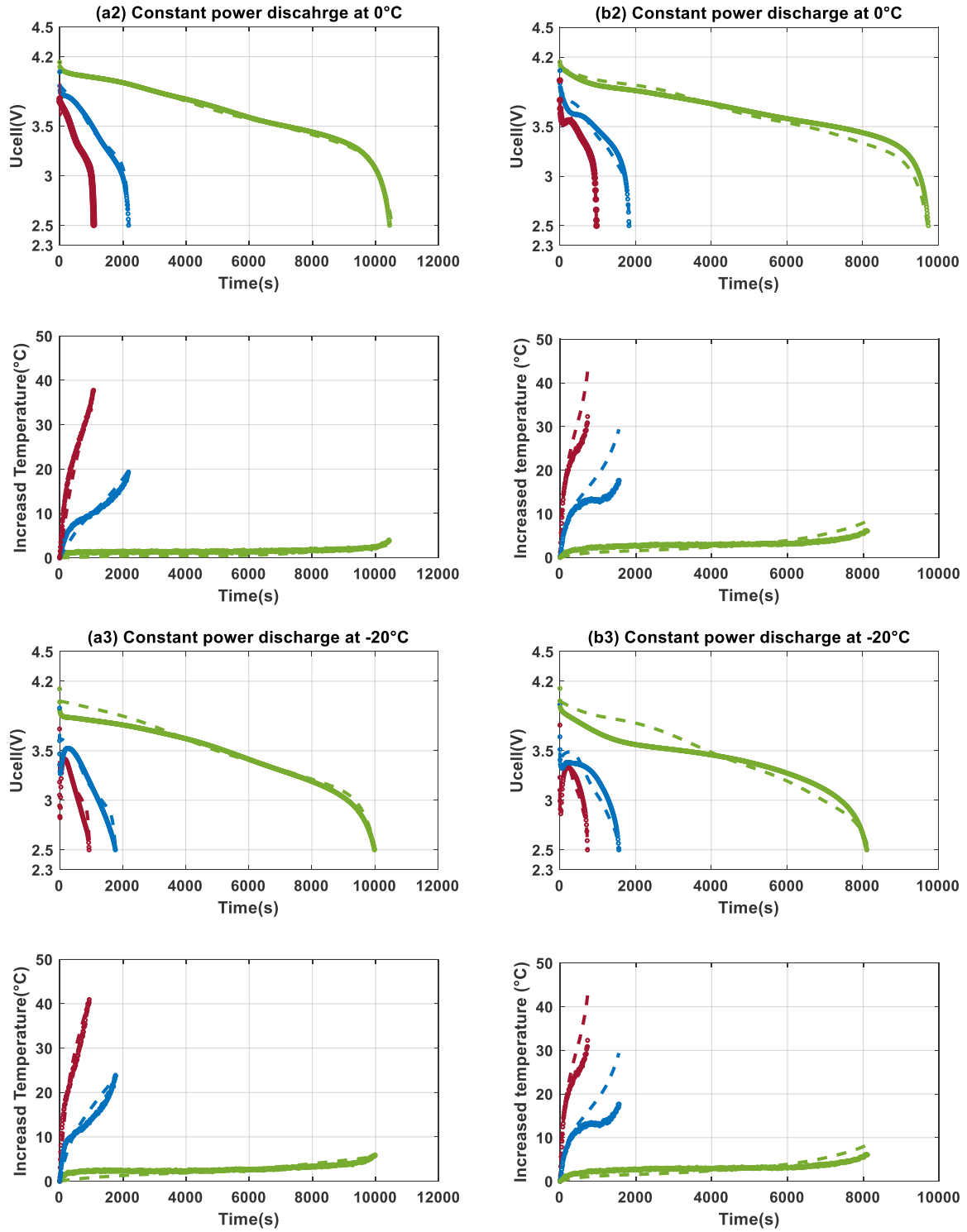


Figure 2-18 Simulation versus experimental data for LG (left) and Samsung (right) under constant power discharge at 3W, 15W and 30W at (a1, b1) 55°C, (a2, b2) 0°C and (a3, b3) -20°C

Finally, the discharged energy can be predicted by integrating the power value for each operating condition. The relative error (Err_{rel}) is determined via equation (2.7), where E_{sim} is the simulated energy and E_{exp} is the experimental data. Table 2-9 lists the experimental and simulated energy densities with the corresponding relative errors for 3W, 15W, and 30W.

$$Err_{rel} = \frac{|E_{sim} - E_{exp}|}{E_{exp}} \times 100\% \quad (2.7)$$

Temperature		55 °C			0 °C			-20 °C		
Parameters	P (W/kg)	E_{exp} (Wh/kg)	E_{sim} (Wh/kg)	Err_{rel} (%)	E_{exp} (Wh/kg)	E_{sim} (Wh/kg)	Err_{rel} (%)	E_{exp} (Wh/kg)	E_{sim} (Wh/kg)	Err_{rel} (%)
LG (NMC/gra.+Si)	62.2	210	212	0.9	200	201	0.5	172	175	1.7
	311	205	204	0.5	190	189	0.5	153	152	0.7
	622	200	197	1.5	186	185	0.5	161	163	1.2
Samsung (NCA/graphite)	61.9	185	187	1.1	167	166	0.6	139	140	0.8
	309	182	183	0.5	156	158	1.3	133	132	0.8
	619	174	171	1.7	166	165	0	125	126	0.8

Table 2-9 E_{exp} E_{sim} and Err_{rel} at 55°C, 0°C and -20°C for LG and Samsung

It can be observed that the energy density decreases with increasing power level. All relative errors are below 2% for both technologies and all temperatures. In addition, the discharge energy decreases with decreasing operating temperature for the same power levels, which means that low temperatures limit the available energy. Surprisingly, LG gains 5% in available energy at -20 °C under 30 W with respect to the value for 15 W. The same behaviour is observed for Samsung at 0 °C. In both cases, the increased temperature at the cell surface is significant. Discharging a Li-ion cell at low temperatures with a high current favors self-heating, which can increase the cell temperature and cause more available energy [54]. This interesting feature indicates that a high current can enhance the available energy of Li-cell at low temperatures.

2.5.6 Enhanced non-isothermal Ragone plot

A non-isothermal Ragone plot can be established to compare the performances of LG and Samsung. In addition to the three power levels (3W, 15W, and 30W), other constant powers are applied to build the Ragone plot via simulation: 5W, 9W, 10W, 18W, 20W, 25W, 28W, and 40W–90W with steps of 10W.

Figure 2-19 presents the available discharged energy density versus the power density for a wide temperature range. This plot can be used as a design aid tool to select the optimal cell for a given application. For all operating temperatures, LG has obviously higher energy densities than Samsung when the power density is below 1200 W/kg. Samsung has higher energy densities when the power density exceeds this value. Therefore, LG is suitable for energy applications, whereas Samsung is suitable for power application. This conclusion is also described by the manufacturer and corresponds to the classification of current level in the reference test design. Although LG demonstrates a better performance at all temperatures under

low power levels, the performance of Samsung is better at 0°C and -20°C under high power. This is consistent with the behaviour under constant current discharge and high currents at -20°C. Surprisingly, the energy density has a sharp decline under high power levels and 55°C in both technologies. This behaviour is owing to the safety conditions regarding the maximal temperature (75°C). The batteries could not be fully discharged, which limits the available energy.

T55 T25 T0 T-20 --o-- LG (NMC/graphite) --△-- Samsung (NCA/graphite)

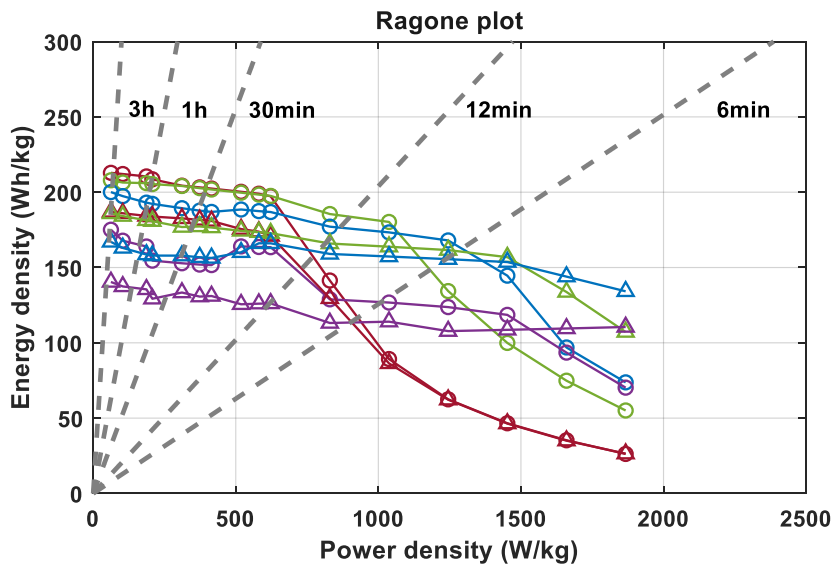


Figure 2-19 Performance comparison of LG and Samsung based on Ragone plot model for -20°C, 0°C, 25°C and 55°C

2.6 Conclusion

In order to select the most promising technology including LiBs, SCaps and LiCs for aeronautical usage. A study focused on the comparative performance quantification is primordial. Thereby, this chapter is dedicated to quantify the performance of all investigated electrochemical energy storage elements by experiments and modelling.

In the first part, all the electrochemical energy storage elements are presented. The classical technologies are not only investigated in this study, but also the electrochemical energy storage elements for the latest generation of electrochemical energy storage elements, such as NMC/graphite+SiO, LTO-based LiBs, LiCs and Li-S. The various equipment in CaCySSEE platform insure the electrical and thermal characterizations. Then, for purpose of the comparative performance quantification study, a reference test design is proposed, including the reception, initial, performance and ageing tests. In this test, all the investigated electrochemical energy storage elements are classified into three types, which is depended on the application (energy-type, power-type and high power-type). Furthermore, this reference test covers a wide temperature range [-20°C, 55°C] for aeronautical usage. The experimental results of available discharged capacity are shown for all the technologies at different temperatures

and under multiple current levels. Finally, a cell-to-cell characterization is carried out to verify the consistency between the cells in the same batch. Overall, a good consistency and authenticity are observed for all tested technologies. This good consistency ensure a high degree of trust for experimental analysis in this study.

In the second part, a non-isothermal Ragone plot is constructed based on experiments and modelling for a four operating temperatures (-20°C, 0°C, 25°C, 55°C) under multiple power levels (3W-90W) for two fresh Li-ion technologies with different chemistries (NMC/graphite+SiO, NCA/graphite). The experimental results indicate that the energy and power densities determined via a galvanostatic (constant current) discharge overestimate the performances of the Li-ion cell relative to the values in the conventional Ragone plot. However, based on the galvanostatic curves, the energy and power densities can be predicted based on a proposed electrical–thermal model with a good accuracy. In this efficient and simple electrical-thermal coupled model, the parameter identification can be directly performed by using the technical datasheets of both Li-ion chemistries. In a real ESS application, the power profile of the system can be predicted from the galvanostatic curves. Finally, a non-isothermal Ragone plot is constructed based on the proposed model. The simulation results exhibit that the operating conditions such as temperature, current or power level, and safety conditions strongly affect the performance of Li-ion cells. Interestingly, the energy density can be enhanced at low temperatures under high power levels based on the significant self-heating of Li-ion cells.

Chapter 3

Ageing study of electrochemical energy storage elements

Table of contents

3.1 Introduction	62
3.2 Overview of ageing mechanisms in electrochemical energy storage elements.....	62
3.2.1. Ageing mechanisms in LiBs	63
3.2.1.1 SEI formation	63
3.2.1.2 Lithium plating	64
3.2.1.3 Dissolution of transition-based materials	65
3.2.1.4 Other ageing mechanisms	65
3.2.2. Ageing mechanisms in SCaps and LiCs	65
3.3 Impact of ageing mechanisms on performance and security.....	66
3.4 Ageing types definition	69
3.4.1. Calendar ageing tests.....	69
3.4.2. Power cycling ageing	69
3.5 Ageing test experiments	69
3.5.1. Characteristics of calendar ageing tests	70
3.5.2. Characteristics of power cycling ageing tests	70
3.5.3. Check-up protocols	71
3.6 Calendar ageing results and analyses	73
3.6.1. Raw tests results	73
3.6.2. Capacity loss analyses under calendar ageing in a wide temperature range... 76	
3.7 Power cycling ageing results and analyses.....	81
3.8 Abuse tests and results.....	87
3.8.1. Thermal stability test.....	87

3.8.2. Overcharge test.....	89
3.8.3. Altitude simulation test	91
3.9 Comparison of different electrochemical energy storage elements.....	92
3.10 Conclusion	94

3.1 Introduction

As the previous chapter is devoted to the quantification performance of different electrochemical energy storage elements in the fresh state, this chapter is mainly focused on the ageing study of these elements. At first, the ageing mechanisms overview of LiBs and SCaps are presented based on several literatures. Next, the ageing experiments including calendar ageing and power cycling ageing tests are carried out on all electrochemical storage elements in a wide operating temperature range under multiple conditions. Then, the experimental ageing results are analysed separately according to two types of ageing tests thanks to the characterizations in the time domain. In addition, abuse tests such as the overcharge, simulation of amplitude and thermal stable tests are performed on several technologies. Finally, a radar chart is investigated by taking account 7 criteria in order to select the two most promising electrochemical energy storage elements for the future tests with a specific aeronautical profile.

3.2 Overview of ageing mechanisms in electrochemical energy storage elements

The electrochemical energy storage elements ageing occurs over time and with utilization, their energy and power capabilities decrease due to the multiple ageing mechanisms. These ageing mechanisms are extremely complex, and they have multiple intrinsic and extrinsic origins. The intrinsic origins include the properties of materials and manufacturing techniques, designs for electrochemical energy storage elements. The extrinsic factors include the practical operating conditions. All these origins can impact on the performance of electrochemical energy storage elements even result in some hazard issues [93]. Most of these ageing mechanisms are coupled and difficult to identify during ageing, the decrease capacity and increase internal resistance can be characterized thanks to the non-destructive method, including continuous current charge/discharge tests, HPPC or EIS. Therefore, understanding the different ageing mechanisms, evaluating the performance, diagnosing or estimating the SOH and preventing the failure mode are the crucial issues especially for reliability mastering purpose.

Abundant researchers over the past decades have provided many studies on the ageing mechanisms in electrochemical energy storage elements. Here, the main ageing mechanisms in the literature will be presented through the multiple origins from negative electrode, positive electrode, electrolyte, current collector of LiBs and SCaps.

3.2.1 Ageing mechanisms in LiBs

Ageing mechanisms in LiBs are mainly caused by the parasite reactions that lead to the change in physical and chemical proprieties of materials, such as the Solid Electrolyte Interphase (SEI) formation, the dissolution of active materials, the current collector corrosion and the electrolyte or binder decomposition [93] [94]. In addition, these ageing mechanisms are strongly influenced by temperature, voltage, current, SOC and composition of electrodes [93] [94] [95] [96]. Figure 3-1 illustrates an overview of principal ageing mechanisms in LiBs.

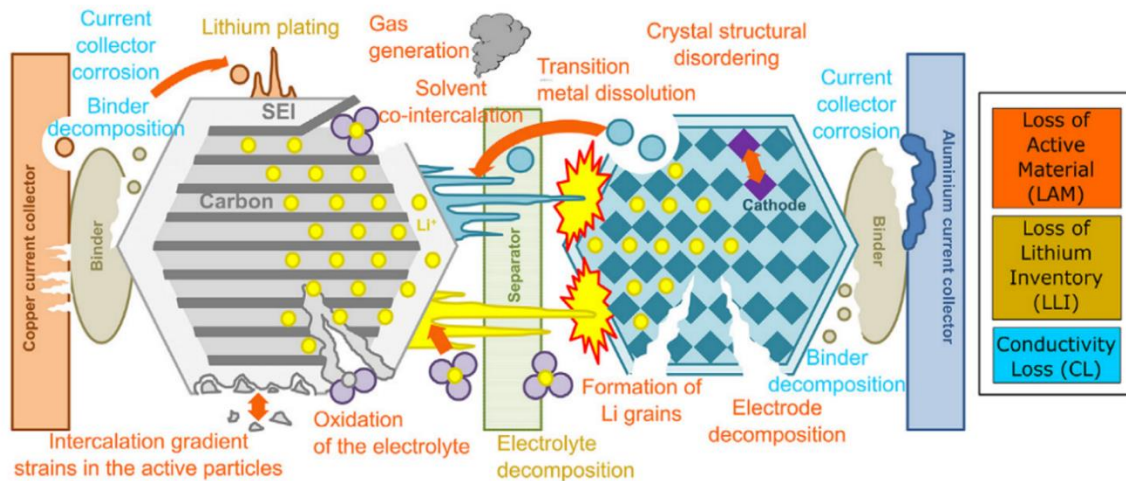


Figure 3-1 Overview of ageing mechanisms in Li-ion cells [94]

3.2.1.1 SEI formation

Many studies showed that the formation of SEI had a strong impact on the cycle life of LiBs [97] [98][99]. In fact, SEI is formed during the reduction of electrolyte at the interphase of negative electrode and electrolyte during the first charging of LiBs, which is a thin passivation layer between 30 to 50nm. Yi et al indicated that graphite electrode works at approximately 0.05V vs. Li/Li⁺, which is outside of the stability window of common liquid organic electrolytes (0.8V-4.5V) [100]. This layer was composed the inorganic (LiF, LiOH) and organic material (CH₂OCO₂Li) [101]. Once this passive layer has been formed, the future reaction between electrode and electrolyte is inhibited [97].

However, SEI is not stable over time and with utilisation that depends on temperature, operating conditions and materials [98]. In the case of graphite, SEI decomposition and dissolution appear during cycling and storage of LiBs, which lead to a direct contact between the negative electrode and electrolyte, then, new SEI can be formed. On one hand, this process consumes additional Li⁺, therefore the available cycling Li⁺ for intercalation reaction decreases and this phenomenon is irreversible, which leads to a decrease of capacity. On the other hand, the SEI growth results in an internal resistance increase. Moreover, the SEI growth it is not homogeneous that can crack the structure of graphite as illustrated in Figure 3-1. Recently, Prakash et al. [102] investigated a new generation material as LTO for negative electrode in LiBs to prevent the SEI formation. Since the electric potential of LTO is nearly 1.55V vs Li/Li⁺, which is in the stability window of electrolyte.

Besides the SEI formation on the anode side, another passive oxide layer is formed on the cathode such as the Solid Permeable Interphase (SPI). Goodenought et al [103] reported firstly this passive layer on LCO electrode. Then, Aurbach et al [104] found out the same oxide layer was formed on LMO electrode. In contrast to negative electrodes, the working potential of cathode materials are all in the stability window of electrolytes, the mainly cause of layer formation is mostly due to the surface chemistry reactions (e.g., nucleophilic attack) [105]. In addition, this layer is electronically resistive, which results in an increase of internal resistance in LiBs.

3.2.1.2 Lithium plating

Metallic lithium plating is a typical ageing mechanism that has drawn increased attention recently [100] [106] [107], since it can lead to the safety hazards issues in LiBs [108]. Lithium plating occurs when the Li^+ ions shuffled from the cathode to anode and intercalate into the graphite under a high level of charging current, by overcharging or at low temperature [108] [109], it also depends on the design of LiBs and manufacturing defects [100]. In fact, under these conditions, Li^+ ions could not intercalate fast enough into the graphite, thus Li deposits are formed on the anode as illustrated in Figure 3-1. Lately, the growth of metallic deposits can form the dendrites and finally destruct the separator, therefore, an internal short-circuit of cell is occurred, which is the principal cause of thermal runaway in LiBs [108].

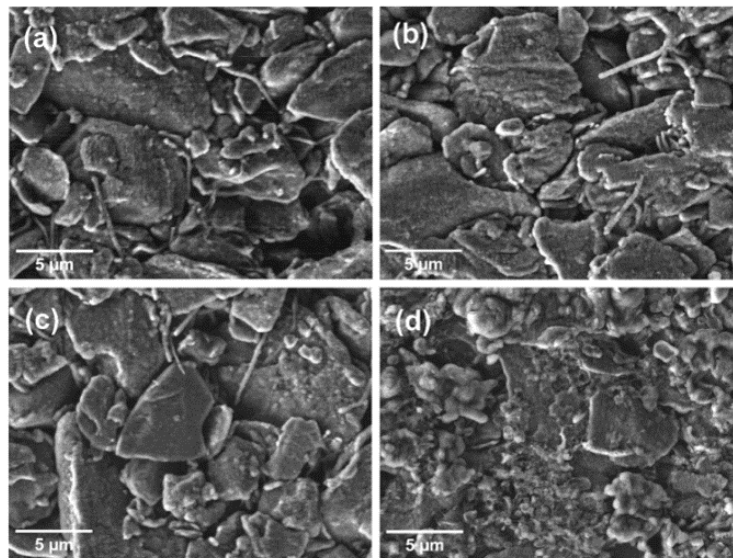


Figure 3-2 SEM images of the graphite electrodes disassembled from the Graphite/LFP full cells (a)Reference; (b)power cycling at 25°C; (c)power cycling at 0 °C; (d) power cycling at -18°C [110]

Rauhala et al. [110] investigated a series of experimental ageing tests in order to follow the formation of lithium plating through an extended post-mortem analysis. The SEM images of disassembled negative electrodes on graphite are illustrated in Figure 3-2 at different operating temperatures after the power cycling ageing tests. In both SEM images, the electrode consists the graphite flakes and a film can be observed at the surface of graphite. This film seems thicker after power cycling at 25°C in Figure 3-2 (b). Relatively to the two firsts images, some unknown particles are obviously at the graphite flaks as presented in Figure 3-2 (c). These particles become large and cover at almost all surfaces of graphite under the power cycling at -

18°C in Figure 3-2 (d), in addition, their forms are not regular under the test of power cycling at -18°C (d). These unknown particles are identified by spectroscopy analyse, which are the oxidation products of plated lithium.

3.2.1.3 Dissolution of transition-based materials

Transition-based materials dissolution is another origin for LiBs degradation. The dissolution of transition metals in various positive electrodes were reported in many studies [94] [111] [112] [113] [114]. This phenomena is common for the positive electrode of LiBs, such as LCO, LMO, NMC, LFP, in the LiPF₆-based electrolyte or at high temperature [112] [115].

Behandari et al. [115] summarized the multiple causes of manganese dissolution in LMO, NMC electrodes, the complex mechanism and several preventions. In fact, the manganese dissolution can be observed especially at high temperatures [111], which leads to a loss of active material and therefore capacity fading. In addition, Dealcourt et al. [114] observed that the manganese can condemn SEI, which leads to a persistent capacity decay of Graphie/LMO cells. The prevention strategies for manganese dissolution are include: doping, coating, surface modification and electrolyte additive [115].

Koltypin et al. [116] demonstrated that the dissolution of iron was unavoidably in LiPF₆ solution due to HF trace. It resulted in a capacity fading. However, the stability of LFP can be enhanced by using sol-gel synthetic method and by adding uncontaminated electrolyte additive.

3.2.1.4 Other ageing mechanisms

There are other contributions to LiBs degradation, such as current collector corrosion on positive side (aluminium), dissolution of current collector on negative side (copper), binder decomposition and gas generation caused by decomposition solvent [94]. In addition, the structural changes can be detected at electrode levels [95] [96]. In fact, the insertion and extraction of Li⁺ during cycling introduces a mechanical stress that with time will lead to the particles cracking, graphite exfoliation, becoming less ordered relatively to the original structure [117]. All these ageing mechanisms result in an internal resistance augmentation [94].

3.2.2 Ageing mechanisms in SCaps and LiCs

The structural changes in porous electrode especially the diminution of active surface are main ageing mechanisms for SCaps, which is due to the side reactions between electrolyte and impurities in activated carbon [118]. Moreover, the side reactions generate gases and solid layer between electrolyte and electrode that has similar property of SEI [119], the gases results in a swelling of SCaps [120], while the solid layer can reduce the specific surface of reaction as illustrated in Figure 3-3.

Multiple factors influence the ageing mechanisms according literatures [118] [119] [120]. Omar et al. [121] investigated different cycle tests at multiple temperatures, they shown that the increase of internal resistance is significantly higher at 60°C. German et al [122] found out that the capacitance decreased with time under a constant high voltage during the storage. Recently, they shown that high frequency current ripple also had significant effects on

capacitance and resistance, in addition an electrolyte leakage at end of floating and ripple test are observed [118].

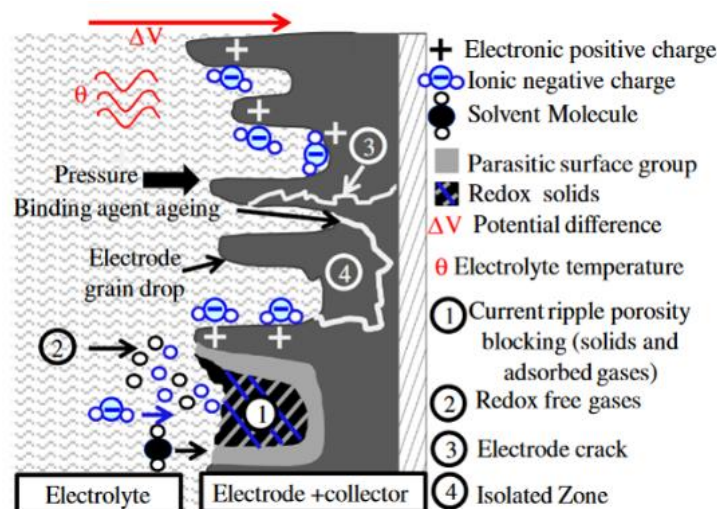


Figure 3-3 Schema of SCaps ageing mechanisms under floating constraints [118]

There are only few studies aimed on the ageing mechanisms of LiCs, since this is the latest generation technology. In the case of asymmetric structure, El. Ghossein et al [123] found out the floating voltage level and temperature during storage had a significant effect on the capacitance decay. They assumed that the ageing mechanisms seem the LIBs for negative electrode and resemble the SCaps for positive electrode. But in the case of hybrid symmetric structure, the ageing mechanisms is not available until now.

3.3 Impact of ageing mechanisms on performance and security

The previous section has been described the main ageing mechanisms in LIBs, SCaps and LiCs according to a hug of literatures. Marco et al. [93] classified them to three degradation modes based on electrochemical viewpoint: Conductivity Loss (CL), Loss Lithium Inventory (LLI) and Loss Active Material (LAM). Table 3-1 lists the relationship between extrinsic factors (Temperature, Current, SOC, Δ DOD and cycle number), affected component (Negative Electrode, Positive Electrode), potential ageing mechanisms, effects (Capacity Fade, Power Fade) and degradation modes (CL, LLI, LAM).

Based on this table, current collector corrosion and binder decomposition are in the CL degradation mode, LLI degradation mode contains the decomposition of electrolytes, lithium plating and formation of lithium grains. LAM includes the oxidation of electrolytes, electrode decomposition, transition metal dissolution, intercalation gradient strains in the active particles and crystal structure disordering. The affected component and potential ageing effects are identified by the post-mortem analysis, such as X-Ray Diffraction (XRD), Photoelectron Spectrometry (XPS) techniques [124] which belong to the destructive battery health diagnosis techniques. Moreover, non-destructive techniques such as capacity and internal resistance measurement, Incremental Capacity Analysis (ICA), Electrochemical Impedance Spectroscopy (EIS) are widely used in the diagnosis of LIBs for the real application.

Extrinsic factor	Level	Affected component	Ageing mechanism	Potential ageing effects	Most pertinent observed effects	Most pertinent DM
T	High (>35 °C)	NE	Electrolyte decomposition.	SEI growth. Micro pore clogging. SEI dissolution.	PF CF & PF CF & PF	LLI LLI LAM
			Transition metal dissolution.	Precipitation of new phases. Formation of dendrites.	PF PF	LAM LAM
		PE	Oxidation of electrolyte. Electrode decomposition.	SPI growth. Gas generation. Precipitation of new phases.	PF CF CF & PF	LLI LAM LAM
T	Low (<5 °C)	NE	Lithium plating.	Dendrite growth. SEI formation.	CF & PF CF & PF	LLI LLI
			Intercalation gradient strains in the active particles (with cycling).	Interstitial site loss.	CF & PF	LAM
C-rate	High (>2C)	NE	Lithium plating.	SEI formation.	CF & PF	LLI
			Intercalation gradient strains in the active particles (with cycling). Formation of Li grains.	Interstitial site loss. Graphite exfoliation. Isolation of active material. SEI formation and growth.	CF CF PF	LAM LAM LLI
SoC	Low (<0%)	NE (high potential)	Current collector corrosion.	Loss of conductivity.	PF	CL
		PE (low potential)	Crystal structure disordering. Binder decomposition.	Phase change. Loss of conductivity.	CF & PF PF	LAM CL
SoC	High (>95%)	NE (low potential)	Binder decomposition. Transition metal dissolution. Solvent co-intercalation.	Loss of conductivity. Precipitation of new phases. Formation of dendrites. Phase change. SEI growth.	CF PF PF CF & PF CF & PF	CL LAM LAM LAM LLI
		PE (high potential)	Electrode decomposition. Transition metal dissolution.	Precipitation of new phases. Exfoliation of active material. Gas generation. Phase change.	PF CF CF CF & PF	LAM LAM LAM LAM
ΔDoD	Large (>70%)	PE & NE	Intercalation gradient strains in the active particles.	Volume change.	CF	LAM
			Crystal structural disordering.	Particle cracking.	PF	LAM
			Solvent co-intercalation.	Phase change. SEI growth.	CF & PF CF & PF	LAM LLI
Cycle number	High ^a	NE & PE	Intercalation gradient strains in the active particles.	Volume change.	CF	LAM
			Crystal structure disordering.	Phase change. Particle cracking.	CF & PF PF	LAM LAM

Table 3-1 Relationship of LiBs ageing extrinsic factors with the affected component, ageing mechanisms, potential ageing effects, most pertinent observed effects and most pertinent degradation mode [93]

The multiple ageing mechanisms cause not only the capacity and power fade, but also result in some safety issues. Figure 3-4 (a) shows a LiB cell swelling after 4500 h storage at high temperature (55°C) and SOC (95%). Kumai et al. [125] found out that the internal pressure of commercial LiBs raised due to the decomposition of electrolytes for the first time, large volumes of gas generation were detected in overcharge and over discharge of LiBs and in aged LiBs. Figure 3-4 (b) presents the electrolyte leakage at the end of power cycling ageing tests for SCaps. In addition, as illustrated in Figure 3-4 (c), the internal pressure is high enough to open the can of SCaps, which introduces the electrolyte injection. Moreover, the acetonitrile in electrolyte of SCaps is harmful and flammable.

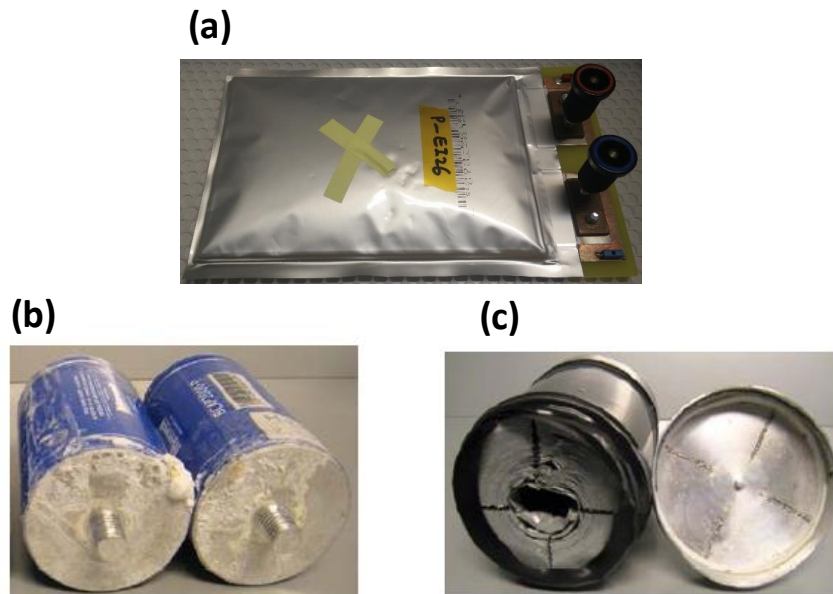


Figure 3-4 Swelling of (a) Graphite/LTO cells after 4500h storage at 55°C and 95% SOC, (b) Electrolyte leakage (c) Can opening of SCaps after 5000h calendar ageing on floating

The cell swelling facilitate the thermal runaway, fire and explosion [54]. As illustrated in Figure 3-5, the internal short circuit is the main cause of thermal runaway due to the mechanical abuse, e.g. the separator tearing caused by nail penetration or crush. Internal short circuit is also due to the electrical abuse, e.g. the separator piercing caused by dendrite formation from lithium plating, which is one of the ageing mechanism in LiBs; the thermal abuse, e.g. the shrinkage and collapse of separator caused by extreme high temperature due to the increase of internal resistance during ageing [54].

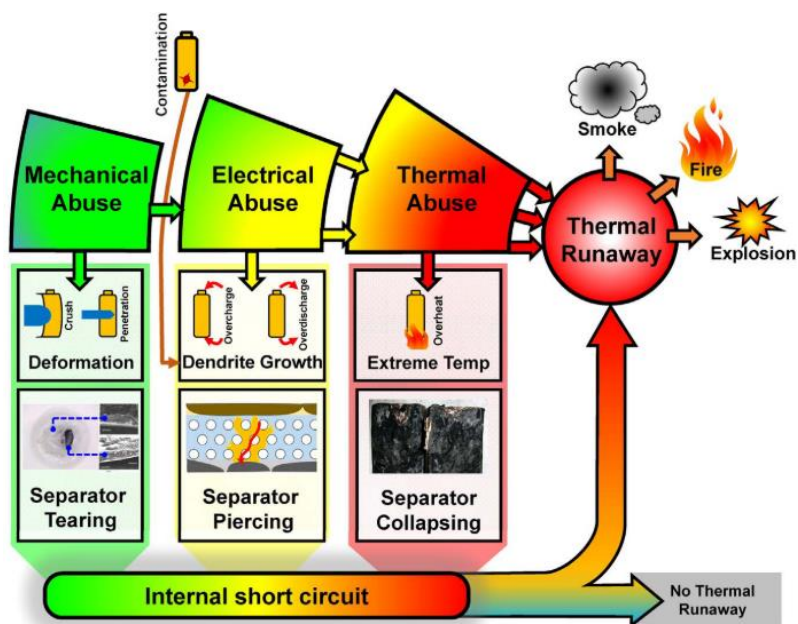


Figure 3-5 Illustration of the most common features of thermal runaway [51]

3.4 Ageing types definition

In order to investigate the ageing study for different electrochemical energy storage elements. Two types of ageing test are performed on LiBs, SCaps and LiC, i.e. calendar ageing test and power cycling ageing test.

3.4.1 Calendar ageing tests

During calendar ageing, LiBs are usually stored under open circuit potential state, the loss of capacity is irreversible with time. LiBs used in the aircraft for emergency system is always on standby, therefore the lifespan under calendar ageing is one of the criterion facing the selection of LiBs for aeronautical usage.

Many studies [126] [127] [128] [129] pointed out that the capacity loss had a linear regression versus a square root of time, which corresponds on the behaviour of SEI formation. Moreover, high temperature and high SOC favours the calendar ageing [126] [127], recently, a few studies shown that the low temperature resulted in the capacity fade in calendar ageing [130] [131]. In the review of Dubarry et al [130], they resumed all the significant studies on calendar ageing for different LiB technologies, they demonstrated that a few studies were focused on the calendar ageing at low temperature and high SOC.

For SCaps and LiCs, calendar ageing tests are performed under a constant voltage, since the self-discharging of SCaps and LiCs are significant. This voltage maintains constant that is also called float voltage to compensate the self-discharge, therefore a leakage current about few milliamps is detected [132]. According to these papers [123] [132] [133], they indicated that the characteristic of leakage current was a State-Of -Health index for electrochemical storage elements.

3.4.2 Power cycling ageing

In contrast to the calendar ageing, power cycling ageing requires the operating conditions (charge/discharge), which signifies the electrochemical storage elements are cycled under the electrical load. The high current level, the elevated temperature and the wide DOD variation result in a severity energy and power fade [128] [134] [135]. Power cycling ageing is one of the ageing type that always found out in a real application, such as in the case of A380, a 28V battery is always connected with DC bars to avoid power cutting in the network of aircraft, which is under operating conditions. Therefore, the number of cycles is another indicator of lifespan during the electrochemical storage element choice.

3.5 Ageing test experiments

For ageing study, the generic calendar ageing and power cycling ageing tests are performed on electrochemical storage elements under different conditions. The large experimental tests with periodic characterization according to LiBs, SCaps and LiCs are presented in this section.

3.5.1 Characteristics of calendar ageing tests

As the calendar ageing tests are defined in the reference tests for all investigated electrochemical energy storage elements for aeronautical usage. Thus, the extreme temperature conditions must be considered for the ageing test design. According to previous literatures, high temperature favours the calendar ageing, 55°C is therefore selected. -20°C is selected due to the lack knowledge of calendar ageing at this temperature. A reference temperature at 25°C is also selected. Furthermore, as the SCaps can be stored at 65°C, therefore, 65°C is added for calendar ageing tests of SCaps.

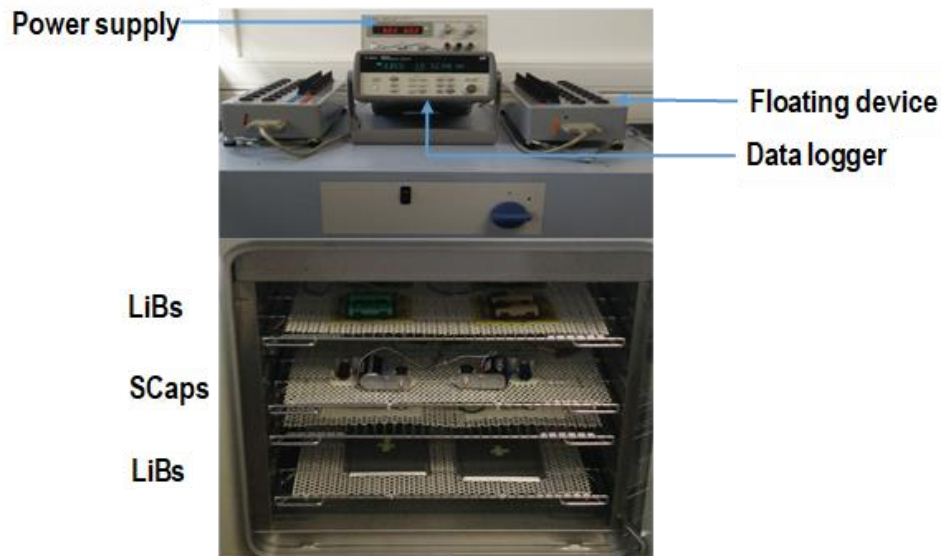


Figure 3-6 Example of experimental setups for LiBs during calendar ageing tests at 25°C

Otherwise, as the electrochemical energy storage elements are always stored at high SOC in the aircraft. Therefore, in the case of LiBs, cells were stored at 95% SOC, which corresponded to the OCV at 95% SOC at the beginning of life (BOL). During the duration of ageing tests, OCV was also measured by a data logger from Agilent in order to follow the self-discharging of LiBs. While, a constant voltage was applied on SCaps (2.85V) and LiCs (2.6V) during calendar ageing thanks to a floating card developed in our group. In parallel, the leakage current was also measured. One example of experimental setups for LiBs is illustrated in Figure 3-6

3.5.2 Characteristics of power cycling ageing tests

As the cycle life is another criterion in the reference test to evaluate the lifespan of different electrochemical energy storage elements, therefore the generic power cycling ageing tests were performed. Because the temperature range of charge (0°C-50°C) is narrow than the temperature of discharge (-20°C-55°C) for the majority LiBs and LiC technologies. In addition, the behaviour of self-heating appears during power cycling ageing tests, which results in an increase of temperature. Therefore, 0°C and 45°C were selected for power cycling ageing tests of LiBs and LiC. The cycling current was 0.5C for LG, 1C for others LiBs and 10C for LiC, which also corresponds the current level in the performance tests in chapter 2. SOC variation was roughly about 100%, which signified the LiBs cycling between minimal voltage and maximal voltage. While, LiC was cycling between 1.4V and 2.7V. In regards to the SCpas, 0°C

and 50°C were selected for the similar reason with 50A between $U_n/2$ (1.425V) and U_n (2.85V) for power cycling ageing tests. Table 3-2 illustrates the temperature increase at BOL and EOT in a classical power cycling ageing tests for all teste electrochemical energy elements. It can be seen that the temperature increase is significant for the 18650 and 26650 Li-ion cell forms. Furthermore, the temperature increase is more important for the power cycling ageing tests at 0°C relatively to 45°C. These behaviours are directly linked with the internal resistance. For the SCaps from Skeleton, the temperature increase will be presented in the following section.

Power cycling tests	Temperature increase at BOL/EOT (°C)						
	LG	Samsung	EAS	K2	Valence	EIG	Yunasko
Power cycling ageing at 45°C	5/6	5/6	1/3	5/5	2/4	1/1	3/4
Power cycling ageing at 0°C	8/13	8/13	3/4	8/9	8/6	1/1	6/11

Table 3-2 Temperature increase at BOL/EOT for investigated technology

A thermocouple was placed in the centre of all electrochemical storage elements in order to measure the skin temperature of cell during power cycling ageing tests. In addition, the power cycling ageing tests program must include the limits for temperature, voltage and current so that the tests were terminated and damages avoided for safety reasons. Figure 3-7 illustrates the experimental setups for power cycling ageing tests.

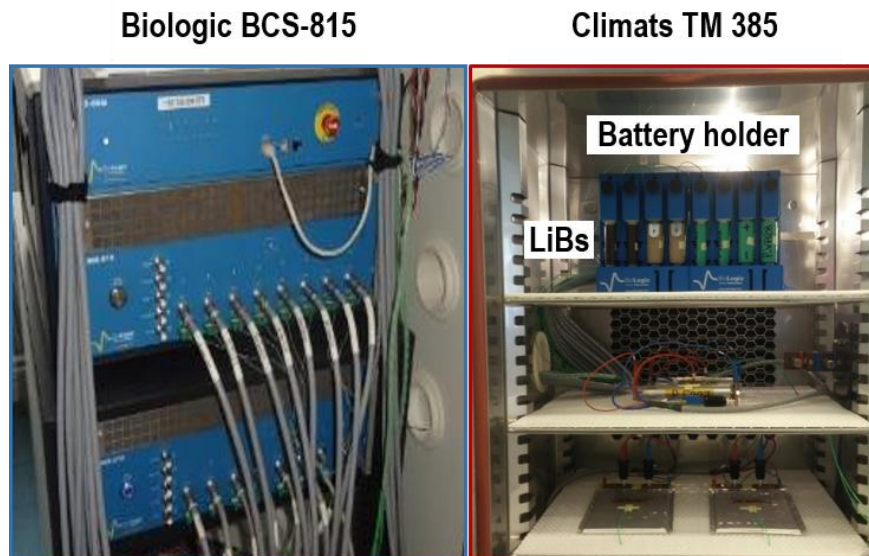


Figure 3-7 Example of experimental setups for LiBs during power cycling tests

3.5.3 Check-up protocols

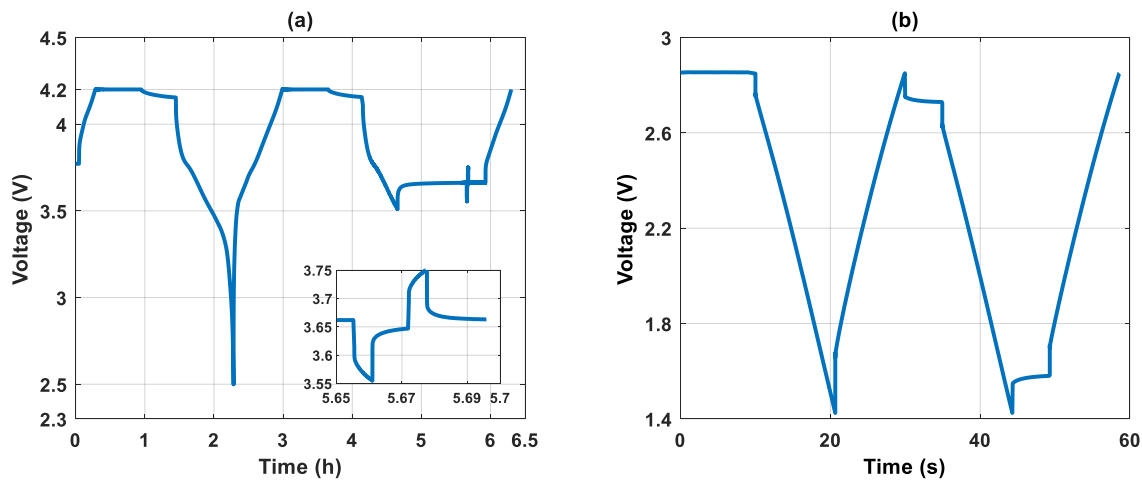
The performance of electrochemical storage elements were checked approximately every three weeks (21 days) for calendar ageing tests at -20°C and 55°C, six weeks (42 days) at 25°C, since a lot of literatures indicated that this duration is considered convenient for this type of ageing [136] [137] [128]. Regarding power cycling ageing tests, as SOC variation was roughly about 100%, the on-line capacity had been tracked to inform the suitable moment for

a check-up. In ageing study, the end of test (EOT) occurs later than the 20% capacity loss which is classically taken as the end of first life criterion.

For LiBs, the check-up was applied at 25°C after 3 hours of thermal stabilization with a profile presented in Figure 3-8 (a). The cells were charged with CC-CV mode at C/2 for LG and at 1C for other LiBs, then fully discharged at the same current. The capacity is the ampere-hour discharged. A new CC-CV charge followed by a CC discharge was needed to reset 50% SOC. The SOC reset signified a 50% ampere hour removal relatively to the capacity at the BOL. Then, after an OCV period of 1h, the resistance was measured at 50% SOC according to a current profile made of 20 seconds discharge followed by 40 seconds OCV and 20 seconds charge, as depicted in the inserted zoom in the voltage curve in Figure 3-8 (a). The cell resistance was calculated after 10s of discharge pulse according to equation (3.1) where U_{ocv} and U_{10s} represented the voltage before and after 10 seconds of pulse, I is the current pulse magnitude corresponding to C-rate. The duration of check-up was 9 hours for LG and 6.5 hours for other technologies of LiBs, which was negligible compared with the ageing duration (~500h).

For SCaps, the profile of check-up is presented in the Figure 3-8 (b). The SCaps were discharged at 5A after the calendar ageing or power cycling ageing tests at 25°C until $0.5U_n$, then fully charge with CC mode at the same current level until U_n . 5 seconds relaxation allowed to calculate the 5 second discharged ESR at U_n according to equation (3.2). Next, the same discharging was applied until $0.5U_n$ followed by a 5s relaxation, which represented the charged ESR at $0.5U_n$. Finally, a fully charging was applied until U_n . The capacitance was the average of two discharges. While, only the discharged ESR at U_n was presented in the experimental results section. For LiCs, the profile of check-up was the same as the LiBs, but the current level is 3C (3.9A) instead of 0.5C or 1C in the case of LiBs.

As the design of experiments for ageing tests was quite large, the experimental results presented were related to only two cells for the same ageing condition. In each curve, one point corresponds the average of the values from two cells.



$$R = \frac{U_{ocv} - U_{10s}}{I} \quad (3.1)$$

$$ESR = \frac{U_n - U_{5s}}{I} \quad (3.2)$$

Figure 3-8 Check-up profile at 25° for (a) LiBs, LiCs, and (b) for SCaps

3.6 Calendar ageing results and analyses

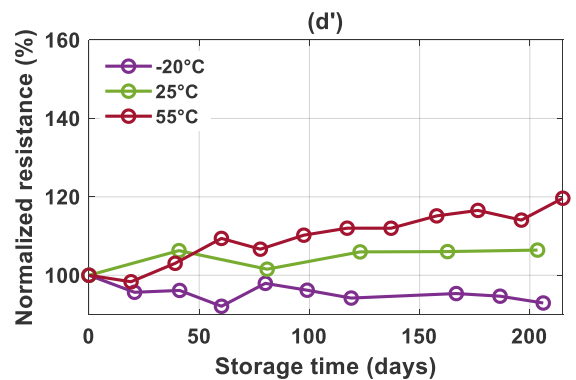
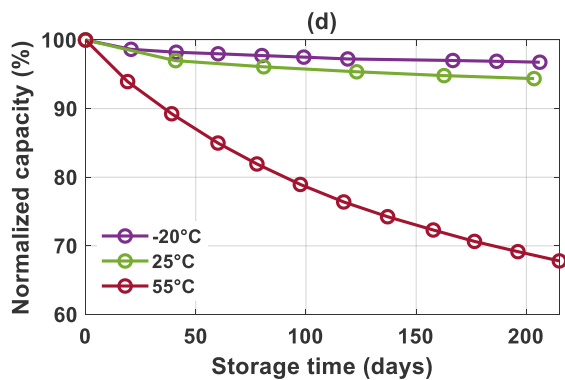
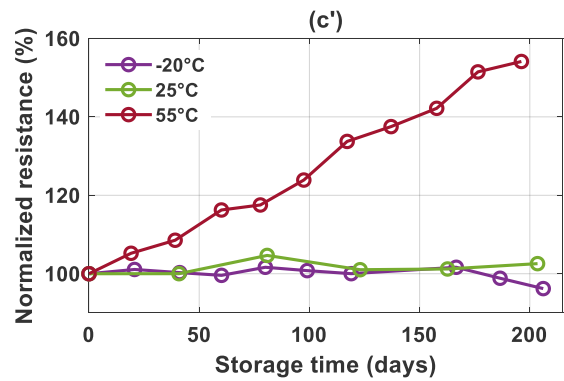
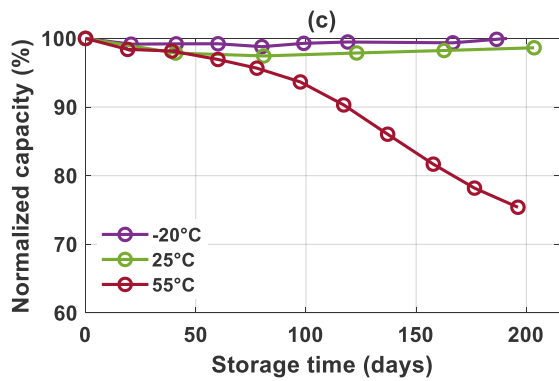
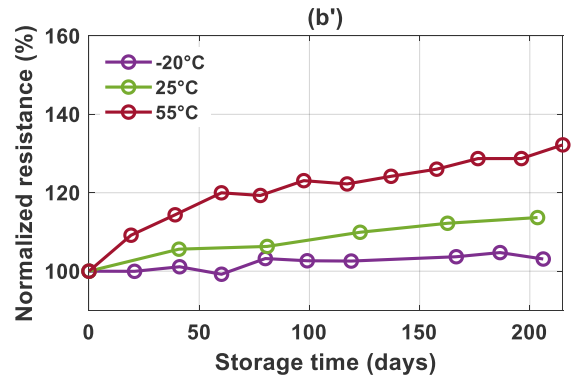
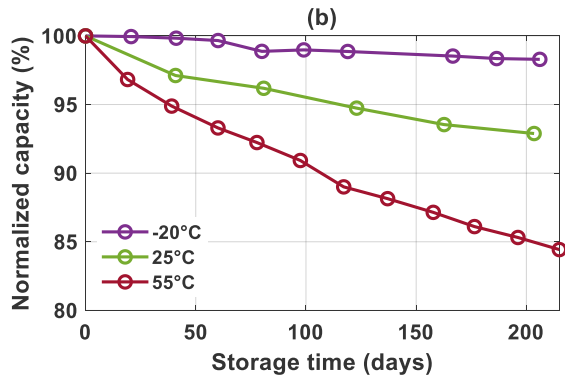
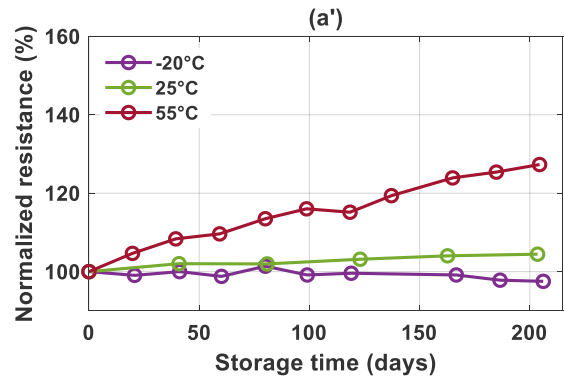
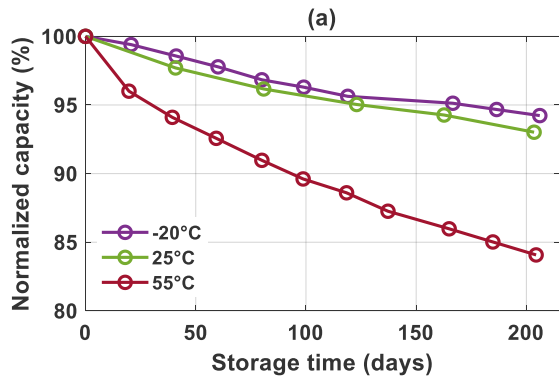
3.6.1 Raw tests results

The evolutions of normalized capacity and resistance at 25°C versus storage time under multiple ageing conditions (-20°C, 25°C, 55°C) are depicted in Figure 3-9 for all technologies of LiBs. The normalization is relative to the capacity and resistance values at the beginning of life (BOL). Since the storage condition at 25°C is considered as a reference temperature in calendar ageing tests, therefore, the check-up for this ageing type are performed every 500h (21 days) for calendar ageing tests at -20°C and 55°C, every 1000h (41 days) at 25°C. The EOT of calendar ageing occurs after 5000h (209 days) of storage.

In Figure 3-9 (a-f), it can be observed that high temperature results in a significant capacity loss for all LiBs, which limits the energy capability. Less than 20% capacity loss occurs at 55°C after 209 storage days for LG (Figure 3-9 (a)) and Samsung (Figure 3-9 (b)), while, more than 20% capacity loss occurs at 55°C for other technologies. Surprisingly, almost 5% capacity loss at -20°C for Samsung, K2 and EIG. However, the curves of normalized capacity versus storage time stay steady for calendar ageing at -20°C for other technologies of LiBs.

In contrast to the capacity loss, the resistance increases in calendar ageing tests. As illustrated in Figure 3-9 (a'-f'), the temperature of calendar ageing has an important impact on the normalized resistance. High temperature leads to a significant increase of resistance, which limits the power capability. In addition, the tendency of normalized resistance over storage time follows the tendency of normalized capacity evolution in the same ageing conditions for all technologies except for the cells from K2 (Figure 3-9 (d')).

Regarding the LiBs chemistry, NCA 18650 cell from Samsung (Figure 3-9 (b,b')) has a better performance relatively to 341440 cell from EAS (Figure 3-9 (c,c')) in term of normalized capacity and resistance during calendar ageing. In addition, the shape of normalized capacity versus storage time curve is different between them. This may be due to the manufacturing process or different forms of cell. For LFP, the cell from K2 (Figure 3-9 (d,d')) and Valence (Figure 3-9 (e,e')) have the similar capacity fade behaviour in calendar ageing tests. However, the increase of resistance is less significant for K2 compared to Valence. In fact, manufacturer adds the magnesium in the LFP electrode of cell from Valence, which could have an impact on the resistance when the cell ageing.



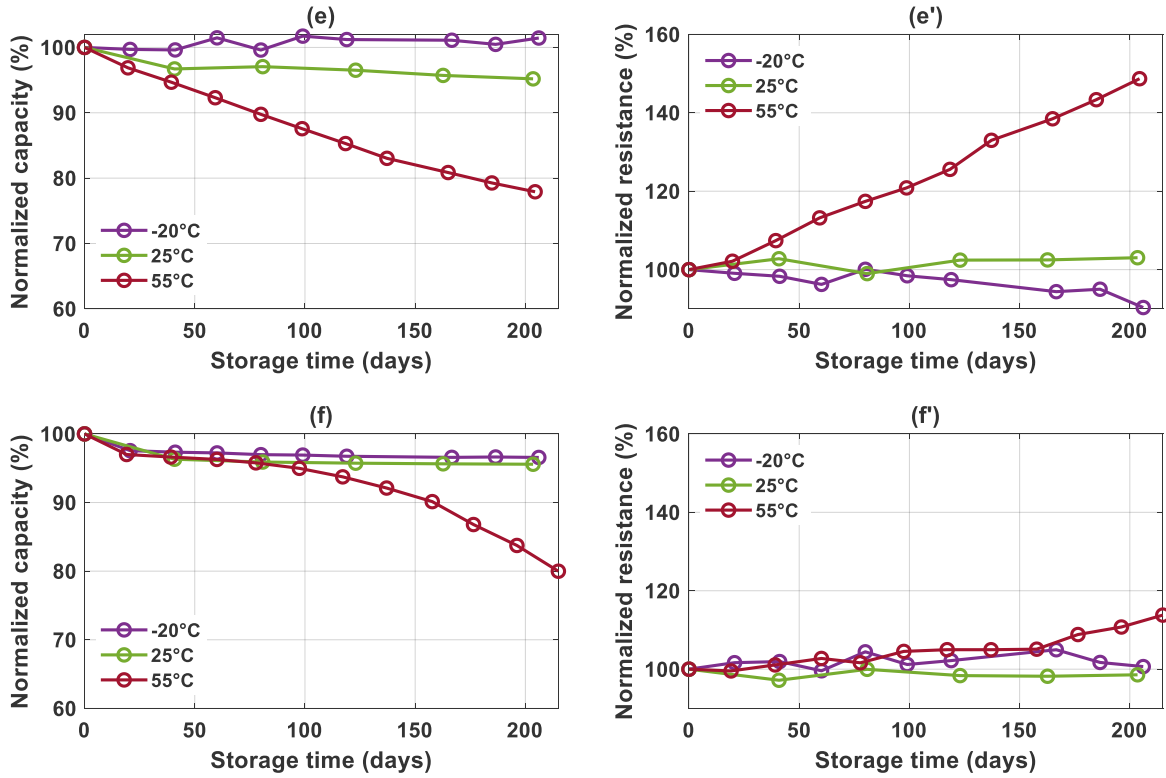


Figure 3-9 Normalized capacity (left) and normalized resistance at 50% SOC (right) from check-up at 25°C for LiBs (a) (a')LG, (b) (b') Samsung, (c) (c') EAS, (d) (d') K2, (e) (e')Valence (f) (f') EIG under 55°C, 25°C and -20°C of calendar ageing tests at 95%SOC

Figure 3-10 illustrates the evolution of normalized capacitance and resistance at 25°C versus storage time for different floating voltage (2.7V) calendar ageing tests (-20°C, 25°C, 55°C and 65°C). In the case of SCaps, temperature affect the normalized capacitance and resistance over storage time, especially the capacitance fade is more important at high temperature, which results in a decrease of power capability. Relatively to the LiBs, the increase of ESR is 10 times more than the increased resistance of LiBs at high temperatures. Otherwise, the measurement of ESR at EOT for calendar ageing at 65°C is not available, since the minimal voltage was reaching at the end of 1 second.

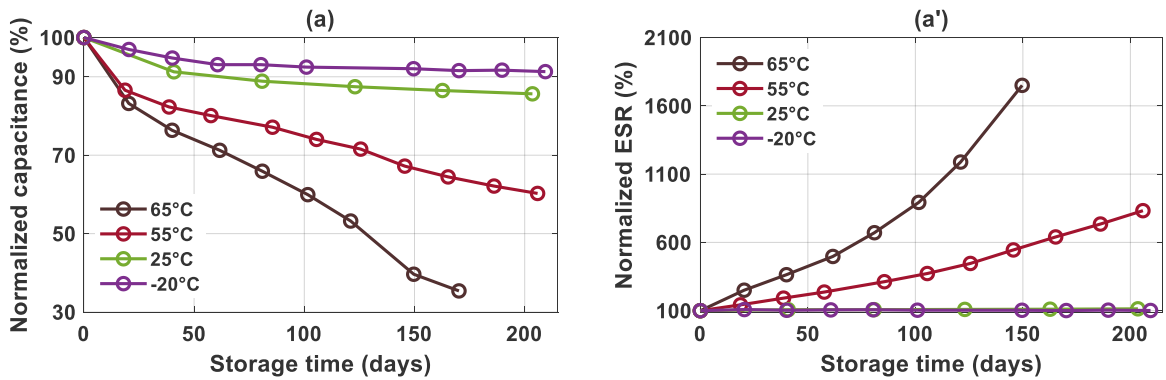


Figure 3-10 (a) Normalized capacitance and (a') normalized ESR at 5s from check-up at 25°C for Skeleton under 65°C, 55°C, 25°C and -20°C of floating calendar ageing(2.7V) tests

Figure 3-11 (a, a') illustrate the evolution of normalized capacity and resistance over the storage time at 25°C and 55°C for floating voltage (2.6V) calendar ageing. The same behaviour is observed for LiCs as in the case of LiBs and SCpas, where the high temperature leads to an important capacity fade and ESR increase. Furthermore, the cell swelling and some electrolyte leakage are appeared at EOT in both calendar ageing conditions (25°C and 55°C), one example is illustrated in Figure 3-11 (b), where the cell is at EOT after 33 storage days at 55°C. Owing to these issues, unfortunately, the calendar ageing at -20°C has not been performed.

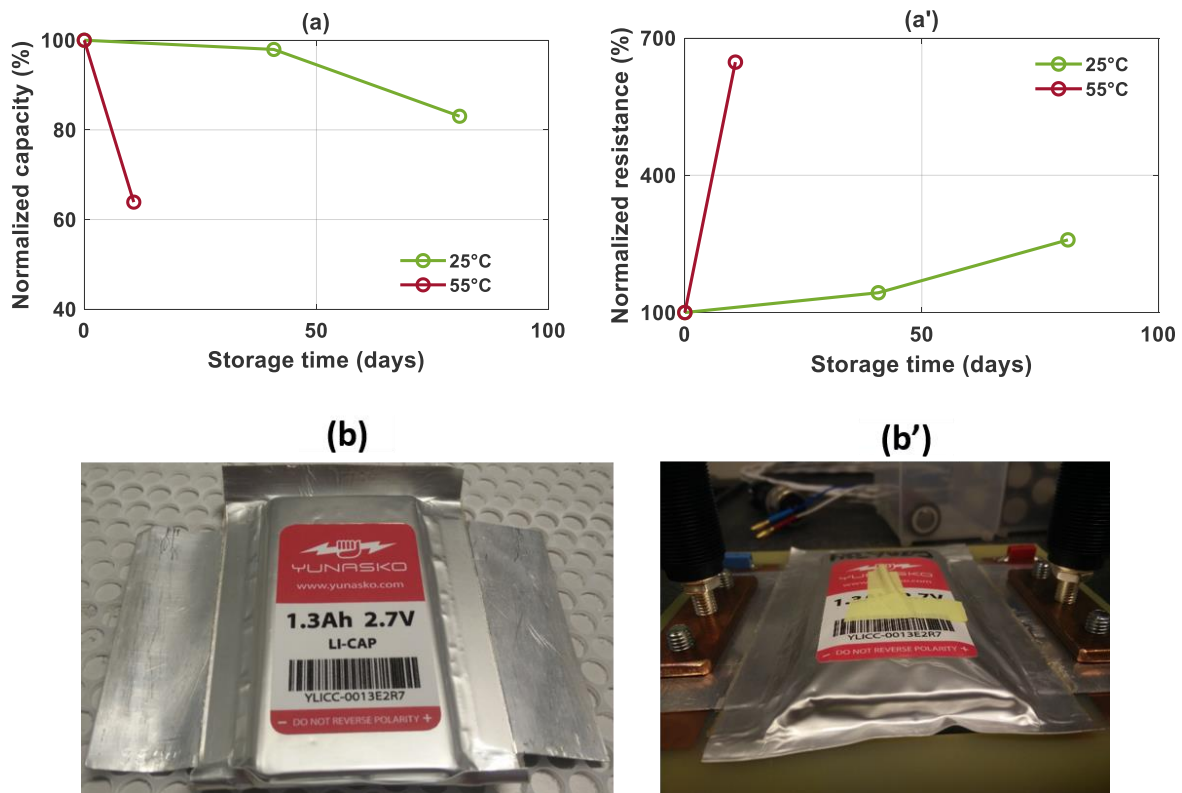


Figure 3-11 (a) Normalized capacitance and (a') normalized resistance from check-up at 25°C for Yunasko under 55°C and 25°C of floating calendar ageing(2.6V) tests, (b) LiC in the fresh state (b')LiC after 33 days floating calendar ageing(2.6V) tests at 55°C

3.6.2 Capacity loss analyses under calendar ageing in a wide temperature range

In order to investigate the impact of storage temperature on capacity fade in calendar ageing tests, the most classic method is establishing a relationship between natural logarithm of degradation rate [138] or capacity loss [139] and storage temperature. The Arrhenius like relationship is always observed in the temperature range from 25°C to 60°C [127] [129] [138]. Naumann et al. [129] found out a good linear relationship between capacity loss and inverse of storage temperature (25°C, 40°C, 60°C) for LFP batteries. Besides the Arrhenius like relationship, the Eyring law was applied by Redondo-Iglesias [140] to predict capacity fade of LFP batteries in the calendar ageing tests.

Until now, few studies show if LiBs or SCaps has the same behaviour in low temperature range relatively to temperature range above 25°C. Baghdadi et al.[128] indicated that two different ageing behaviours were noticed for the range of -5°C to 25°C and 25°C to 60°C for

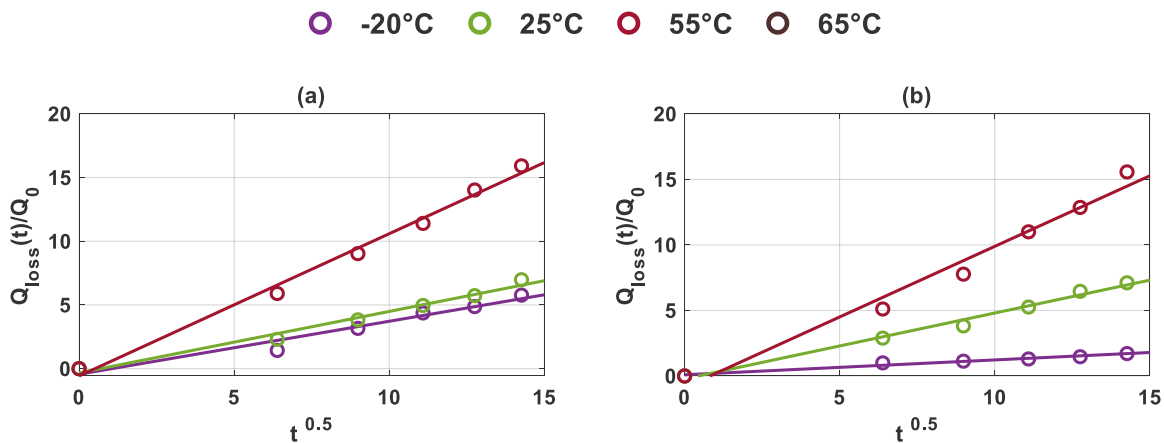
LMO cells in power cycling ageing tests. The temperature dependent ageing mechanism were also observed in power cycling ageing tests by Waldmann et al. [141]. The Arrhenius like relationship between degradation rate and temperature is different and it depends on temperature range.

The relationship between capacity fade rate and storage temperature (-20°C-65°C) is therefore investigated according to the different technologies. Among multiple technologies of LiBs, different chemistries are selected to be analysed, such as NMC (LG), NCA (Samsung), LFP (K2), LTO (EIG). In addition, SCaps from Skeleton is also studied. The capacity fade rate (k) is determined by equation (3.3), where $Q_{loss}(t)$ is the capacity loss after t days, Q_0 is the capacity at BOL, t is the ageing time (days), α is the time-dependant factor. Since many studies [128] [129] [142] indicated that the capacity fade had a linear regression with the square root of ageing time for LFP, NMC, NCA LiBs, therefore α is 0.5.

Based on this approach, Figure 3-12 illustrate the normalized capacity or capacitance loss over the square root of time ($t^{0.5}$) for each technology at different temperatures. It can be observed that a linear regression is obvious for almost all technologies at ageing temperatures for -20°C, 25°C and 55°C. The slop and the determination coefficient of these curves are listed below the corresponding figure. It can been concluded that the slop increased with the ageing temperature, which is logical. Because the high temperature favours the calendar ageing degradation mechanisms. Regarding the coefficient of determination, most of them are nearly 1, which significates a good linear dependency.

$$\frac{Q_{loss}(t)}{Q_0} = k \times t^\alpha \tag{3.3}$$

However, a worse linear dependency of technology LTO from EIG is appeared relatively to other LiBs. This may be due to the choice of time-dependant factor (α) for LTO negative electrode. In fact, SEI growth has a linear relationship with the square root of time [143]. Furthermore, SEI growth is one of the principal ageing mechanisms in calendar ageing. 0.5 is therefore selected for the LiBs with a graphite negative electrode.



NMC (LG)	-20°C	25°C	55°C
Slop (day ^{-0.5})	0.42	0.48	1.12
R ²	0.96	0.98	0.99

NCA (Samsung)	-20°C	25°C	55°C
Slop (day ^{-0.5})	0.11	0.50	1.08
R ²	0.97	0.99	0.98

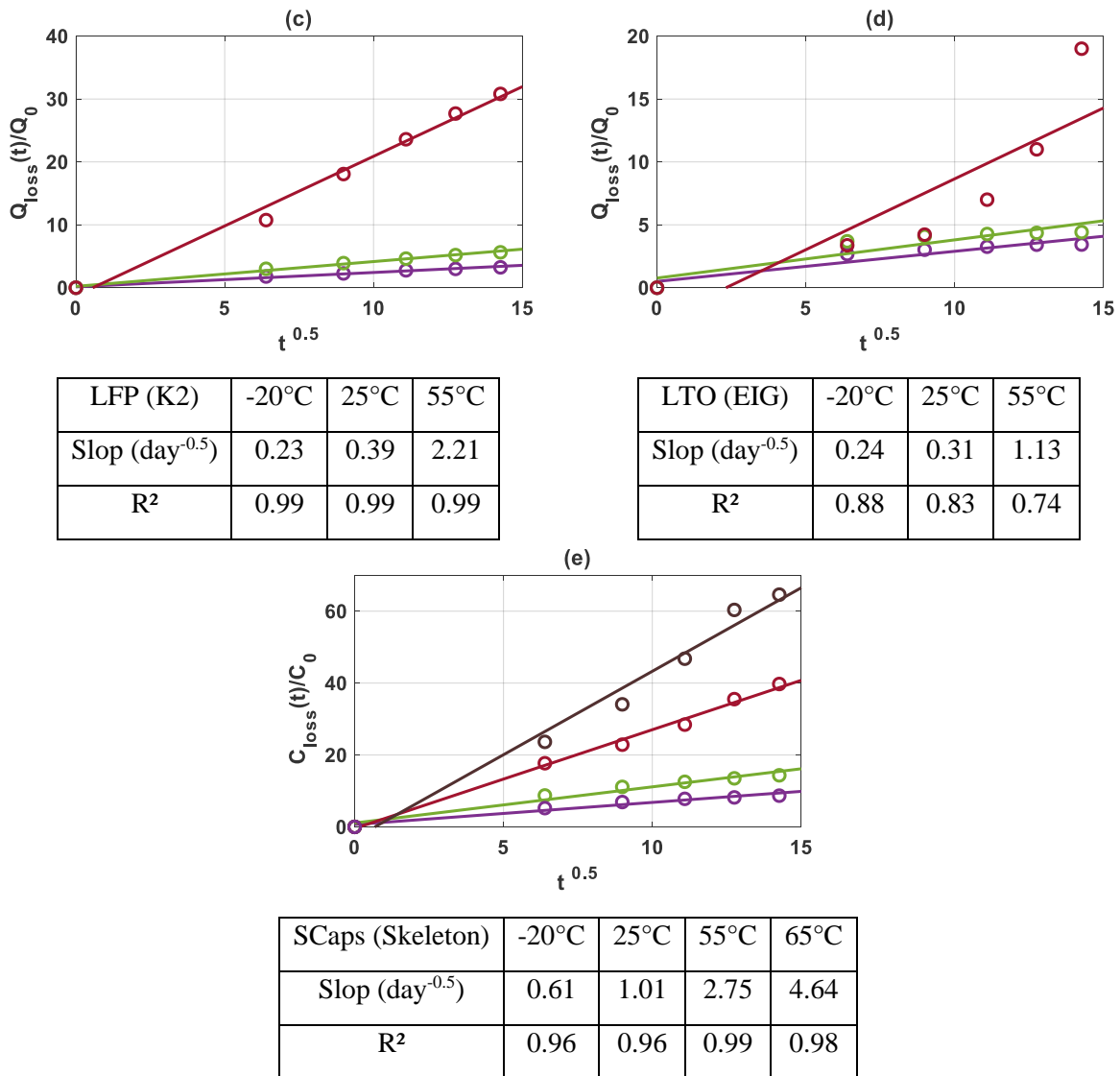


Figure 3-12 Capacitance loss over square root of time at -20°C, 25°C, 55°C, 65°C and corresponding linear regressions values for (a) NMC (LG), (b) NCA (Samsung), (c) LFP (K2), (d) LTO (EIG), (e) SCaps (Skeleton)

The Arrhenius' law is defined in equation (3.4), where k is the rate constant for reaction, T is the absolute temperature (K), A is the pre-exponential factor, E_a is the activation energy for the reaction, R is the gas constant ($8.314\text{Jmol}^{-1}\text{K}^{-1}$). In order to verify whether the relationship between degradation rate and temperature following the Arrhenius function, the natural logarithm of slopes ($\ln k$) are plotted over the inverse of temperature ($\frac{1}{T}$).

$$k = A \times e^{\frac{-E_a}{RT}} \quad (3.4)$$

Figure 3-13 illustrates the relationship for all technologies. It is obvious that the technology of NCA from Samsung shows a good linear dependency, which signifies the Arrhenius dependency. According to equation (3.4), the energy activation of NCA from Samsung is 21kJ mol^{-1} , which is similar the value in the paper of Xu et al. [144]. But Waag et al found a higher energy activation value that is between 50 and 60kJmol^{-1} for the same

chemistry of LiB. In fact, they determined this value according to the increase of resistance, not according to the rate of capacity fade.

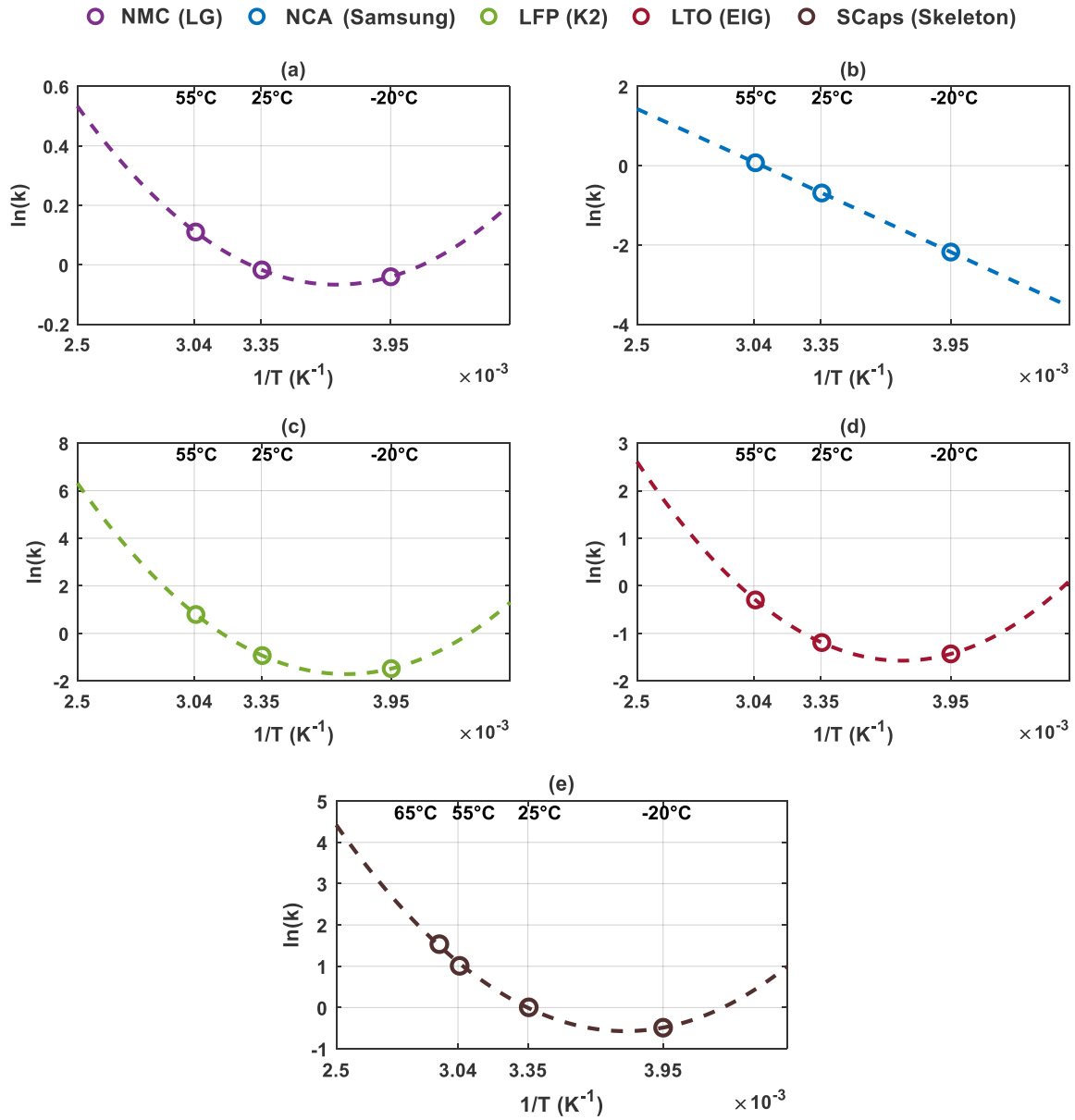


Figure 3-13 Influence of calendar ageing temperatures (-20°C, 25°C, 55°C 65°C) on degradation rate for (a) NMC (LG), (b) NCA (Samsung), (c) LFP (K2), (d) LTO (EIG), (e) Activated Carbone (Skeleton)

Contrary to the NCA LiBs from Samsung, a non-linear dependency is observed for other technologies, such as LiBs (NMC, LFP, LTO) in the temperature range from -20°C to 55°C and SCaps (activated carbon) from -20°C to 65°C. A simply quadratic regression is applied to fitting these data. The optimal calendar ageing temperature can be identified thanks to the parabolas fitting according to equation (3.5), where a , b and c is the fitting parameters. The rate of capacity fade is minimal when the temperature is at $-\frac{b}{2a}$.

$$\ln k = a \times \left(\frac{1}{T}\right)^2 + b \times \frac{1}{T} + c \quad (3.5)$$

Table 3-3 lists the optimal calendar ageing temperature for different chemistries of LiBs and SCaps. This interesting finding indicates that above or below this optimal temperature, LiBs age at 95% SOC and SCaps degrade at 2.7V in calendar ageing test conditions. Furthermore, this particular temperature depends on chemistries of electrochemical energy storage elements, which comprises from -3°C to -10°C. This information can help users to store the LiBs and SCaps under the optimal thermal condition. However, the results need to be consolidated with additional temperatures.

Technology	Chemistry	Optimal calendar ageing temperature (°C)
LiBs	NMC (LG)	-2.7
	LFP (K2)	-5.8
	LTO (EIG)	-4.6
SCaps	Activated Carbon (Skeleton)	-8.7

Table 3-3 Optimal calendar ageing temperatures for multiple chemistries (NMC, LFP, LTO and Activated Carbon) based on quadratic-type fitting

The similar behaviour is shown in literatures [128] [141]. In [128], a quadratic function was applied to fitting the curve of logarithm degradation rate versus temperature, 27°C and 17.5°C was identified as optimal temperatures for each current condition. This plot is presented in Figure 3-14 (a). In fact, the degradation rate in this plot was determined by a mixed ageing type, which included the power cycling and calendar ageing. Since the degradation mechanism is quite different between these two ageing types, therefore, their optimal temperatures are not similar as ours.

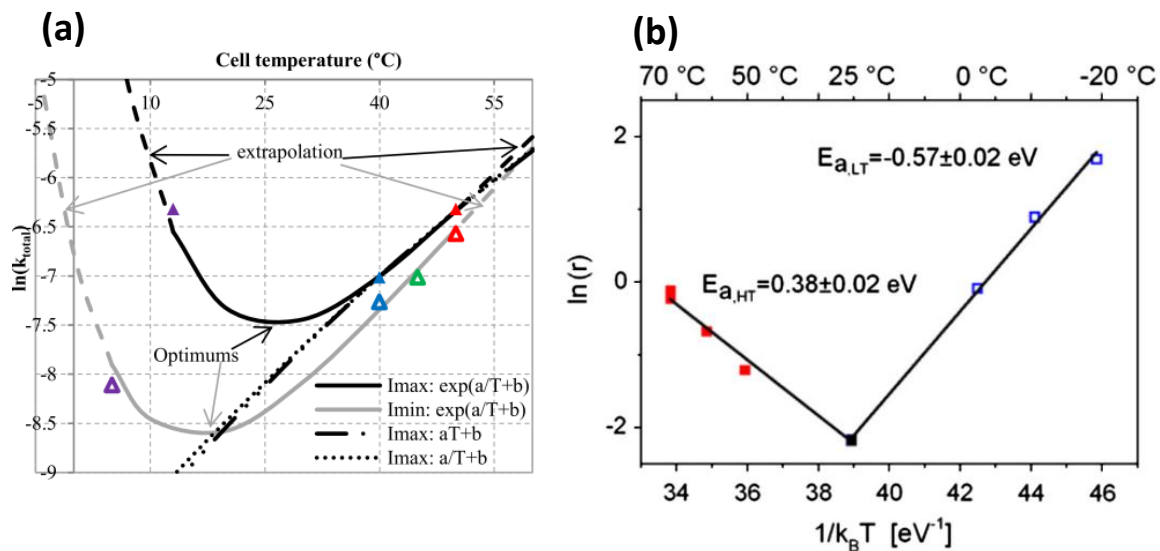


Figure 3-14 (a) Logarithm of total ageing rate function of temperature, I_{max} and I_{min} [128] (b) Arrhenius plot of the ageing behaviour of 18650 cells cycled at 1C in the temperature range from -20°C to 70°C [141]

In [141], two linear regressions were observed, which are separated by an optimal temperature at 27°C as illustrated in Figure 3-14 (b). In addition, the energy activation had an opposite sign, which was positive between 27°C and 70°C and negative between -20°C and 27°C. They demonstrated that the degradation rate is extreme high in power cycling tests at low temperature, which was due to the lithium plating.

The previous analyses indicate that the rate of capacity fade over the ageing temperature does not all follow the Arrhenius' law. There is an optimal temperature between -20°C and 55°C for the LiBs (NMC, LFP, LTO) and SCaps (Activated Carbon) in calendar ageing tests, where the capacity fade rate is the lowest. In addition, this assumption is supported by the literatures in the combined ageing tests or power cycling ageing tests in a wide operating temperature range (-20°C-70°C). Regarding the two linear regressions were demonstrated by Waldmann et al. [141], our proposed fitting is based on a quadratic regression due to the temperature lack. In fact, as the calendar ageing at low temperature is not considered as the common ageing tests, which risks non-capacity fade. Furthermore, the calendar ageing tests are time-consuming and costly. Thereby, only three temperature are investigated in our study with a reference temperature at 25°C. Otherwise, it is recommended to verify the regression type with other several temperatures.

3.7 Power cycling ageing results and analyses

The power cycling ageing tests are performed with a 100% DOD at 0°C and 45°C under 0.5C for LG and 1C for other LiBs. As in the case of calendar ageing, the normalized capacity and resistance are followed to evaluate the power cycling ageing behaviour. The normalization is relative to the capacity and resistance values at the BOL. The evolutions of the normalized capacity and resistance over cycle number are depicted in Figure 3-15 for all LiBs technologies. Two types of normalized capacity are shown on the plots. The independent symbol in circle represents the classical periodic check-up at 25°C according to the corresponding power cycling. While, the circles with a line represents the on-line characterization.

Item	LG	Samsung	EAS	K2	Valence	EIG
Chemistry	NMC/ graphite+SiO	NCA/ graphite	NCA/ graphite	LFP/ graphite	LiFeMgPO ₄ / graphite	NMC/ LTO
Time (days) Power cycling at 45°C	180	125 (C _{loss} >50%)	115 (C _{loss} >50%)	182	181	180
Time (days) Power cycling at 0°C	26 (C _{loss} >50%)	80 (C _{loss} >50%)	182	183	182	182

Table 3-4 Ageing duration of power cycling ageing tests at 0°C and 45°C for each LiBs

Furthermore, the power cycling ageing tests duration is listed in Table 3-4 with corresponding cycling temperature and stop criterion of tests. In fact, power cycling ageing tests had been planned for 6 months. Since Sauer et al. [137] showed that more than 20% capacity loss was observed for a NMC Li-ion cell under the power cycling ageing tests at 40°C

with 100% DOD. However, in practice, the EOT of investigated LiBs occurred before this duration for some reasons, such as the capacity loss is too significant to could not apply a classical check-up at 25°C or cell swelling. Besides these constraints, all the power cycling ageing tests were performed almost 6 months. A classic check-up at 25°C was performed each 20 days, otherwise, it can be informed by the on-line characterization.

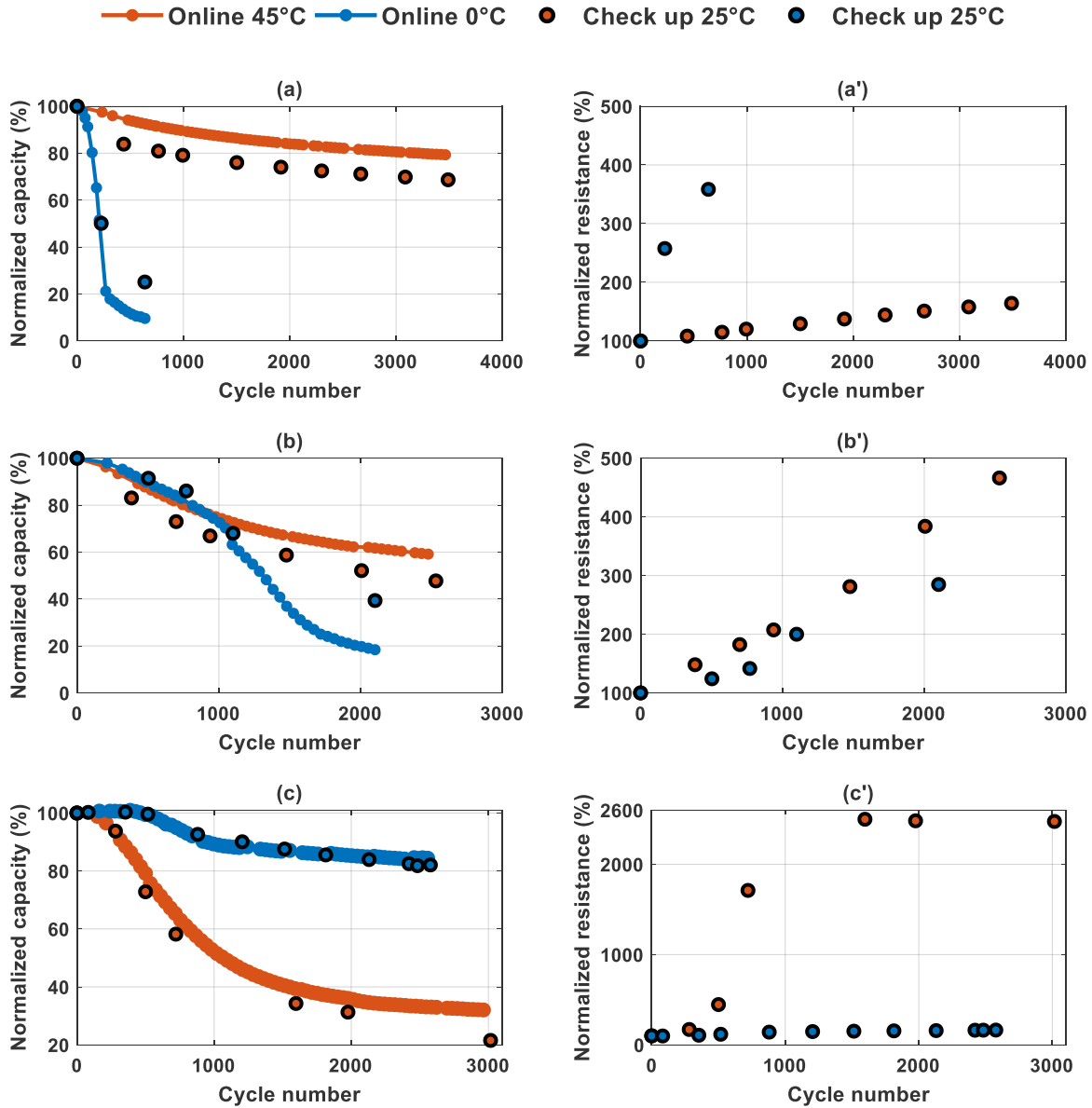
In Figure 3-15, for all LiBs, it can be observed that the normalized capacity values obtained according to the classical check-up are always below the online values at 45°C, while, they are always above the online values at 0°C for all technologies. This behaviour is due to the temperature of characterization. In fact, high temperature enhances the available capacity of LiBs, therefore, the capacity is smaller at 25°C than the capacity obtained from the power cycling ageing tests at 45°C, and vice versa for the power cycling ageing tests at 0°C.

In contrast to the calendar ageing, power cycling ageing test at low temperature leads to a significant capacity loss for all LiBs within 6 months except EIG, especially for technology LG. More than 80% capacity decrease is observed only after 26 days (638 full cycles) of power cycling ageing test for LG as presented in Figure 3-15 (a). The similar behaviour is found for technology Samsung after cycling 80 days (Figure 3-15 (b)). The degradation rate is higher in the case of LG, which may be due to the silicon addition in negative electrode [145]. Since Shang et al. [145] indicated that the volume variation of negative electrode with graphite silicone induced the mechanical stresses, resulting in electrode disintegration with consequent failure during cycling. However, this behaviour is less significant compared to the power cycling ageing tests at 45°C for LG. The cells of technology EAS lose 20% capacity after 6 months of power cycling ageing tests with the same condition (Figure 3-15 (c)). However, it has the same chemistry as Samsung. Overall, all the tested chemistries have the same ageing behaviour under 0°C.

In Figure 3-15 (d, e), technologies K2 and Valence both have the LFP positive electrodes. A capacity regeneration phenomena is noticed under the power cycling ageing at 0°C. This phenomena can be observed when the power cycling ageing tests are stop or in the early hours of power cycling after a classical check-up at 25°C. A lot of papers highlighted the capacity regeneration phenomena in Li-ion cells [110] [146] [147] [148]. Eddahech et al. [146] pointed out that the stop-SOC value impacts on the regeneration phenomena for an NMC Li-ion cell in power cycling ageing tests at 45°C. They assumed that this phenomena was due to the electrical charge redistribution during the relaxation period of cell. Sauer et al. [148] indicated that the relaxation phase enhanced the homogeneity of Li⁺ distribution for NMC/graphite LiBs. Furthermore Rauhala et al. [110] highlighted that an improved capacity was observed for the LFP Li-ion cells during power cycling ageing tests at low temperatures (-18°C and 0°C). They indicated that the graphite structure cracking and disordering of the graphite sometimes could create more site for the insertion of Li⁺, thereby leading to an improved capacity.

Based on Figure 3-15 (f), a slight capacity fade is observed in both power cycling conditions (0°C and 45°C) for technology EIG. For the power cycling ageing tests at 45°C, an increase of the capacity is observed at the beginning of power cycling, then it starts to decrease slowly. However, no increase of capacity is appeared in the case of power cycling ageing tests at 0°C. After a sharp drop at the beginning of test, the normalized capacity remains stable. These

results suggest that LTO Li-ion cells have a long lifetime in the power cycling ageing type. Stroe et al. [149] shown the similar results for the LTO Li-ion cells under 1C power cycling ageing tests at 50°C with 50% DOD. But, they observed a fast capacity fade behaviour after 3000 full equivalent cycles. They indicated that the capacity fade evolution could be divided into three regions. The two first regions were similar as our funding, the third region was where a fast capacity loss occurred. They highlighted that each region associated with a specific ageing mechanism.



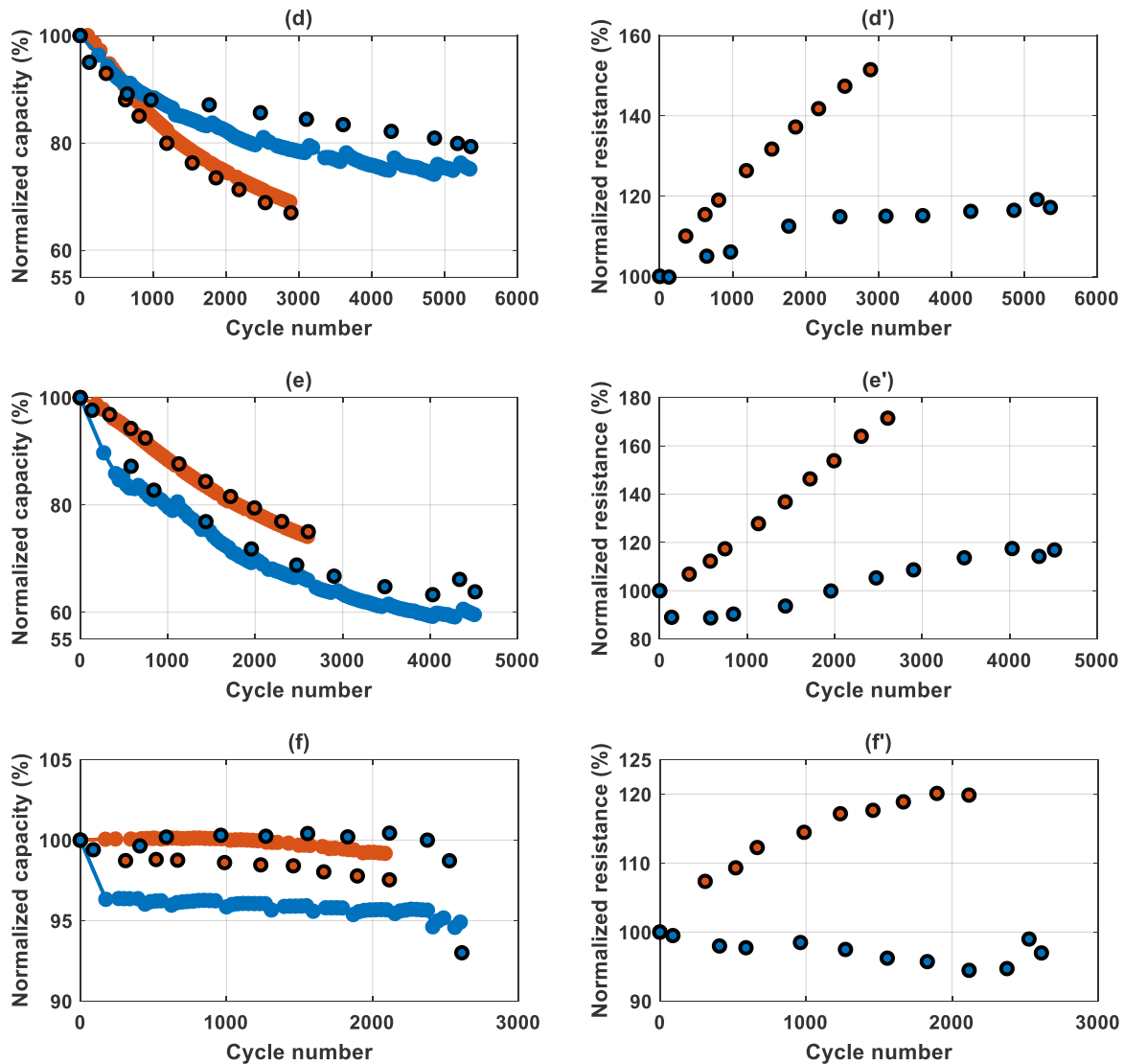


Figure 3-15 Normalized capacity (left) and normalized resistance at 50% SOC (right) for LiBs according to online and classical check-up for (a) (a') LG, (b) (b') Samsung, (c) (c') EAS, (d) (d') K2, (e) (e') Valence (f) (f') EIG under 0°C and 45°C power cycling ageing tests (100% DOD, 0.5C/1C)

In Figure 3-15 (a'-f'), it can be observed that the internal resistance at 50% SOC increases with the cycle number. Furthermore, the evolution of normalized internal resistance has the similar tendency with the evolution of normalized capacity over the cycle number for almost of Li-ion technologies. However, in Figure 3-15 (c'), the internal resistance at the EOT is more than 2000 times higher relatively to the initial internal resistance for the power cycling at 45°C. In fact, the values of normalized resistance after 720 cycles are could not been taken into account. Since the reset of 50% SOC in the classical check-up is based on the initial capacity, as the capacity fade is significant after 720 cycles at 45°C, thereby, the internal resistance is not exactly measured at 50% SOC.

Figure 3-16 (a, a') depicts the evolution of normalized capacitance and ESR over cycle number for SCaps. More than 4 months tests are performed, 131 days for power cycling at 50°C, 125 days for power cycling at 0°C. Nearly 5% capacity fade is observed at the EOT (3.9e+5 cycles) at 0°C and 25% capacity loss is found at the EOT (4.8e+5 cycles) at 50°C. In

Figure 3-16 (a), it can be observed that the normalized capacitance from off-line check-up is quite different compared to the on-line values at 50°C. But, these values are quasi identical at 0°C. In fact, as illustrated in Figure 3-16 (b), for power cycling at 50°C and 0°C in the end of tests, the self-heating leads 25°C and 5°C temperature increase respectively. Thereby, the difference between on-line and off-line normalized capacitance is more significant at 50°C.

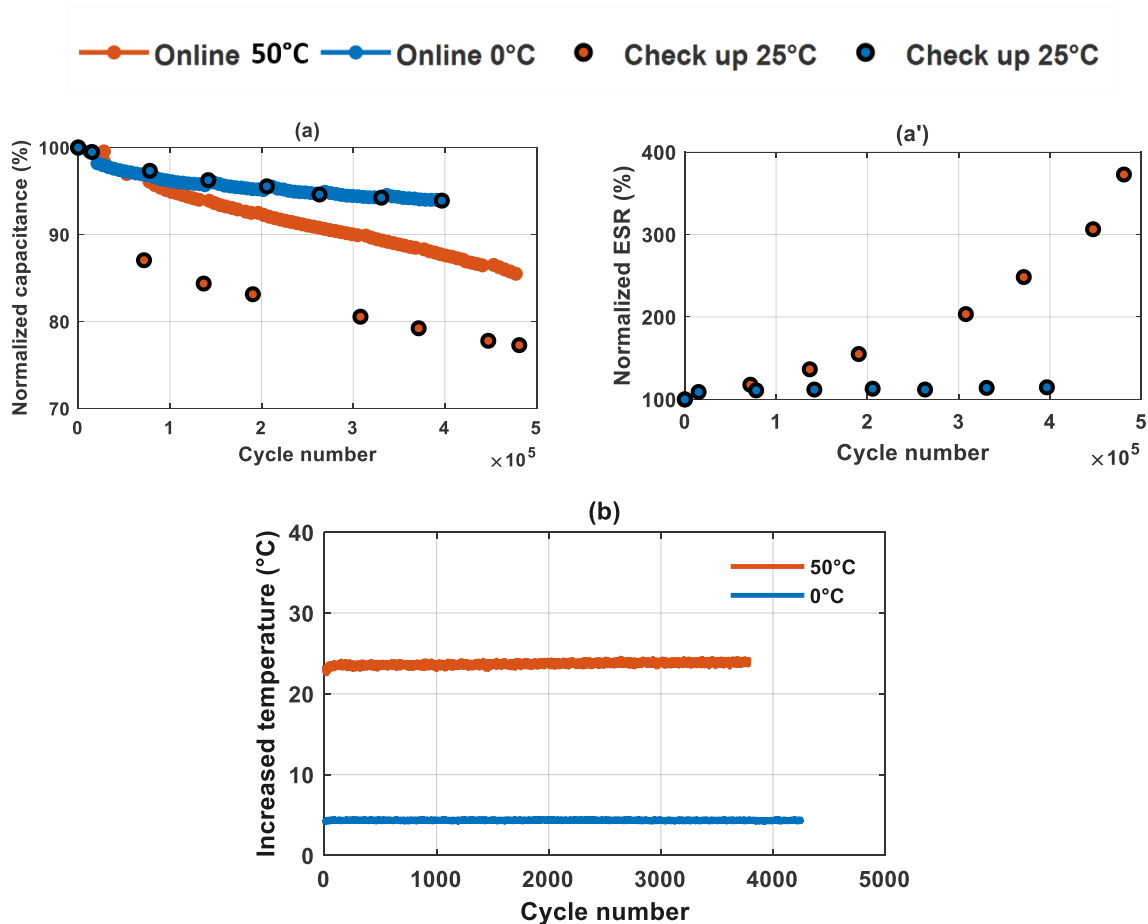


Figure 3-16 (a) Online and classical check-up normalized capacitance (a') classical check-up normalized ESR at 5s for Skeleton under 50°C and 0°C of power cycling ($0.5U_n-U_n$, 50A) ageing tests (b) Temperature increase at the surface of SCaps before EOT power cycling at 0°C and 50°C

Furthermore, the capacitance regeneration phenomena is observed in both conditions. According to Chaari et al. [150], the maximum voltage and temperature during power cycling were the main factors of this phenomena for SCaps. They announced that the charge redistribution inside the porous carbon electrodes when the power cycling stopped is the origin of capacitance regeneration. In Figure 3-16 (a'), ESR increases with the cycle number and its evolution tendency corresponds the evolution of normalized capacitance.

In the case of LiCs, 160 days of power cycling ageing tests are performed at 0°C and 18 days for 45°C. As illustrated in Figure 3-17, a sharp drop of normalized capacity is observed at the beginning of power cycling ageing test at 45°C, while, a slight increase is appeared at 0°C. The capacity regeneration phenomena can be found in LiCs as in the case of SCaps and LFP

Li-ion cells. The evolution of normalized resistance is significant in both power cycling conditions. Furthermore, the cell swelling is observed at EOT of power cycling at 45°C as in the calendar ageing tests (Figure 3-17 (b)).

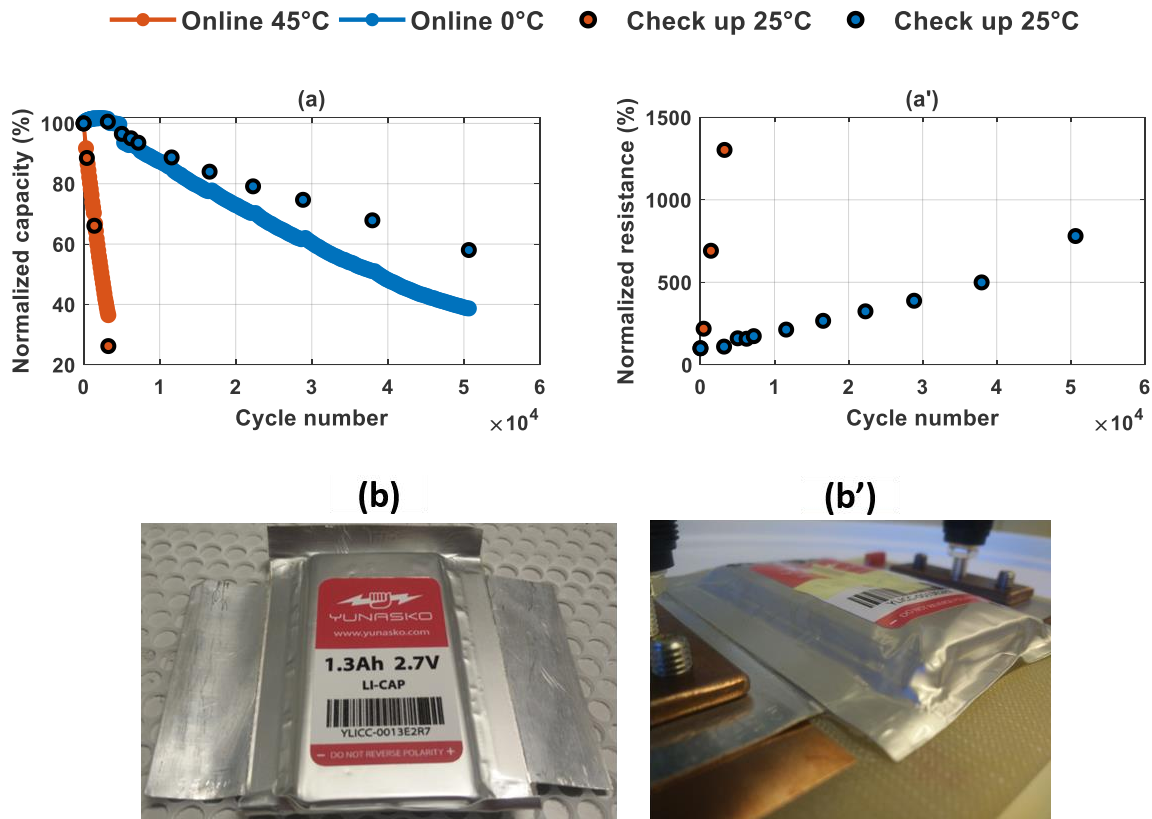


Figure 3-17 (a) Online and classical check-up normalized capacitance (a') classical check-up normalized resistance at 50% SOC for Yunasko under 0°C and 45°C power cycling (1.4V-2.7V) tests (b) LiC after 3251 cycles (18 days) power cycling ageing tests(1.4V-2.7V, 10C-13A) at 45°C

The experimental power cycling ageing tests and their results tests are presented and analysed in this section for each technology respectively. A first observation is the power cycling ageing tests spend a lot of time and need many equipment. The whole tests last more than 6 months, the battery cyclers and the climatic chambers must ensure the operating conditions during this long period. In addition, the tests design requests lots of precautions, since the power cycling ageing behaviour of LiBs, SCaps and LiCs is quite different. For example, it is difficult to prevent the most suitable moment for the periodic characterization due to the diverse ageing behaviours. Therefore, the online characterizations should set up. Two temperatures are selected for the power cycling study, because 0°C and 45°C is the maximal cycling temperature of LiBs and LiCs, which are also in the operating temperature range for aeronautical usage.

Overall, all the electrochemical storage elements lose more than 20% capacity in all power cycling conditions besides LTO Li-ion cell from EIG. The results indicates that the cycling ageing behaviour is dependent on the cycling temperature, on the technologies, on the

DOD. Low temperature leads a significant capacity fade for almost LiBs. The internal resistance evolution over cycle number is less important compared to the normalized capacity evolution. The capacity regeneration phenomena is observed for LFP Li-ion cells, SCaps and LiC. Surprisingly, the self-heating is more significant at the EOL for SCaps cycling at 50°C. The swelling is appeared for the pouch cell of LiCs. All these signify that the power cycling ageing is a complex process, which leads to in multiple ageing results.

3.8 Abuse tests and results

Besides the ageing study, safety focused study on electrochemical energy storage elements are also investigated. The abuse tests are based on the international abuse testing standards and regulations for Li-ion rechargeable batteries, which are classified according to the nature of misuses (mechanical, electrical, environmental and chemical) [151]. In the standard of UL-1642, the short-circuit test, heating test, altitude simulation (low pressure), temperature cycling test, shock test and crush test are defined to verify the safety of Li-ion rechargeable batteries for general application [152]. While, in the review of Ruiz et al. [151], they listed the abuse tests for electric and hybrid electric vehicles application. In the RCTA/DO-311, the overcharge, deep discharge, crash safety, temperature shock, external short-circuit, altitude simulation tests are defined with evaluation criteria for aeronautical usage. In this study, three main types of abuse tests are performed on several electrochemical energy storage elements: thermal stability, overcharge and altitude simulation. As listed in Table 3-5, a hazard level classification defined by EUCAR is widely applied about the safety of electrochemical energy storage elements. In this section, the safety evaluation of elements under abuse conditions are based on this table.

Hazard level	Description	Classification criteria & Effect
0	No effect	No effect. No loss of functionality.
1	Passive protection activated	No defect; no leakage; no venting, fire, or flame; no rupture; no explosion; no exothermic reaction or thermal runaway. Cell reversibly damaged. Repair of protection device needed,
2	Defect/Damage	No leakage; no venting, fire, or flame; no rupture; no explosion; no exothermic reaction or thermal runaway. Cell irreversibly damaged. Repair needed,
3	Leakage $\Delta_{\text{mass}} < 50\%$	No venting, fire, or flame; no rupture; no explosion, Weight loss $< 50\%$ of electrolyte weight
4	Venting $\Delta_{\text{mass}} \geq 50\%$	No fire or flame; no rupture; no explosion, Weight loss $\geq 50\%$
5	Fire or Flame	No rupture; no explosion
6	Rupture	No explosion, but flying parts of the active mass
7	Explosion	Explosion (<i>i.e.</i> , disintegration of cell)

Table 3-5 Hazard level with risk assessment defined in EUCAR

3.8.1 Thermal stability test

Thermal stability test were performed on two technologies for the safety focused study: the 26650 LFP/Graphite cell from K2 and the pouch Li-S cell from Oxis. Since the

LFP/Graphite is well-known for the safety during operation and few safety focused studies are carried on the Li-S cell. ARC (Accelerated Rate Calorimeter) was used to run the thermal stability test. All the cells were charged to 100% SOC with CC-CV method according to the technical datasheet. Then, they were installed in the ARC at 40°C during 3 hours of thermal stabilization. Next, the temperature of ARC increases by steps of 5°C with 1°C/min and it kept constant for 30 minutes at each step. While a thermal runaway was detected, the ARC was stopped to heat the cell. The end of thermal stability test occurred when the maximal temperature of cell exceeded 200°C or the maximal increased/decreased temperature rate exceeded 3°C/min, which is considered the limits in thermal stability test for Li-ion cells. During this test, thermocouples were installed at the positive, negative electrode, the centre of cell and in the ARC, the cell voltage was recorded. Furthermore, the weight of cell was also measured. The evolution of temperature and voltage of each technology during the test are presented in annexe 1 and 2 respectively.

For LFP/graphite cell, a moderate thermal runaway started between 98°C and 126°C. Vent opening of cell was observed at 126°C due to the internal pressure increase, this behaviour was probable caused by electrolyte decomposition. At 166°C, a sharp voltage drop was detected accompanying some ejected materials because of the the high internal pressure. The test was therefore stopped when the increased temperature rate exceeded 3°C. Several photos after the abuse test are shown in Figure 3-18. It can be observed that some plastic materials were ejected from the side of positive electrode, which might be the recrystallization of melted separator. But there was no significant modification on the side of negative electrode. Overall, this cell started a thermal runaway at 100°C, vent opening was exhibited at 126°C and no fire, explosion were observed up to 166°C. 10% of weight loss was measured.

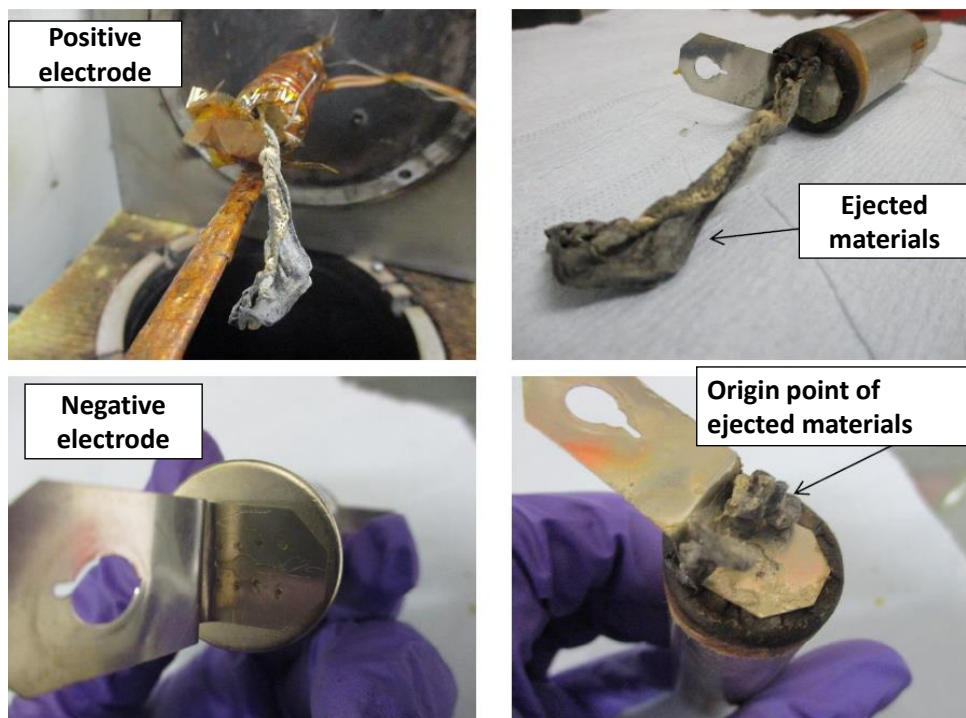


Figure 3-18 Photos after thermal stability test for LFP/Graphite 26650 cell from K2 energy

In the case of Li-S cell, a moderate thermal runaway was observed from 60°C to 100°C. An accelerated thermal runaway begun at 100°C. Then, an endothermic phenomena resulted in a vent opening at 130°C. From 137°C, the temperature of cell increased sharply and the voltage drop was detected at 170°C. The test was stopped at 200°C (annexe 2). The photos after thermal stability test are presented in Figure 3-19. Cell swelling was observed. Furthermore, the vent opening of cell occurred at 130°C was most likely located at the cell edge or at the weld of pouch. No visible combustion or explosion were detected. Only 2% weight lost after the test. According to these discussions, the behaviour of both cells under thermal abuse condition belongs to the hazard level 3.



Figure 3-19 Photos after the thermal stability test for Li-S pouch cell from Oxis

3.8.2 Overcharge test

Overcharge tests were performed on all electrochemical energy storage elements. All cells were charged to 100% SOC with CC-CV method based on the technical data-sheet. Then the charged cell were placed in a thermal chamber at 55°C more than 4 hours. After that, the cell were charged with CC under recommended current. The end of overcharge test occurred when the cell was in the open circuit state. The cell temperature, voltage, current and weight were measured during the overcharge test. Furthermore, a surveillance video was used to record the abuse test scenario.

Technology	U_{max} (V)	T_{max} (°C)	Observations
LG (NMC/graphite+SiO)	20	100	Off-gas generation, Vent opening, Electrolyte ejection, 1% weight loss
Samsung (NCA/graphite)	20	68	No
EAS (NCA/graphite)	20	321	Cell swelling, Off-gas generation, Electrolyte and solid ejection, Smoke, Explosion, Disintegrated cell
K2 Energy (LFP/graphite)	20	219	Off-gas generation, Electrolyte and solid ejection, Smoke, Vent opening, Sparks, Fire, 16% mass loss
Valence (LFP/graphite)	20	107	Cell swelling, Electrolyte ejection, Vent opening, 10% weight loss

EIG (NMC/LTO)	13.3	81	Cell swelling, Off-gas generation, Fire, 26% weight loss
Oxis (Li-S)	2.41	56	No
Skeleton (AC)	20	54	Off-gas generation, Electrolyte ejection, Vent opening, 11% weight loss
Yunasko (AC/Li-doped carbon)	5.2	90	Cell swelling, Electrolyte ejection, 12% weight loss

Table 3-6 Overview of overcharge test results for all technologies

Table 3-6 summarizes the main results obtained from overcharge tests. Such as the maximum value of voltage, temperature and significant observations during the overcharge test. It can be seen from Figure 3-20, only EAS was exploded after 40min of overcharge test. However, only the packaging deformation was observed on the positive electrode side for with the same chemistry cell from Samsung. A significant cell swelling was noticed for the technology from EIG. For LFP-based cell, a sign of fire was found for cell from K2, while only a vent opening was observed for the cell from Valence. These results indicate that the vent opening is often found for cylindrical cell and the swelling cell is always observed for pouch form. Cells from Samsung and Oxis shown an outstanding safe proprieties under overcharge conditions compared to other technologies.

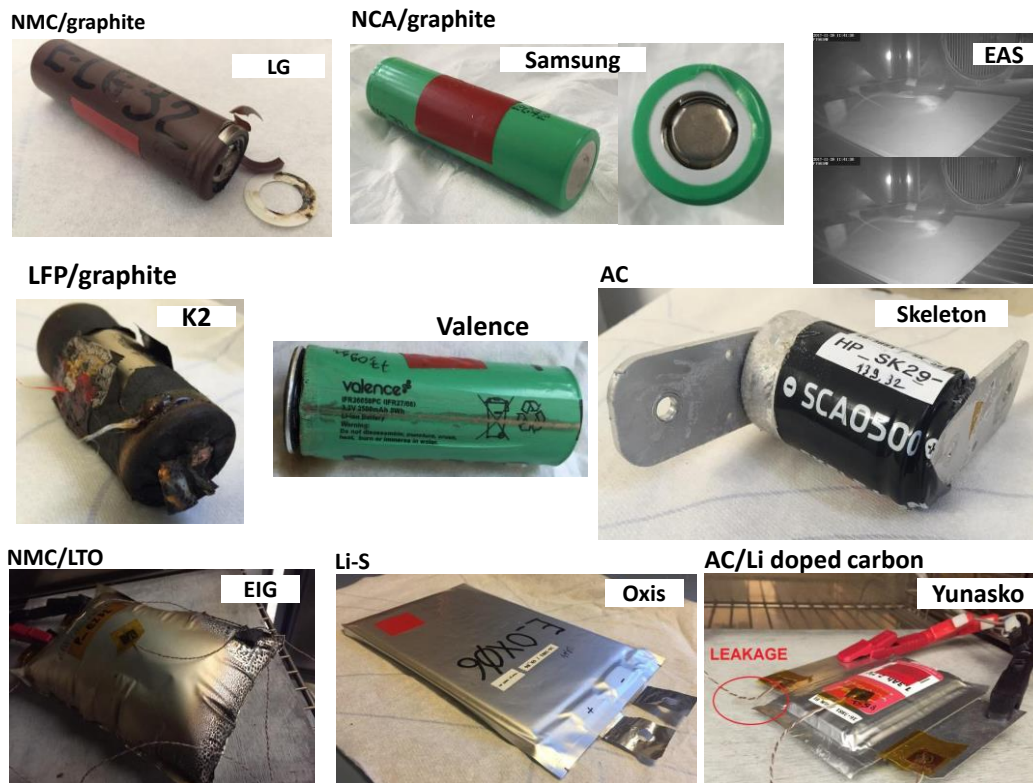


Figure 3-20 Photos after the overcharge tests

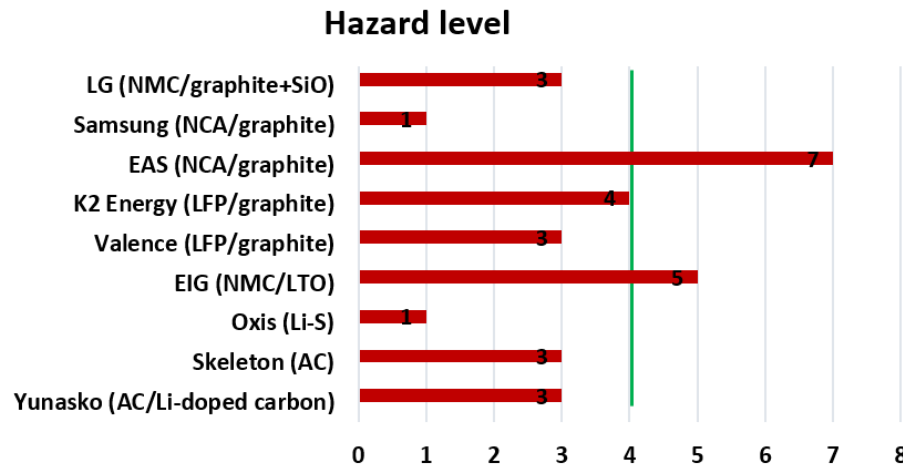


Figure 3-21 Hazard level comparison of different technologies based on overcharge tests

Cell swelling, off-gas generation, electrolyte and solid ejection, smoke, sparks, fire, explosion and percentage of weight loss are the main criteria to classify the hazard level. Figure 3-21 presents therefore the hazard level of different technologies. In fact, the elements that have a hazard level under 4 are recognised as the safe cells under abuse conditions. It can be concluded the NCA/graphite cell from EAS, NMC/LTO pouch cell from EIG have potential danger under overcharge.

3.8.3 Altitude simulation test

The deflation and ignition can be appeared for numerous Li-ion cells under low pressure in the aeronautical environment [153]. The altitude simulation tests are therefore necessary. Three technologies from Samsung, EIG and Yunasko were selected for this test. All cells were placed in a pressure tank in order to set them in the aeronautical environment. Then, they were charged to 100% with CC-CV at 25°C under atmosphere pressure. Next, the pressure was decreased to 9.109kPa that corresponded the maximum operating altitude (55 000ft~16764m) in 15min. This pressure should be maintained for 2h after the cells thermal stabilization. At last, the pressure must be increased to ambient pressure nearly 101.325kPa in 15min. All the cells were incurred 2 cycles. The experimental set up and pressure profile of altitude simulation are illustrated in Figure 3-22. As the overcharge test, the temperature and voltage of cell were recorder by thermocouples, a surveillance video was used. In addition, the cell in pouch form were placed between 2 compression plates with 10psi (~0.07MPa) tightening to avoid the displacement. Before and after the test, the capacity and internal resistance at 100% SOC measurement were carried out with respect the technical datasheet.

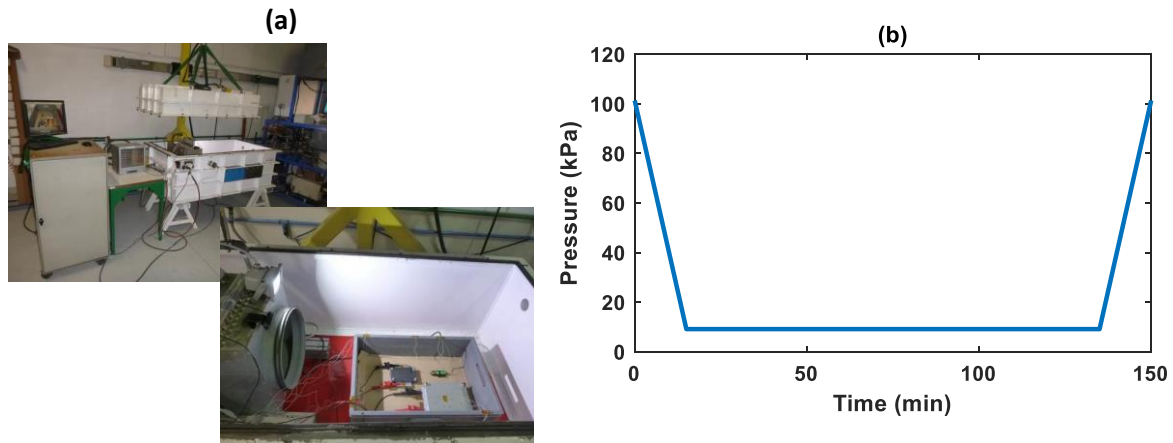


Figure 3-22 (a) Experimental set up (b) pressure profile of altitude simulation test

During the altitude simulation tests, none of the cells showed a deflation or deterioration. The voltage of cell remained constant, the temperature changed only when the pressure evolved. No singular events were detected compared to the overcharge tests during the 2 cycles of altitude simulation tests. In addition, there was not significant variation for the capacity and internal resistance values.

3.9 Comparison of different electrochemical energy storage elements

This section discusses which cells are of two most interests to test further with an aeronautical profile. Based on the performance quantification in a wide temperature range (-20°C - 55°C) in chapter 2, energy density, power density, capacity are selected as the comparative parameters. Furthermore, according to the lifetime and abuse tests investigated in chapter 3, calendar life, self-discharge, cycling life and safety are also taken into account. A total 7 proprieties are envisaged to establish the radar diagrams to compare the various electrochemical energy storage elements.

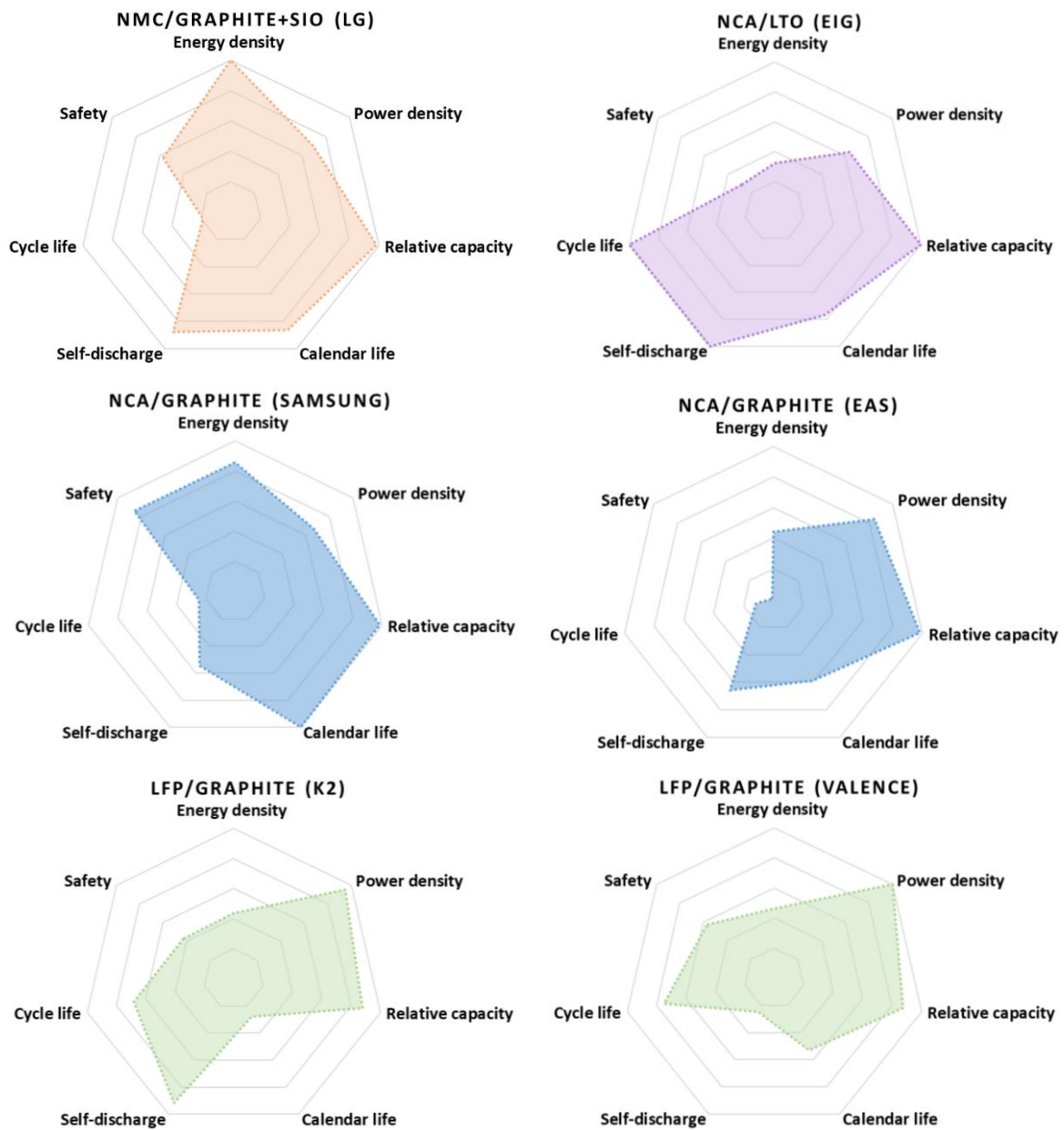
For this, the energy density (Wh/kg) and power density (W/kg) values are obtained from the galvanostatic discharge. The relative capacity value are the sum of capacities at -20°C and 55°C versus to the capacity at 25°C based on the continuous discharge. The value of calendar life are the sum of days when 20% capacity loss occurred under two extreme temperatures conditions (-20°C , 55°C). The same concept for the values of cycling life, but with the cycle number. Self-discharge is the voltage drop (mV/day) rate at the BOL in calendar ageing. The safety value are based on the hazard level defined from overcharge tests. In addition, all these parameters must be normalized relatively to the maximal value in each type (Energy, Power, High Power).

The radar diagrams of various electrochemical technologies are illustrated in Figure 3-23. Safety is the primarily criterion to be considered for aeronautical application. Therefore, NCA/graphite cell from EAS, NCA/LTO cell from EIG and LFP/graphite cell from K2 are eliminated firstly, despite EIG have a long cycling life and all of them have a high capacity in a wide temperature range.

Then, LiC from Yunasko can be removed because of short calendar and cycling life, in addition, electrolyte leakage is observed during ageing tests. LFP/Graphite cell from Valence

represents a long cycling life and high power density, however, the characteristic of voltage plateau in LFP-based cells leads to a low energy density relatively to other Li-ion batteries. Thus, they can be omitted.

As the radar diagram is normalized by the maximum value of each criterion, therefore the more shadow area is significant, the more promising technology has. In addition, a good compromise between energy density and power density ensures the electrical needs for aeronautical usage, thereby 18650 NMC/graphite+SiO cell from LG and 18650 NCA/graphite from Samsung are outstanding among the other technologies thanks to a high energy density and power density, but their cycle life is limited. Furthermore, both have a good calendar life and high capacity in the aeronautical environment.



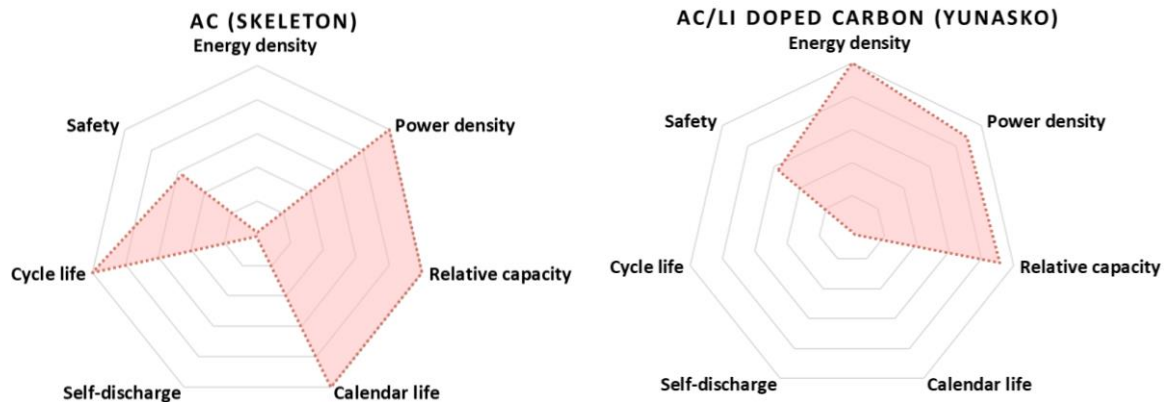


Figure 3-23 Radar diagram of various electrochemical energy storage elements (a) LG, (b) Samsung, (c) K2 (d) Valence, (e) EAS, (f) EIG, (g) Skeleton, (h) Yunasko

3.10 Conclusion

Ageing and safety focused studies are investigated in this chapter throughout 3 parts, since lifespan and safety of electrochemical energy storage elements are the essential criteria should be taken into account during the selection of promising cell.

The first part dedicated to an overview of multiple ageing behaviours in LiBs and SCaps thought several literatures. Various ageing mechanisms are given especially for LiBs, such as SEI formation, lithium plating, loss active materials and collector corrosion. Furthermore, these ageing mechanisms are extremely complex that are caused by multiple intrinsic (manufacturing) and extrinsic (T, SOC, DOD, I) origins. They can be classified into three degradation modes: CL, LAM and LLI, which result in not only the capacity and power fade, but also some safe issues such as the thermal runaway.

Thereby, calendar ageing and power cycling ageing tests are performed for all electrochemical energy storage elements in the second part. For calendar ageing tests, -20°C , 25°C and 55°C under 95% SOC are selected as tests condition. The power cycling tests are investigated at 45°C and 0°C with 100% DOD. These generic ageing conditions correspond to the temperature range for aeronautical environment. A period check-up are carried out at 25°C to follow the evolution of capacity and internal resistance during ageing. The experimental results show that a capacity fade and an internal increase are observed within 8 months ageing tests. Furthermore, the calendar ageing results allows to quantify the influence of temperature on the evolution of capacity.

A quadratic regression relationship is found between ageing temperature ($1/T$) and degradation rate ($\ln(k)$) for almost all LiBs and SCaps, which is contrary to the Arrhenius like relationship in almost papers. This interesting finding indicate that there is an optimal temperature between -20°C and 55°C for the LiBs (NMC, LFP, LTO) and SCaps (Activated Carbon) in the proposed calendar ageing conditions, where the capacity fade rate is the lowest. The experimental results of power cycling ageing tests indicate that the ageing behaviours depend on the cycling temperature and on the technologies. Low temperature leads a significant capacity fade for almost LiBs. The capacity regeneration phenomena, cell swelling, significant self-heating are observed through multiple electrochemical energy storage elements. It can be concluded that ageing behaviour is a complex process under calendar ageing and power cycling

ageing tests. A SOH estimation tool seems necessary to evaluate the performance of electrochemical energy storage elements during ageing.

The final part is dedicated to the abuse tests. Thermal stability, overcharge and altitude simulation tests are performed to evaluate the safety of investigated LiBs, SCaps and LiCs. For thermal stability and overcharge tests, all elements are classified into hazard level according to the observations and effects during tests, such as vent opening, electrolyte leakage, fire and explosion. No significant deflation and ignition are detected in the altitude simulation tests for LiBs of Samsung, SCaps from Skeleton and LiC of Yunasko.

Finally, several radar diagrams are established based on 7 criteria for all investigated electrochemical energy storage elements. These criteria include not only the performance (energy, power) but also the life span and safety properties, especially in the aeronautical environment. Furthermore, all the parameters in the radar diagrams are determined by experimental tests, which is based on a common test reference. Two most promising technologies: NMC/graphite+SiO cell of LG, NCA/graphite cell of Samsung are selected to test further with a specific aeronautical profile.

Chapter 4

SOH estimation of electrochemical energy storage elements

Table of contents

4.1 Introduction	97
4.2 Overview of SOH estimation methods.....	98
4.2.1. Experimental methods.....	99
4.2.2. Model-based estimation methods.....	99
4.3 Principles of Incremental Capacity Analysis.....	100
4.4 Raw tests results for qualitative and quantitative ICA study.....	101
4.5 Enhanced IC by moving average filter	102
4.6 ICA study.....	103
4.6.1. Current influence on ICA	103
4.6.2. Qualitative influence of different ageing types on ICA	105
4.6.3. Decomposition of IC curves based on Gaussian Lorentzian mixed function	107
4.6.4. Peak features with respect to normalized capacity and normalized resistance	108
4.6.5. Method validation for cells with unknown SOH	110
4.7 Conclusion.....	112

4.1 Introduction

Mastering the performance evaluation of ElectroChemical Energy Storage (ECES) elements for the multitude of degradation modes (CL, LLI, LAM) is essential for users. Therefore, an accurate SOH estimation is necessary for the investigated electrochemical energy storage elements, especially for the two selected promising technologies, which are 18650 LG NMC/graphite+SiO cell from LG and 18650 NCA/graphite cell from Samsung. This chapter is dedicated to the SOH estimation study based on the qualitative and quantitative Incremental

Capacity (IC) method throughout the whole lifespan of LG and Samsung cells. The proposed efficient method is able to not only determine which types of ageing a Li-ion cell has historically endured but also determine the normalized resistance for an unknown-SOH Li-ion cell.

For this, the experimental results of LG and Samsung in chapter 3 from calendar ageing and power cycling ageing over a wide temperature range of -20°C to 55°C for the duration of approximately 250 days are used to obtain the different SOHs. Then, the qualitative IC is employed to identify the possible degradation modes according to various literatures. Next, the extracted area and location of the peaks on the IC curves according to Gaussian Lorentzian mixed function allowed to establish two quick and simple linear regressions to predict which types of ageing the Li-ion cells historically underwent, then, the normalized resistance can be estimated without specific experimental tests.

4.2 Overview of SOH estimation methods

For evaluating the performance of lithium-ion batteries, the state of health (SOH) is the indicator to assess their health level. The SOH is always defined according to the normalized capacity and the normalized resistance. Over the past decades, researchers have proposed numerous methods for estimating the performance of lithium-ion batteries with different chemistries [154] [155]. In general, they are divided into two categories: experimental methods and model-based estimation methods according to the review article of Xiong et al. [155]. It can be seen that each category contains different methods as illustrated in Figure 4-1. The characteristic and limits of each approach are described below.

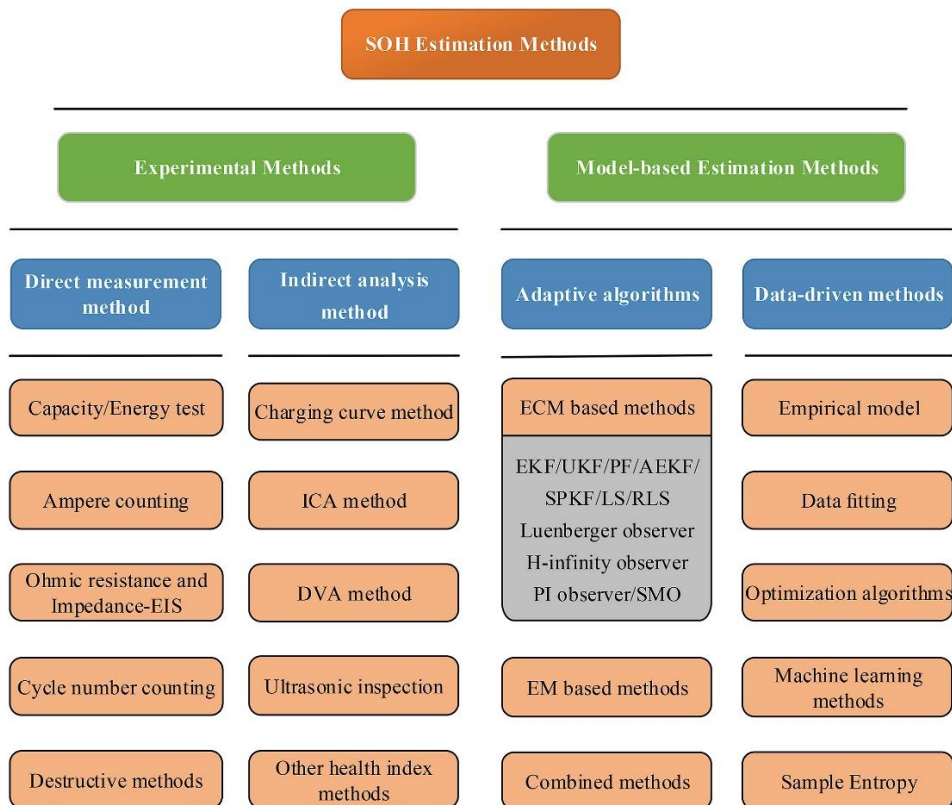


Figure 4-1 Classification of battery SOH estimations method [155]

4.2.1 Experimental methods

In the category of experimental methods, the direct measurement method requires physical information of the battery from off-line measurement, such as the capacity or energy (Capacity/Energy test, Ampere counting) internal resistance or impedance over time. Low computational effort is needed, but high-accuracy equipment is required; thus, the integration in the Battery Management System (BMS) is difficult [154] [156] [157] [158]. Regarding the cycle number counting, Wang et al. [158] proposed a cycle life model based on a semi-empirical approach for predicting the evolution of the capacity of a lithium-ion cell based on an iron phosphate (LFP) cathode. A large test matrix, including the temperature, Depth Of Discharge (DOD), discharge current, and duration of cycling, was applied. They reported a function that could predict the capacity loss according to the temperature, DOD, current rate, and ampere hour throughput. However, this semi-empirical model requires a large amount of experimental tests, which provide the capacity evolution over time in different operating conditions. Moreover, the obtained ageing law must be validated in a lower temperature range. Besides this, the destructive methods include the Raman spectroscopy, X-Ray Diffraction (XRD) and Scanning Electron Microscope (SEM). These methods are able to detect directly the ageing mechanisms at the microscopic scale [158]. However, the electrochemical elements are usually completely disassembly.

The indirect analysis method are based on the analysis and processing for SOH related parameter. For charging curve method, Eddahech et al. [159] investigated a method to determine the SOH of Li-ion cell by tracking the leakage current during CV charge phase. In addition to this, Dubarry et al. investigated the incremental capacity analysis (ICA) based on the quasi-equilibrium OCV to evaluate the capacity fading for commercial lithium batteries for the first time [33]. These methods highlight the capacity fading due to different degradation modes [33] [34] [160] [161]. Ultrasonic inspection is used to detect some kinds of minor defects inside the cells during battery ageing [155]. Other health index such as the cell OCV [31], stress evolution [162] [163] [164], thickness changes [165] [166] and gas generation [167] can be found in several literatures. Sauer et al. studied the dependency of the OCV on SOH for various lithium-ion battery chemistries (NMC/graphite, LFP/graphite, and NMC/LTO) [11]. They focused on the battery relaxation behaviour at different temperatures and SOHs. It was found that the relaxation time increased with the decrease of the temperature and SOC; moreover, the OCV changed over the battery lifetime. A simple OCV model based on the SOC, temperature and SOH was proposed. However, they neglected the OCV variation between individual cells. As the OCV curve of the LFP/C battery is flat, a slight difference of the OCV between cells can lead to significant errors in the SOH estimation.

4.2.2 Model-based estimation methods

Adaptive algorithms and data-drive methods are both in the category of model-based estimation. The method based on adaptive approaches can identify and adapt the battery model parameters in real time, ensuring a high accuracy for SOH estimation. However, the high computational requirements and the complexity of the algorithms limit the lifetime prediction [156] [157].

ECM has been widely applied for SOH estimation. Based on the battery model, the identification of parameters such as OCV, internal resistance, capacitor is achieved by adaptive filtering. [168] The Extended Kalman Filters (EKF) can accurately estimate the SOH, however there are potential issues due to the poor physical and chemical meanings for ageing mechanisms. Electrochemical Model (EM) based methods used a series of differential equations to simulate the particle behaviours in the batteries [169]. But, multiple parameters (diffusion coefficient, particle size, ionic conductivity) need to be provided for the model implementation and these parameters, which depends on the manufacturer that are not always available.

The main concept of data-drive methods is focused on the large experimental data collection without the elements working principles knowledge and an explicit model. However, high requirements on the algorithm is needed. Furthermore, the accuracy of these models depends on the size of database.

4.3 Principles of Incremental Capacity Analysis

After the overview of multiple SOH estimation methods, the ICA methods are selected for several reasons. Firstly, the obtained ageing results are based on the generic ageing tests, only depends on temperature, current, SOC, DOD are not be considered in the ageing tests. Therefore, the semi-empiric approach seems difficult to establish. Secondly, the ICA methods can be used to study ageing mechanisms in real time, which could be implanted in a BMS. Thirdly, according a lot of literatures, this method can indicate the degradation modes thanks to the peak features of the IC curve. There is a strong physical and chemical signification compared to the data-driven methods. Furthermore, the continuous discharge from check-up at 25°C can be directly used for ICA investigation.

The incremental capacity (IC) is defined by equation (4.1), where Q is the discharged capacity or charged capacity, and V is the voltage of the cell during discharging and charging. In practice, continuous discharging or charging with a small constant current ($C/25$) is applied to determine the IC [33]. By analogy with the IC, the differential voltage (DV) can be determined using Equation (4.2). The IC is always plotted with respect to the voltage, whereas the DV is plotted with respect to the capacity.

$$IC = \frac{dQ}{dV} = I \times \frac{\Delta t}{\Delta V} \quad (4.1)$$

$$DV = \frac{dV}{dQ} = \frac{\Delta V}{I \times \Delta t} \quad (4.2)$$

According to literatures, the qualitative and quantitative IC/DV Analysis (ICA/DVA) are widely investigated. Han et al. [142] identified the origins of degradation for a LTO-based cell. The cells were cycled at 55°C with a charge current of 3C and a discharge current of 2C. In the first stage, the capacity fading was mainly due to the degradation of the anode material. In the second stage, the decrease of the capacity was mainly caused by the loss of cathode materials. Two stages of ageing were detected by using the ICA and DVA methods that highlighted the differences of degradation. However, the analysis of the peak features via the two methods with ageing is just qualitative.

In contrast to the qualitative ICA, Weng et al. [170] proposed an OCV-SOC model based on ICA for SOH estimation for an LFP cells. Instead of directly using the OCV-SOC obtained via charging or discharging from experimental data, their OCV-SOC curve was based on the average charging and discharging curve at C/20; moreover, the curve was fitted by a sigmoid function. This strategy allows to reduce the noise of the OCV-SOC measurement, which can be amplified by the derivative term in equation (4.1). A series of IC curves were used to examine the cell SOH variation during a power cycling ageing test at different temperatures (35, 22, and 10°C).

To increase the accuracy of the methods based on fitting by a mathematical function, Riviere et al. applied a low-pass Butterworth filter to reduce the measurement noise [171]. This filter uses experimental data and appears to be insensitive to the SOC range. Therefore, three peaks were detected on the IC curves for the LFP cell, compared with the two peaks in the study of Weng [170]. Riviere et al. observed that the area of a peak decreased linearly with the SOH. However, ICA is based on a charged curve at C/3.

Recently, Li et al. [172] proposed an on-line method for estimating the SOH of NMC cells via ICA. They proposed using a Gaussian filter to smooth the charge curve for obtaining clear IC curves; then, a linear dependency was observed between the peak features on the IC curves and the cell SOH. Moreover, a multi-stage SOH identification method was investigated, which depends on the initial SOC. It was shown that ICA based on a charging curve for 60% SOC cannot detect the peak features. However, 60% SOC does not correspond to the same amount of ampere hours between a fresh cell and an aged cell, it appears to be difficult to define the “60% SOC” before evaluating an unknown-SOH cell.

According to the quick literature review, the ICA approach can be widely applied to different lithium-ion battery chemistries, such as LFP/graphite [173], NMC/graphite (as presented by Yang et al. [174]), and NMC/LTO [142]. Tracking the evolution of the peak features is an efficient method for qualifying and quantifying the lithium-ion battery SOH [175]. However, few studies have investigated a method for estimating the historical ageing that a Li-ion cell has undergone and estimating its normalized resistance.

4.4 Raw tests results for qualitative and quantitative ICA study

As the matrix of ageing results is large, only the results of check-up at 25°C with 50 days period under all ageing types are used in this chapter to investigate the qualitative and quantitative ICA. The evolution of the normalised capacity and resistance over time are depicted in Figure 4-2 for LG and Samsung. Figure 4-2 (a, a') show the normalized capacity and resistance, respectively, for LG. For calendar ageing, a high temperature causes a loss of capacity. When the storage temperature is high, side reactions involving the dissolution of the active material occur [176], leading to significant capacity loss.

Under power cycling ageing tests at 0°C, the capacity loss reached 75% after 26 days, which corresponds to 638 full cycles. Under power cycling ageing tests at 45°C, the capacity loss reached 40% after 180 days, which corresponds to 3556 full cycles. Ecker et al. [177] reported that a low temperature could slow the diffusion process owing to the decrease of the

reaction kinetic, which introduces a reduction of the anode potential during charging. This behaviour gives rise to lithium plating; therefore, lithium is scarce.

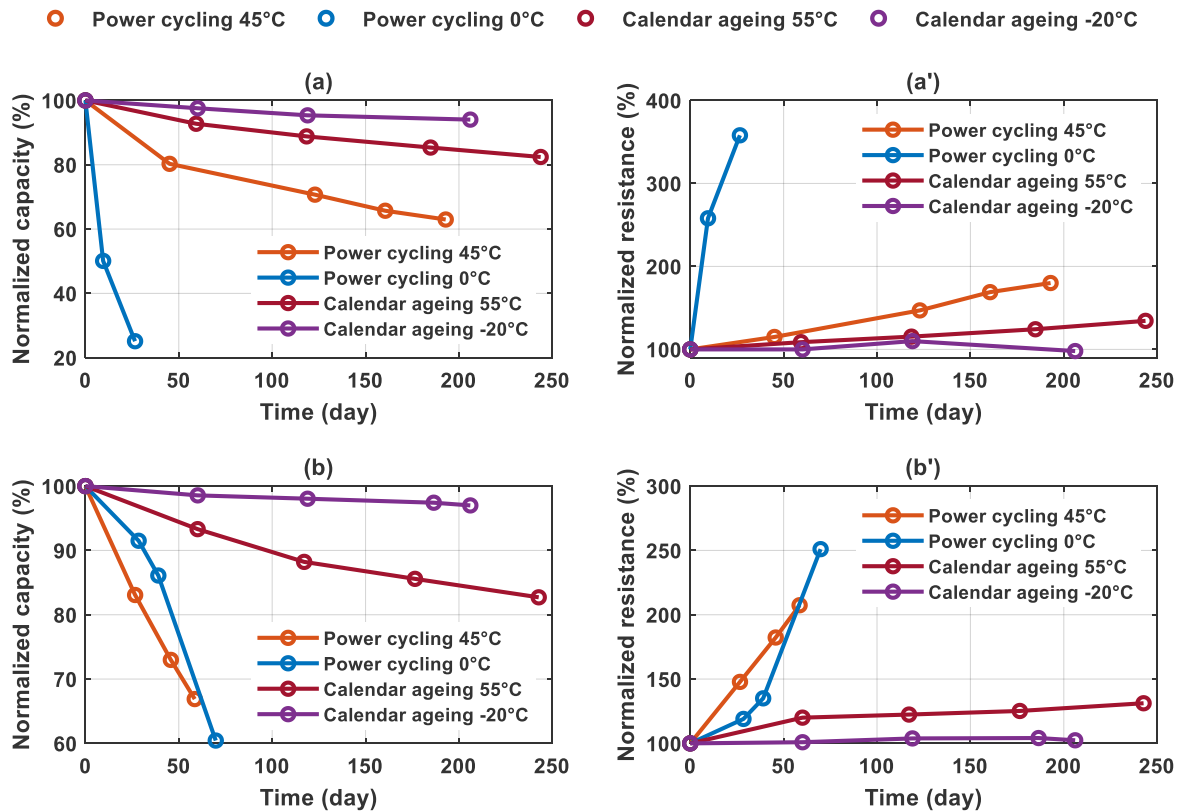


Figure 4-2 Normalized capacity and normalized resistance at 50% SOC at 25°C for (a, a') LG and (b, b') Samsung

The normalized capacity and resistance for Samsung are presented in Figure 4 2 (b, b'), respectively. Samsung exhibited the same behaviour as LG for calendar ageing, and it lost more capacity at 55°C than at -20°C. However, for power cycling, Samsung exhibited similar behaviour at 0 and 45 °C. The capacity loss was approximately 35% after 59 days (938 full cycles) at 45 °C and approximately 40% after 70 days (1,574 full cycles) at 0°C.

For both technologies, the capacity loss exhibited the same tendency as the resistance increase, except in the case of calendar ageing at -20 °C, where the resistance variations were very small and sensitive to measurement inaccuracies.

4.5 Enhanced IC by moving average filter

Before applying the ICA, it can be seen from Figure 4-3 (a) that the direct use of experimental data brings a lot of noise on IC curve for LG cell at C/20 at the BOL. A moving average (MA) filter is applied on the voltage measurement to get a clear curve for dQ/dV vs. voltage. The MA filter is determined in equation (4.3), where N is the number of samples in the average window, V_{ji} is the measurement voltage and \bar{V}_j is the smooth voltage.

$$\bar{V}_j = \frac{1}{N} \sum_{i=0}^{N-1} V_{j-i} \quad (4.3)$$

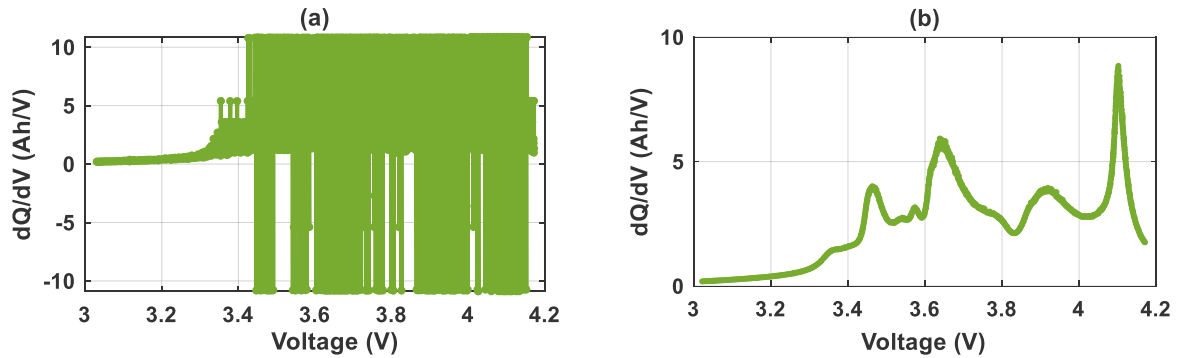


Figure 4-3 IC curves for LG cell at C/20 at the BOL based on (a) experimental data (b) MA filter smoothing

In our study, 10mV is selected as the voltage sampling for discharge curves at C/20, N is equal to 100. The smooth IC curve obtained thanks to MA filter is shown in Figure 4-3 (b). Clear peaks appear on IC curve, which insures the qualification and quantification of ICA. The root-mean-square deviation of voltage remains below 0.05% with MA filter.

4.6 ICA study

4.6.1 Current influence on ICA

Although IC curves are usually obtained from a charge/discharge curve for very small current, such as C/25 [33], a higher current rate can be applied to save time for on-board applications [170] [171]. In this study, check-up was performed with C/2 for LG and 1C for Samsung. For evaluating the effect of the current on ICA, Figure 4-4 presents the discharge curves and the corresponding IC curves at different current rates (C/20, C/10, C/5, C/3, C/2, 1C) from the initial characterisation for LG and Samsung at the BOL. The voltage was recorded with a sampling step of either 10s or 1mV to ensure that no information was missing in the discharge curves [172]. The clear IC curves are obtained thanks to the enhanced MA filter. The number of points for the average was adapted to each current regime so that the root-mean-square deviation of the voltage remained below 0.08%.

The IC curves in Figure 4-4 (a) and (b) show several peaks from 3 to 4.2 V for both technologies at all current rates. These peaks represent the convolution of one reaction at the negative electrode and another reaction at the positive electrode [33] [34] [109]. The shape of the IC curves is similar between technologies LG and Samsung, because they have a similar anode and the same crystal structure of the cathode (layered). However, the amplitudes of these peaks differ owing to the capacity difference.

For both technologies, a drift to the right is observed in the IC curves with the increase of current, which is due to the polarization resistance [160]. The location of peak 1 was tracked to quantify this resistance, as this peak is located at the beginning of the discharging, where the cell has a similar SOC. Peak 1 regularly shifted towards the lower voltages with the increase of the current. Figure 4-5 (a, b) shows the location of peak 1 at different C rates for LG and Samsung. A linear relationship is observed between the voltage and the current rate. The polarization resistance can be determined by the corresponding slope: it was 41.7 m Ω for LG and 64.8 m Ω for Samsung. According to Dubarry et al., the linearity between the voltage and

current occurs when the applied current is $<1C$, owing to the Tafel behaviour in the ohmic zone [160]. Additionally, it can be observed that the number of peaks depends on the current rate, each peak corresponds to a complex reaction, and the quantification of the peak position, amplitude, or area directly using the IC curves in a high-current regime appears unreliable.

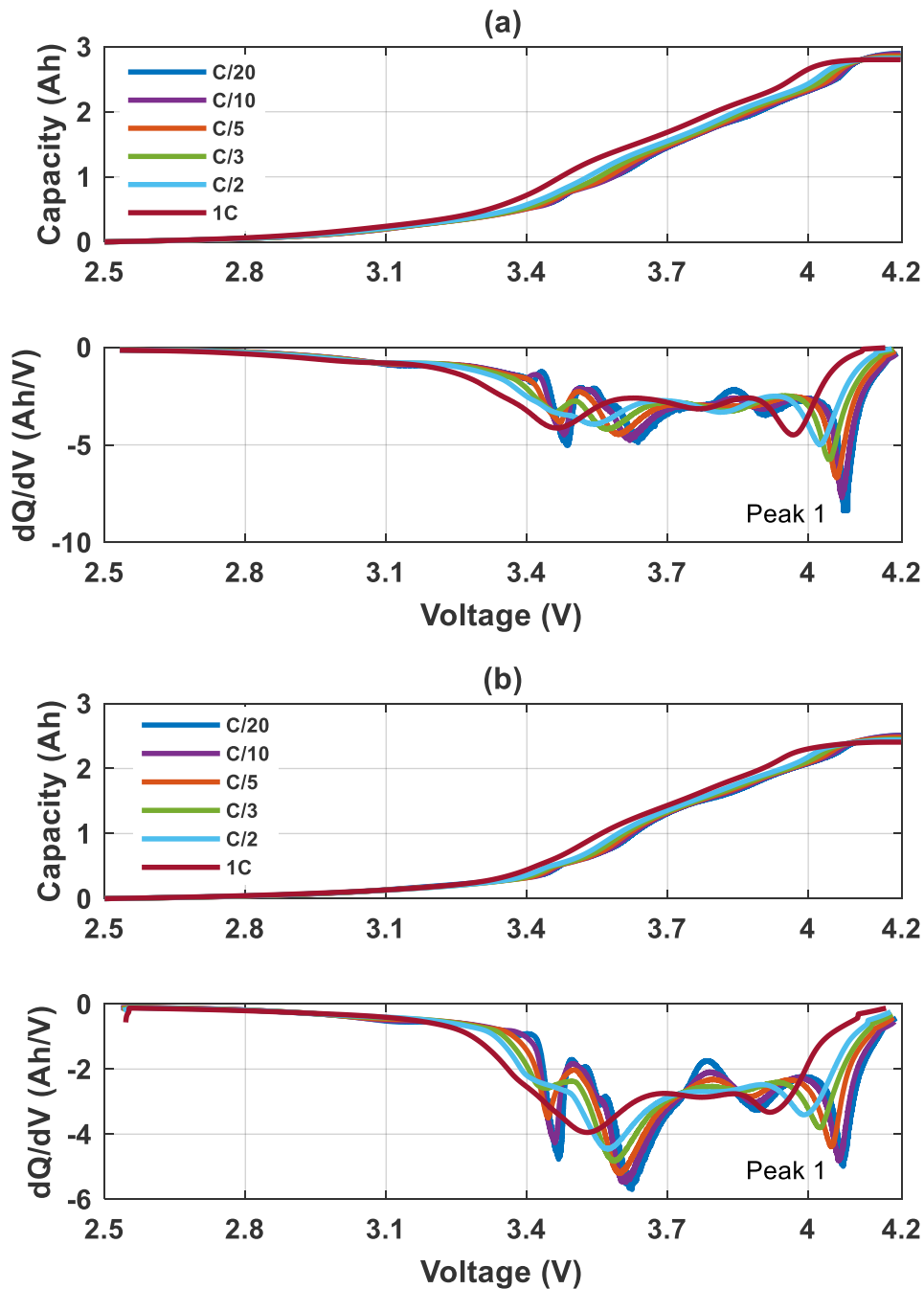


Figure 4-4 Discharge curves at C/20, C/10, C/5, C/3, C/2 and 1C with the corresponding IC curves for (a) LG and (b) Samsung

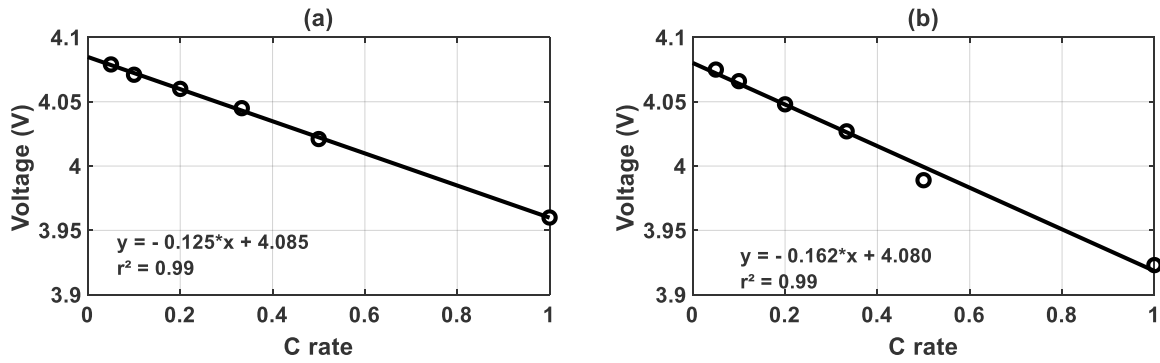


Figure 4-5 Location of peak 1 at different C rates for (a) LG and (b) Samsung

4.6.2 Qualitative influence of different ageing types on ICA

Figure 4-6 and Figure 4-7 present the IC based on the discharge curve during check-up at 25 °C for each ageing type for LG and Samsung, where the normalized capacity and resistance correspond to the data points in Figure 4-2. First, it can be observed that all the IC curves at the BOL have the same shape for the same technology, which indicates good consistency between the cells. Second, the evolution of the IC curve according to the ageing duration or number of cycles depends strongly on the ageing test, because various ageing tests lead to different degradation modes.

Dubarry et al. [178] built a diagnostic and prognostic model based on the voltage curve of a half-cell. They defined two parameters, which are directly linked to specific degradation mechanisms. In our study, the voltage curves of the separated electrode were not accessible. Therefore, the identification of the degradation mode was based on the study of Feng et al. [179]. Their model links the changes of the IC curve with the different degradation modes for a whole cell.

As shown in Figure 4-6 (a, b), the comparison of the IC curves for calendar ageing at 55 and -20°C for LG reveals that peak 2 maintains the same location and amplitude under both ageing conditions, and the amplitude of peak 3 decreases with ageing, where the variation is significant at 55 °C than at -20 °C. This may be due to the LAM degradation mode reported by Feng et al. [179]. Peak 1 shifts towards the low voltages only for calendar ageing at 55°C, owing to the increase of the internal resistance [160] [180].

For the power cycling ageing test at 45°C, the amplitude of peak 2 decreased with increasing cycles at the same location, because of the LLI, in accordance with [100] [179] [178]. Moreover, significant amplitude reductions of peaks 3 and 1 accompanying a voltage shift to the left are observed in Figure 4-6 (c), which correspond to the LAM [179]. Concerning the power cycling at 0 °C in Figure 4-6 (d), peaks 2 and 3 disappeared in the IC curve with increasing cycles. Instead of these peaks, a plateau is observed. This behaviour is similar to that reported by Feng et al. [179], which may be due to the LLI. Although the evaluation of the peak features in the IC curve can be identified with the literature, a post-mortem analysis is recommended to verify the degradation modes.

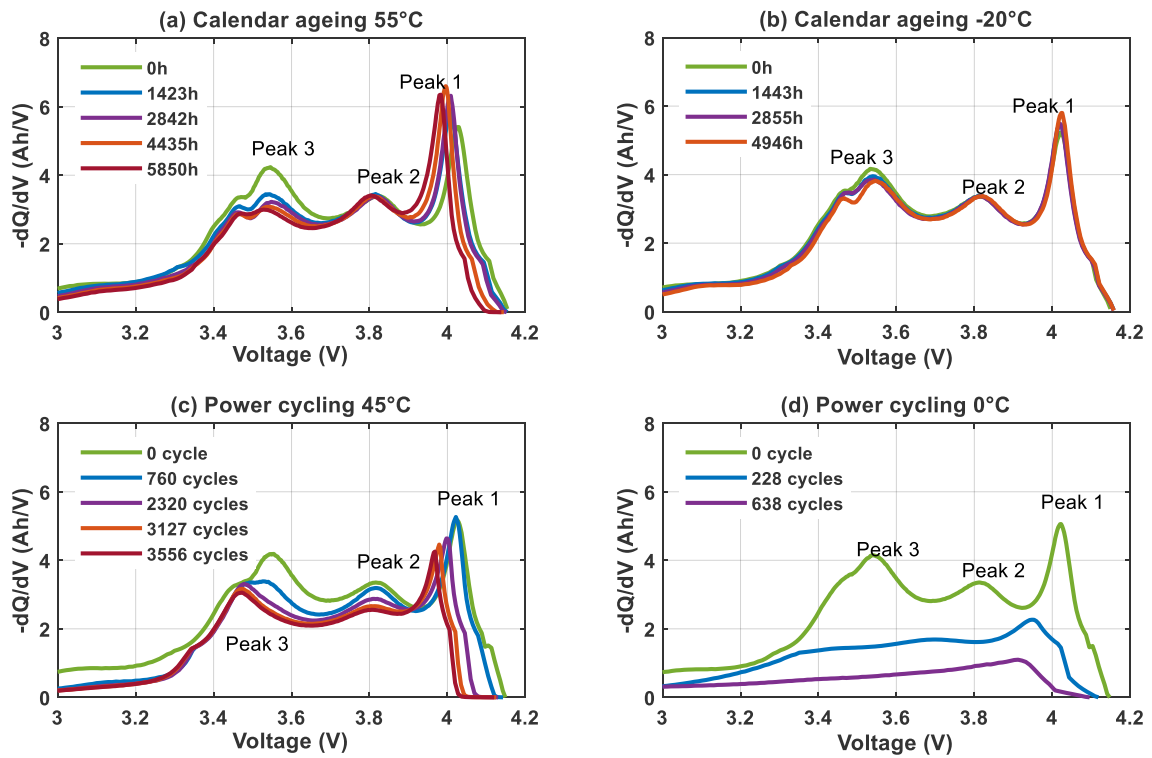


Figure 4-6 IC based on the discharge curves for check-up at 25°C for LG

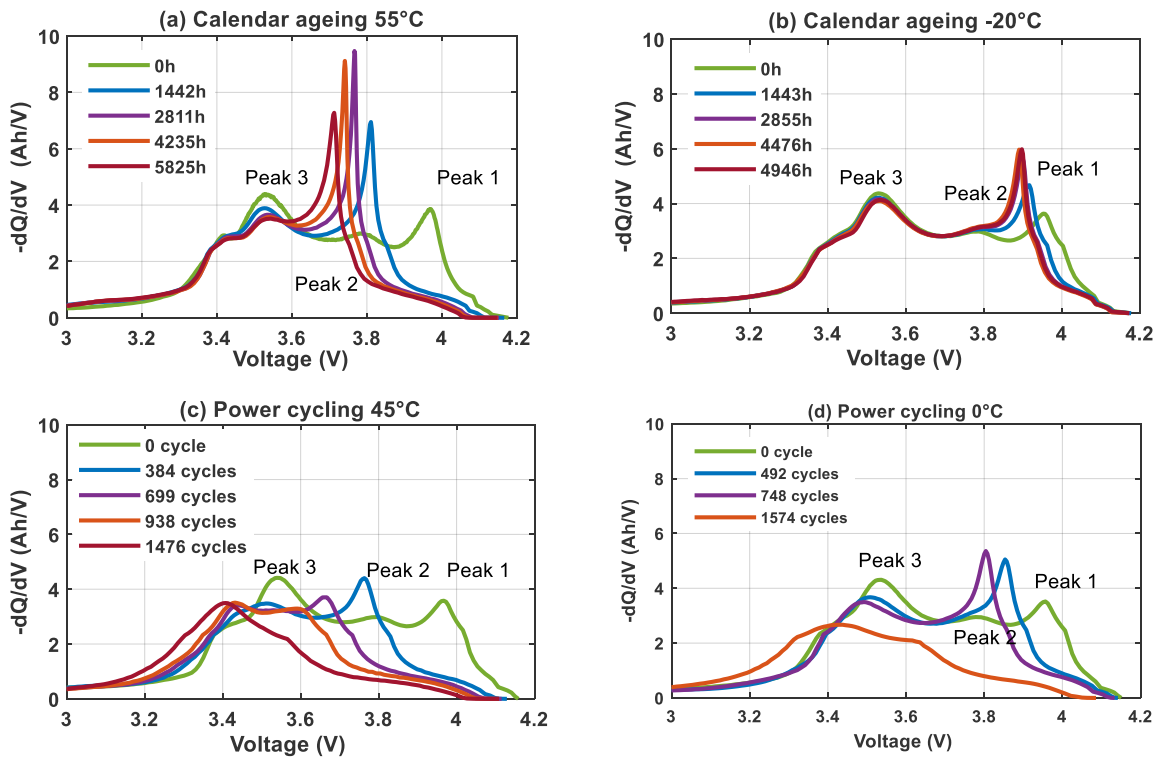


Figure 4-7 IC based on the discharge curves for check-up at 25°C for Samsung

Figure 4-7 (a–d) present the IC curves for Samsung under different types of ageing. All the IC curves at the BOL have three peaks, but the peak evolution is not as clear as expected. Peak 1 shifts to the left gradually, owing to the increase of the polarization resistance [34]. Moreover, peaks can disappear from the IC curves after the ageing test [181]. Therefore, a new and efficient method for quantifying the features on these IC curves must be developed.

4.6.3 Decomposition of IC curves based on Gaussian Lorentzian mixed function

Inspired by the XPS analysis, the IC curves can be decomposed into several independent spectra, each of which contains only one peak. XPS is a quantitative spectroscopic technique that is used to determine the chemical element composition, chemical state, electronic state and homogeneity of materials. In the case of a battery, the IC curves appear as XPS spectra and the decomposition of the IC curves can be performed to quantify the peak features.

Zhang et al. [182] used the Lorentzian function to fit the IC curves of lithium-ion batteries with different chemistries (such as LFP, LTO, and NMC) and reported an error of < 4% between the experiments and curve fitting. However, only two different ageing states were demonstrated with Lorentzian function fitting; thus, the rules governing the evolution of the peak features with different types of ageing have not been established.

To investigate the dependency between the normalized capacity/resistance and the fitting parameters for different ageing types, the IC curves based on the discharge curve from check-up were fitted by a Gaussian Lorentzian mixed function. This function is expressed by equation (4.4), where n is the peak number, A_i is the area under the peak with index i , V_{0i} is the centre location of the peak, ω_i is the half-width of each peak, and c_1 is the percentage of the Lorentzian shape [33]. The Gaussian Lorentzian mixed function is proposed to fit the IC curve throughout the whole lifespan for both technologies. For both technologies, there are three peaks on the IC curve at the BOL.

$$\frac{dQ}{dV} = (1 - c_1) \sum_{i=1}^n \frac{A_i}{\omega_i \times \sqrt{\frac{\pi}{2}}} e^{(-2 \times (\frac{V - V_{0i}}{\omega_i})^2)} + c_1 \sum_{i=1}^n \frac{2 \times A_i}{\pi} \times \frac{\omega_i}{4(V - V_{0i})^2 + \omega^2} \quad (4.4)$$

Figure 4-8 presents the decomposition of the IC curves based on the Gaussian Lorentzian mixed function and the corresponding residual for (a) LG and (b) Samsung at the BOL. The IC curves can be decomposed into three individual spectra. The residual of the experiment and fitting data is between -0.4 and 0.4 Ah/V in the voltage interval, which appears to be small.

This function provides a good fit for the IC curve at not only the BOL but also the EOT. For both technologies, the maximal capacity loss occurred in the power cycling ageing tests. Figure 4-8 (a) presents the decomposition of the IC curve after 638 cycles at 0 °C for LG. Figure 4-8 (b) presents the decomposition of the IC curve after 1,476 cycles at 45 °C for Samsung. Good accuracy is observed at the extreme ageing states (BOL and EOT) for both technologies.

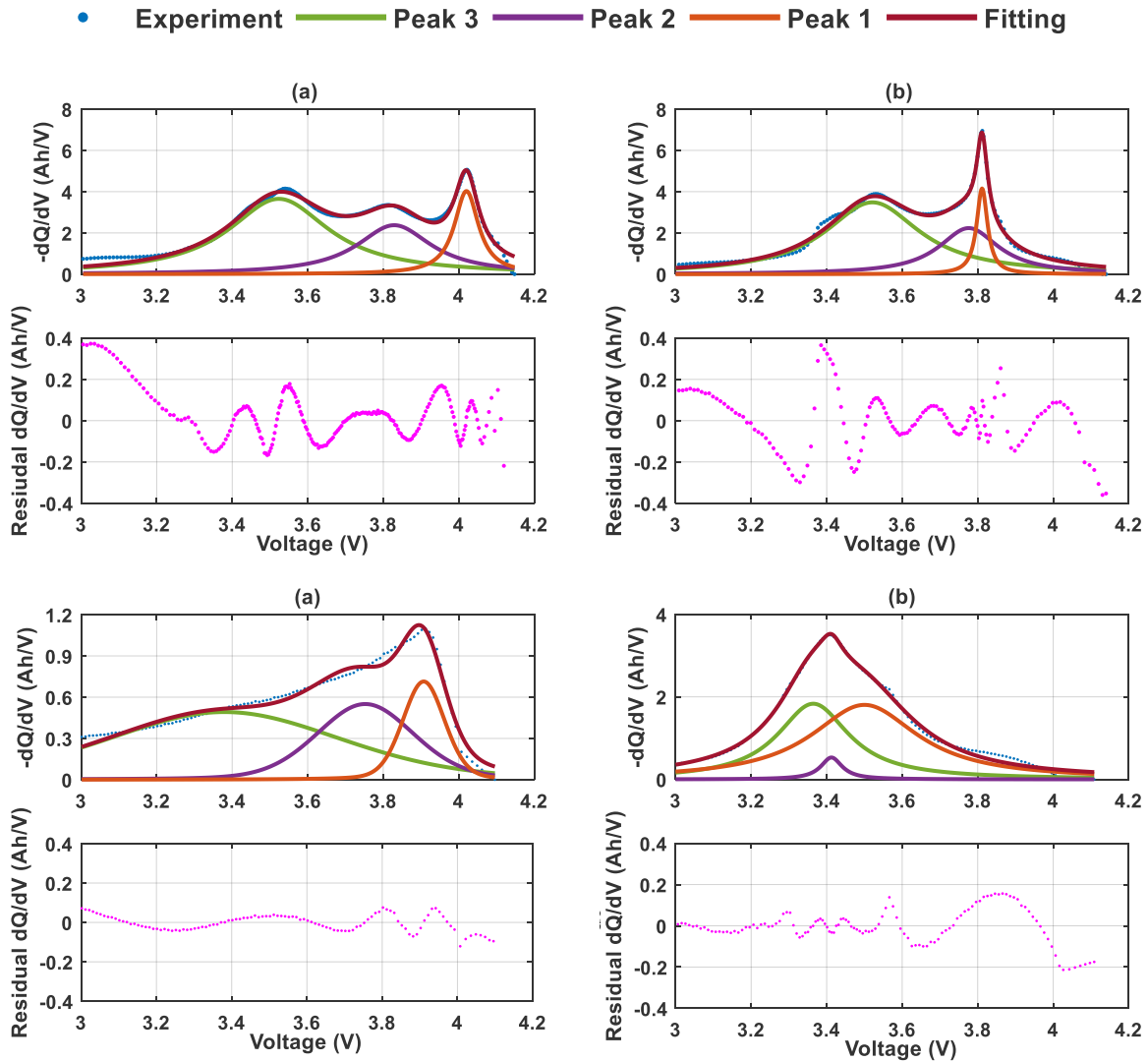


Figure 4-8 Decomposition of the IC curve based on the Gaussian Lorentzian function at the EOL for (a) LG and (b) Samsung

4.6.4 Peak features with respect to normalized capacity and normalized resistance

The parameters fitted by the Gaussian Lorentzian mixed function could have a dependency on the normalised capacity and the normalised resistance. The area under each peak in the IC curve represents the capacity implied in the related reaction, which could be linked to the normalised capacity. To establish this dependency, the area under peak 3 is selected. Because Feng et al. [179] indicated that the integrated area under peak 3 was helpful for establishing a quantitative relationship with the battery SOH for the NMC chemistry cell. The increase of the polarisation resistance always follows a shift to the left of peak 1 [34] [178] [183], therefore, a relationship can be established between the normalised resistance and the location of peak 1.

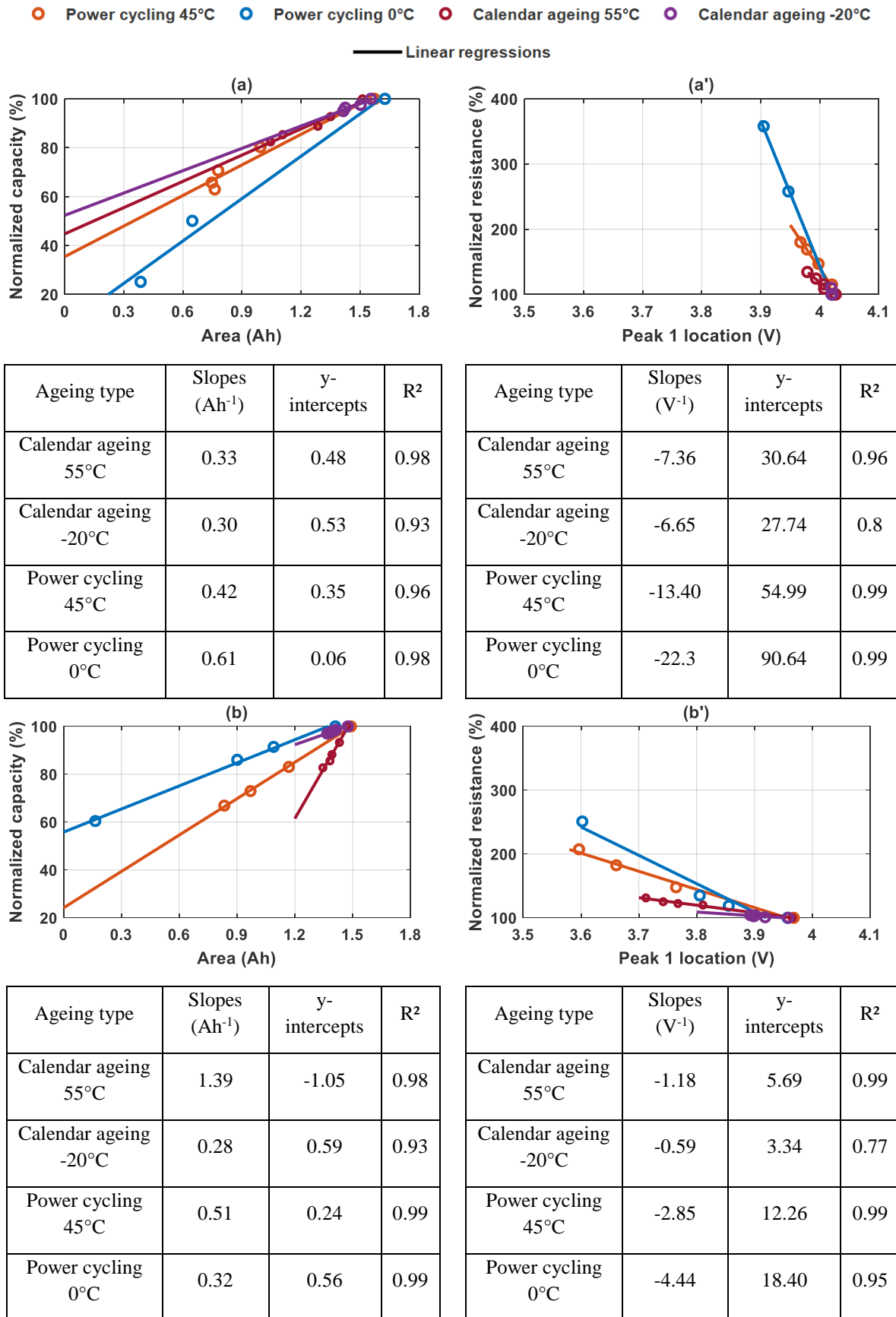


Figure 4-9 Normalized capacity vs. the area under peak 3 (left) and normalized resistance vs. the location of peak 1 (right) at 25°C for (a, a') LG and (b, b') for Samsung with the corresponding fitting parameters for several ageing types

To ensure better visibility of the fitted IC curves, only the dependency is illustrated in Figure 4-8. The complete list of the peak features and the corresponding values are presented in Annexe 3 and 4 respectively.

Figure 4-9 (a, b) presents the dependency between the normalised capacity and the area under peak 3 for technologies LG and Samsung, and Figure 4-9 (a', b') show the dependency between the location of peak 1 and the normalised resistance. Linear correlations are observed for both ageing types and technologies. The slopes, y-intercepts and regression coefficients (R^2) are listed in the corresponding tables. All the regression coefficients are close to 1, indicating linear dependency. These dependencies for all ageing types over the whole lifespan can provide historical ageing information and help us to estimate the resistance for unknown-SOH cells.

4.6.5 Method validation for cells with unknown SOH

To determine the type of ageing that has been imposed previously and to estimate the normalised resistance, two cells of each technology with an unknown SOH were discharged at a current of 1C. The decomposition of the IC curves based on the Gaussian Lorentzian mixed function is shown in Figure 4-10.

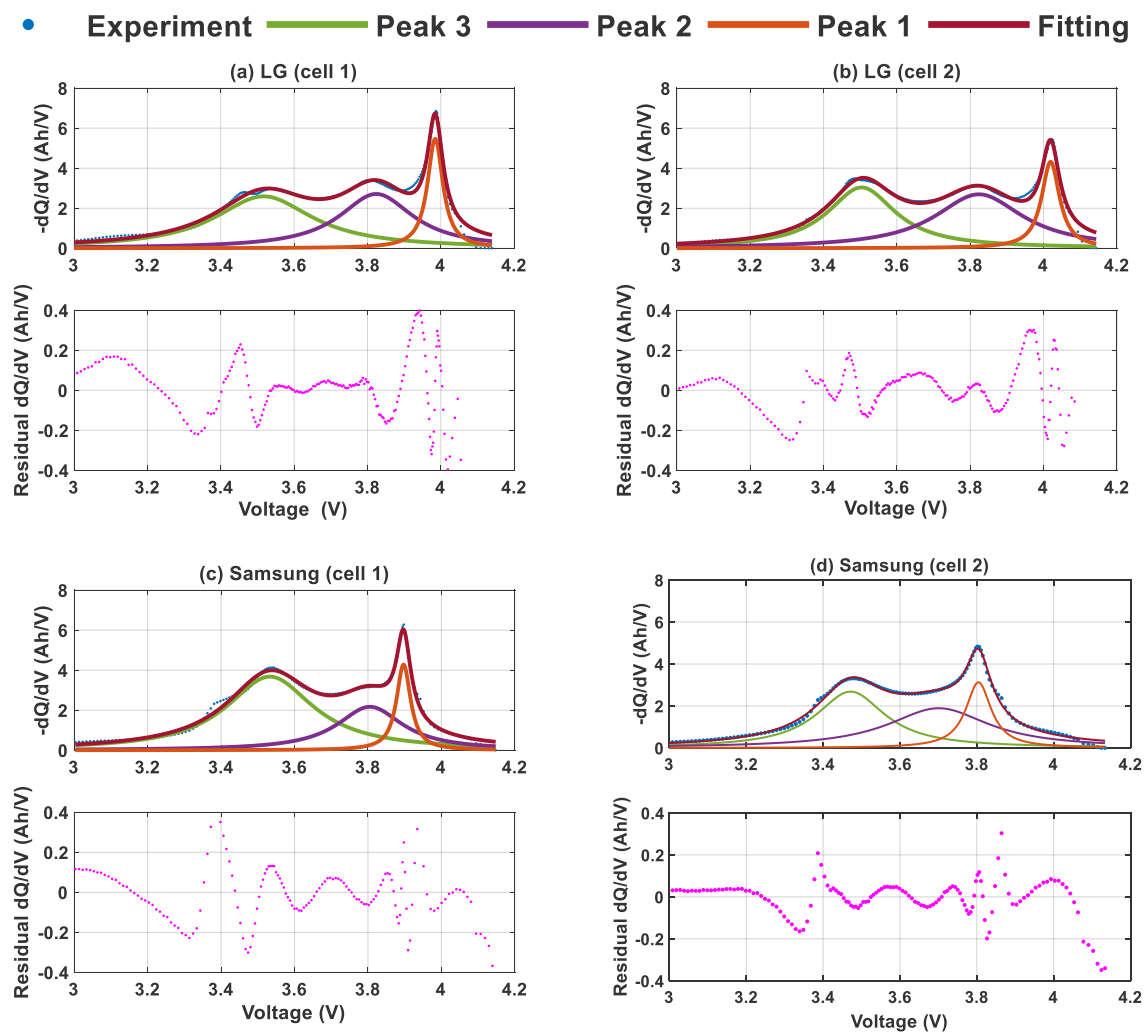


Figure 4-10 Decomposition of the IC curve based on Gaussian Lorentzian function for (a, b) two cells of LG, (c, d) two cells of Samsung

The Gaussian Lorentzian mixed function provided a good fit for all the IC curves for all the unknown-SOH cells, and the term dQ/dV had a small residual in the voltage interval. Moreover, the normalized capacity obtained via 1C discharge and the area under peak 3 obtained via the decomposition of the IC curve can be put into the corresponding Figure 4-10 (a–c) for technologies LG and Samsung. For each cell, the type of ageing that the battery has historically undergone can be identified according to the previously established linear regressions.

	LG (cell 1)	LG (cell 2)	Samsung (cell 1)	Samsung (cell 2)
Normalized capacity (%)	82.3	79.1	98.6	82.7
Area under peak 3 (Ah)	1.10	0.95	1.40	0.81
Ageing type that the cell has historically undergone	Calendar ageing at 55°C + Power cycling at 45°C	Calendar ageing at 55°C	Calendar ageing at -20°C	Power cycling at 0°C + calendar ageing at -20°C
Location of peak 1 (V)	3.98	4.02	3.9	3.80
Estimated normalized resistance (%)	131	113	104	142
Measured normalized resistance (%)	134	120	102	141
Error of normalized resistance (%)	3	7	2	1

Table 4-1 Normalized capacity and fitted parameters for cells with an unknown SOH

As shown in Table 4-1, the values of the normalized capacity and the area under peak 3 for LG (cell 1) are between the linear regressions of calendar ageing at 55°C and power cycling at 45 °C. We can assume that the cell suffered this combination of ageing types, and the normalized resistance can be estimated by using the average linear regressions of the calendar ageing at 55 °C and power cycling at 45 °C in Figure 4-10 (b). In the case of cell 2 for LG, these values are located exactly on the linear regression of calendar ageing at 55°C; therefore, this cell may have suffered from calendar ageing at 55°C. Then, the estimated normalized resistance can be obtained directly with the corresponding linear regression.

The same method is applied for Samsung. It can be found that cell 1 (Samsung) suffered calendar ageing at -20 °C, while cell 2 (Samsung) suffered from a combination of ageing modes at a low temperature (power cycling at 0°C and calendar ageing at -20°C). Overall, the error between the estimated normalised resistance and the measured normalised resistance is <5%.

A diagram in Figure 4-11 illustrates the proposed method for estimating which types of ageing a Li-ion cell has undergone historically and estimating the normalized resistance. First, the cell is discharged at a current of C/2 or 1C, and then a decomposition of the IC curve obtained using the Gaussian Lorentzian mixed function is employed to extract the peak features after applying an MA filter. Subsequently, the ageing type can be identified with the normalized capacity and the area under peak 3 according to the linear regression. Finally, the normalized resistance can be estimated with the identification of the ageing type and the peak 1 thanks to the corresponding linear regression.

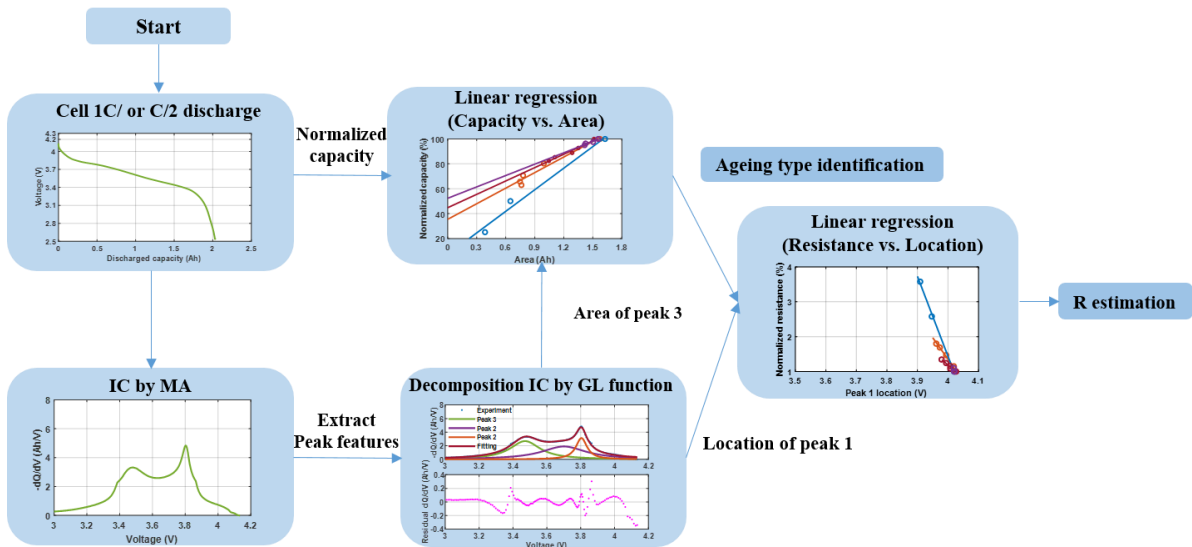


Figure 4-11 Illustration of the proposed method for determining the ageing type and resistance of a cell with unknown SOH

4.7 Conclusion

Mastering the performance evaluation to predict the SOH of electrochemical energy storage elements is essential for the practical application. In this chapter, an efficient SOH estimation is investigated based on the qualitative and quantitative ICA for the two most promising technologies: NMC/graphite+SiO Li-ion cells from LG and NCA/graphite Li-ion cells from Samsung.

At first, an overview of SOH estimation methods are presented according to the latest literatures. ICA method displays several advantages in our case: the simplicity for establishing SOH estimation with the experimental ageing results; the good physical-chemical signification of degradation modes linked with the two ageing types (calendar ageing, power cycling ageing); the on-line characteristic gives the possibilities to implementer in BMS application. Thus, ICA method is selected for SOH estimation. However, a lot of studies focused on the qualitative ICA, which highlighted the different ageing mechanisms. Few studies investigated the evolution of capacity and internal resistance with the quantitative ICA.

For this, an efficient method for not only revealing which ageing types a cell has endured historically but also estimating the normalized resistance for an unknown-SOH Li-ion cell is

investigated. Various possible ageing mechanisms are identified according to a qualitative ICA over the whole lifespan. Moreover, we observed that the current can influence the shape of the IC curve: the amplitude, area, and location of the peak features on the IC curve are difficult to extract, especially at a high current level. Therefore, an enhanced Gaussian Lorentzian mixed function is proposed to fit the IC curves throughout all ageing states with a high accuracy under a current of $C/2$ or $1C$ for both technologies. A simple linear dependency is observed between the area of peak 3 and the normalized capacity, and another linear regression is observed between the location of peak 1 and the normalized resistance. The proposed method is suitable for estimating which type of ageing the cell has historically undergone, as well as the normalized resistance.

Chapter 5

Experiments and modelling of accelerated ageing with a specific aeronautical profile

Table of contents

5.1 Introduction	115
5.2 Design of the accelerated ageing tests	115
5.2.1. Proposed aeronautical profile	116
5.2.2. Characteristics of accelerated ageing tests	118
5.3 Experiments and raw results	119
5.4 Ageing modelling and SOH estimation	121
5.4.1. Temperature effects on the degradation rate of capacity	121
5.4.2. SOH estimation	123
5.4.2.1 Qualitative and quantitative ICA	123
5.4.2.2 Validation of the proposed method	126
5.5 Conclusion	127

5.1 Introduction

In this chapter, the study of accelerated ageing tests with a specific aeronautical profile is investigated for the two most promising technologies: NMC/graphite+SiO cell from LG and NCA/graphite cell from Samsung. For this, a specific aeronautical profile is firstly established at different temperature conditions (0°C, 25°C, 45°C). Then the raw experimental results are compared and analysed. Finally, two different modelling methods are developed to investigate the temperature effects on degradation rate and to estimate the SOH of aged Li-ion cells.

5.2 Design of the accelerated ageing tests

As indicated in chapter 3, the energy density, power density, lifespan and safety of LG and Samsung are outstanding compared to the other investigated electrochemical energy

storage elements, it seems necessary to evaluate their robustness under an aeronautical profile. So, a specific aeronautical profile must be established at the first. Then, the Li-ion cells are endured with this specific aeronautical profile at different temperatures (0°C, 25°C, 45°C).

5.2.1 Proposed aeronautical profile

To date, there has been few studies published on aircraft mission profile for a civil electrical aircraft [184]. Thereby, the proposed aeronautical profile is based on the typical aircraft mission profile, including the flight mission phases: Auxiliary Power Unit (APU) start, Taxiing, Take-off, Cruise, Landing, Towing, Refuel and Recovery for an air travel in metropolitan France. Furthermore, it must be insured that the LiBs would age by enduring this profile with a moderate duration.

The specific aeronautical profile is for a domestic flight mission in metropolitan France, therefore the flight duration is fixed to less than 2 hours. Next, this profile must contain all the previously listed phases and the current/power levels must be defined in each of them. For this, the endured current level can be referred to the Li-ion battery capacity of 45Ah installed in A350 XWB. However, the proposed aeronautical profile is designed for 18650 Li-ion cells, thus a current level conversion is performed at cell scale. In fact, the Li-ion battery in the A350 XWB to start the APU provides three times 15kW triangular power pulses of 15s duration as shown in Figure 5-1 (a). As the terminal voltage of the battery is 28V, the current rate is approximately of 12C. Since the LG and Samsung cells have a similar voltage as the cells used in the 45Ah battery, the current rate at cell scale would also be 12C. But, for experimental facility reasons, the cells can only be tested at a maximum of 15A because of the cell holder maximal capabilities. Finally, instead of a triangular shape, a rectangular one with half magnitude of 6C is rather considered as depicted in Figure 5-1 (b).

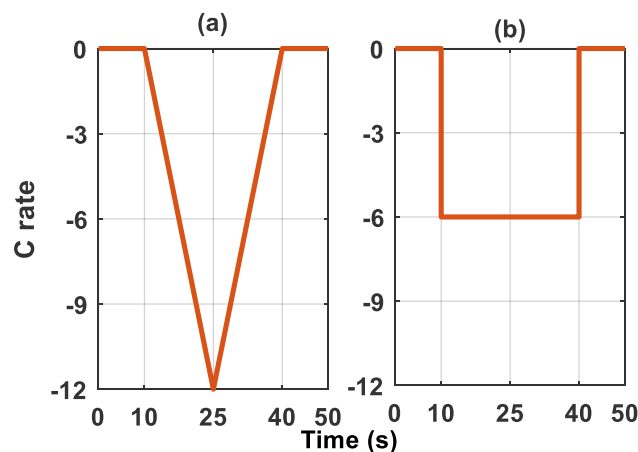


Figure 5-1 Example of power level (a) APU start pulse power, (b) modified power level for APU start phase

With the similar approach, a dedicated profile made of 9 phases is proposed. Figure 5-2 shows the voltage, current, temperature increase and SOC versus time for cell from Samsung in case of 45°C temperature environment at the BOL. Relatively to the 8 phases in the classical aircraft mission profile, the phase number 5 is added in the proposed aeronautical profile to increase the Δ SOC and the cell self-heating. The mission, current level, Δ SOC and time

duration in each phase are presented in Table 5-1. It must be noticed that this aeronautical profile is created to be applied on the selected Li-ion cells technologies, thus, it should be modified for a real application in the future.

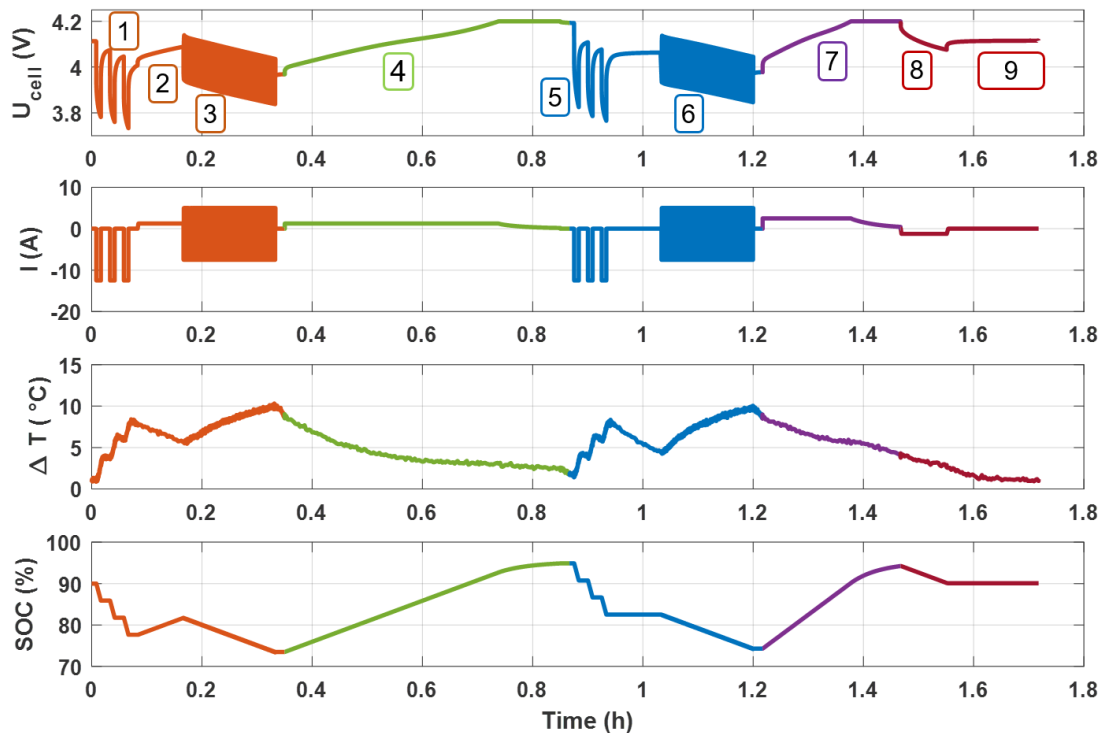


Figure 5-2 Curves of the proposed aeronautical profile: voltage, current, temperature increase and SOC vs. time for Samsung cell at 45°C and BOL

Phase No.	Mission	Details	SOC (%)	Time (min)
1	APU start	30s OCV + 3 × (30s DCH @5C + 1min OCV)	90-77	5
2	Taxiing	5min CH CC @0.5C	77-81	5
3	Take-off	150 cycles × (2s DCH @3C + 2s CH @2C) + 1min OCV	81-73	11
4	Cruise	30min CC-CV CH @0.5C + 1min OCV	73-98	31
5	Emergency APU start	30s OCV + 3 × (30s DCH @5C-1min OCV)	98-85	5
6	Landing	150 cycles × (2s DCH @3C + 2s CH @2C) + 1min OCV	85-77	11
7	Towing	15min CC-CV CH@1C	77-99	15
8	Refuel	5min DCH @0.5C	99-90	5
9	Recovery	10min OCV	90	10

Table 5-1 Mission, details, SOC and duration for each phase in proposed aeronautical profile

APU start profile consists of three 30s current pulses at 5C for both technologies. Li-ion cells must be reset to 90% SOC, which is classical value for at the beginning of the flight to start the power cycling ageing tests with the proposed aeronautical profile.

Taxiing phase concerns the movement of an aircraft on the ground. During this phase, it can be considered that Li-ion cells are charged 5min with a medium current of 0.5C.

For Take-off phase, the power requirements can be considered as 1C discharge over all the Take-off duration. An alternative could be to take consider several cycles (e.g.150 cycles) of discharge at 3C and charge at 2C that correspond both to the transitional periods and to the stabilisation of the on-board DC network.

Li-ion cells are charged during Cruise phase, thus, a classical CC-CV charge is applied during 30min.

An emergency phase is added in our proposed aeronautical profile. It has the same profile as the APU start at the beginning of the profile. In fact, this pattern leads to a larger SOC variation and higher temperature increase in order to obtain an accelerated ageing.

Landing phase is identical as the Take-off phase. During Towing, Li-ion cells are charged with classical CC-CV method at 1C. For Refuel, Li-ion cells are discharged at 0.5C during 5min.

In the end, 10min OCV measurement is performed on the Recovery phase. Li-ion cells are set again at 90% SOC, so they are ready to the next cycle.

Overall, the proposed aeronautical profile is investigated for both technologies based on a 45Ah capacity Li-ion battery in A350 XWB. It can be observed that this aeronautical profile can be divided into two similar parts that artificially double the thermal cycling at the same time. Finally, in this proposed aeronautical profile, the SOC level between 77%-99% added to the high current level pulses leads to a quite high stress that is supposed to enhance the degradation rate of cells.

5.2.2 Characteristics of accelerated ageing tests

In order to ensure the selected Li-ion cells may be aged during the power cycling tests with the proposed aeronautical profile, they were performed at three temperatures: 0°C and 45°C correspond to the conditions of generic power cycling in the reference test; 25°C was considered as a reference temperature.

Relatively to the generic power cycling ageing tests, three 18650 Li-ion cells of both technologies were used on accelerated ageing tests with the proposed aeronautical profile for each temperature. In addition, three cycles of charge/discharge were applied before accelerated ageing tests to form a homogenous SEI.

For the periodic characterization, the on-line characterization was always carried out after 40 aeronautical profile cycles to inform about the most suitable moment for check-up. The on-line characterization and check-up profile is identical as presented in Figure 5-3. At the beginning of the periodic characterization/check-up, all Li-ion cells were reset to nominal voltage (3.6V) with 1C current level, then three 20s discharge/charge current pulses at 1C, 3C and 5C were applied alternatively to measure the internal resistance. Next, the classical CC-CV

charge followed by a continuous discharge at 1C on both technologies for capacity measurement was performed. Then, Li-ion cells were reset to 90% SOC to start the power cycling tests. On-line characterization was done at ambient temperature of test, while, check-up is applied at 25°C. Compared to the check-up in the reference tests mentioned in chapter 3, the internal resistance measurement was performed at a fix voltage (3.6V) instead of 50% SOC through the whole lifespan.

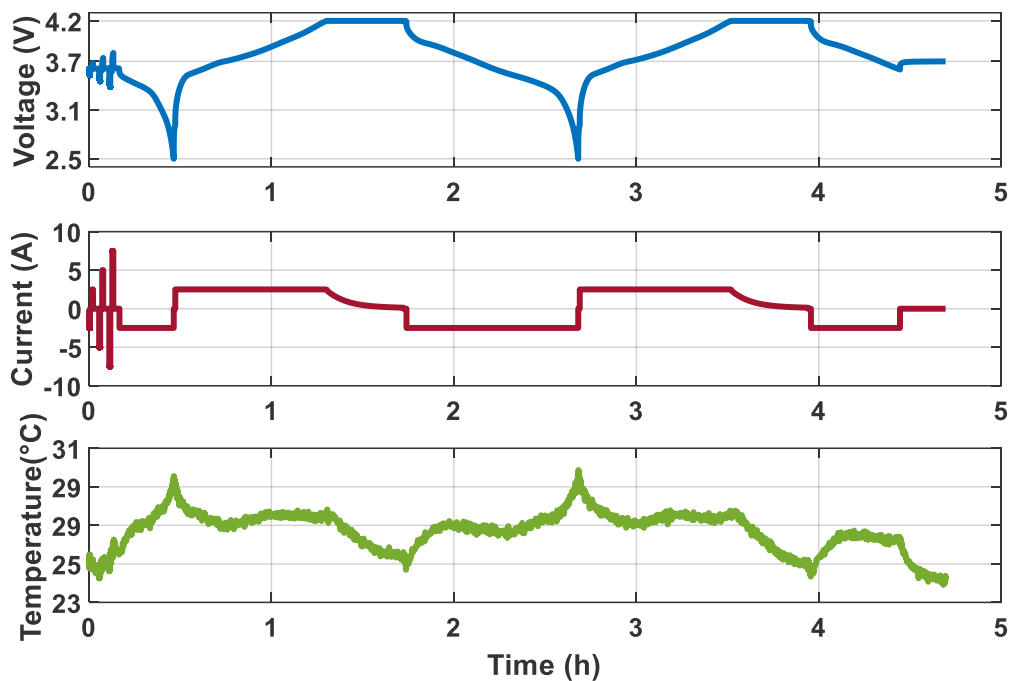


Figure 5-3 On-line characterization and check-up profile for Samsung at 25°C (Voltage, Current and Temperature vs. Time)

5.3 Experiments and raw results

The evolutions of the normalized capacity and resistance at 3.6V over equivalent full cycles number at 0°C, 25°C and 45°C are depicted in Figure 5-4 for technologies of LG and Samsung. As for generic power cycling results, two types of normalized capacity are presented on the plots. The independent symbol in circle represents the average value of 3 cells for classical periodic check-up at 25°C. While, the coloured line represents the on-line characterization at ambient temperature of test. In addition, the error bars are shown to verify the reproducibility between the three tested cells.

The accelerated test duration for EOT with corresponding cycling temperature are listed in Table 5-2. It can be observed that the duration strongly depends on the temperature and technology. For the same capacity loss, the duration may vary from one month to seven months.

Item	LG	Samsung
Chemistry	NMC/ graphite+SiO	NCA/ graphite
Time (days) Power cycling at 45°C	138 ($T_{cell} > T_{max}$)	118 ($T_{cell} > T_{max}$)
Time (days) Power cycling at 25°C	98 ($T_{cell} > T_{max}$)	180
Time (days) Power cycling at 0°C	24 ($C_{loss} > 50\%$)	221

Table 5-2 Duration of accelerated ageing tests at EOT with the aeronautical profile at 0°C, 25°C and 45°C for LG and Samsung

From Figure 5-4 (a, b), for both technologies, it can be observed that the normalized capacity of the three cells have a good reproducibility in the accelerated tests at 45°C and 25°C. However, the error bars for the average value increases proportionally with the equivalent full cycles for the tests performed at 0°C, the difference between maximal and minimal normalized capacity can even reach about 12%. In fact, this dispersion is due to the inhomogeneous lithium plating as indicated by Liu et al [108]. Few papers reported the reproducibility of cycling ageing behaviors at low temperature. It can be supposed that the lithium plating formation is less regular than SEI formation, so a slight sample difference leads to different ageing results. Therefore, ensuring the manufacturing processes to improve the consistency of 18650 Li-ion cell is important for application in a cold environment.

As in the generic power cycling, the normalized capacity values obtained according to the classical check-up are always below the online values at 45°C, while, they are always above the online values at 0°C for all technologies. This behaviour is due to the temperature as explained in the chapter 3. Relatively to Samsung, LG has a high degradation rate for the accelerated ageing tests with the aeronautical profile performed at 0°C. While at 45°C, LG can perform 20 days more than Samsung for 20% capacity loss.

In Figure 5-4 (a', b'), the presented values are the normalized resistances at 10s with 1C pulse current. The evolution of other normalized resistances obtained with 3C and 5C rates exhibits an identical tendency. For both technologies, the value of normalized resistance based on check-up at 25°C is higher than the on-line characterization at 45°C and vice versa for 0°C. Furthermore, the tendency of normalized resistance capacity evolution follows the tendency of normalized capacity evolution

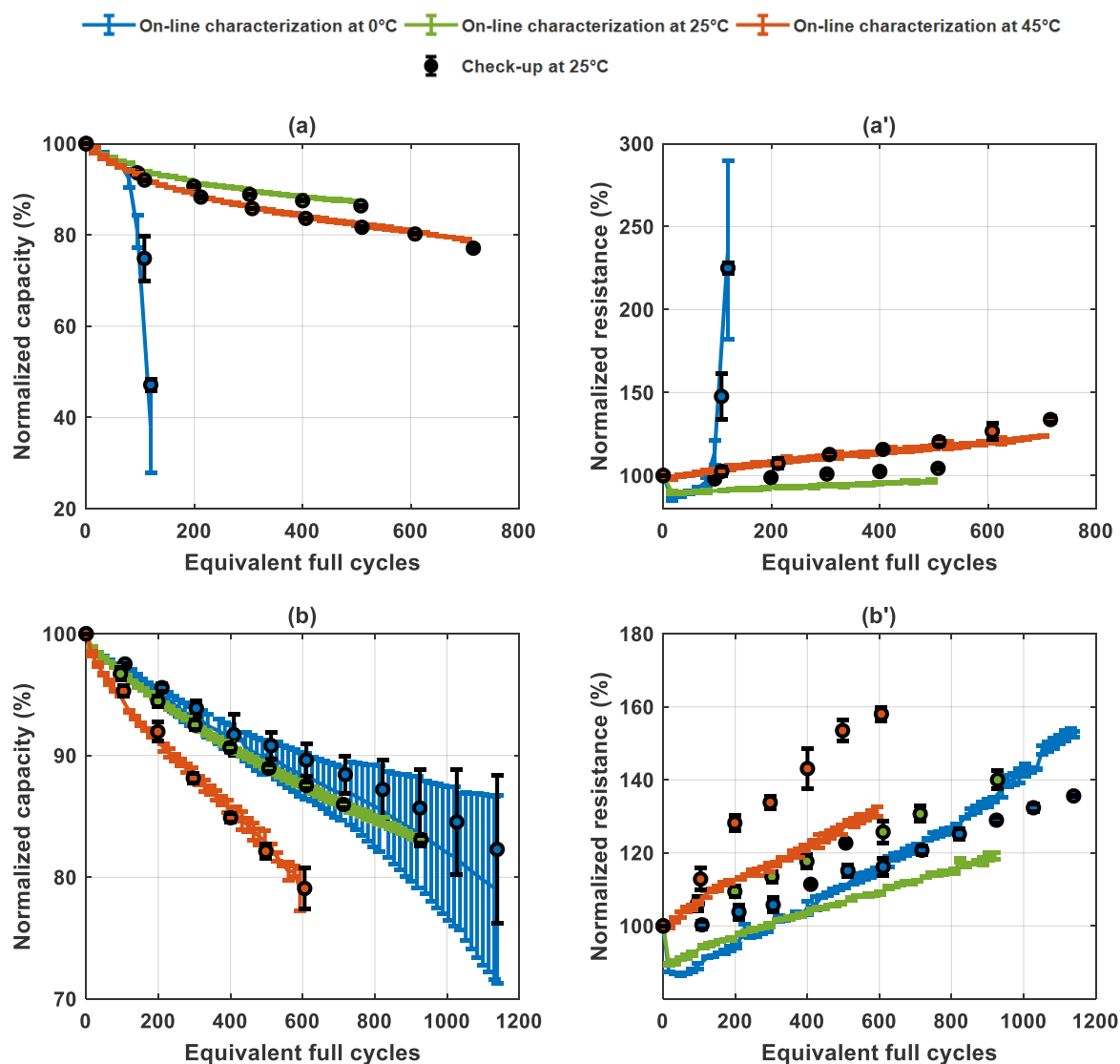


Figure 5-4 Normalized capacity and normalized resistance at 3.6V vs. equivalent full cycles for (a, a') LG and (b, b') Samsung at 0°C 25°C and 45°C with aeronautical profile

5.4 Ageing modelling and SOH estimation

Two modelling methods are proposed in this section. At first, the influence of temperature on the degradation rate of Li-ion cells aged with the specific aeronautical profile is investigated. Then, an efficient and simple method is proposed to predict the SOH of Li-ion cells for both technologies with a good accuracy.

5.4.1 Temperature effects on the degradation rate of capacity

As three temperatures were selected for the accelerated ageing tests with the specific aeronautical profile, the impact of temperature on capacity degradation rate is investigated. The same method used in chapter 3 to analyse the dependency between temperature and degradation rate in calendar ageing is applied here.

Figure 5-5 (a, b) presents the average value of normalized capacity fade at 0°C, 25°C and 45°C versus the square root of time. The circle represents the normalized capacity loss from

check-up at 25°C. Besides the accelerated ageing tests performed at 0°C for LG, it can be observed that a linear relationship is found out for all the other conditions of test. Furthermore, the slope and determination coefficient (R^2) are listed below the corresponding plots. This may be due to the selection of time factor (α) for linearization, few studies investigated this topic.

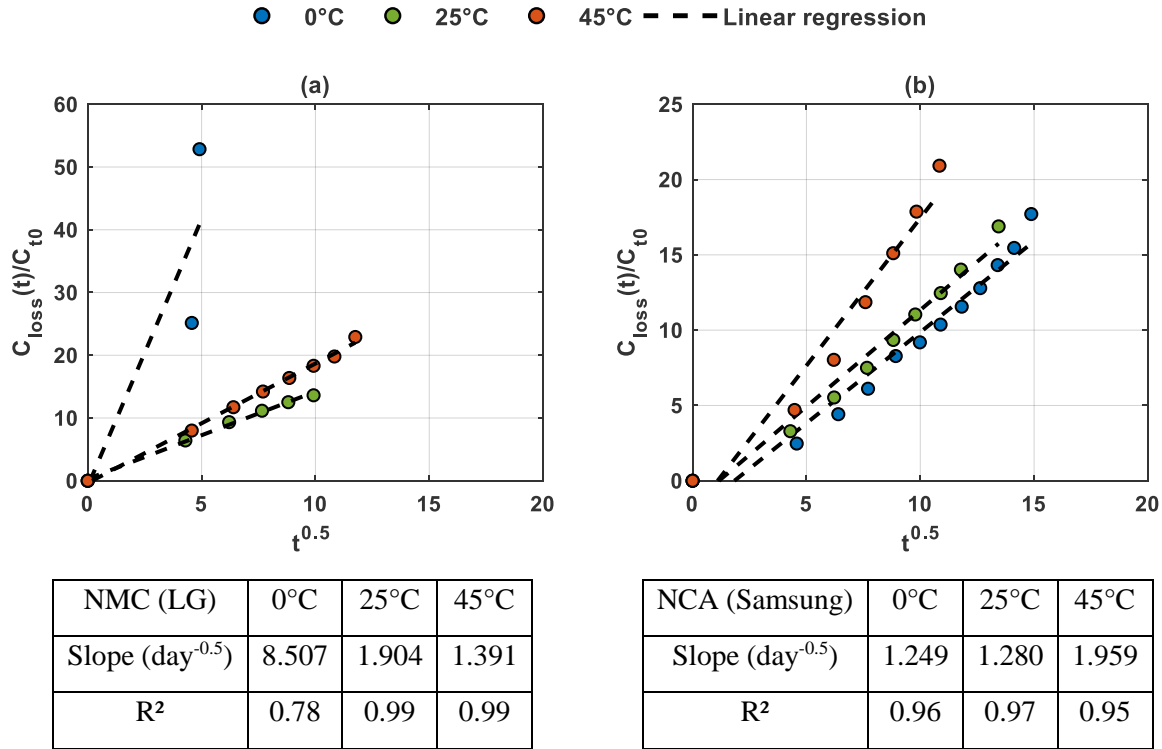


Figure 5-5 Capacity loss over square root of time at 0°C, 25°C and 45°C for accelerated ageing tests with corresponding linear regressions values for (a) NMC (LG), (b) NCA (Samsung)

Then, the natural logarithm of degradation rate ($\ln(k)$) is plotted versus the inverse of temperature ($1/T$) in order to verify whether the relationship follows the Arrhenius's law. Figure 5-6 shows the relationship between the degradation rate and temperature for both technologies. It is obvious that 18650 Li-ion cell from Samsung shows a linear dependency, which is the same as in the case of calendar ageing in chapter 3. In addition, the degradation rate at 0°C is nearly three times higher than the degradation rate at 45°C. The similar behaviour is also indicated by Baghdadi [128] et Waldmann [141] (Figure 3-14). In addition, as the dispersion of normalized capacity increases with the ageing time at 0°C for both technologies, besides the average capacity fade value of three cells, the maximum (red triangle) and minimum (blue triangle) capacity fade values are also used to determine the degradation rate. Then, they are plotted versus the temperature.

The relationship between capacity loss and temperature stays always linear for LG. For Samsung, there are always two linear regressions with opposite sign. The optimal temperature can be determined by a simple quadratic regression, LG has a low degradation rate at 30°C with the specific aeronautical profile. Thus, it can be confirmed that the NMC/graphite+SiO 18650 Li-ion cell from LG has two different ageing behaviours for the temperature above 30°C and below 30°C. While, Samsung ageing behaviours (calendar ageing and power cycling ageing) follow the Arrhenius's law, which signifies that these cells age slowly at low temperatures.

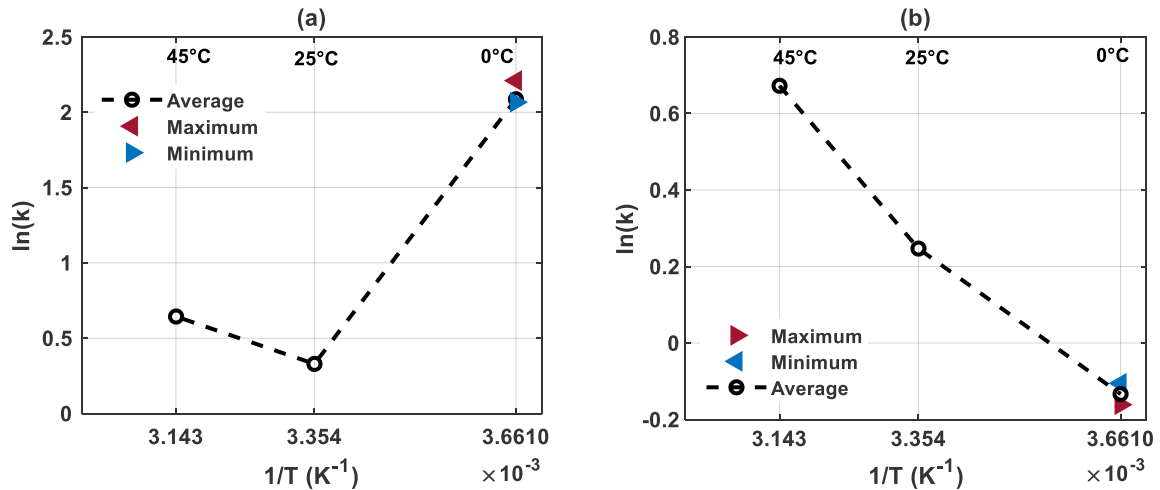


Figure 5-6 Influence of temperature (0°C, 25°C, 45°C) on degradation rate for (a) LG (NMC/graphite+SiO), (b) Samsung (NCA/graphite) in accelerated ageing test with the specific aeronautical profile

This interesting finding indicates that the capacity fade rate over the temperature of accelerated ageing tests does not always follow the Arrhenius's law, it depends on the degradation mechanisms in Li-ion cells. Despite the dispersion of normalized capacity between samples increases with the ageing duration, the same ageing behaviours are confirmed by maximum and minimum capacity loss values. In addition, this assumption has a good coherence with the temperature effects on ageing behaviours in calendar ageing tests. It is also supported by the literatures [128] [141]. This modelling could help users to define an optimal temperature in order to minimise the degradation rate of Li-ion cells for the aeronautical usage.

5.4.2 SOH estimation

5.4.2.1 Qualitative and quantitative ICA

In order to investigate the SOH estimation for Li-ion cells endured with the aeronautical profile at 0°C, 25°C and 45°C, incremental capacity analysis methods are applied. The discharge curves (voltage vs. capacity) based on check-up at 25°C of LG and Samsung at 1C are presented in Figure 5-7 (a, b). The black curve represents one cell at fresh state (BOL), the three other curves correspond to the discharged curve of cells at EOT throughout different temperature (0°C, 25°C, 45°C) of accelerated ageing tests with the aeronautical profile. These curves provide discharged capacity for each cell. As all the tested cells have almost the same capacity at BOL, only one curve is presented for both technologies. Then, the enhanced IC by moving average filter is applied on the discharged curves, which is presented in Figure 5-7 (a', b'). All the IC curves at the BOL have three peaks, but the peak evolution is not as clear as expected. Peak 1 shifts to left gradually, corresponding to the increase of the polarization resistance [183]. Moreover, peaks can disappear from the IC curves after the ageing test [181]. Therefore, the decomposition of IC curves based on Gaussian and Lorentzian mixed function is used to extract all the peak features.

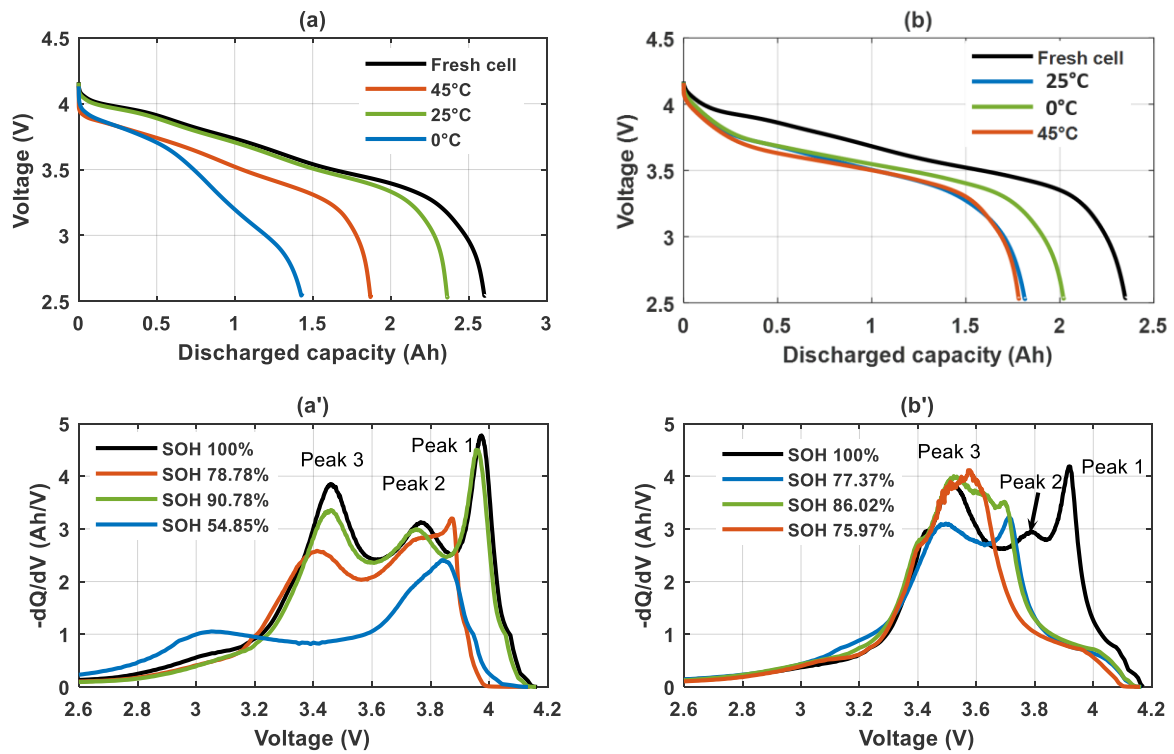


Figure 5-7 Discharge curves for check-up at 25°C with corresponding IC curves for (a, a') LG and (b, b') Samsung

As indicated previously in chapter 4, the area of peak 3 and location of peak 1 have been selected as peak features to quantify the SOH and normalized resistance. Figure 5-8 presents the peak features versus the SOH and normalized resistance for 18650 cells from LG. It can be seen from Figure 5-8 (a) that a linear regression is found out between SOH and area of peak 3 based on the IC curve decomposition. While, another linear relationship is observed between the location of peak 1 and normalized resistance. Two linear regressions are listed below each plot, the corresponding values of peak feature are listed in the Table 5-3.

LG	SOH (%)	Normalized resistance (%)	Location of peak 1 (V)	Area of peak 3 (Ah)
BOL	100	100	3.99	1.56
EOT 25°C	90.78	111	3.96	1.36
EOT 45°C	78.78	145	3.89	0.98
EOT 0°C	54.85	220	3.84	0.59

Table 5-3 SOH and normalized resistance with location of peak 1 and area under peak 3 for cells from LG

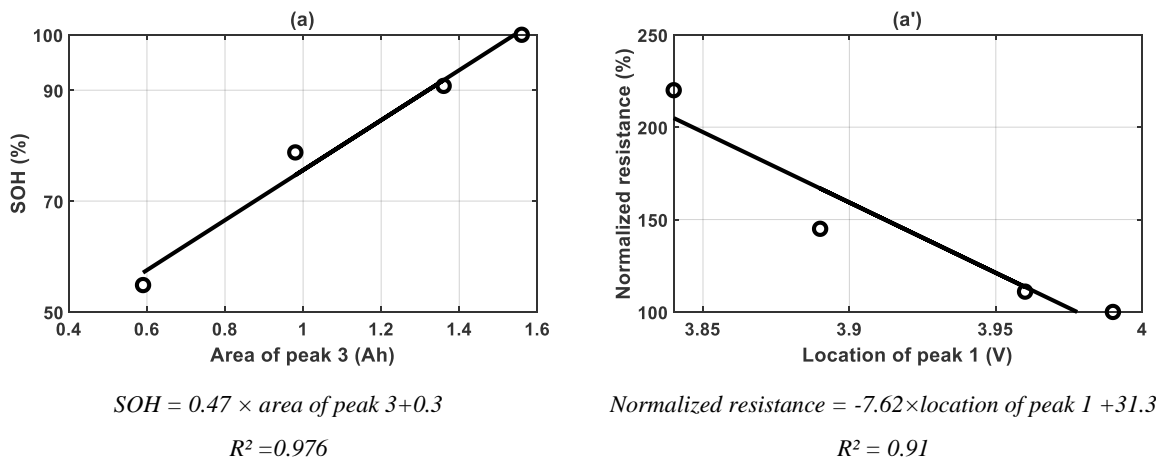


Figure 5-8 Relationship between (a) area under peak 3 vs. SOH and (a') location of peak 1 vs. normalized resistance for LG

The same type of regression is observed for 18650 cells from Samsung. Table 5-4 lists all the values of peak features, especially the location of peak 1 and area of peak 3. Then two liner correlation are established thanks to these values, which are illustrated in Figure 5-9.

Samsung	SOH (%)	Normalized resistance (%)	Location of peak 1 (V)	Area of peak 3 (Ah)
BOL	100	100	3.96	1.47
EOT 45°C	77.37	160	3.59	0.0007
EOT 25°C	86.02	140	3.70	0.99
EOT 0°C	75.97	139	3.61	0.1759

Table 5-4 SOH and and normalized resistance with location of peak 1 and area under peak 3 for cells from Samsung

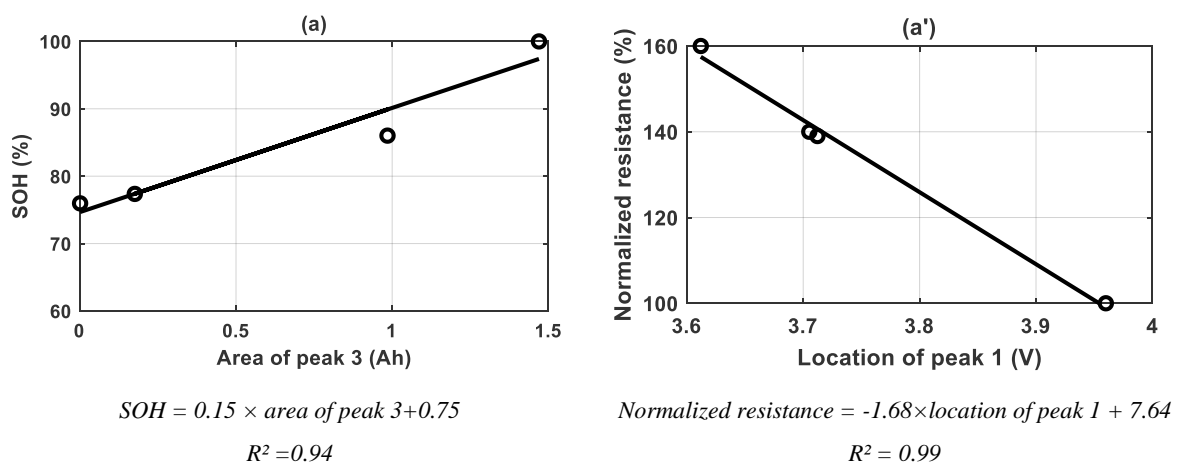


Figure 5-9 Relationship between (a) area under peak 3 vs. SOH and (a') location of peak 1 vs. normalized resistance for Samsung

These results suggest that cell SOH and normalized resistance can be determined according to the area of peak 3 and location of peak 1 according to the corresponding linear regression. In addition, the peak features are the same as in the generic ageing tests.

5.4.2.2 Validation of the proposed method

In order to validate the proposed SOH estimation method for the cells endured by the specific aeronautical profile, one 18650 cells for each technology with unknown SOH is used. Figure 5-10 presents the decomposition IC curves based on Gaussian Lorentzian function for unknown SOH cells. A good fitting is shown for both technologies. The area of peak 3 and the location of peak 1 can be extracted from the IC curves, which can help determine the SOH and normalized resistance.

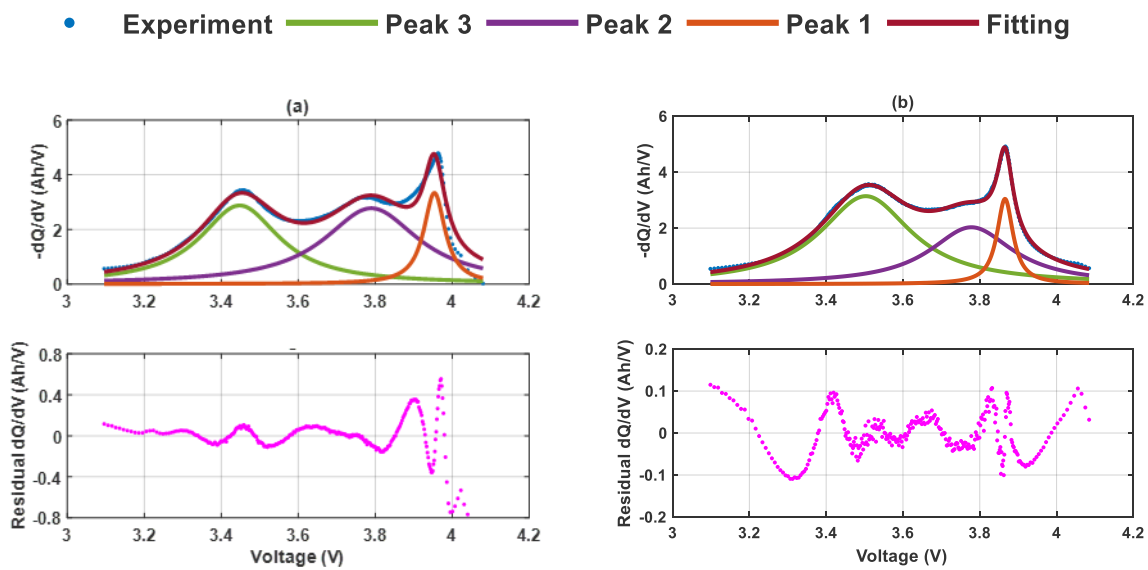


Figure 5-10 Decomposition of the IC curve based on the Gaussian Lorentzian function of unknown SOH cells from (a) LG and (b) Samsung

	LG	Samsung
Area of peak 3	0.938	1.169
Estimated SOH (%)	74.08	92.67
Measured SOH (%)	79.48	93.16
Error SOH (%)	5.4	0.49
Location of peak 1	3.954	3.866
Estimated normalized resistance (%)	118	114
Measured normalized resistance (%)	117	108
Error normalized resistance (%)	1	6

Table 5-5 Summary of peak features based on IC curves with SOH and normalized resistance estimation for unknown cells

Table 5-5 summarizes all the values of peak features with the corresponding estimated SOH and estimated normalized resistance. The estimated values are obtained by the fitting equations presented in Figure 5-8 and Figure 5-9. In addition, SOH error represents the difference between the estimated values and experimental values. From these data, the estimated SOH determined by the area of peak 3 shows a good accuracy compared with the measured SOH for both technologies. Concerning the estimated normalized resistance obtained by the location of peak1, the same conclusion can be drawn. The error between the estimated and measured SOH or normalized resistance is less than 6%. These results point out that the quantitative ICA method has a good accuracy, therefore it is suitable for estimating the SOH of cells endured by the specific aeronautical profile.

5.5 Conclusion

In this chapter, the two most promising selected technologies (LG, Samsung) of Li-ion cells (NMC/graphite+SiO, NCA/graphite) endured by an accelerated ageing tests with a specific aeronautical profile are investigated. This study can be divided into two main sections.

The first section concerns the experimental tests. A specific aeronautical profile including 9 phases (APU start, Taxiing, Take-off, Cruise, Emergency, Landing, Towing, Refuel, and Recovery) is investigated. This aeronautical profile corresponds to a 2 hours domestic flight in Metropolitan France. The current level and SOC variation of this aeronautical profile are defined based on a 28V Li-ion battery installed in A350 XWB. However, they are modified and adapted to the 18650 cell scale. Then three cells of both technologies are performed at three temperatures more than 6 months. The periodic characterization and classical check-up are applied to follow the available capacity and internal resistance. More than 20% capacity loss is obtained for both technologies in each tests conditions. The modelling can be developed thanks to these results.

The second section is dedicated to the modelling of ageing behaviour for Li-ion cell. The first modelling approach is to evaluate the influence of temperature on degradation rate throughout the specific aeronautical profile for both technologies. For this, the degradation rate determined by capacity loss is defined. Then, the natural logarithm of this degradation rate is plotted versus the temperature of tests. For 18650 NMC/graphite+SiO Li-ion cell from LG, two linear regressions with opposite sign are shown between 0°C to 45°C, which indicates two different ageing mechanisms. Thus, an optimal temperature (30°C) is defined, where the degradation rate is the lowest. In contrast to the Li-ion cell from LG, the 18650 NCA/graphite Li-ion cell from Samsung follows the Arrhenius's law. In addition, these ageing behaviours have a good coherence with the ageing behaviours found out in the calendar ageing type. The second modelling approach is to estimate the SOH of Li-ion cells during the accelerated ageing tests. This modelling is based on the qualitative and quantitative incremental capacity analysis method. For both technologies, a linear regression is established between the SOH and the area of peak 3. Another linear regression is obtained between the normalized resistance and the location of peak 1. SOH and normalized resistance of two unknown SOH Li-ion cells can be predicted with a good accuracy thanks to the proposed method. Users can master the ageing

behaviours in a wide temperature range [0°C, 45°C] and anticipate the replacement of cells with low SOH for aeronautical usage with these proposed modelling methods.

General conclusion

This thesis contributes to the topic of electrochemical energy storage systems issues for aeronautical usage. The goal is achieved by evaluating the performance, reliability and robustness of nine electrochemical energy storage elements, including the latest generation commercial elements: Lithium-ion (NMC/graphite + SiO, NCA/graphite, LFP/graphite, NMC/LTO), Lithium-Sulfur (Li-S), supercapacitors (SCaps) and Lithium-ion capacitors (LiCs). The following section presents the investigations and results in details.

The first chapter presents at first the working principle, the materials, the forms and characteristics of different electrochemical energy storage types (LiBs, SCaps, LiCs, Li-S). Then, the characteristic of LiBs, SCaps and LiCs are compared with each other. Furthermore, the characterization methods used for electrochemical energy storage elements are listed. The state of art for electrochemical energy storage elements indicates that the characteristic of different elements are sensitive to temperature, SOC, current. Thus, specific protocols are required to characterize all the investigated electrochemical energy storage elements. Next, the electrochemical energy storage elements for aeronautical usage is introduced. The energy and power needs for more electrical aircraft are presented according to multiple literatures. Finally, the current issues concerning the reliability, the performance in extreme aeronautical conditions, the safety and the robustness of electrochemical energy storage elements are summarized.

The second chapter concerns the comparative performance quantification by experiments and modelling. For this, a common reference tests are proposed to quantify the energy and power density of the different electrochemical energy storage elements. Since the characteristic of these elements are quite different, a classification is defined in this reference tests according to the type of application (energy, power, high power). In addition, the condition of the reference tests correspond to the aeronautical usage (multiple current levels) and environment (-20°C-55°C). Then, an electro-thermal model based on a few number of parameters, which has the physics links with the elements and is easily identified, is developed and validated. For the most promising technologies of Li-ion cells, the performances (energy density, power density) are represented in the Ragone plane in non-isothermal conditions. The simulation results exhibit that the operating conditions such as temperature, current, power level and safety conditions strongly affect the performance of Li-ion cells. This model could be employed as a conception aid tool for the selection of Li-ion cells in system design process.

The third chapter is devoted to the study of calendar ageing and active cycling as well as to the presentation of abuse test results. For calendar ageing, the elements are stored in a high state of charge (95%) and at extreme temperatures (-20°C, 55°C). Particular attention was given to the ageing behavior of Li-ion elements at low temperatures. The results indicated on one hand, that the dependence between the rate of loss of capacity and the storage temperature is not linear over the temperature range [-20°C, 55°C] and on the other hand that there is an optimum temperature for which the degradation rate of capacity is minimal. For power cycling ageing, the results showed different behavior regarding the temperature and the technology.

Finally, a radar diagram is established thanks to the experimental results from reference tests in order to select the most promising technologies. This radar diagram represents a summary of performance, safety, reliability and robustness based on seven criteria (energy density, power density, available capacity at extreme temperatures, life in calendar ageing type, self-discharge, number of cycles and safety). Finally, the performance, safety, reliability and robustness 18650 Li-ion cells from LG (NMC/graphite + SiO) and Samsung (NCA/graphite) are outstanding relatively to other technologies.

In the fourth chapter, a SOH estimation method is proposed thanks to the results of various periodic characterizations in the third chapter. This efficient method is based on the Incremental Capacity Analysis. Thus, the main mechanisms of degradation (Conductivity Loss, Loss of Active Material, Loss of Lithium Inventory) are identified from the changes of peak features during a constant current discharge. Then a decomposition of IC curves according to Gaussian Lorentzian mixed function allows to extract the peak features. The quantification of ICA can be performed thanks to the characteristic of several peaks. The ageing type of Li-ion cells endured can be determined thanks to a simple linear dependency between the area under a peak and the normalized capacity. Then, the position of peak allows to predict the evolution of resistance thanks to another linear regression. This proposed method is able to estimate which type of ageing the cell has historically undergone, as well as the evolution of normalized resistance during ageing.

The last chapter is focused on the robustness of the electrochemical energy storage elements in an accelerated ageing tests with a specific profile for the aeronautical usage. Only the most promising Lithium-ion technologies (LG, Samsung) are retained in this chapter. These tests are based on a profile in current, corresponding to a series of flight mission phases for an air travel in metropolitan France. The ageing models proposed in the previous chapters are applied here to evaluate the impact of temperature on the rate of degradation and to estimate the SOH of the cells endured by this aeronautical profile. Two linear regressions with opposite sign are observed between 0°C to 45°C for Li-ion from LG (NMC/graphite + SiO), which indicates two different ageing mechanisms in this temperature range. While, a linear regression is observed for Li-ion cells from Samsung (NCA/graphite). These interesting findings have a good consistency with the ageing behaviours in the calendar ageing type. Then, the normalized capacity and resistance of two unknown-SOH Li-ion cells can be predicted with a good accuracy thanks to the efficient qualitative and quantitative ICA. Finally, users can master the ageing behaviours of Li-ion cells in the aeronautical environment and anticipate the replacement of cells with low SOH for aeronautical usage.

Major contributions

The major contributions of this work could be summarized as follows:

Reference tests for three types of electrochemical energy storage elements (LiBs, SCaps, LiCs) have been proposed to quantify the performance and ageing in aeronautical environment and for aeronautical usage.

A non-isothermal Ragone plot based on the electrical-thermal model by determining the energy density and power density of electrochemical energy storage elements is investigated in order to select the most convenient available technology.

In the same aim, an original Radar diagram that takes into accounts the aeronautical criteria regarding performance, reliability, safety and robustness thanks to the experimental results from reference tests is developed.

A semi-empiric calendar ageing model has been proposed in a wide temperature range [-20°C, 55°C], a minimal capacity loss rate was observed in this temperature range for the first time.

A SOH estimation method based on the qualitative and quantitative Incremental Capacity Analysis is investigated in order to not only identify the degradation mode, but also to predict which type of ageing has been historically underwent and to determine the normalized resistance for two chemistries of Li-ion cells.

An accelerated test with 9 mission phases that combines calendar and power cycling ageing types for aeronautical usage has been proposed, which corresponds to the 2 hours air travel in Metropolitan France. In addition, the current level defined in this specific aeronautical profile is adapted to 18650 Li-ion scale in order to take advantage of the best capability of the cells.

A semi-empiric ageing model to determine the minimal capacity loss rate during the accelerated ageing tests with a specific aeronautical profile is developed in the operating temperature [0°C, 45°C].

Prospects

The current work in this manuscript can suggest the future research opportunities, including the following issues:

Regarding the thermal modelling, a generic method to determine an accurate heat transfer coefficient for multiple operating conditions, such as the high current or power level, the low temperatures, could be proposed. In addition, a couple electrical-thermal failure model could be developed for predicting the thermal runaway of Li-ion batteries.

On a system level, ageing modelling could be added to our macro model used in the non-isothermal Ragone plot approach.

The calendar ageing tests and power cycling ageing tests with other temperatures and other SOCs could be performed to validate the relationship between the degradation rate and temperature.

Concerning the mechanical behaviour, ageing under different external or internal pressures for a cell in pouch form could be evaluated according to the first results obtained in the team [185].

With regard to the SOH estimation method, the qualitative and quantitative ICA method at different temperatures could be validated. The SOH estimation method could be expanded to a battery pack scale for BMS implementation.

Table of figures

Figure 0-1 Electrical power generating capacity vs. introduction year [4]	5
Figure 0-2 Li-ion battery of Boeing 787 Dreamliner airline before and after accident [5].....	6
Figure 1-1 Ragone diagram of the main electrochemical energy storage elements	11
Figure 1-2 Classification for the main electrochemical energy storage elements (LiBs, SCaps) based on the way of storing electric charges [8]	11
Figure 1-3 Working principle of Li-ion cell.....	12
Figure 1-4 Different forms of Li-ion cell (a) Cylindrical, (b) Prismatic, (c) Pouch [20]	15
Figure 1-5 Composition of SCaps	16
Figure 1-6 LiCs compositions with working principle.....	17
Figure 1-7 Examples of commercial LiCs from different manufacturers	18
Figure 1-8 Schematic representation of OCV measurement by GITT for a Li-ion cell (a) voltage profile (b) current profile (c) OCV vs. SOC [32].....	19
Figure 1-9 Pseudo OCV-SOC curves based on discharge at different temperatures for a LFP/graphite cell [35]	20
Figure 1-10 Relaxation time required at different temperatures and varied SOC by technique of GITT for a NMC/LTO Li-ion cell [31]	20
Figure 1-11 (a) Pulse current profile for R_{int} determination of LiBs (b) Voltage profile for ESR determination of SCaps in IEC 62576 standard [30].....	21
Figure 1-12 Impedance spectrum for NMC/graphite Li-ion cell at 30% SOC at 45°C in galvanostatic mode [10mHz-10kHz] with corresponding equivalent circuit model	22
Figure 1-13 Example of batteries used in aircrafts.....	25
Figure 1-14 Battery technologies overview regarding energy densities (current, expected) and price [50]	27
Figure 1-15 On-board multiple electrical energy requirements in aircraft [51]	27
Figure 1-16 Discharged capacity and resistance of Li-ion cells at different temperatures (-20°C, 0°C, 25°C et 55°C) [58].....	29
Figure 2-1 Overview of main equipment in CaCySSEE platform	35
Figure 2-2(a) Voltage profile during incremental discharge at 1C and 25°C (b) Zoom on voltage drop ($U_{10s}-U_{ocv}$) at 50% SOC and -20, 0, 25, 55°C under 1C discharge current pulse for EAS cell	38
Figure 2-3 Available discharged capacity for all electrochemical energy storage elements at 55°C, 25°C, 0°C and -20°C under 3 C rates (C/3, 1C, 3C for energy type, 1C, 3C, 5C for power type, 3C, 5C and 10C for high power type)	40
Figure 2-4 Boxplot of the cell-to-cell variation vs. datasheet and statistics results based on 20 cells measurements of (a) mass, (b) Discharged capacity at 25°C	41

Figure 2-5 Experimental constant power discharge procedure for Samsung at 25°C; power, cell voltage, current and temperature versus time, respectively	42
Figure 2-6 Experimental Ragone plot for LG (NMC) and Samsung (NCA) at -20°C, 0°C, 25°C and 55°C.....	43
Figure 2-7 U_{cell} and increased temperature versus discharged capacity at -20°C, 0°C, 25°C, 55°C during constant current discharge under 1C, 3C and 5C for LG (left) and Samsung (right).....	44
Figure 2-8 Energy density versus power density at -20°C, 0°C, 25°C and 55°C determined for constant current discharge (1C, 3C, 5C) and constant power discharge (3W, 15W, 20W) for LG (left) and Samsung (right).....	45
Figure 2-9 Overview of electrical-thermal model structure	46
Figure 2-10 (a) R_{int} equivalent circuit model (b) n-RC equivalent circuit model.....	46
Figure 2-11 Pseudo-OCV at -20°C, 0°C, 25°C and 55°C for (a) LG (b) Samsung	48
Figure 2-12 Experimental internal resistance and 3D mapping of $R_{int} = f(SOC, T)$ at 1C, 3C and 5C for LG (left) and Samsung (right) according to stepwise regression. The coloured axis represents the value of R_{int}	50
Figure 2-13 Potentiometric tests results for Samsung at 60% SOC (a)Temperature versus time, (b) OCV versus time, (c) OCV versus temperature.....	52
Figure 2-14 Entropic potential versus SOC for Technology LG (NMC/graphite+SiO) and technology Samsung (NCA/graphite).....	53
Figure 2-15 Constant current discharges curves at 25°C for multiple C rates of LG (left) [91] and Samsung (right) [92]	54
Figure 2-16 Simulation versus experimental data for cell voltage and increased temperature for LG (a) and Samsung (b) under constant power discharge (3W, 15W and 30W) at 25°C	55
Figure 2-17 Comparison of simulated energy density versus power density: galvanostatic-based, datasheet-based and experimental results for LG (left) and Samsung (right)	55
Figure 2-18 Simulation versus experimental data for LG (left) and Samsung (right) under constant power discharge at 3W, 15W and 30W at (a1, b1) 55°C, (a2, b2) 0°C and (a3, b3) -20°C	57
Figure 2-19 Performance comparison of LG and Samsung based on Ragone plot model for -20°C, 0°C, 25°C and 55°C.....	59
Figure 3-1 Overview of ageing mechanisms in Li-ion cells [94].....	63
Figure 3-2 SEM images of the graphite electrodes disassembled from the Graphite/LFP full cells (a)Reference; (b)power cycling at 25°C; (c)power cycling at 0 °C; (d) power cycling at -18°C [110]	64
Figure 3-3 Schema of SCaps ageing mechanisms under floating constraints [118]	66
Figure 3-4 Swelling of (a) Graphite/LTO cells after 4500h storage at 55°C and 95% SOC, (b) Electrolyte leakage (c) Can opening of SCaps after 5000h calendar ageing on floating.....	68
Figure 3-5 Illustration of the most common features of thermal runaway [51]	68
Figure 3-6 Example of experimental setups for LiBs during calendar ageing tests at 25°C.....	70
Figure 3-7 Example of experimental setups for LiBs during power cycling tests	71
Figure 3-8 Check-up profile at 25° for (a) LiBs, LiCs,and (b) for SCaps.....	72

Figure 3-9 Normalized capacity (left) and normalized resistance at 50% SOC (right) from check-up at 25°C for LiBs (a) (a')LG, (b) (b') Samsung, (c) (c') EAS, (d) (d') K2, (e) (e')Valence (f) (f') EIG under 55°C, 25°C and -20°C of calendar ageing tests at 95%SOC.....	75
Figure 3-10 (a) Normalized capacitance and (a') normalized ESR at 5s from check-up at 25°C for Skeleton under 65°C, 55°C, 25°C and -20°C of floating calendar ageing(2.7V) tests	75
Figure 3-11 (a) Normalized capacitance and (a') normalized resistance from check-up at 25°C for Yunasko under 55°C and 25°C of floating calendar ageing(2.6V) tests, (b) LiC in the fresh state (b')LiC after 33 days floating calendar ageing(2.6V) tests at 55°C	76
Figure 3-12 Capacitance loss over square root of time at -20°C, 25°C, 55°C, 65°C and corresponding linear regressions values for (a) NMC (LG), (b) NCA (Samsung), (c) LFP (K2), (d) LTO (EIG), (e) SCaps (Skeleton).....	78
Figure 3-13 Influence of calendar ageing temperatures (-20°C, 25°C, 55°C 65°C) on degradation rate for (a) NMC (LG), (b) NCA (Samsung), (c) LFP (K2), (d) LTO (EIG), (e) Activated Carbone (Skeleton)	79
Figure 3-14 (a)Logarithm of total ageing rate function of temperature, I_{\max} and I_{\min} [128] (b)Arrhenius plot of the ageing behaviour of 18650 cells cycled at 1C in the temperature range from -20°C to 70°C [141]	80
Figure 3-15 Normalized capacity (left) and normalized resistance at 50% SOC (right) for LiBs according to online and classical check-up for (a) (a')LG, (b) (b') Samsung, (c) (c') EAS, (d) (d') K2, (e) (e')Valence (f) (f') EIG under 0°C and 45°C power cycling ageing tests (100% DOD, 0.5C/1C)	84
Figure 3-16 (a) Online and classical check-up normalized capacitance (a') classical check-up normalized ESR at 5s for Skeleton under 50°C and 0°C of power cycling (0.5U _n -U _n , 50A) ageing tests (b) Temperature increase at the surface of SCaps before EOT power cycling at 0°C and 50°C	85
Figure 3-17 (a) Online and classical check-up normalized capacitance (a') classical check-up normalized resistance at 50% SOC for Yunasko under 0°C and 45°C power cycling (1.4V-2.7V) tests (b) LiC after 3251 cycles (18 days) power cycling ageing tests(1.4V-2.7V, 10C-13A) at 45°C	86
Figure 3-18 Photos after thermal stability test for LFP/Graphite 26650 cell from K2 energy	88
Figure 3-19 Photos after the thermal stability test for Li-S pouch cell from Oxis	89
Figure 3-20 Photos after the overcharge tests	90
Figure 3-21 Hazard level comparison of different technologies based on overcharge tests	91
Figure 3-22 (a) Experimental set up (b) pressure profile of altitude simulation test.....	92
Figure 3-23 Radar diagram of various electrochemical energy storage elements (a) LG,(b) Samsung, (c) K2 (d) Valence, (e) EAS, (f) EIG, (g) Skeleton, (h) Yunasko	94
Figure 4-1 Classification of battery SOH estimations method [155]	98
Figure 4-2 Normalized capacity and normalized resistance at 50% SOC at 25°C for (a, a') LG and (b, b') Samsung.....	102
Figure 4-3 IC curves for LG cell at C/20 at the BOL based on (a) experimental data (b) MA filter smoothing.....	103
Figure 4-4 Discharge curves at C/20, C/10, C/5, C/3, C/2 and 1C with the corresponding IC curves for (a) LG and (b) Samsung	104

Figure 4-5 Location of peak 1 at different C rates for (a) LG and (b) Samsung	105
Figure 4-6 IC based on the discharge curves for check-up at 25°C for LG	106
Figure 4-7 IC based on the discharge curves for check-up at 25°C for Samsung	106
Figure 4-8 Decomposition of the IC curve based on the Gaussian Lorentzian function at the EOL for (a) LG and (b) Samsung.....	108
Figure 4-9 Normalized capacity vs. the area under peak 3 (left) and normalized resistance vs. the location of peak 1 (right) at 25°C for (a, a') LG and (b, b') for Samsung with the corresponding fitting parameters for several ageing types.....	109
Figure 4-10 Decomposition of the IC curve based on Gaussian Lorentzian function for (a, b) two cells of LG, (c, d) two cells of Samsung.....	110
Figure 4-11 Illustration of the proposed method for determining the ageing type and resistance of a cell with unknown SOH.....	112
Figure 5-1 Example of power level (a) APU start pulse power, (b) modified power level for APU start phase.....	116
Figure 5-2 Curves of the proposed aeronautical profile: voltage, current, temperature increase and SOC vs. time for Samsung cell at 45°C and BOL	117
Figure 5-3 On-line characterization and check-up profile for Samsung at 25°C (Voltage, Current and Temperature vs. Time)	119
Figure 5-4 Normalized capacity and normalized resistance at 3.6V vs. equivalent full cycles for (a, a') LG and (b, b') Samsung at 0°C 25°C and 45°C with aeronautical profile.....	121
Figure 5-5 Capacity loss over square root of time at 0°C, 25°C and 45°C for accelerated ageing tests with corresponding linear regressions values for (a) NMC (LG), (b) NCA (Samsung)	122
Figure 5-6 Influence of temperature (0°C, 25°C, 45°C) on degradation rate for (a) LG (NMC/graphite+SiO), (b) Samsung (NCA/graphite) in accelerated ageing test with the specific aeronautical profile.....	123
Figure 5-7 Discharge curves for check-up at 25°C with corresponding IC curves for (a, a') LG and (b, b') Samsung.....	124
Figure 5-8 Relationship between (a) area under peak 3 vs. SOH and (a') location of peak 1 vs. normalized resistance for LG	125
Figure 5-9 Relationship between (a) area under peak 3 vs. SOH and (a') location of peak 1 vs. normalized resistance for Samsung.....	125
Figure 5-10 Decomposition of the IC curve based on the Gaussian Lorentzian function of unknown SOH cells from (a) LG and (b) Samsung	126

References

- [1] Air transport action group (ATAG), “Action on climatic change,” 2018. .
- [2] Roland Berger, “Electrical propulsion promises greener flight,” 2018. .
- [3] International Air Transport Association (IATA), “Three targets for Carbon Dioxide emissions from air transport:,” 2016.
- [4] R. Thomson, N. Sachdeva, M. Nazukin, and N. Martinez, “Aircraft Electrical Propulsion – The Next Chapter of Aviation,” Roland Berger, 2017.
- [5] National Transportation Safety Board, “Auxiliary Power Unit Battery Fire Japan Airlines Boeing 787-8,” 2014.
- [6] G. Kalghatgi, “Is it really the end of internal combustion engines and petroleum in transport?,” *Applied Energy*, vol. 225, no. February, pp. 965–974, 2018.
- [7] Engie, *Un monde d’énergie*. 2018.
- [8] P. Simon, “Le stockage électrochimique de l ’énergie : principes , applications et futurs défis,” *Annales des Mines - Responsabilité et environnement*, pp. 67–72, 2015.
- [9] H. D. Yoo, E. Markevich, G. Salitra, D. Sharon, and D. Aurbach, “On the challenge of developing advanced technologies for electrochemical energy storage and conversion,” *Materials Today*, vol. 17, no. 3, pp. 110–121, 2014.
- [10] B. Multon and J. Peter, “Le stockage de l’énergie électrique . Moyens et applications,” *Revue 3E.I*, pp. 59–64, 1996.
- [11] S. Chhor, “Etude et modélisation de l ’ interface graphite / électrolyte dans les batteries lithium-ion,” 2014.
- [12] S. Goriparti, E. Miele, F. De Angelis, E. Di Fabrizio, R. Proietti Zaccaria, and C. Capiglia, “Review on recent progress of nanostructured anode materials for Li-ion batteries,” *Journal of Power Sources*, vol. 257, pp. 421–443, 2014.
- [13] I. Baghdadi, “Prise en compte des modes de vieillissement dans la modelisation des performances de batteries lithium-ion pour l’évaluation de leur duree de vie en usage automobile,” Thèse de Doctorat, Univerité de Bordeaux, 2017.
- [14] C. M. Julien, A. Mauger, K. Zaghbi, and H. Groult, “Comparative Issues of Cathode Materials for Li-Ion Batteries,” *Inorganics*, vol. 2, pp. 132–154, 2014.
- [15] N. Nitta, F. Wu, J. T. Lee, and G. Yushin, “Li-ion battery materials: Present and future,” *Materials Today*, vol. 18, no. 5, pp. 252–264, 2015.
- [16] A. Fotouhi, D. J. Auger, K. Propp, and S. Longo, “Lithium-Sulfur Battery State-of-Charge Observability Analysis and Estimation,” *IEEE Transactions on Power Electronics*, vol. 33, no. 7, pp. 5847–5859, 2017.
- [17] M. Park, X. Zhang, M. Chung, G. B. Less, and A. M. Sastry, “A review of conduction phenomena in Li-ion batteries,” *Journal of Power Sources*, vol. 195, no. 24, pp. 7904–7929, 2010.
- [18] S. S. Zhang, “A review on the separators of liquid electrolyte Li-ion batteries,” *Journal of Power Sources*, vol. 164, pp. 351–364, 2007.

- [19] D. Aurbach, Y. Talyosef, B. Markovsky, E. Markevich, E. Zinigrad, L. Asraf, J. S. Gnanaraj, and H. J. Kim, “Design of electrolyte solutions for Li and Li-ion batteries: A review,” *Electrochimica Acta*, vol. 50, pp. 247–254, 2004.
- [20] J. W. Choi and D. Aurbach, “Promise and reality of post-lithium-ion batteries with high energy densities,” *Nature Reviews Materials*, vol. 1, pp. 1–15, 2016.
- [21] A. Eddahech, “Modélisation du vieillissement et détermination de l’état de santé de batteries lithium-ion pour application véhicule,” Thèse de Doctorat, Université de Bordeaux, 2013.
- [22] O. Briat, “Performances et fiabilité du stockage d’énergie pour le véhicule électrique et hybride,” HDR, Université de Bordeaux, 2016.
- [23] Y. C. Zhang, O. Briat, J. Y. Deletage, C. Martin, G. Gager, and J. M. Vinassa, “Characterization of external pressure effects on lithium-ion pouch cell,” in *Proceedings of the IEEE International Conference on Industrial Technology (ICIT) Lyon (France), 20-22 Feb, 2018*.
- [24] L. Zhang, X. Hu, Z. Wang, F. Sun, and D. G. Dorrell, “A review of supercapacitor modeling, estimation, and applications: A control / management perspective,” *Renewable and Sustainable Energy Reviews*, vol. 81, no. May 2017, pp. 1868–1878, 2018.
- [25] A. Cappelto, W. J. Cao, J. F. Luo, M. Hagen, D. Adams, A. Shelikeri, K. Xu, and J. P. Zheng, “Performance of wide temperature range electrolytes for Li-Ion capacitor pouch cells,” *Journal of Power Sources*, vol. 359, pp. 205–214, 2017.
- [26] N. El Ghossein, A. Sari, and P. Venet, “Nonlinear Capacitance Evolution of Lithium-Ion Capacitors Based on Frequency- and Time-Domain Measurements,” *IEEE Transactions on Power Electronics*, vol. 33, no. 7, pp. 5909–5916, 2018.
- [27] F. Sun, J. Gao, Y. Zhu, X. Pi, L. Wang, X. Liu, and Y. Qin, “A high performance lithium ion capacitor achieved by the integration of a Sn-C anode and a biomass-derived microporous activated carbon cathode,” *Nature*, no. September 2016, pp. 1–10, 2017.
- [28] Internatinal standard IEC 62660-1, *Secondary lithium-ion cells for the propulsion of electric road vehicles – Part 1: Performance testing*, IEC 62660. 2010.
- [29] Internatinal standard IEC62660-2, *Secondary lithium-ion cells for the propulsion of electric road vehicles – Part 2: Reliability and abuse testing*, IEC 62660. 2010.
- [30] Internatinal standard IEC62576, “Electric double-layer capacitors for use in hybrid electric vehicles – Test methods for electrical characteristics,” 2009.
- [31] A. Farmann and D. U. Sauer, “A study on the dependency of the open-circuit voltage on temperature and actual aging state of lithium-ion batteries,” *Journal of Power Sources*, vol. 347, pp. 1–13, 2017.
- [32] A. Marongiu, F. G. W. Nußbaum, W. Waag, M. Garmendia, and D. U. Sauer, “Comprehensive study of the influence of aging on the hysteresis behavior of a lithium iron phosphate cathode-based lithium ion battery - An experimental investigation of the hysteresis,” *Applied Energy*, vol. 171, pp. 629–645, 2016.
- [33] M. Dubarry, V. Svoboda, R. Hwu, and B. Yann Liaw, “Incremental capacity analysis and close-to-equilibrium OCV measurements to quantify capacity fade in commercial rechargeable lithium batteries,” *Electrochemical and Solid-State Letters*, vol. 9, p. A454, 2006.

- [34] C. Pastor-Fernandez, K. Uddin, G. H. Chouchelamane, W. D. Widanage, and J. Marco, "A comparison between electrochemical impedance spectroscopy and incremental capacity-Differential Voltage as Li-ion Diagnostic Techniques to Identify and Quantify the Effects of Degradation Modes within Battery Management Systems," *Journal of Power Sources*, vol. 360, pp. 301–318, 2017.
- [35] C. Lin, Q. Yu, R. Xiong, and L. Y. Wang, "A study on the impact of open circuit voltage tests on state of charge estimation for lithium-ion batteries," *Applied Energy*, vol. 205, no. 5, pp. 892–902, 2017.
- [36] N. Damay, C. Forgez, G. Friedrich, and M. P. Bichat, "Heterogeneous behavior modeling of a LiFePO₄-graphite cell using an equivalent electrical circuit," *Journal of Energy Storage*, vol. 12, pp. 167–177, 2017.
- [37] I. Baccouche, S. Jemmali, B. Manai, N. Omar, and N. Essoukri Ben Amara, "Improved OCV model of a Li-ion NMC battery for online SOC estimation using the extended Kalman filter," *Energies*, vol. 10, no. 6, pp. 1–22, 2017.
- [38] J. Kowal, E. Avaroglu, F. Chamekh, A. Šenfělds, T. Thien, D. Wijaya, and D. U. Sauer, "Detailed analysis of the self-discharge of supercapacitors," *Journal of Power Sources*, vol. 196, no. 1, pp. 573–579, 2011.
- [39] H. A. Andreas, "Self-Discharge in Electrochemical Capacitors," *Journal of The Electrochemical Society*, vol. 162, no. 5, 2015.
- [40] J. A. Rosero, J. A. Ortega, E. Aldabas, and L. Romeral, "Moving towards a more electric aircraft," *IEEE Aerospace and Electronic Systems Magazine*, vol. 22, no. 3, pp. 3–9, 2007.
- [41] C. Pernet and A. T. Isikveren, "Conceptual design of hybrid-electric transport aircraft," *Progress in Aerospace Sciences*, vol. 79, pp. 114–135, 2015.
- [42] D. Vutetakis, "Applications - Transportation Aviation: Battery," *Chemistry, Molecular Sciences and Chemical Engineering*, no. June, pp. 1–14, 2013.
- [43] M. Tariq, A. I. Maswood, C. J. Gajanayake, and A. K. Gupta, "Aircraft batteries: current trend towards more electric aircraft," *IET Electrical Systems in Transportation*, vol. 7, no. 2, pp. 93–103, 2016.
- [44] E. Iwama, P. L. Taberna, P. Azais, L. Brégeon, and P. Simon, "Characterization of commercial supercapacitors for low temperature applications," *Journal of Power Sources*, vol. 219, pp. 235–239, 2012.
- [45] X. Giraud, "Méthodes et outils pour la conception optimal des réseaux de distribution d'électricité dans les aéronefs," Thèse de Doctorat, Institut national des sciences appliquées de Toulouse, 2014.
- [46] N. Devillers, "Caractérisation et modélisation de composants de stockage électrochimique et électrostatique," Thèse de Doctorat, Université de Franche-Comté, 2012.
- [47] A. Nishizawa, J. Kallo, O. Garrot, and J. Weiss-Ungethüm, "Fuel cell and Li-ion battery direct hybridization system for aircraft applications," *Journal of Power Sources*, vol. 222, pp. 294–300, 2013.
- [48] R. Guo, Y. Zhang, and Q. Wang, "Comparison of emerging ground propulsion systems for electrified aircraft taxi operations," *Transportation Research Part C: Emerging Technologies*, vol. 44, pp. 98–109, 2014.

- [49] M. Hepperle, “Electric Flight–Potential and Limitations,” 2012.
- [50] “Graphene oxide for Lithium-Sulfur batteries,” Printed Electronics World, 2015.
- [51] F. Fusalba and J. Oriol, “L’électrification des aéronefs,” *Techniques de l’ingénieur*, 2018.
- [52] N. Williard, W. He, C. Hendricks, and M. Pecht, “Lessons learned from the 787 dreamliner issue on Lithium-Ion Battery reliability,” *Energies*, vol. 6, no. 9, pp. 4682–4695, 2013.
- [53] T. Song, Y. Li, J. Song, and Z. Zhang, “Airworthiness considerations of supply chain management from Boeing 787 Dreamliner battery issue,” *Procedia Engineering*, vol. 80, pp. 628–637, 2014.
- [54] X. Feng, M. Ouyang, X. Liu, L. Lu, Y. Xia, and X. He, “Thermal runaway mechanism of lithium ion battery for electric vehicles: A review,” *Energy Storage Materials*, vol. 10, no. May 2017, pp. 246–267, 2018.
- [55] S. Abada, “Compréhension et modélisation de l’emballage thermique de batteries Li-ion neuves et vieilles,” Thèse de Doctorat, Université Pierre et Marie Curie, 2016.
- [56] Anne-Marie BARES, “A350XWB Lithium Batteries A guide for fire fighters,” Airbus, 2015.
- [57] J. Jeevarajan, “Tolerance of Li-ion Pouch Cells to Varied Space Environment Pressures Lithium Power,” NASA, 2012.
- [58] Y. Zhang, O. Briat, J. Deletage, C. Martin, G. Gager, and J.-M. Vinassa, “Performance quantification of latest generation Li-ion batteries in wide temperature range,” in *Proceedings of the 43rd Annual Conference of the IEEE Industrial Electronics Society (IECON), Beijing (China), 29 Oct-01 Nov, 2017*.
- [59] M. Jenny, “RTCA Background on Standards for Lithium Batteries,” National Transportation Safety Board, 2013.
- [60] H. Liu, Z. Wei, W. He, and J. Zhao, “Thermal issues about Li-ion batteries and recent progress in battery thermal management systems: A review,” *Energy Conversion and Management*, vol. 150, no. May, pp. 304–330, 2017.
- [61] Y. Ji, Y. Zhang, and C.-Y. Wang, “Li-Ion Cell Operation at Low Temperatures,” *Journal of the Electrochemical Society*, vol. 160, no. 4, pp. A636–A649, 2013.
- [62] S. Günther, A. Bensmann, and R. Hanke-Rauschenbach, “Theoretical dimensioning and sizing limits of hybrid energy storage systems,” *Applied Energy*, vol. 210, no. October 2017, pp. 127–137, 2018.
- [63] I. S. Sarpal, A. Bensmann, J. Mähliß, D. Hennefeld, and R. Hanke-Rauschenbach, “Characterisation of batteries with E–P-curves: Quantifying the impact of operating conditions on battery performance,” *International Journal of Electrical Power and Energy Systems*, vol. 99, no. January, pp. 722–732, 2018.
- [64] X. Hu, S. Li, and H. Peng, “A comparative study of equivalent circuit models for Li-ion batteries,” *Journal of Power Sources*, vol. 198, pp. 359–367, 2012.
- [65] M. Ayadi, O. Briat, R. Lallemand, A. Eddahech, R. German, G. Coquery, and J. M. Vinassa, “Description of supercapacitor performance degradation rate during thermal cycling under constant voltage ageing test,” *Microelectronics Reliability*, vol. 54, no. 9–10, pp. 1944–1948, 2014.

- [66] R. Cousseau, N. Patin, C. Forgez, E. Monmasson, and L. Idkhajine, "Improved electrical model of aluminum electrolytic capacitor with anomalous diffusion for health monitoring," *Mathematics and Computers in Simulation*, vol. 131, pp. 268–282, 2017.
- [67] X. Tang, Y. Wang, C. Zou, K. Yao, Y. Xia, and F. Gao, "A novel framework for Lithium-ion battery modeling considering uncertainties of temperature and aging," *Energy Conversion and Management*, vol. 180, no. October 2018, pp. 162–170, 2019.
- [68] H. He, R. Xiong, H. Guo, and S. Li, "Comparison study on the battery models used for the energy management of batteries in electric vehicles," *Energy Conversion and Management*, vol. 64, pp. 113–121, 2012.
- [69] I. Baghdadi, O. Briat, A. Eddahech, J. M. Vinassa, and P. Gyan, "Electro-thermal model of lithium-ion batteries for electrified vehicles applications," in *Proceeding of IEEE International Symposium on Industrial Electronics (ISIE), Buzios (Brazil), 03-05 juin., 2015*.
- [70] M. Dubarry and B. Y. Liaw, "Development of a universal modeling tool for rechargeable lithium batteries," *Journal of Power Sources*, vol. 174, no. 2, pp. 856–860, 2007.
- [71] J. V. Barreras, E. Schaltz, S. J. Andreasen, and T. Minko, "Datasheet-based modeling of Li-Ion batteries," in *Proceedings of IEEE Vehicle Power and Propulsion Conference (VPPC), Seoul (Korea), 09-12 Oct., 2012*.
- [72] S. K. Kumar, A. A. B. M. Abduh, O. Sabih, and R. Yazami, "Temperature Effect on 'Ragone Plots' of Lithium-Ion Batteries," *Journal of the Electrochemical Society*, vol. 165, no. 3, pp. 674–679, 2018.
- [73] J. Jaguemont, L. Boulon, and Y. Dube, "Characterization and Modeling of a Hybrid-Electric-Vehicle Lithium-Ion Battery Pack at Low Temperatures," *IEEE Transactions on Vehicular Technology*, vol. 65, no. 1, pp. 1–14, 2016.
- [74] R. Mathieu, I. Baghdadi, O. Briat, P. Gyan, and J. M. Vinassa, "D-optimal design of experiments applied to lithium battery for ageing model calibration," *Energy*, vol. 141, pp. 2108–2119, 2017.
- [75] H. J. K. Shelley Derksen, "Backward, forward and stepwise automated subset selection algorithms: Frequency of obtaining authentic and noise variables," *The British Psychological Society*, pp. 265–282, 1992.
- [76] S. Waag, Wladislaw, Käbitz and D. U. Sauer, "Experimental investigation of the lithium-ion battery impedance characteristic at various conditions and aging states and its influence on the application," *Applied Energy*, vol. 102, pp. 885–897, 2013.
- [77] D. U. S. A. Farmann, W. Waag, "Application-specific electrical characterization of high power batteries with lithium titanate anodes for electric vehicles," *Energy*, vol. 112, pp. 294–306, 2016.
- [78] P. Cicconi, D. Landi, and M. Germani, "Thermal analysis and simulation of a Li-ion battery pack for a lightweight commercial EV," *Applied Energy*, vol. 192, pp. 159–177, 2017.
- [79] W. B. Gu and C. Y. Wang, "Thermal-Electrochemical Modeling of Battery Systems," *Journal of The Electrochemical Society*, vol. 147, no. 8, p. 2910, 2000.
- [80] J. Jaguemont, N. Omar, M. Abdel-Monem, P. Van den Bossche, and J. Van Mierlo, "Fast-charging investigation on high-power and high-energy density pouch cells with 3D-thermal model development," *Applied Thermal Engineering*, vol. 128, pp. 1282–1296, 2018.

- [81] G. Liu, M. Ouyang, L. Lu, J. Li, and J. Hua, "A highly accurate predictive-adaptive method for lithium-ion battery remaining discharge energy prediction in electric vehicle applications," *Applied Energy*, vol. 149, pp. 297–314, 2015.
- [82] Q. Huang, M. Yan, and Z. Jiang, "Thermal study on single electrodes in lithium-ion battery," *Journal of Power Sources*, vol. 156, no. 2, pp. 541–546, 2006.
- [83] B. Manikandan, C. Yap, and P. Balaya, "Towards Understanding Heat Generation Characteristics of Li-Ion Batteries by Calorimetry, Impedance, and Potentiometry Studies," *Journal of The Electrochemical Society*, vol. 164, no. 12, pp. A2794–A2800, 2017.
- [84] A. Eddahech, O. Briat, and J. M. Vinassa, "Thermal characterization of a high-power lithium-ion battery: Potentiometric and calorimetric measurement of entropy changes," *Energy*, vol. 61, pp. 432–439, 2013.
- [85] J. Marcicki and X. G. Yang, "Model-Based Estimation of Reversible Heat Generation in Lithium-Ion Cells," *Journal of the Electrochemical Society*, vol. 161, no. 12, pp. A1794–A1800, 2014.
- [86] G. Liu, M. Ouyang, L. Lu, J. Li, and X. Han, "Analysis of the heat generation of lithium-ion battery during charging and discharging considering different influencing factors," *Journal of Thermal Analysis and Calorimetry*, vol. 116, no. 2, pp. 1001–1010, 2014.
- [87] C. Forgez, D. Vinh Do, G. Friedrich, M. Morcrette, and C. Delacourt, "Thermal modeling of a cylindrical LiFePO₄/graphite lithium-ion battery," *Journal of Power Sources*, vol. 195, no. 9, pp. 2961–2968, 2010.
- [88] I. Zilberman, A. Rheinfeld, and A. Jossen, "Uncertainties in entropy due to temperature path dependent voltage hysteresis in Li-ion cells," *Journal of Power Sources*, vol. 395, no. February, pp. 179–184, 2018.
- [89] M. Nakayama, K. Fukuda, T. Araki, and K. Onda, "Thermal behavior of nickel metal hydride battery during rapid charge and discharge cycles," *Journal of Power Sources*, vol. 157, no. 4, pp. 30–39, 2006.
- [90] T. Wang, K. J. Tseng, J. Zhao, and Z. Wei, "Thermal investigation of lithium-ion battery module with different cell arrangement structures and forced air-cooling strategies," *Applied Energy*, vol. 134, pp. 229–238, 2014.
- [91] LG, *Technical Information of LG 18650HG2 (3.0Ah)*, vol. 2. 2014.
- [92] SAMSUNG, *Introduction of INR18650 - 25R*. 2013.
- [93] C. Pastor-Fernandez, K. Uddin, G. H. Chouchelamane, W. D. Widanage, and J. Marco, "A comparison between electrochemical impedance spectroscopy and incremental capacity-differential voltage as Li-ion diagnostic techniques to identify and quantify the effects of degradation modes within battery management systems," *Journal of Power Sources*, vol. 360, pp. 301–318, 2017.
- [94] C. R. Birkl, M. R. Roberts, E. McTurk, P. G. Bruce, and D. A. Howey, "Degradation diagnostics for lithium ion cells," *Journal of Power Sources*, vol. 341, pp. 373–386, 2017.
- [95] P. B. Matthieu Dubarry, Nan Qin, "Calendar Aging of commercial Li-ion cells of different chemistries – A review," *Current Opinion in Electrochemistry*, 2018.
- [96] Y. Gao, J. Jiang, C. Zhang, W. Zhang, Z. Ma, and Y. Jiang, "Lithium-ion battery aging mechanisms and life model under different charging stresses," *Journal of Power*

- Sources, vol. 356, pp. 103–114, 2017.
- [97] H. Buqa, A. Würsig, J. Vetter, M. E. Spahr, F. Krumeich, and P. Novák, “SEI film formation on highly crystalline graphitic materials in lithium-ion batteries,” *Journal of Power Sources*, vol. 153, no. 2, pp. 385–390, 2006.
- [98] M. Broussely, S. Herreyre, P. Biensan, P. Kasztejna, K. Nechev, and R. J. Staniewicz, “Aging mechanism in Li ion cells and calendar life predictions,” *Journal of Power Sources*, vol. 97–98, pp. 13–21, 2001.
- [99] K. Edström, T. Gustafsson, and J. O. Thomas, “The cathode-electrolyte interface in the Li-ion battery,” *Electrochimica Acta*, vol. 50, no. 2–3 SPEC. ISS., pp. 397–403, 2004.
- [100] X. Han, M. Ouyang, L. Lu, J. Li, Y. Zheng, and Z. Li, “A comparative study of commercial lithium ion battery cycle life in electrical vehicle: Aging mechanism identification,” *Journal of Power Sources*, vol. 251, pp. 38–54, 2014.
- [101] E. Peled, “Advanced Model for Solid Electrolyte Interphase Electrodes in Liquid and Polymer Electrolytes,” *Journal of The Electrochemical Society*, vol. 144, no. 8, p. 208, 1997.
- [102] A. S. Prakash, P. Manikandan, K. Ramesha, M. Sathiya, J. M. Tarascon, and A. K. Shukla, “Solution-combustion synthesized nanocrystalline $\text{Li}_4\text{Ti}_5\text{O}_{12}$ as high-rate performance li-ion battery anode,” *Chemistry of Materials*, vol. 22, no. 9, pp. 2857–2863, 2010.
- [103] M. G. S. R. Thomas, “AC Impedance Analysis of Polycrystalline Insertion Electrodes: Application to $\text{Li}(1-x)\text{CoO}_2$,” *Journal of The Electrochemical Society*, vol. 132, no. 7, p. 1521, 1985.
- [104] D. Aurbach, “Review of selected electrode–solution interactions which determine the performance of Li and Li ion batteries,” *Journal of Power Sources*, vol. 89, pp. 206–218, 2000.
- [105] M. Gauthier, T. J. Carney, A. Grimaud, L. Giordano, N. Pour, H.-H. Chang, D. P. Fenning, S. F. Lux, O. Paschos, C. Bauer, F. Maglia, S. Lupart, P. Lamp, and Y. Shao-Horn, “Electrode – Electrolyte Interface in Li-Ion Batteries: Current Understanding and New Insights,” *The Journal of Physical Chemistry Letters*, vol. 6, no. 4653–4672, 2015.
- [106] A. Senyshyn, M. J. Mühlbauer, O. Dolotko, and H. Ehrenberg, “Low-temperature performance of Li-ion batteries: The behavior of lithiated graphite,” *Journal of Power Sources*, vol. 282, pp. 235–240, 2015.
- [107] F. Savoye, P. Venet, M. Millet, and J. Groot, “Impact of periodic current pulses on Li-ion battery performance,” *IEEE Transactions on Industrial Electronics*, vol. 59, no. 9, pp. 3481–3488, 2012.
- [108] Q. Liu, C. Du, B. Shen, P. Zuo, X. Cheng, Y. Ma, G. Yin, and Y. Gao, “Understanding undesirable anode lithium plating issues in lithium-ion batteries,” *RSC Advances*, vol. 6, no. 91, pp. 88683–88700, 2016.
- [109] M. Dubarry, C. Truchot, B. Y. Liaw, K. Gering, S. Sazhin, D. Jamison, and C. Michelbacher, “Evaluation of commercial lithium-ion cells based on composite positive electrode for plug-in hybrid electric vehicle applications. Part II. Degradation mechanism under 2 C cycle aging,” *Journal of Power Sources*, vol. 196, pp. 10336–10343, 2011.
- [110] T. Rauhala, K. Jalkanen, T. Romann, E. Lust, N. Omar, and T. Kallio, “Low-temperature

- aging mechanisms of commercial graphite/LiFePO₄ cells cycled with a simulated electric vehicle load profile—A post-mortem study,” *Journal of Energy Storage*, vol. 20, no. June, pp. 344–356, 2018.
- [111] M. Wohlfahrt-Mehrens, C. Vogler, and J. Garche, “Aging mechanisms of lithium cathode materials,” *Journal of Power Sources*, vol. 127, no. 1–2, pp. 58–64, 2004.
- [112] J. Xu, S. Dou, H. Liu, and L. Dai, “Cathode materials for next generation lithium ion batteries,” *Nano Energy*, vol. 2, no. 4, pp. 439–442, 2013.
- [113] M. Bercibar, F. Devriendt, M. Dubarry, I. Villarreal, N. Omar, W. Verbeke, and J. Van Mierlo, “Online state of health estimation on NMC cells based on predictive analytics,” *Journal of Power Sources*, vol. 320, pp. 239–250, 2016.
- [114] C. Delacourt, A. Kwong, X. Liu, R. Qiao, W. L. Yang, P. Lu, S. J. Harris, and V. Srinivasan, “Effect of Manganese Contamination on the Solid-Electrolyte-Interphase Properties in Li-Ion Batteries,” *Journal of the Electrochemical Society*, vol. 160, no. 8, pp. A1099–A1107, 2013.
- [115] A. Bhandari and J. Bhattacharya, “Review—Manganese Dissolution from Spinel Cathode: Few Unanswered Questions,” *Journal of The Electrochemical Society*, vol. 164, no. 2, pp. A106–A127, 2017.
- [116] M. Koltypin, D. Aurbach, L. Nazar, and B. Ellis, “More on the performance of LiFePO₄ electrodes—The effect of synthesis route, solution composition, aging, and temperature,” *Journal of Power Sources*, vol. 174, no. 2, pp. 1241–1250, 2007.
- [117] J. Vetter, P. Novak, M. R. Wagner, C. Veit, K. C. Moeller, J. O. Besenhard, M. Winter, M. Wohlfahrt-Mehrens, C. Vogler, and A. Hammouche, “Ageing mechanisms in lithium-ion batteries,” *Journal of Power Sources*, vol. 147, no. 1–2, pp. 269–281, 2005.
- [118] R. German, O. Briat, A. Sari, P. Venet, M. Ayadi, Y. Zitouni, and J. M. Vinassa, “Impact of high frequency current ripple on supercapacitors ageing through floating ageing tests,” *Microelectronics Reliability*, vol. 53, no. 9–11, pp. 1643–1647, 2013.
- [119] Y. Liu, B. Soucaze-Guillous, P. L. Taberna, and P. Simon, “Understanding of carbon-based supercapacitors ageing mechanisms by electrochemical and analytical methods,” *Journal of Power Sources*, vol. 366, pp. 123–130, 2017.
- [120] M. He, K. Fic, E. Frackowiak, P. Novák, and E. J. Berg, “Ageing phenomena in high-voltage aqueous supercapacitors investigated by in situ gas analysis,” *Energy and Environmental Science*, vol. 9, no. 2, pp. 623–633, 2016.
- [121] N. Omar, H. Gualous, J. Salminen, G. Mulder, A. Samba, Y. Firouz, M. A. Monem, P. Van Den Bossche, and J. Van Mierlo, “Electrical double-layer capacitors: Evaluation of ageing phenomena during cycle life testing,” *Journal of Applied Electrochemistry*, vol. 44, no. 4, pp. 509–522, 2014.
- [122] R. German, A. Sari, P. Venet, Y. Zitouni, O. Briat, and J. M. Vinassa, “Ageing law for supercapacitors floating ageing,” *IEEE International Symposium on Industrial Electronics*, pp. 1773–1777, 2014.
- [123] N. El Ghossein, A. Sari, and P. Venet, “Effects of the Hybrid Composition of Commercial Lithium-Ion Capacitors on their Floating Aging,” *IEEE Transactions on Power Electronics*, vol. 8993, no. c, pp. 1–8, 2018.
- [124] B. P. Matadi, S. Geniès, A. Delaille, C. Chabrol, E. de Vito, M. Bardet, J.-F. Martin, L. Daniel, and Y. Bultel, “Irreversible Capacity Loss of Li-Ion Batteries Cycled at Low Temperature Due to an Untypical Layer Hindering Li Diffusion into Graphite

- Electrode,” *Journal of The Electrochemical Society*, vol. 164, no. 12, pp. A2374–A2389, 2017.
- [125] K. Kumai, H. Miyashiro, Y. Kobayashi, K. Takei, and R. Ishikawa, “Gas generation mechanism due to electrolyte decomposition in commercial lithium-ion cell,” *Journal of Power Sources*, vol. 81–82, pp. 715–719, 1999.
- [126] M. Ecker, N. Nieto, S. Käbitz, J. Schmalstieg, H. Blanke, A. Warnecke, and D. U. Sauer, “Calendar and cycle life study of Li(NiMnCo)O₂-based 18650 lithium-ion batteries,” *Journal of Power Sources*, vol. 248, pp. 839–851, 2014.
- [127] J. Schmalstieg, S. Käbitz, M. Ecker, and D. U. Sauer, “A holistic aging model for Li(NiMnCo)O₂ based 18650 lithium-ion batteries,” *Journal of Power Sources*, vol. 257, pp. 325–334, 2014.
- [128] I. Baghdadi, O. Briat, J.-Y. Delétage, P. Gyan, and J.-M. Vinassa, “Lithium battery aging model based on Dakin’s degradation approach,” *Journal of Power Sources*, vol. 325, pp. 273–285, 2016.
- [129] M. Naumann, M. Schimpe, P. Keil, H. C. Hesse, and A. Jossen, “Analysis and modeling of calendar aging of a commercial LiFePO₄/graphite cell,” *Journal of Energy Storage*, vol. 17, pp. 153–169, 2018.
- [130] M. Dubarry, N. Qin, and P. Brooker, “Calendar aging of commercial Li-ion cells of different chemistries – A review,” *Current Opinion in Electrochemistry*, vol. 9, pp. 106–113, 2018.
- [131] J. Jaguemont, L. Boulon, and Y. Dubé, “A comprehensive review of lithium-ion batteries used in hybrid and electric vehicles at cold temperatures,” *Applied Energy*, vol. 164, pp. 99–114, 2016.
- [132] E. H. El Brouji, O. Briat, J. M. Vinassa, N. Bertrand, and E. Woïrgard, “Impact of calendar life and cycling ageing on supercapacitor performance,” *IEEE Transactions on Vehicular Technology*, vol. 58, no. 8, pp. 3917–3929, 2009.
- [133] M. Lewerenz, S. Käbitz, M. Knips, J. Münnix, J. Schmalstieg, A. Warnecke, and D. U. Sauer, “New method evaluating currents keeping the voltage constant for fast and highly resolved measurement of Arrhenius relation and capacity fade,” *Journal of Power Sources*, vol. 353, pp. 144–151, 2017.
- [134] J. Jaguemont, L. Boulon, P. Venet, Y. Dube, and A. Sari, “Lithium-Ion Battery Aging Experiments at Subzero Temperatures and Model Development for Capacity Fade Estimation,” *IEEE Transactions on Vehicular Technology*, vol. 65, no. 6, pp. 4328–4343, 2016.
- [135] J. Jaguemont, L. Boulon, P. Venet, Y. Dube, and A. Sari, “Lithium Ion Battery Aging Experiments at Sub-Zero Temperatures and Model Development for Capacity Fade Estimation,” *IEEE Transactions on Vehicular Technology*, vol. 9545, no. c, pp. 1–1, 2015.
- [136] M. Ecker, J. B. Gerschler, J. Vogel, S. Käbitz, F. Hust, P. Dechent, and D. U. Sauer, “Development of a lifetime prediction model for lithium-ion batteries based on extended accelerated aging test data,” *Journal of Power Sources*, vol. 215, pp. 248–257, 2012.
- [137] S. Kabitz, J. B. Gerschler, M. Ecker, Y. Yurdagel, B. Emmermacher, D. André, T. Mitsch, and D. U. Sauer, “Cycle and calendar life study of a graphite|LiNi_{1/3}Mn_{1/3}Co_{1/3}O₂ Li-ion high energy system. Part A: Full cell characterization,” *Journal of Power Sources*, vol. 239, pp. 572–583, 2013.

- [138] M. Dubarry, V. Svoboda, R. Hwu, and B. Y. Liaw, "Capacity and power fading mechanism identification from a commercial cell evaluation," *Journal of Power Sources*, vol. 165, pp. 566–572, 2007.
- [139] B. Y. Liaw, E. P. Roth, R. G. Jungst, G. Nagasubramanian, H. L. Case, and D. H. Doughty, "Correlation of Arrhenius behaviors in power and capacity fades with cell impedance and heat generation in cylindrical lithium-ion cells," *Journal of Power Sources*, vol. 119–121, pp. 874–886, 2003.
- [140] E. Redondo-Iglesias, P. Venet, and S. Pelissier, "Eyring acceleration model for predicting calendar ageing of lithium-ion batteries," *Journal of Energy Storage*, vol. 13, pp. 176–183, 2017.
- [141] T. Waldmann, M. Wilka, M. Kasper, M. Fleischhammer, and M. Wohlfahrt-Mehrens, "Temperature dependent ageing mechanisms in Lithium-ion batteries - A Post-Mortem study," *Journal of Power Sources*, vol. 262, pp. 129–135, 2014.
- [142] X. Han, M. Ouyang, L. Lu, and J. Li, "Cycle life of commercial lithium-ion batteries with lithium titanium oxide anodes in electric vehicles," *Energies*, vol. 7, pp. 4895–4909, 2014.
- [143] M. B. Pinson and M. Z. Bazant, "Theory of SEI Formation in Rechargeable Batteries : Capacity Fade , Accelerated Aging and Lifetime Prediction," vol. 160, no. 2, 2013.
- [144] J. Xu, S. L. Chou, Q. F. Gu, H. K. Liu, and S. X. Dou, "The effect of different binders on electrochemical properties of $\text{LiNi}_{1/3}\text{Mn}_{1/3}\text{Co}_{1/3}\text{O}_2$ cathode material in lithium ion batteries," *Journal of Power Sources*, vol. 225, pp. 172–178, 2013.
- [145] H. Shang, Z. Zuo, L. Yu, F. Wang, F. He, and Y. Li, "Low-Temperature Growth of All-Carbon Graphdiyne on a Silicon Anode for High-Performance Lithium-Ion Batteries," *Advanced Materials*, vol. 30, no. 27, pp. 1–9, 2018.
- [146] A. Eddahech, O. Briat, and J. M. Vinassa, "Lithium-ion battery performance improvement based on capacity recovery exploitation," *Electrochimica Acta*, vol. 114, pp. 750–757, 2013.
- [147] D. Liu, J. Pang, J. Zhou, Y. Peng, and M. Pecht, "Prognostics for state of health estimation of lithium-ion batteries based on combination Gaussian process functional regression," *Microelectronics Reliability*, vol. 53, no. 6, pp. 832–839, 2013.
- [148] M. Lewerenz, P. Dechent, and D. U. Sauer, "Investigation of capacity recovery during rest period at different states-of-charge after cycle life test for prismatic $\text{Li}(\text{Ni}_{1/3}\text{Mn}_{1/3}\text{Co}_{1/3})\text{O}_2$ -graphite cells," *Journal of Energy Storage*, vol. 21, no. January, pp. 680–690, 2019.
- [149] Daniel-Ioan, A. Stroe, and V. Knap, "Accelerated Lifetime Testing of High Power Lithium Titanate Oxide Batteries," in *Proceedings of the 10th Annual Conference of the IEEE Energy Conversion Congress and Expo (ECCE), Portland (USA), 23-27 Sept, 2018*, pp. 3857–3863.
- [150] R. Chaari, O. Briat, J. Y. Delétage, and J. Vinassa, "Performances regeneration of supercapacitors during accelerated ageing tests in power cycling Keywords Power cycling tests for accelerated ageing of supercapacitors," in *Proceedings of the 14th Annual Conference of the IEEE European Conference on Power Electronics and Applications, Birmingham(UK), 23-27 Sept, 2011*, pp. 1–7.
- [151] V. Ruiz, A. Pfrang, A. Kriston, N. Omar, P. Van den Bossche, and L. Boon-Brett, "A review of international abuse testing standards and regulations for lithium ion batteries

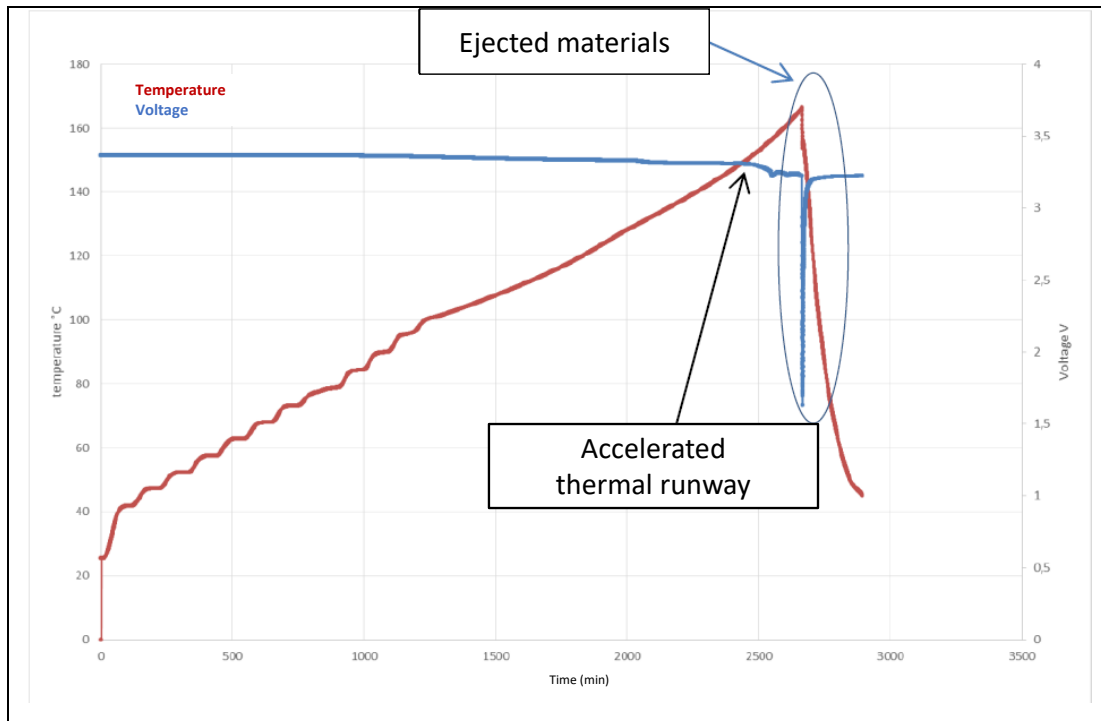
- in electric and hybrid electric vehicles,” *Renewable and Sustainable Energy Reviews*, vol. 81, no. June 2016, pp. 1427–1452, 2018.
- [152] European Commission, “General overview on safety/abuse test standards for Li-ion batteries,” 2013.
- [153] Y. Fu, S. Lu, L. Shi, X. Cheng, and H. Zhang, “Ignition and combustion characteristics of lithium ion batteries under low atmospheric pressure,” *Energy*, vol. 161, pp. 38–45, 2018.
- [154] A. Barré, B. Deguilhem, S. Grolleau, M. Gérard, F. Suard, and D. Riu, “A review on lithium-ion battery ageing mechanisms and estimations for automotive applications,” *Journal of Power Sources*, vol. 241, pp. 680–689, 2013.
- [155] R. Xiong, L. Li, and J. Tian, “Towards a smarter battery management system: A critical review on battery state of health monitoring methods,” *Journal of Power Sources*, vol. 405, no. 5, pp. 18–29, 2018.
- [156] Y. Zou, X. Hu, H. Ma, and S. E. Li, “Combined State of Charge and State of Health estimation over lithium-ion battery cell cycle lifespan for electric vehicles,” *Journal of Power Sources*, vol. 273, pp. 793–803, 2015.
- [157] L. Ungurean, G. Carstoiu, M. V. Micea, and V. Groza, “Battery state of health estimation: a structured review of models, methods and commercial devices,” *International Journal of Energy Research*, vol. 41, pp. 151–181, 2017.
- [158] J. Wang, P. Liu, J. Hicks-Garner, E. Sherman, S. Soukiazian, M. Verbrugge, H. Tatara, J. Musser, and P. Finamore, “Cycle-life model for graphite-LiFePO₄ cells,” *Journal of Power Sources*, vol. 196, no. 8, pp. 3942–3948, 2011.
- [159] A. Eddahech, O. Briat, and J. M. Vinassa, “Determination of lithium-ion battery state-of-health based on constant-voltage charge phase,” *Journal of Power Sources*, vol. 258, pp. 218–227, 2014.
- [160] M. Dubarry, C. Truchot, M. Cugnet, B. Y. Liaw, K. Gering, S. Sazhin, D. Jamison, and C. Michelbacher, “Evaluation of commercial lithium-ion cells based on composite positive electrode for plug-in hybrid electric vehicle applications. Part I: Initial characterizations,” *Journal of Power Sources*, vol. 196, pp. 10328–10335, 2011.
- [161] T. Goh, M. Park, M. Seo, J. G. Kim, and S. W. Kim, “Capacity estimation algorithm with a second-order differential voltage curve for Li-ion batteries with NMC cathodes,” *Energy*, vol. 135, pp. 257–268, 2017.
- [162] J. Cannarella and C. B. Arnold, “Stress evolution and capacity fade in constrained lithium-ion pouch cells,” *Journal of Power Sources*, vol. 245, pp. 745–751, 2014.
- [163] X. M. Liu and C. B. Arnold, “Effects of Cycling Ranges on Stress and Capacity Fade in Lithium-Ion Pouch Cells,” *Journal of The Electrochemical Society*, vol. 163, no. 13, pp. A2501–A2507, 2016.
- [164] H. Dai, C. Yu, X. Wei, and Z. Sun, “State of charge estimation for lithium-ion pouch batteries based on stress measurement,” *Energy*, vol. 129, pp. 16–27, 2017.
- [165] B. Rieger, S. Schlueter, S. V Erhard, J. Schmalz, G. Reinhart, and A. Jossen, “Multi-scale investigation of thickness changes in a commercial pouch type lithium-ion battery,” *Journal of Energy Storage*, vol. 6, pp. 213–221, 2016.
- [166] J. H. Lee, H. M. Lee, and S. Ahn, “Battery dimensional changes occurring during charge / discharge cycles - Thin rectangular lithium ion and polymer cells cycles — thin

- rectangular lithium ion and polymer cells,” *Journal of po*, no. June 2003, pp. 1–6, 2003.
- [167] Z. Mao, M. Farkhondeh, M. Pritzker, M. Fowler, and Z. Chen, “Calendar Aging and Gas Generation in Commercial Graphite/NMC-LMO Lithium-Ion Pouch Cell,” *Journal of The Electrochemical Society*, vol. 164, no. 14, pp. A3469–A3483, 2017.
- [168] B. Fridholm, T. Wik, and M. Nilsson, “Robust recursive impedance estimation for automotive lithium-ion batteries,” *Journal of Power Sources*, vol. 304, pp. 33–41, 2016.
- [169] and J. N. Marc Doyle, Thomas F. Fuller, “Modeling of Galvanostatic Charge and Discharge of the Lithium/Polymer/Insertion Cell,” *Journal of The Electrochemical Society*, vol. 140, no. 6, p. 1526, 1993.
- [170] C. Weng, J. Sun, and H. Peng, “A unified open-circuit-voltage model of lithium-ion batteries for state-of-charge estimation and state-of-health monitoring,” *Journal of Power Sources*, vol. 258, pp. 228–237, 2014.
- [171] E. Riviere, P. Venet, A. Sari, F. Meniere, and Y. Bultel, “LiFePO₄ battery state of health online estimation using electric vehicle embeded incremental capacity analysis,” 11th IEEE Vehicle Power and Propulsion Conference (VPPC), Canada (Montreal), 19–22 oct., 2015.
- [172] Y. Li, M. Abdel-Monem, R. Gopalakrishnan, M. Berecibar, E. Nanini-Maury, N. Omar, P. van den Bossche, and J. Van Mierlo, “A quick on-line state of health estimation method for Li-ion battery with incremental capacity curves processed by Gaussian filter,” *Journal of Power Sources*, vol. 373, pp. 40–53, 2018.
- [173] M. Berecibar, M. Garmendia, I. Gandiaga, J. Crego, and I. Villarreal, “State of health estimation algorithm of LiFePO₄ battery packs based on differential voltage curves for battery management system application,” *Energy*, vol. 103, pp. 784–796, 2016.
- [174] F. Yang, D. Wang, Y. Zhao, K. L. Tsui, and S. J. Bae, “A study of the relationship between coulombic efficiency and capacity degradation of commercial lithium-ion batteries,” *Energy*, vol. 145, pp. 486–495, 2018.
- [175] L. Zheng, J. Zhu, D. D. C. Lu, G. Wang, and T. He, “Incremental capacity analysis and differential voltage analysis based state of charge and capacity estimation for lithium-ion batteries,” *Energy*, vol. 150, pp. 759–769, 2018.
- [176] J. Jaguemont, L. Boulon, and Y. Dubé, “A comprehensive review of lithium-ion batteries used in hybrid and electric vehicles at cold temperatures,” *Applied Energy*, vol. 164, pp. 99–114, 2016.
- [177] M. Ecker, P. Shafiei Sabet, and D. U. Sauer, “Influence of operational condition on lithium plating for commercial lithium-ion batteries – Electrochemical experiments and post-mortem-analysis,” *Applied Energy*, vol. 206, no. March, pp. 934–946, 2017.
- [178] M. Dubarry, C. Truchot, and B. Y. Liaw, “Synthesize battery degradation modes via a diagnostic and prognostic model,” *Journal of Power Sources*, vol. 219, pp. 204–216, 2012.
- [179] X. Feng, J. Sun, M. Ouyang, X. He, L. Lu, X. Han, M. Fang, and H. Peng, “Characterization of large format lithium ion battery exposed to extremely high temperature,” *Journal of Power Sources*, vol. 272, pp. 457–467, 2014.
- [180] A. Eddahech, O. Briat, and J. M. Vinassa, “Performance comparison of four lithium-ion battery technologies under calendar aging,” *Energy*, vol. 84, pp. 542–550, 2015.
- [181] M. Berecibar, M. Dubarry, N. Omar, I. Villarreal, and J. Van Mierlo, “Degradation

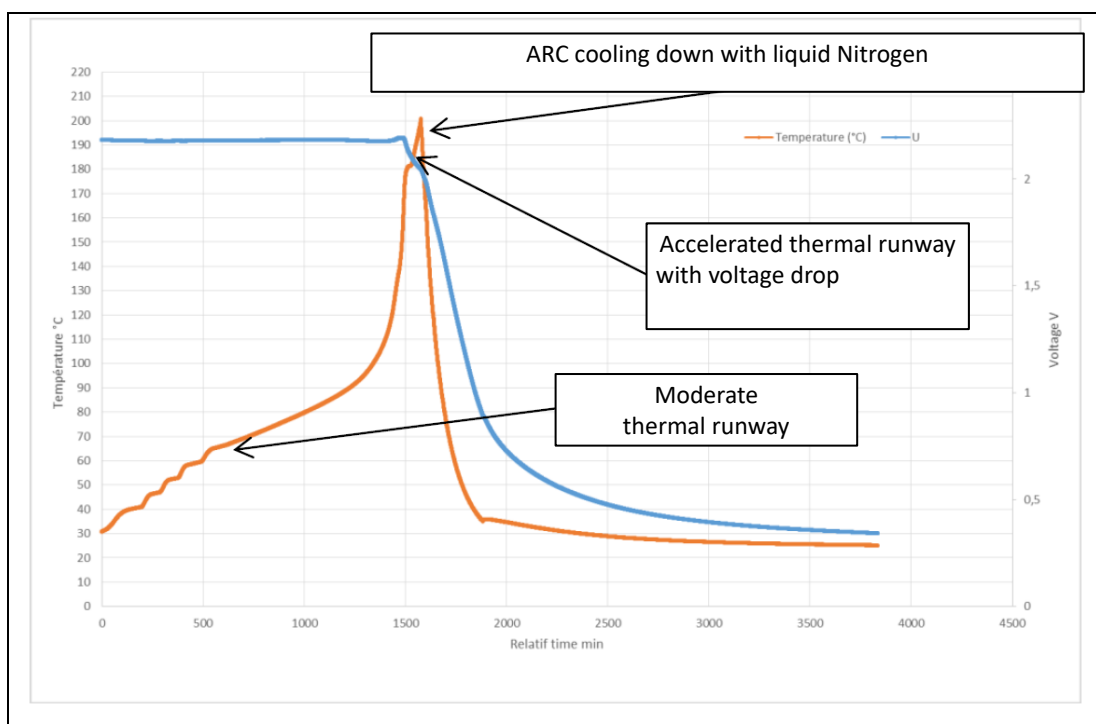
- mechanism detection for NMC batteries based on Incremental Capacity curves,” 12th IEEE Vehicle Power and Propulsion Conference (VPPC), China (Hangzhou), 17-20 Oct., 2016.
- [182] X. Li, J. Jiang, L. Y. Wang, D. Chen, Y. Zhang, and C. Zhang, “A capacity model based on charging process for state of health estimation of lithium ion batteries,” *Applied Energy*, vol. 177, pp. 537–543, 2016.
- [183] Y. C. Zhang, O. Briat, J. Delétage, C. Martin, N. Chadourne, and J. M. Vinassa, “Efficient state of health estimation of Li-ion battery under several ageing types for aeronautic applications,” *Microelectronics Reliability*, vol. 88–90, no. May, pp. 1231–1235, 2018.
- [184] U. Ozdemir, Y. O. Aktas, A. Vuruskan, Y. Dereli, A. F. Tarhan, K. Demirbag, A. Erdem, G. D. Kalaycioglu, I. Ozkol, and G. Inalhan, “Design of a commercial hybrid VTOL UAV system,” *Journal of Intelligent and Robotic Systems: Theory and Applications*, vol. 74, no. 1–2, pp. 371–393, 2014.
- [185] Y. Zhang, O. Briat, J.-Y. Deletage, C. Martin, G. Gager, and J.-M. Vinassa, “Characterization of external pressure effects on lithium-ion pouch cell,” in *2018 IEEE International Conference on Industrial Technology (ICIT)*, 2018, pp. 2055–2059.

Annexe

Annexe 1 Temperature and voltage of LFP/Graphite 26650 cell from K2 Energy during thermal stability test



Annexe 2 Temperature and voltage of Li-S pouch cell from Oxis during thermal stability test



Annexe 3 Fitted parameters on IC curves by Gaussian Lorentzian mixed function for
LG

Ageing type	Time (h)	Cycle No.	Normalized capacity (%)	Normalized resistance (%)	Area of peak 3 (Ah)	Location of peak 1 (V)
Calendar ageing 55°C	0	n/a	100	100	1.57	4.03
	1423		92.75	109	1.35	4.01
	2843		88.82	115	1.29	4.01
	4435		85.35	124	1.11	3.99
	5850		82.42	134	1.05	3.98
Calendar ageing - 20°C	0	n/a	100	100	1.56	4.02
	1443		97.57	99	1.50	4.02
	2855		96.37	104	1.42	4.02
	4946		95.40	98	1.41	4.023
Power cycling 45°C	0	0	100	100	1.57	4.025
	1082	760	80.29	115	0.99	4.021
	2950	2320	70.70	147	0.78	3.99
	3853	3127	65.70	169	0.75	3.98
	4301	4301	62.98	180	0.76	3.97
Power cycling 0°C	0	0	100	100	1.57	4.02
	530	228	50.10	258	0.65	3.95
	590	638	25.13	358	0.39	3.91

Annexe 4 Fitted parameters on IC curves by Gaussian Lorentzian mixed function for
Samsung

Ageing type	Time (h)	Cycle No.	Normalized capacity (%)	Normalized resistance (%)	Area of peak 3 (Ah)	Location of peak 1 (V)
Calendar ageing 55°C	0	n/a	100	100	1.47	3.96
	1442		93.31	120	1.43	3.81
	2811		88.22	122	1.39	3.77
	4235		85.58	125	1.38	3.74
	5828		82.71	131	1.34	3.71
Calendar ageing - 20°C	0	n/a	100	100	1.47	3.96
	1443		98.56	100	1.41	3.92
	2855		98.04	101	1.40	3.90
	4476		97.42	104	1.38	3.89
	4946		97	102	1.37	3.89
Power cycling 45°C	0	0	100	100	1.49	3.97
	639	384	83.07	148	1.16	3.76
	1098	699	72.98	182	0.97	3.66
	1405	938	66.89	207	0.83	3.60
Power cycling 0°C	0	0	100	100	1.42	3.9
	684	492	91.45	119	1.09	3.85
	937	748	86.05	135	0.9	3.80
	1675	1574	60.44	251	0.16	3.60

Titre : Evaluation des performances et du vieillissement des éléments de stockage d'énergie électrochimiques pour l'usage aéronautique

Résumé : Dans un contexte de progression du stockage d'énergie sous forme électrochimique dans les transports, notamment dans l'aéronautique, les problématiques de performance, de fiabilité, de sûreté de fonctionnement et de durée de vie du stockeur sont essentielles pour utilisateurs. Cette thèse se focalise ces voltes pour l'avion plus électrique. Les technologies étudiées correspondent à des éléments commerciaux de dernière génération de type Lithium-ion (NMC/graphite+SiO, NCA/graphite, LFP/graphite, NMC/LTO), Lithium-Soufre (Li-S), supercondensateur et hybride (LiC). Une première partie de ce manuscrit s'attache à la quantification des performances des différents éléments dans l'environnement aéronautique [-20°C, 55°C] et pour l'usage aéronautique. Un modèle comportemental de type électro-thermique est développé et validé. La seconde partie est consacrée à la quantification du vieillissement des différents éléments. Les résultats de vieillissement calendaire et en cyclage actif sont présentés ainsi que ceux des tests abusifs. Une méthode d'estimation de l'état de santé (SOH) des éléments basés sur l'analyse de la capacité incrémentale (ICA) est proposée. Enfin, l'évaluation de la robustesse des éléments de stockage lors de tests de vieillissement accéléré avec un profil spécifique à l'usage aéronautique est proposé. Les modèles de vieillissement et la méthode d'estimation de SOH proposés précédemment sont utilisés ici pour évaluer l'impact de la température sur la vitesse de dégradation et pour estimer le SOH des cellules vieilles à l'aide de ce profil aéronautique.

Mots clés : Batteries Lithium, Supercondensateurs, Lithium-ion capacitors, performance, basse température, vieillissement calendaire, cyclage actif, tests abusifs, modèle électro-thermique, Ragone non-isotherme, loi de vieillissement, estimation de SOH, capacité incrémentale, profil aéronautique

Title : Performance and ageing quantification of electrochemical energy storage elements for aeronautical usage

Abstract : In the context of progress in the electrochemical energy storage systems in the transport field, especially in the aeronautics, the issues of performance, reliability, safety and robustness of these elements are essential for users. This thesis is focused on these issues for the more electric aircraft. The technologies studied correspond to the latest generation commercial elements of Lithium-ion batteries (NMC/ graphite + SiO, NCA/graphite, LFP/graphite, NMC/LTO), Lithium-Sulfur (Li-S), Supercapacitor and Lithium-ion capacitors. The first part of this manuscript is dedicated to the performance quantification of the different electrochemical energy storage elements in aeronautical environment [-20°C, 55°C] and usage. An efficient and accurate electro-thermal model is developed and validated. The second part is devoted to the calendar and power cycling ageings as well as to the presentation of abuse testing results. A State Of Health (SOH) estimation based on incremental capacity analysis method is proposed. Finally, the robustness of the storage elements during accelerated ageing tests with a specific profile for the aeronautical usage is evaluated. The ageing models and SOH estimation methods proposed in the previous sections are used here to evaluate the impact of temperature on the degradation rate and to estimate the SOH of the cells with this aeronautical profile.

Keywords : Lithium batteries, Supercapacitors, Lithium-ion capacitors, performance, low temperatures, calendar ageing, power cycling, abuse testing, electro-thermal model, non-isothermal Ragone plot, ageing laws, SOH estimation, incremental capacity, aeronautical profile